Solid State NMR Relaxation Studies of Triosephosphate Isomerase

Caitlin M Quinn

Submitted in partial fulfillment of the
requirements for the degree
of Doctor of Philosophy
in the Graduate School of Arts and Sciences

COLUMBIA UNIVERSITY
2013

ABSTRACT

Solid State NMR Relaxation Studies of Triosephosphate Isomerase

Caitlin Marie Quinn

Both protein structure and dynamics are essential to understanding biological function. NMR is a powerful technique for the observation of protein dynamics in that dynamics can be observed site-specifically over a wide range of timescales from picoseconds to seconds. Spin relaxation measurements, including relaxation in the rotating frame ($R_{1\rho}$), can be very sensitive to exchange processes in proteins, particularly on the millisecond-to-microsecond timescale. Using solid state NMR, few techniques exist that can *quantify* dynamics on this timescale.

Previous $R_{1\rho}$ measurements in the solid state have utilized reorientation of a dipole tensor to observe dynamics. This application is limited to systems where the nucleus of interest has an attached proton. Relaxation studies using the reorientation of a chemical shift tensor are applicable to a broader range of systems. Furthermore, solid state $R_{1\rho}$ experiments do not require a change in the isotropic chemical shift as is necessary in solution NMR.

We combined $R_{1\rho}$ measurements of the model compound dimethyl sulfone (DMS) with data-fitting routines in Spinevolution to show that $R_{1\rho}$ relaxation due to reorientation of a chemical shift tensor is a large effect in the solid state and these measurements can be used to quantify chemical exchange processes. The temperature dependence of the exchange rates determined with $R_{1\rho}$ measurements is in agreement with other measurements of the dynamics of DMS with various solid state NMR techniques. Deuteration and sparse isotropic labeling were necessary to

obtain quantitative results. To distinguish the exchange contribution to relaxation from other effects (R_2^0 relaxation), low temperatures and high spin-lock field strengths were utilized.

$R_{1\rho}$ experiments and magic angle spinning (MAS) one-dimensional spectra were used to characterize PO_4^{3-} ligand binding in the glycolytic protein triosephosphate isomerase. 1D spectra indicated the presence of both isotropic and anisotropic PO_4^{3-} populations. These states included an unbound state with an isotropic chemical shift tensor, and a protein-bound state in which the anisotropic features are reintroduced through chelation with protein backbone amides. The chemical shift anisotropy tensor of the bound PO_4^{3-} ligand was fit using spinning sideband analysis of slow MAS spectra and suggest the ligand is in a dianionic state. The temperature dependence of $R_{1\rho}$ measurements indicated a fast dynamic process above the microsecond timescale at physiological temperatures.

Table of Contents

Figures

Chapter 1

Chapter 2

Chapter 3

Chapter 4

Chapter 5

Chapter 6

Chapter 8

Tables

Chapter 2

Chapter 3

Chapter 4

Chapter 5

Chapter 6

Chapter 8

Acknowledgements

Doing all the work that has gone into this thesis has been a challenging and rewarding experience, one that I certainly could not have completed on my own. First and foremost, I would like to thank my advisor, Professor Ann McDermott, for her support and encouragement regarding every aspect of science and life. Every meeting gave me exciting new insight and ideas for my projects. She has challenged me scientifically and allowed me to grow as a critical thinking scientist. Her guidance has led this project to where it is today and formed me into the scientist that I am.

I would also like to acknowledge and thank my thesis committee members, Professor Ruben Gonzalez, Professor Arthur Palmer, who I also had the great experience of running with on Central Park Track Club, as well as Professors Angelo Cacciuto and Koji Nakanishi for participating in my thesis defense.

The National Institutes of Health have provided funding through the Biophysics Training Grant (T32GM 008281).

I have had the privilege of working with many people in the McDermott lab who are both great scientists and friends. They have contributed a great deal to this thesis. I would like to thank the following current and former McDermott lab members: Dr. Yimin Xu who built the foundation for my work on TIM and taught me the protein prep; Dr. Kuo-ying Huang and Dr. Wenbo Li for

many helpful discussions and sub-groups on protein dynamics and Spinevolution; Dr. Benjamin Wylie, our lab CSA expert, who always had insightful ideas; Dr. Manasi Bhate for helpful discussions on biochemistry, chemical shifts, and being a great friend, I will never forget all the laughs we shared over nitrogen fills; Dr. Ivan Sergyev, who was always selflessly willing to help with software and hardware issues; Claribel Nuñez and Salima Bahri who have been unfaltering sources of support and friendship in the many challenges that both a PhD and life in general can throw at you. Thank you girls! To Drs. Jaclyn Catalano and Simone Giechler who taught me a lot of biology, but more importantly, have been great friends; Dr. Ségolène Laage for her great ideas; Rivkah Rozowsky who always provided a bright outlook on things and asked great questions, and Dr. Ansgar Siemer who first taught me solid state NMR. And thank you to all my other friends in the chemistry department who made each day a little brighter. I could not have done this without any of you.

I would also like to thank my undergraduate advisor, Professor Matthew Kubasik of Fairfield University. He first introduced me to scientific research, brought me into the lab, and gave me a love for physical chemistry in general and NMR specifically. I would not have chosen this path without his support and guidance.

Last but certainly not least, I would like to thank my family for their unwavering support through the last 28 years, and especially the last 5. I know it hasn't always been easy! Mom and Dad, thank you for being there, no matter the time of day, for listening to my disappointments and celebrating my accomplishments. Your love and support has meant the world to me. I could not have done it without you! You have taught me the true meaning of strength in the face of

adversity. To my “little” sister Cara, words cannot express how much your support has meant to me. And of course thank you to the rest of my family who have supported me as well!

To my parents, who have supported me
from the very beginning

Chapter 1

Introduction to Solid State NMR and Protein Dynamics

With recent methodological and technological advances, solid state nuclear magnetic resonance (NMR) is an increasingly powerful technique for the study of protein dynamics. These advances include increasingly rapid magic angle spinning, improvements in decoupling, and efficient magnetization transfer through cross polarization. Numerous nuclear properties can be exploited for the study of dynamics in the solid state, including the chemical shift tensor, dipolar coupling, and quadrupolar tensor. These various NMR interactions allow for the study of protein dynamics on timescales ranging from picoseconds to seconds.

1.1 Introduction to Solid State Nuclear Magnetic Resonance

1.1.1 NMR Theory: Relaxation and Chemical Exchange

Relaxation in the Bloch Equations Spin angular momentum (**I**) is an inherent property of all nuclei, and is defined by the spin quantum number, *I*.

$$|\boldsymbol{I}| = [\boldsymbol{I} \cdot \boldsymbol{I}]^{1/2} = \hbar[I(I+1)]^{1/2} \quad (1)$$

The quantum number is quantized and can take on the values 0, +1/2, 1, +3/2, 2… Nuclei with a non-zero spin angular momentum also have a nuclear magnetic moment (**μ**) and are NMR active. These 2 quantities are related via the gyromagnetic ratio (γ), characteristic of each nucleus:

$$\boldsymbol{\mu} = \gamma \boldsymbol{I} \quad (2)$$

In the presence of an external magnetic field (**B**), the spin angular momentum energy levels split (Zeeman splitting), which causes a small spin population difference between energy levels (Boltzmann equilibrium distribution) and gives rise to a bulk magnetic moment of the spins, **M**.

Throughout this chapter, vector quantities are represented in bold. The bulk magnetization is the sum of the individual magnetic moments of all nuclei:

$$\boldsymbol{M} = \sum_i \mu_i \tag{3}$$

The simplest model to describe the behavior of spins in a magnetic field is the Bloch equations:

$$\frac{d\boldsymbol{M}(t)}{dt} = \boldsymbol{M}(t) \times \gamma \boldsymbol{B}(t) \tag{4}$$

where

$$M(t) = \begin{bmatrix} M_x(t) \\ M_y(t) \\ M_z(t) \end{bmatrix} \tag{5}$$

In the rotating frame, for a frequency $\omega = \gamma B(t)$, **M** is time-independent and precesses around **B** at a frequency $\omega_0 = \gamma B_0$. ω_0 is the Larmor frequency and B_0 is the static, external magnetic field (generally regarded to be along the z-axis in the laboratory frame). This simple semi-classical treatment of spins in nuclear magnetic resonance (NMR) spectroscopy requires that the spins are non-interacting (i.e. no scalar or dipolar couplings, see Section 1.1.2) spin-1/2 nuclei, coherent evolution is ignored, and the spin system is homogeneous (no anisotropic interactions). A spin-1/2 nucleus is one where the spin quantum number is ½.

The system can be perturbed by radio frequency irradiation (a B_1 field) such that the magnetization is no longer parallel to B_0 and has components in the x,y-plane. When the B_1 field is turned off, the system returns to equilibrium through an increase in longitudinal magnetization $M_z(t)$ and a decrease in transverse magnetization, $M_x(t)$ and $M_y(t)$. This evolution of magnetization can be described through the relaxation rates R_1 and R_2:

$$M_z(t) = M_0 - [M_0 - M_z(0)]e^{-R_1 t} \tag{6}$$

$$M_x(t) = M_x(0)e^{-R_2 t}$$

$$M_y(t) = M_y(0)e^{-R_2 t}$$

R_1 and R_2 are the longitudinal (spin-lattice) and transverse (spin-spin) relaxation rates, respectively. The resulting Bloch equations can be written in matrix form as

$$\frac{d\boldsymbol{M}(t)}{dt} = \begin{bmatrix} -R_2 & -\Omega & \omega_1 sin\phi \\ \Omega & -R_2 & -\omega_1 cos\phi \\ -\omega_1 sin\phi & \omega_1 cos\phi & -R_1 \end{bmatrix} \boldsymbol{M}(t) + R_1 M_0 \begin{bmatrix} 0 \\ 0 \\ 1 \end{bmatrix} \quad (7)$$

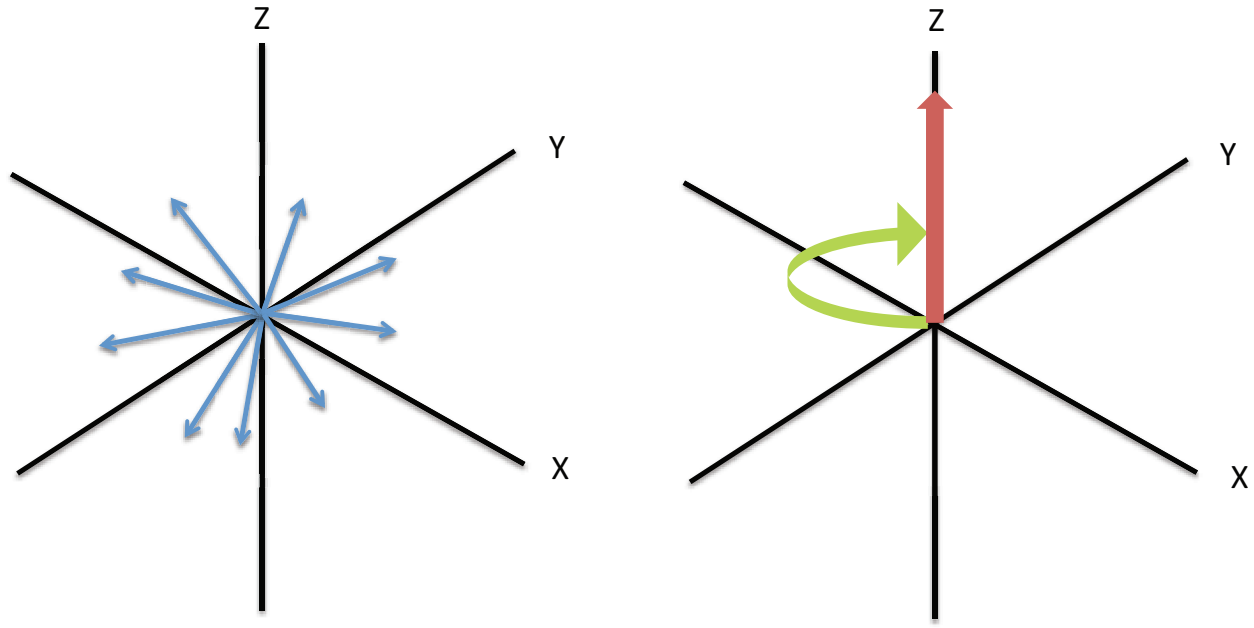

Figure 1.1 Depiction of longitudinal relaxation. After perturbation by an RF field, the magnetization is randomized with regard to the z-axis (left). R_1 is the rate at which the magnetization returns to being aligned along the z-axis.

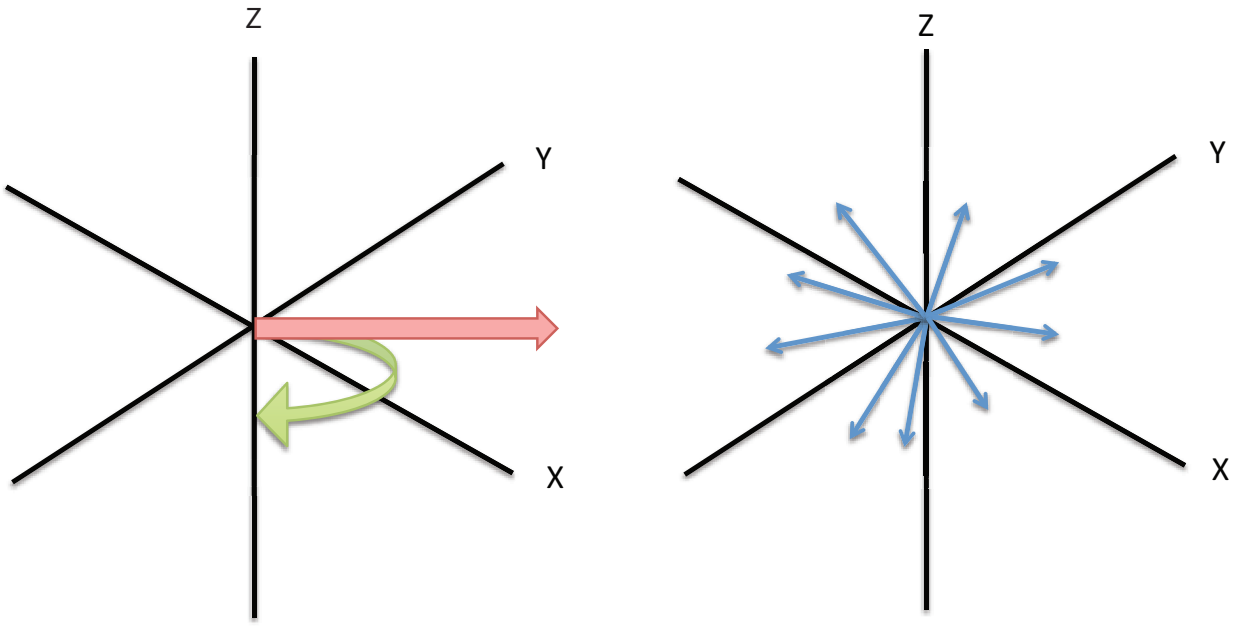

Figure 1.2. Depiction of transverse relaxation. After magnetization is flipped coherently into the x,y-plane, the magnetization dephases in this plane with the rate R_2.

The Solomon Equations The Solomon equations are a more advanced treatment of spin-lattice relaxation in nuclear magnetic resonance than the Bloch equations [1]. The Solomon equations are able to account for interactions between spins. This treatment considers the rate of transitions of the spins between energy levels, reflected in changes in spin state. W_I and W_s are the rate constants for flipping spin I and spin S respectively. W_0 is known as a flip-flop transition where the spins flip in opposite directions. W_2 is a flip-flip transition where the spins flip in the same direction. The auto- and cross-relaxation rates are derived from the changes in the relative populations of the states. W_0 and W_2 constitute the cross-relaxation in which the return of each spin to Boltzmann equilibrium is coupled to the other spin.

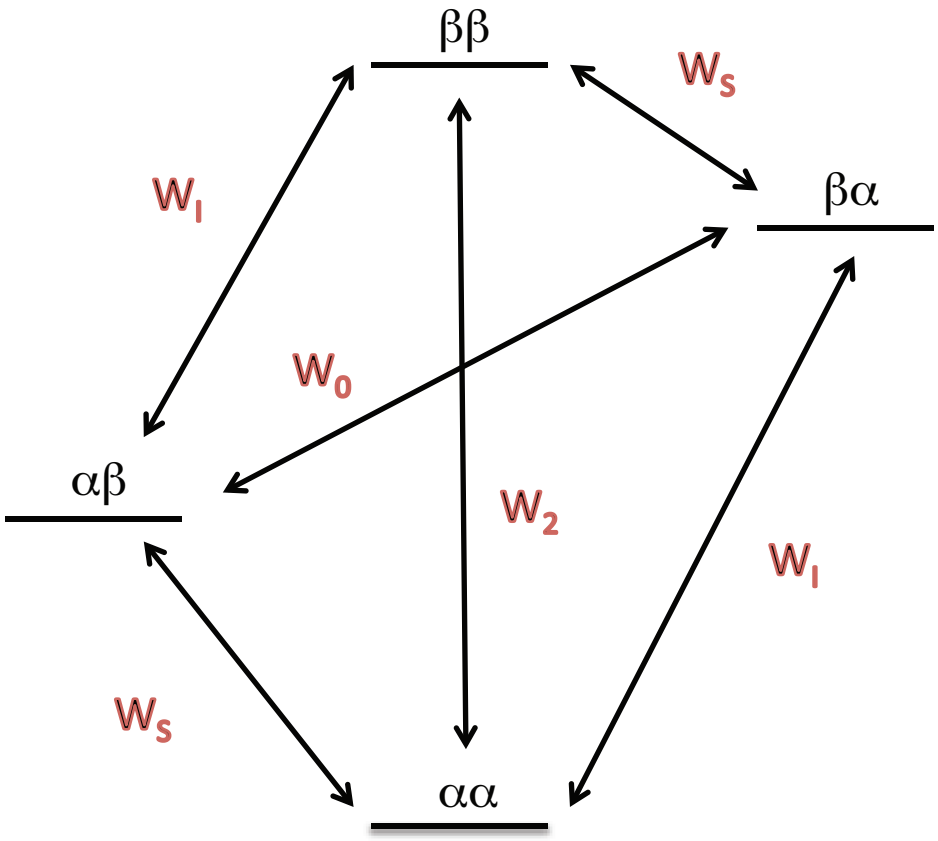

Figure 1.3 Depiction of spin transitions between spin states as defined according to the Solomon equations.

$$\langle I_z \rangle(t) = P_{\alpha\alpha} + P_{\alpha\beta} - P_{\beta\alpha} - P_{\beta\beta} \tag{8}$$

$$\langle S_z \rangle(t) = P_{\alpha\alpha} - P_{\alpha\beta} + P_{\beta\alpha} - P_{\beta\beta}$$

$$\frac{d\Delta I_z(t)}{dt} = -(W_0 + 2W_I + W_2)\Delta I_z(t) - (W_2 - W_0)\Delta S_z(t) \tag{9}$$

$$\frac{d\Delta S_z(t)}{dt} = -(W_0 + 2W_S + W_2)\Delta S_z(t) - (W_2 - W_0)\Delta I_z(t)$$

Relaxation is an important concept in nuclear magnetic resonance (NMR). Consequences of relaxation include resonance linewidth, signal decay, and recycle delays. Relaxation also assists

in structure determination via NOEs (Nuclear Overhauser Effect) [2-4], and is a key method for monitoring chemical exchange and protein dynamics [5-7].

Chemical Exchange Chemical exchange monitors the movement of a nucleus between two or more environments due to chemical processes or conformational changes. NMR is a powerful method for observing chemical exchange [1, 6]. In the simplest case, a spin exchanges between 2 magnetic environments separated by $\Delta\omega$. This process can be described as follows:

$$A \underset{k_{-1}}{\overset{k_1}{\rightleftharpoons}} B \tag{10}$$

The exchange rate $k_{ex} = k_1 + k_{-1}$. The isotropic chemical shift difference between the 2 sites is defined as $\omega_A - \omega_B = \Delta\omega$. The relative populations of the two exchanging sites are determined by the exchange rates: $p_A k_1 = p_B k_{-1}$. When $k_{ex} > \Delta\omega$, chemical exchange is fast and a single resonance is observed at the population-weighted average chemical shift of the two sites. When $k_{ex} < \Delta\omega$, exchange is slow on the chemical shift timescale and two separate resonances are observed in the spectrum. When k_{ex} is on the order of $\Delta\omega$, known as the coalescence condition, the system is in intermediate exchange and the resonance lines coalesce. The one-dimensional NMR spectrum as a system with $p_A = p_B = 1/2$ moves from slow to intermediate to fast exchange is shown in Figure 1.4.

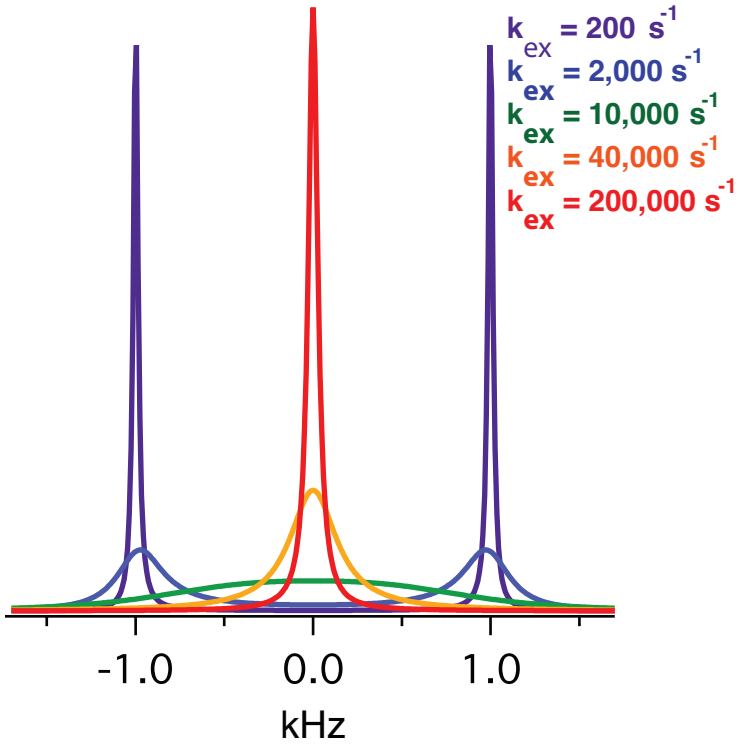

Figure 1.4 Chemical exchange lineshapes for a system undergoing chemical exchange showing the transition from 2 sharp peaks, through coalescence to a single peak at the population-weighted average shift of the 2 exchanging sites. Spectra simulated using Spinevolution [8], with $p_A = p_B = 0.5$, $\Delta\omega = 2000$ Hz, and k_{ex}: (–) 200 s^{-1}, (–) 2,000 s^{-1}, (–) 10,000 s^{-1}, (–) 40,000 s^{-1}, (–) 200,000 s^{-1}.

Advances in nuclear magnetic resonance now allow for the observation of chemical exchange in large biomolecules; this is particularly powerful for detecting high energy protein conformers with small populations that are important for function [9].

1.1.2 NMR Interactions

The Chemical Shift Tensor The chemical shift tensor arises from a change in the resonance frequency of a nucleus due to shielding by its surrounding electrons, which produce a secondary field in a static magnetic field. The chemical shielding Hamiltonian acting on spin I is

$$H_{cs} = \gamma \boldsymbol{I} \cdot \boldsymbol{\sigma} \cdot \boldsymbol{B_0} \tag{11}$$

where σ is the shielding tensor and B_0 is the applied magnetic field.

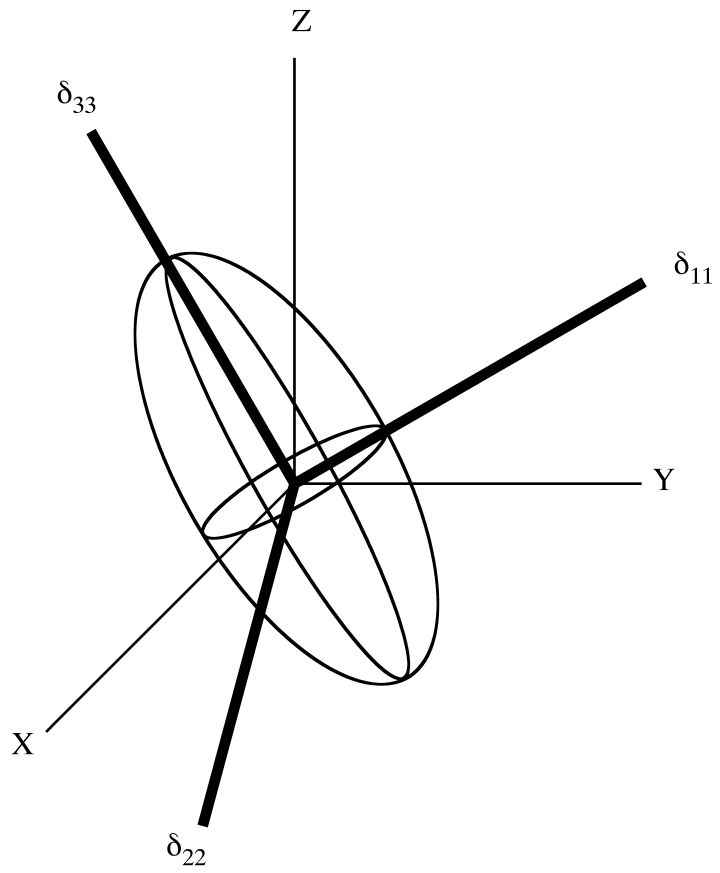

Figure 1.5 Depiction of a chemical shift tensor and its components relative to the X,Y,Z laboratory frame.

The chemical shift tensor can be broken down into isotropic and anisotropic components. The principal values of a chemical shift tensor are defined such that $\delta_{11} > \delta_{22} > \delta_{33}$. δ_{11} is the most downfield, or least shielded component. To determine the anisotropy and asymmetry of the chemical shift tensor, these components are mapped to δ_{xx}, δ_{yy}, and δ_{zz} relative to the isotropic chemical shift. In the principle axis system (PAS), chosen such that the shielding tensor is diagonal, the chemical shift can be defined in terms of the isotropic shift (δ_{iso}), reduced anisotropy (δ), and asymmetry (η) in the Haeberlen convention [10]:

$$\delta_{iso} = \frac{1}{3}(\delta_{xx}+\delta_{yy} + \delta_{zz}) \quad (12)$$

$$\delta = \delta_{zz}-\delta_{iso} \quad (13)$$

$$\eta = \frac{\delta_{xx}-\delta_{yy}}{\delta} \quad (14)$$

δ_{xx}, δ_{yy}, and δ_{zz} are defined such that $|\delta_{zz} - \delta_{iso}| \geq |\delta_{xx} - \delta_{iso}| \geq |\delta_{yy} - \delta_{iso}|$.

The chemical shift tensor is a powerful reporter of local chemical/magnetic environment. In recent years, the development of high-resolution NMR techniques, including magic angle spinning (MAS), high power decoupling, and cross polarization (CP) [11], have allowed the resolution and assignment of isotropic chemical shifts and anisotropic interactions [12-17] in macromolecules including proteins. Significant differences in isotropic chemical shift are observed for C_α, CO, and C_β sites in proteins among a wide variety of structural features (α-helix, β-sheet, random coil, triple helix, etc) [18-20], with α-helices tending to be downfield relative to β-sheets for C_α and CO by an average of 4-5 ppm, while the opposite trend is observed for C_β, with random coils falling in the average of the two other secondary structural elements. Numerous programs exist to predict chemical shifts of proteins based upon different methods (i.e. SPARTA [21], SHIFTX [22], etc), or alternatively predict torsion angles from experimental chemical shifts (TALOS, [23]).

Given its orientation dependence, the CSA of a protein resonance is sensitive to key structural features, such as secondary structure, hydrogen bonding, and electrostatics [24] and thus can be used to monitor protein dynamics and calculate structures. The chemical shift anisotropy tensor has a broad variety of applications in nuclear magnetic resonance, from characterizing relaxation

pathways and dynamics, to optimizing TROSY conditions [25]. Ab initio quantum chemical studies of the dependence of the C_α and C_β CSA tensors of the 20 amino acids on torsion angles have been reported by Oldfield and co-workers [24, 26]. Generally, they observed the CSA tensors of all amino acids to have relatively large spans (≈ 34 ppm) with virtually no difference between α-helix and β-sheet conformations (the notable exception being the C_α of β-disubstituted amino acids, i.e. Val, Ile, Thr). Ramamoorthy and co-workers reported experimental measurements of the conformation dependence of C_α, C_β, and CO CSA tensors for Ala and Gly in polypeptides [27]. This work supported the work of Oldfield, observing that carbonyl and C_α CSA tensors in various conformations have similar spans, though different isotropic shifts and principle components. Only the δ_{22} element depends on the CO-NH hydrogen bond length in the polypeptides. This idea can be extended to state that while the overall magnitude of the CSA tensor may not be particularly sensitive, the individual tensor components can be [25]. Systematic measurements of carbon and nitrogen CSA tensors of GB1 by Wylie et al revealed several trends regarding the correlation of the principle values with structure [28, 29]. The anisotropy averages 6 ppm higher for ^{15}N tensors in α-helicies relative to β-sheets; the asymmetry parameter η averages 0.53 in α-helixical residues and 0.72 in β-sheets. The sensitivity of the chemical shift tensor to local environment and/or orientation of the chemical shift tensor as it changes during chemical exchange make the CSA tensor an excellent probe of dynamics in biomolecules.

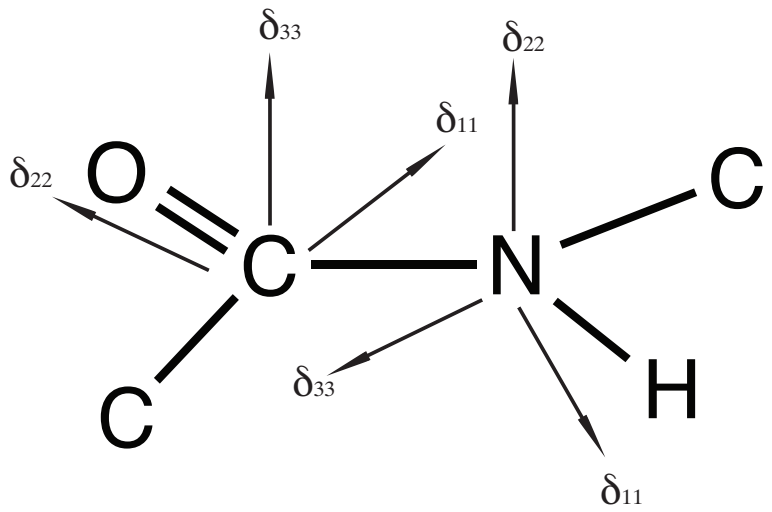

Figure 1.6 Average orientations for the principle axes of the chemical shift tensor for a peptide fragment. For the carbonyl carbon, the most shielded component, δ_{33}, is perpendicular to the plane of the peptide backbone. δ_{22} is along the C-O bond, and δ_{11} is along the CO-C_α bond [27]. For nitrogen, the least shielded component, δ_{11}, lies along the N-H bond [30].

The Dipolar Tensor The dipolar tensor is a through-space interaction of two or more nuclear spin magnetic moments. The strength of a dipolar coupling has a distance-dependence of $1/r^3$, as well as an orientation-dependence (Figure 1.7). The dipolar Hamiltonian can be expressed as

$$H_{dd} = -2\boldsymbol{I} \cdot \boldsymbol{D} \cdot \boldsymbol{S} \tag{15}$$

where **D** is the dipolar coupling tensor which takes on values of *–d/2, -d/2, +d* (for values of *d* see equation 18). For homonuclear dipolar couplings, where the 2 interacting spins are the same, the first-order average Hamiltonian is given by

$$H_{dd} = -d\frac{1}{2}(3cos^2\boldsymbol{\theta} - 1)[3I_zS_z - \boldsymbol{I} \cdot \boldsymbol{S}] \tag{16}$$

and for heteronuclear systems is

$$H_{dd} = -d(3cos^2\theta - 1)I_zS_z \tag{17}$$

where *d* is the dipolar coupling constant, which is on the order of kHz and varies greatly depending on the nuclei of interest:

$$d = \hbar\left(\frac{\mu_0}{4\pi}\right)\frac{1}{r^3}\gamma_I\gamma_S \quad (18)$$

where μ_0 is the permativity of free space and θ is the angle between the internuclear vector and the static magnetic field, B_0.

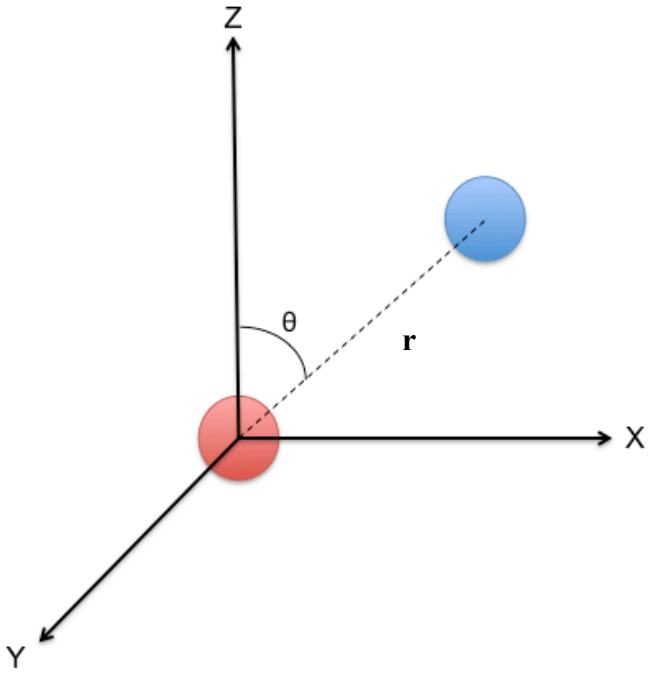

Figure 1.7 Distance and orientation dependence of the dipolar interaction between 2 nuclei. The static magnetic field B_0 is assumed to be along the z-axis in the laboratory frame. θ is the angle between the internuclear vector and the static magnetic field. r is the distance between the 2 nuclei.

Heteronuclear dipolar couplings are an inhomogeneous interaction that can largely be averaged out by magic angle spinning given that the MAS frequency is greater than the dipolar coupling. An inhomogeneous interaction shifts the energies of the Zeeman states, or is a so-called 'flip-flip' transition in which the 2 spins (in a simplified 2 spin system) are flipped in the same direction. Homonuclear dipolar coupling (i.e. among protons) is a homogeneous interaction that is a greater challenge to remove. This interaction mixes degenerate Zeeman states and involves a 'flip-flop' transition where the spins are flipped in opposite directions. A flip-flip transition is depicted by the transition W_2 in Figure 1.2, and a flip-flop transition is depicted by W_0. α and β

represent the direction of the spins. The appearance of these terms in the Solomon equations is discussed in Section 1.1.1. Important consequences of the homonuclear coupling are rapid spin diffusion among the coupled spins and linebroadening [31].

Dipolar interactions are on the order of kHz and are a major source of linebroadening in solid state NMR spectroscopy; decoupling techniques and magic angle spinning are utilized to reduce this broadening (discussed below). However, there is a great deal of structural and dynamic information contained in dipolar interactions as well [32, 33].

The Quadrupolar Tensor Quadrupolar nuclei are nuclei with spin > ½. These nuclei possess an electric quadrupole moment that interacts with electric field gradients (EFGs) arising from variation in nuclear charge distribution. The quadrupolar moment of a particular nucleus is constant and does not change with chemical environment [34]. However, the electric field gradient of the quadrupole does depend on surrounding electrons and other nuclei, and thus depends on the orientation relative to the applied magnetic field B_0.

The quadrupolar Hamiltonian can be expressed as

$$H_Q = \frac{eQ}{2I(2I-1)\hbar} \boldsymbol{I} \cdot \boldsymbol{V} \cdot \boldsymbol{I} \tag{19}$$

where V is the 2nd rank tensor for the electric field gradient and Q is the nuclear quadrupolar moment. The quadrupolar coupling constant is:

$$C_Q = \frac{e^2 qQ}{\hbar} \tag{20}$$

Here *e* is the charge of an electron and e*q* is the anisotropy of the EFG tensor, analogous to the anisotropy of a chemical shift tensor as described above [35]. The most commonly used quadrupolar nucleus, particularly in dynamics studies of proteins, is deuterium (^{2}H), which has the spin I = 1. The relatively small dipolar couplings between quadrupolar nuclei and neighboring spin-1/2 nuclei make quadrupolar nuclei an important component of high resolution studies of protein dynamics [34, 36].

1.1.3 Experimental Techniques for Solid State NMR

Magic Angle Spinning Due to the absence of molecular tumbling that allows for narrow linewidths and high resolution in solution NMR, solid state NMR suffers from broad resonances due to the random molecular orientations in a powder sample. The observed linewidths arise from anisotropic interactions including the chemical shift, dipole-dipole couplings, and quadrupolar interactions, giving each orientation in the sample a unique frequency. θ is the angle between the z-axis of the tensor in the PAS and the B_0 field. The random orientation of the molecules in a powder sample causes θ to take on all values and would give the broad spectrum seen in the bottom panel of Figure 1.8. The form of the orientation dependence of the interaction tensor for interactions such as the chemical shift anisotropy and heteronuclear dipolar pair is $3\cos^2\theta - 1$. In order to obtain high resolution in the solid state, magic angle spinning (MAS), developed by Andrew et al [37] and Lowe [38], is utilized.

Magic angle spinning involves rotating a sample at an angle of $\theta_R = 54.7°$ which is the angle between the rotor axis and the static magnetic field B_0. θ varies with time as the interaction

tensors rotate within the sample. The average orientation dependence of the interaction tensor becomes

$$\langle 3cos^2\theta - 1\rangle = \frac{1}{2}(3cos^2\theta_R - 1)(3cos^2\beta - 1) \quad (21)$$

β is the angle between the z-axis of the tensor in the PAS and the rotor axis. When $\theta_R = 54.7°$, $3\cos^2\theta_R - 1 = 0$ and the average orientation dependence of the anisotropic interaction averages to zero for orientations along the rotor axis.

For magic angle spinning to effectively average an anisotropic interaction, the rate of spinning has to be fast relative to the magnitude of the interaction. This concept is depicted in Figure 1.8. When the spinning speed is 0 kHz, a CSA tensor of 5 kHz gives the powder pattern seen on the bottom. As the spinning gradually increases, this powder pattern splits into several lines spaced apart by the rotor speed in kHz (spinning sidebands), and eventually forms a sharp peak at the isotropic chemical shift. The development of larger B_0 fields has led to greater sensitivity but requires ever faster MAS to average out the CSA, which scales with the square of the field [39, 40]. Magic angle spinning speeds upwards of 70 kHz can now be achieved

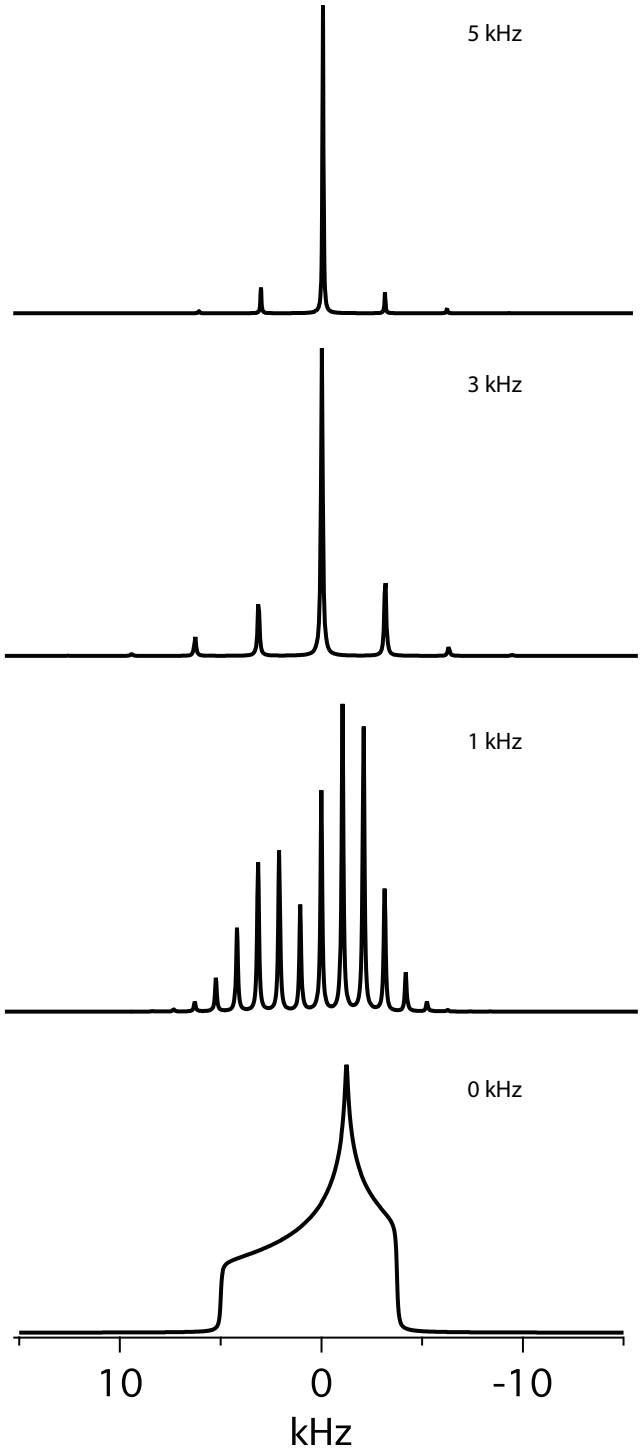

Figure 1.8 The effect of magic angle spinning (MAS) on a chemical shift tensor. As the MAS rate is increased, the powder pattern becomes a single peak at the isotropic chemical shift. Spectra were simulated with a CSA of 5 kHz and an asymmetry of 0.5 [8].

Cross Polarization Cross polarization (CP) is used in solid state NMR to transfer magnetization from an abundant nucleus (i.e. protons) to a sparse nucleus (i.e. carbon or nitrogen, referred to here collectively as X). Cross polarization can help compensate for some issues that arise from the detection of these sparse nuclei. Due to the low number of spins, signal-to-noise is often a challenge. The weaker dipolar couplings of these nuclei mean long relaxation times. Cross polarization is mediated by the dipolar coupling between protons and carbon or nitrogen. The key component is the simultaneous irradiation of the carbon and proton channels at the optimal frequencies and field strengths (ω_1, the power of the applied irradiation) for maximum magnetization transfer after exciting proton magnetization with a 90° pulse. In order for efficient magnetization transfer to occur, the H and X fields must be set to the Hartmann-Hahn condition [11]:

$$\gamma_H B_1^H = \gamma_X B_1^X \tag{22}$$

B_1 are the spin-lock fields applied on the proton and X channels. The Hartmann-Hahn condition is set such that their nutation frequencies (ω_1) are equal. Under modern fast MAS, this condition can become narrow and inefficient. However, rotational resonance [41] gives rise to higher order matching conditions at integer multiples of the rotor frequency:

$$\omega_1^H - \omega_1^X = n\omega_R \tag{23}$$

$n = \pm 1, \pm ½$. Utilizing cross polarization can give sensitivity enhancement of up to γ_H/γ_X. However the experimental signal intensity depends on the proton relaxation rate, $R_{1\rho}{}^H$, and length of spin-lock (CP contact time); because magnetization originates on proton, the repetition rate (pulse delay) now depends only on the proton R_1, which is generally considerably faster than the X nucleus R_1.

Homonuclear and Heteronuclear Decoupling Dipolar coupling of sparse spins to more abundant protons and coupling among protons lead to significant broadening in carbon and nitrogen spectra (heteronuclear and homonuclear coupling respectively). Proton-X nucleus dipolar couplings are on the order of 10s of kHz. The coupling of proton or carbon spins to one another can also contribute to line broadening (homonuclear coupling, ~ 2 kHz for carbon, up to 120 kHz for protons depending on internuclear distance). Removing the effects of these spin-spin interactions (i.e. through decoupling) is an important pulse sequence element to attain high resolution spectra [42].

As mentioned above, attenuating the dipolar couplings among protons requires homonuclear decoupling schemes [31]. Many homonuclear decoupling schemes utilize the combined rotation and multiple pulse sequences (CRAMPS) technique [43]. Homonuclear decoupling schemes can be broken into groups: Solid-echo based sequences which include WAHUHA [44] and MREV [45], Lee-Goldburg based sequences including LG [46] and PMLG [47] decoupling, and rotor-synchronized sequences such as CN_n^v and RN_n^v [48]. The basic setup of solid-echo based sequences is an on-resonance pulse train: 90_x-τ-90_{-y}-2τ-90_y-2τ-90_{-x} [31]. Due to interference effects between simultaneous radio frequency (RF) irradiation and magic angle spinning these decoupling schemes are not effective at fast MAS rates. Lee-Goldburg (LG) type decoupling is achieved through off-resonance irradiation of the protons to generate a 360° nutation frequency. One of the most effective LG decoupling schemes is phase-modulated Lee-Goldburg decoupling (PMLG), which utilizes on-resonance application of a series of pulses with discrete phases. PMLG decoupling has been shown to be effective at spinning speeds of up to 65 kHz [49]. Rotor-synchronized decoupling schemes were pioneered by Malcom Levitt, and utilize the fact

that different spin interactions behave differently under rotation [31]. These decoupling schemes apply 180° pulses for *n* rotor periods, divided into *N* (CN) or *N/2* (RN) intervals, each element with a phase shift. RN_n^v sequences are successful at spinning speeds of up to 30 kHz.

Heteronuclear decoupling, particularly decoupling of protons from carbons, is critical to achieve high resolution and signal-to-noise. Generally speaking, the inherently broader linewidths of solid state NMR dictate that dipolar decoupling, but not J-decoupling, is necessary to achieve maximum resolution. Experimental setup is critical to decoupling efficiency; a key is setting the carrier to the frequency of the spins to be decoupled. Continuous wave decoupling (the application of continuous RF irradiation to protons) can be effective at lower B_0 fields when the RF power is on the order of the proton bandwidth [50]. Decoupling schemes can be very sensitive to resonance offsets, which can arise from many factors including protons in the sample having a range of frequencies, resonance offset of the proton carrier, and even magic angle spinning. An important experimental consideration is the high power levels that are necessary to sufficiently decouple protons (typically ~50 – 100 kHz). Recent developments in ultrafast magic angle spinning have been effective at reducing the required power levels, but power-handling limitations of probes must be considered in any solid state experiment.

Advanced composite pulse sequences help overcome these effects, including two pulse phase modulation (TPPM) [51], SPINAL [52], and x-inverse-x (XiX) [53]. TPPM decouping consists of a train of 2 repeating pulses with a constant nutation angle (~170°) and a phase difference of ~ 15°. SPINAL 'super-cycled' decoupling schemes consist of a series of pulses with a nutation angle of ~ 165° and phases 10°, -10°, 15°, -15°, 20°, -20°, 15°, -15°, which is then repeated a

certain number of times [50]. XiX decoupling consists of a pair of pulses with alternating phases, x and –x. TPPM and SPINAL have been shown to perform better at slower spinning speeds, while XiX is comparable to TPPM at speeds of ~ 30 kHz [50].

Proton decoupling during acquisition is important for spectral resolution, but is also utilized during other pulse sequence elements to remove effects of couplings of carbon to protons. This decoupling during the evolution of magnetization is particularly important in studies of dynamics. Interference effects are common in decoupling, and include the HORROR (Half of Rotational Resonance) condition when RF irradiation is ~ 1/2 the MAS rate which recouples homonuclear dipolar interactions [54]. The dynamics of a molecule, while reducing the strength of couplings, can also interfere with decoupling efficiency [55].

1.2 High Resolution Methods for Studying Protein Dynamics in the Solid State

Protein structure has been a key area of study for biologists, chemists, and physicists for many years. Numerous Nobel prizes have been given for protein structures determined using x-ray crystallography and nuclear magnetic resonance spectroscopy. The first were Max Perutz and John Kendrew (1962) and Kurt Wüthrich (2002) for crystallography and NMR structures respectively [56]. More recently, it has been acknowledged by the scientific community that in addition to structure, studies of protein dynamics are critical to the understanding of biological function [57-60]. Biological processes occur on a wide range of timescales, ranging from femtoseconds to seconds, as shown in Figure 1.9. Many biophysical techniques exist to monitor protein dynamics. Each of these techniques has inherent advantages and disadvantages and is

applicable to particular timescales of dynamics, which often dictate the choice of method to probe the dynamics of a particular protein. Techniques to probe protein dynamics include small angle x-ray scattering (SAXS, [61]), near-IR femtosecond spectroscopy [62], Raman scattering [63], numerical simulations, nuclear magnetic resonance (NMR) spectroscopy [58], fluorescence resonance energy transfer (FRET, [64]), terahertz spectroscopy [65], hydrogen/deuterium exchange [66], atomic force microscopy (AFM, [67]), and single-molecule optical tweezers pulling experiments [68] to name a few.

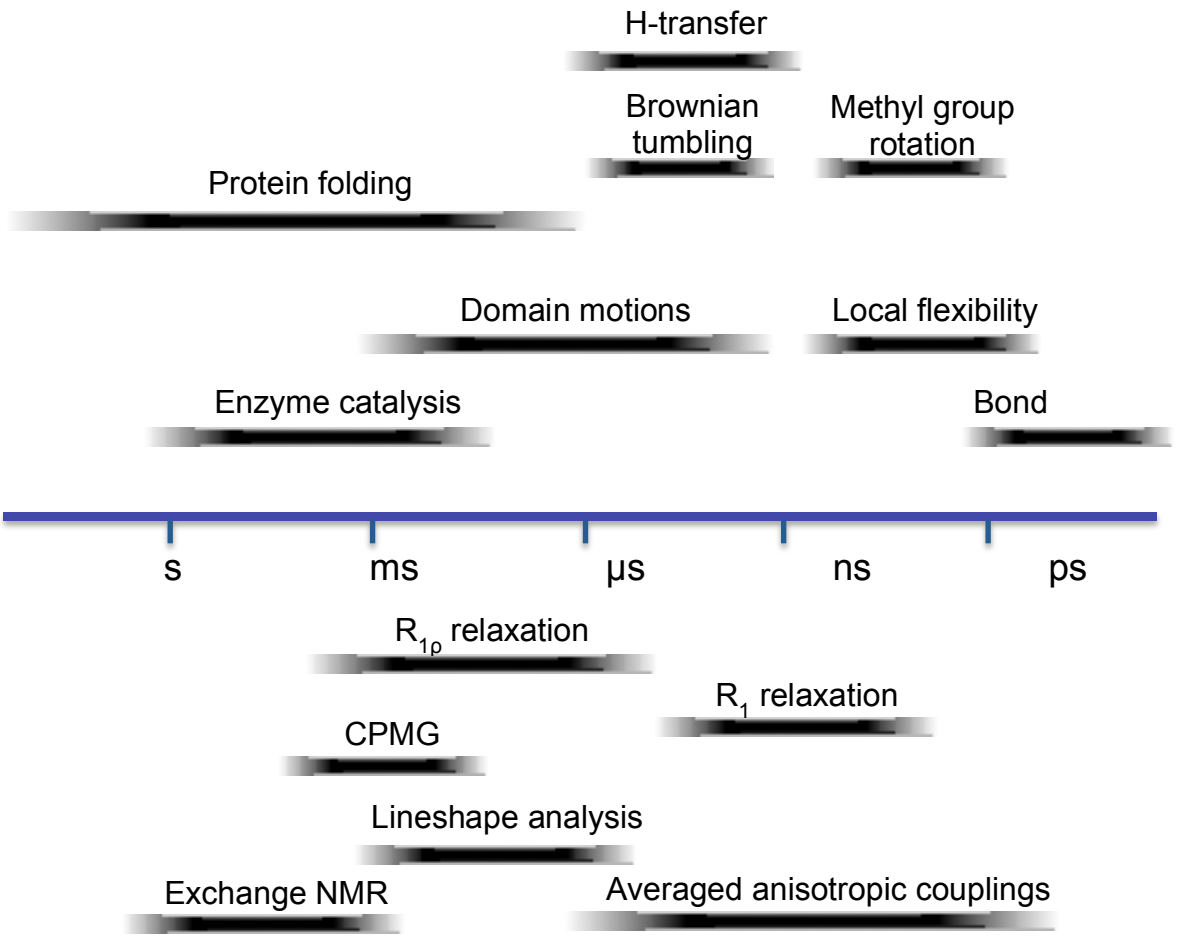

Figure 1.9 Timescales of dynamics for various motional processes in biological systems and NMR experiments used to observe dynamics on these timescales [69].

NMR has a unique advantage over other biophysical techniques in that it has the capacity to site-specifically monitor multiple sites of a protein simultaneously. Furthermore, solid state NMR can access systems that are not available to solution NMR spectroscopists, including large and insoluble systems such as membrane proteins and amyloid fibrils, as well as possessing the ability to observe the hydration-dependence of dynamics. In solution NMR, molecular tumbling can obscure internal dynamics, requiring methods that indirectly probe changes in isotropic chemical shift [70]. Solid state NMR studies do not have this limitation. A wide range of observables in nuclear magnetic resonance, including chemical shift, dipolar, and quadrupolar tensors discussed above allow NMR to access a wide range of dynamic timescales from picoseconds to seconds. Techniques exist to observe protein dynamics in both solution and the solid state over all these timescales. Averaged anisotropic couplings (RDCs, order parameters, [71, 72]) and laboratory-frame spin-lattice relaxation (R_1, [73]) are sensitive to microsecond-to-picosecond dynamics. Line shape analysis [74, 75] and rotating-frame spin-lattice relaxation [76-78] detect millisecond-to-microsecond dynamics. Exchange techniques such as CODEX are sensitive to millisecond and slower dynamics [79-81].

Recent developments in solid state NMR spectroscopy now allow for the relatively efficient acquisition of atomic resolution protein spectra in both solution and the solid state. These developments include uniform and sparse labeling schemes and deuteration [82, 83], high power proton decoupling, and fast magic angle spinning. Work on perdeuterated proteins is becoming an increasing common practice. Deuteration allows for high resolution studies of protons, which have high sensitivity due to their large gyromagnetic ratio [36]. With the ability to collect high resolution, high signal-to-noise protein spectra with relative ease [69, 84, 85], comes the

opportunity to study site specific quantitative protein dynamics as well. Emerging techniques in the measurement of protein dynamics via nuclear magnetic resonance can detect dynamics ranging from the picosecond to second timescales, as well as measure multiple sites within a protein and obtain information about mobility for various regions of a protein simultaneously [86]. Dynamics studies in the solid state present the unique ability to measure dynamics in membrane proteins and amyloids [87, 88]. Key techniques are discussed below and sample pulse programs are shown in Figure 1.10.

Spin Relaxation R_1, $R_{1\rho}$, and R_2 relaxation monitor longitudinal relaxation, longitudinal relaxation in the rotating frame, and transverse relaxation in the laboratory frame respectively. R_1 studies are particularly useful for the study of fast timescale dynamics (nanosecond regime), and in the solid state allow for the measurement of local structural fluctuations and can provide information on both geometry and timescale of motion [89]. This method has been used to study the dynamics of amide nitrogens in the protein backbone including Crh [90], and α-spectrin SH3 [91], and more recently R_1 studies of carbons C', C_α and C_β [89]. In these experiments, there is access to a greater range of timescales than complementary solution NMR experiments, which can miss fast dynamics due to molecular tumbling. Solid state nitrogen R_1 values have been shown to map very closely to values measured in solution [36]. The labeling of only nitrogen atoms reduces the spin-diffusion contribution to relaxation. Quantitative rates of dynamics can be extracted using a spectral density analysis [73]. Moving beyond nitrogen labels to carbon resonances, spin diffusion becomes a concern but it has been shown that fast magic angle spinning (> 60 kHz, now attainable with modern instruments) can reduce proton spin diffusion to rates lower than R_1.

Complementary to R_1 studies is the technique of using a 'model-free' approach to analyze site-specific order parameters, giving information on amplitudes of motion [72, 87, 92]. The model-free formalism assumes a Lorentzian spectral density function [93]. While experimentally, the form of the spectral density function is not necessarily Lorentzian, it has been shown that for many cases, this approximation is excellent [94]. Order parameters are generally determined from dipolar interactions. Reductions in order parameters for the colicin Ia channel domain upon membrane association indicated increased flexibility of the system in a lipid bilayer [87]. Measured order parameters for ubiquitin gave a global perspective on the flexibility of the protein in a crystalline state [72]. Other recent examples include the study of arginine dynamics in a membrane-bound peptide [95]; Polenova and co-workers combined order parameter measurements with other dynamics techniques to observe that irregular secondary structural elements have greater internal mobility than helices or sheets [96]. Many additional examples of applying order parameters to observe dynamics in both solid state and solution NMR can be found in the literature.

$R_{1\rho}$ experiments measure spin-lattice relaxation in the rotating frame. Various techniques have been reported in the literature for this method of monitoring protein dynamics [97-99] utilizing proton and heteronuclear relaxation. In an $R_{1\rho}$ experiment, magnetization is spin-locked along an effective field in the rotating frame by the application of a continuous wave pulse on the nucleus of interest. The rate of decay during the spin-lock is measured to determine $R_{1\rho}$. $R_{1\rho}$ relaxation for dynamic processes possesses a characteristic field strength dependence, or dispersion [6]. A challenge of $R_{1\rho}$ experiments, particularly to quantify protein dynamics in the

solid state, is to avoid a variety of interfering effects. $R_{1\rho}$ studies have been used to observe μs dynamics of backbone nitrogens in U-^{15}N α-spectrin SH3 [100], and hydration-dependence of dynamics in T4 lysozyme and αβ-crystallin [101]. The derivation of $R_{1\rho}$ that results from the reorientation of a chemical shift tensor is outlined in the Appendix, Chapter 8, Section 8.1.

The analysis of R_2 in the solid state is somewhat ambiguous [69]. Static (coherent) contributions to the R_2 relaxation rate are difficult to separate from dynamic contributions. As a result, R_2 experiments are not widely used, but recently these measurements have been accomplished on ubiquitin by Schanda and co-workers [102]. An additional method to study intermediate timescale dynamic processes frequently used in solution NMR is Carr-Purcell-Meiboom-Gill (CPMG) relaxation dispersion [103, 104]. CPMG experiments observe R_2 relaxation as a function of the CPMG frequency (related to length of time between 180° pulses during the CPMG periods).

The number of free parameters in $R_{1\rho}$ measurements allows much information to be determined at a single B_0 magnetic field strength. The continuous wave spin-lock used in $R_{1\rho}$ experiments is far less susceptible to interference effects from anisotropic interactions, magic angle spinning, and the CPMG frequency related to the 180° pulses utilized in CPMG.

Exchange Experiments Exchange spectroscopy techniques probe dynamics on slower timescales than spin relaxation (millisecond-to-second timescale) [70].

Centerband Only Detection of Exchange (CODEX) is one of the most powerful and widely used exchange techniques [105]. The original CODEX experiment first evolves the spins under the chemical shift anisotropic interaction. The magnetization is returned to the z-axis for the mixing time. If dynamics occur during the mixing time, the orientation-dependent frequency changes, and the anisotropic chemical shift is not fully refocused. Derivatives that utilize dipolar interactions have also been developed [106, 107]. The power of this technique is in the ability to analyze peaks in one dimension without sidebands and the ability to use faster magic angle spinning, while previous 2D exchange experiments were limited by spectral overlap and broad lines. CODEX and dipolar CODEX have been used to study a broad range of proteins and smaller biomolecules, including α-spectrin SH3 [106], the membrane-bound peptide(s) protegrin-1 [108], as well as numerous organic polymers [109-111]. Given the long exchange times necessary to detect slow dynamics, there are important experimental considerations, including T_1 effects and coherent and diffusive magnetization exchange.

Additional one-dimensional exchange experiments have been proposed, but have not been widely applied to biological systems. These include One-Dimensional Exchange spectroscopy of Spinning Sideband Alternation (ODESSA, [112]), time-reverse ODESSA [113], and Exchange-Induced Spinning Sidebands (EIS, [114]). Time-reverse ODESSA experiments were used to probe the hydration-dependence of dynamics in U-^{15}N barstar [115].

Though primarily only used for studies of small peptides and model proteins to date, there is great promise that continued advancement in solid state NMR technology and experimental techniques will allow for the study of systems with greater complexity.

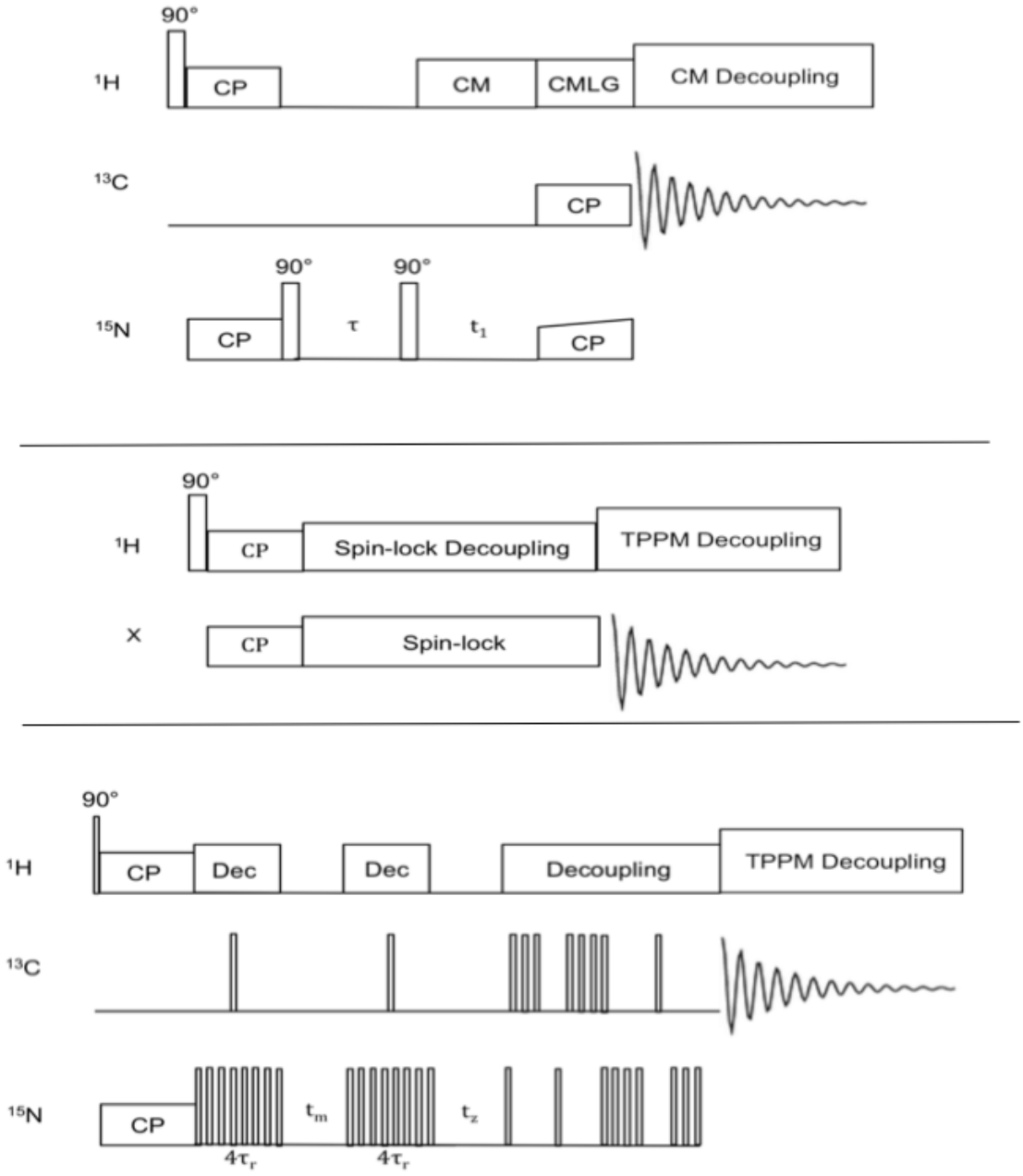

Figure 1.10 Sample pulse programs for some commonly used solid state NMR techniques to observe protein dynamics. (A) Pulse program for measurement of ^{15}N R_1 through N-C correlation spectra applied to Crh [90]. The period τ is incremented to obtain the R_1 relaxation curve. CM and CMLG stand for cosine modulated and cosine modulated Lee-Goldburg decoupling respectively. (B) General scheme for the $R_{1\rho}$ measurement of heteronuclei. They key element is the time-incremented spin-lock applied on the X channel. (C) ^{13}C-detected ^{15}N CODEX pulse program, as applied to colicin Ia [87]. Dynamics are indicated by the decay in intensity as a function of the mixing time, t_m.

1.3 Conclusions

Nuclear magnetic resonance is a powerful technique to study protein dynamics. The chemical shift, dipolar tensor, and quadrupolar tensor are information-rich NMR parameters, but also present spectroscopic challenges and complications. Recent advances in solid state NMR, in combination with critical experimental techniques such as magic angle spinning, high power decoupling, and cross polarization now allow for the high resolution study of dynamics for multiple sites simultaneously in the solid state. Many techniques have been developed that can observe protein dynamics via solid state NMR over a wide range of timescales, from picoseconds to seconds.

1.4 References

[1] W.J.F. John Cavanaugh, Arthus G Palmer III, Mark Rance, Nicholas J Skelton, Protein NMR Spectroscopy: Principles and Practices, 2nd ed., Elsevier, Burlington, MA, 2007.

[2] G. Wagner, S.G. Hyberts, T.F. Havel, Nmr Structure Determination in Solution - a Critique and Comparison with X-Ray Crystallography, Annu Rev Bioph Biom, 21 (1992) 167-198.

[3] M.A. Massiah, M.R. Starich, C. Paschall, M.F. Summers, A.M. Christensen, W.I. Sundquist, 3-Dimensional Structure of the Human-Immunodeficiency-Virus Type-1 Matrix Protein, J Mol Biol, 244 (1994) 198-223.

[4] C. Fernandez, C. Hilty, S. Bonjour, K. Adeishvili, K. Pervushin, K. Wuthrich, Solution NMR studies of the integral membrane proteins OmpX and OmpA from Escherichia coli, Febs Lett, 504 (2001) 173-178.

[5] N.A. Farrow, R. Muhandiram, A.U. Singer, S.M. Pascal, C.M. Kay, G. Gish, S.E. Shoelson, T. Pawson, J.D. Formankay, L.E. Kay, Backbone Dynamics of a Free and a Phosphopeptide-

Complexed Src Homology-2 Domain Studied by N-15 Nmr Relaxation, Biochemistry-Us, 33 (1994) 5984-6003.

[6] A.G. Palmer, NMR characterization of the dynamics of biomacromolecules, Chem Rev, 104 (2004) 3623-3640.

[7] M. Tollinger, N.R. Skrynnikov, F.A.A. Mulder, J.D. Forman-Kay, L.E. Kay, Slow dynamics in folded and unfolded states of an SH3 domain, J Am Chem Soc, 123 (2001) 11341-11352.

[8] M. Veshtort, R.G. Griffin, SPINEVOLUTION: A powerful tool for the simulation of solid and liquid state NMR experiments, J Magn Reson, 178 (2006) 248-282.

[9] A.J. Baldwin, L.E. Kay, NMR spectroscopy brings invisible protein states into focus, Nat Chem Biol, 5 (2009) 808-814.

[10] U. Haeberlen, High resolution NMR in solids : selective averaging, Academic Press, New York, 1976.

[11] S.R. Hartmann, E.L. Hahn, Nuclear Double Resonance in Rotating Frame, Phys Rev, 128 (1962) 2042-&.

[12] B.J. Wylie, C.M. Rienstra, Multidimensional solid state NMR of anisotropic interactions in peptides and proteins, J Chem Phys, 128 (2008).

[13] B.J. Wylie, L.J. Sperling, H.L. Frericks, G.J. Shah, W.T. Franks, C.M. Rienstra, Chemical-shift anisotropy measurements of amide and carbonyl resonances in a microcrystalline protein with slow magic-angle spinning NMR spectroscopy, J Am Chem Soc, 129 (2007) 5318-+.

[14] T.I. Igumenova, A.E. McDermott, K.W. Zilm, R.W. Martin, E.K. Paulson, A.J. Wand, Assignments of carbon NMR resonances for microcrystalline ubiquitin, J Am Chem Soc, 126 (2004) 6720-6727.

[15] T.I. Igumenova, A.J. Wand, A.E. McDermott, Assignment of the backbone resonances for microcrystalline ubiquitin, J Am Chem Soc, 126 (2004) 5323-5331.

[16] A. McDermott, T. Polenova, A. Bockmann, K.W. Zilm, E.K. Paulsen, R.W. Martin, G.T. Montelione, Partial NMR assignments for uniformly (C-13, N-15)-enriched BPTI in the solid state, J Biomol Nmr, 16 (2000) 209-219.

[17] J. Pauli, M. Baldus, B. van Rossum, H. de Groot, H. Oschkinat, Backbone and side-chain C-13 and N-15 signal assignments of the alpha-spectrin SH3 domain by magic angle spinning solid-state NMR at 17.6 tesla, Chembiochem, 2 (2001) 272-281.

[18] D.S. Wishart, B.D. Sykes, The C-13 Chemical-Shift Index - a Simple Method for the Identification of Protein Secondary Structure Using C-13 Chemical-Shift Data, J Biomol Nmr, 4 (1994) 171-180.

[19] I. Ando, H. Saito, R. Tabeta, A. Shoji, T. Ozaki, Conformation-Dependent C-13 Nmr Chemical-Shifts of Poly(L-Alanine) in the Solid-State - Fpt Indo Calculation of N-Acetyl-N'-Methyl-L-Alanine Amide as a Model-Compound of Poly(L-Alanine), Macromolecules, 17 (1984) 457-461.

[20] S. Spera, A. Bax, Empirical Correlation between Protein Backbone Conformation and C-Alpha and C-Beta C-13 Nuclear-Magnetic-Resonance Chemical-Shifts, J Am Chem Soc, 113 (1991) 5490-5492.

[21] Y. Shen, A. Bax, SPARTA plus : a modest improvement in empirical NMR chemical shift prediction by means of an artificial neural network, J Biomol Nmr, 48 (2010) 13-22.

[22] S. Neal, A.M. Nip, H.Y. Zhang, D.S. Wishart, Rapid and accurate calculation of protein H-1, C-13 and N-15 chemical shifts, J Biomol Nmr, 26 (2003) 215-240.

[23] G. Cornilescu, F. Delaglio, A. Bax, Protein backbone angle restraints from searching a database for chemical shift and sequence homology, J Biomol Nmr, 13 (1999) 289-302.

[24] H.H. Sun, L.K. Sanders, E. Oldfield, Carbon-13 NMR shielding in the twenty common amino acids: Comparisons with experimental results in proteins, J Am Chem Soc, 124 (2002) 5486-5495.

[25] H. Saito, I. Ando, A. Ramamoorthy, Chemical shift tensor - The heart of NMR: Insights into biological aspects of proteins, Prog Nucl Mag Res Sp, 57 (2010) 181-228.

[26] R.H. Havlin, H.B. Le, D.D. Laws, A.C. deDios, E. Oldfield, An ab initio quantum chemical investigation of carbon-13 NMR shielding tensors in glycine, alanine, valine, isoleucine, serine, and threonine: Comparisons between helical and sheet tensors, and the effects of (x)(1) on shielding, J Am Chem Soc, 119 (1997) 11951-11958.

[27] Y.F. Wei, D.K. Lee, A. Ramamoorthy, Solid-state C-13 NMR chemical shift anisotropy tensors of polypeptides, J Am Chem Soc, 123 (2001) 6118-6126.

[28] B.J. Wylie, W.T. Franks, C.M. Rienstra, Determinations of N-15 chemical shift anisotropy magnitudes in a uniformly N-15, C-13-labeled microcrystalline protein by three-dimensional magic-angle spinning nuclear magnetic resonance spectroscopy, J Phys Chem B, 110 (2006) 10926-10936.

[29] B.J. Wylie, T. Franks, D.T. Graesser, C.M. Rienstra, Site-specific C-13 chemical shift anisotropy measurements in a uniformly N-15,C-13-labeled microcrystalline protein by 3D magic-angle spinning NMR spectroscopy, J Am Chem Soc, 127 (2005) 11946-11947.

[30] D. Sitkoff, D.A. Case, Theories of chemical shift anisotropies in proteins and nucleic acids, Prog Nucl Mag Res Sp, 32 (1998) 165-190.

[31] S. Paul, P.K. Madhu, Homonuclear dipolar decoupling in solid-state nuclear magnetic resonance under the regime to moderate to high magic-angle spinning frequencies: a status report, Journal of the Indian Institue of Science, 90 (2010) 69-86.

[32] N. Tjandra, A. Bax, Direct measurement of distances and angles in biomolecules by NMR in a dilute liquid crystalline medium (vol 278, pg 1111, 1997), Science, 278 (1997) 1697-1697.

[33] J.R. Tolman, J.M. Flanagan, M.A. Kennedy, J.H. Prestegard, Nuclear Magnetic Dipole Interactions in Field-Oriented Proteins - Information for Structure Determination in Solution, P Natl Acad Sci USA, 92 (1995) 9279-9283.

[34] M.J. Duer, Introduction to solid-state NMR spectroscopy, Blackwell, Oxford, UK ; Malden, MA, 2004.

[35] M.H. Cohen, F. Reif, Quadrupole Effects in Nuclear Magnetic Resonance Studies of Solids, Solid State Phys, 5 (1957) 321-438.

[36] B. Reif, Ultra-high resolution in MAS solid-state NMR of perdeuterated proteins: Implications for structure and dynamics, J Magn Reson, 216 (2012) 1-12.

[37] E.R. Andrew, A. Bradbury, R.G. Eades, Removal of Dipolar Broadening of Nuclear Magnetic Resonance Spectra of Solids by Specimen Rotation, Nature, 183 (1959) 1802-1803.

[38] I.J. Lowe, Free Induction Decays of Rotating Solids, Phys Rev Lett, 2 (1959) 285-287.

[39] O. Millet, J.P. Loria, C.D. Kroenke, M. Pons, A.G. Palmer, The static magnetic field dependence of chemical exchange linebroadening defines the NMR chemical shift time scale, J Am Chem Soc, 122 (2000) 2867-2877.

[40] J.W. Peng, G. Wagner, Frequency spectrum of NH bonds in eglin c from spectral density mapping at multiple fields, Biochemistry-Us, 34 (1995) 16733-16752.

[41] E.O. Stejskal, J. Schaefer, J.S. Waugh, Magic-Angle Spinning and Polarization Transfer in Proton-Enhanced Nmr, J Magn Reson, 28 (1977) 105-112.

[42] T. Brauniger, P. Wormald, P. Hodgkinson, Improved proton decoupling in NMR spectroscopy of crystalline solids using the SPINAL-64 sequence, Monatsh Chem, 133 (2002) 1549-1554.

[43] C.E. Bronnimann, B.L. Hawkins, M. Zhang, G.E. Maciel, Combined Rotation and Multiple Pulse Spectroscopy as an Analytical Proton Nuclear Magnetic-Resonance Technique for Solids, Anal Chem, 60 (1988) 1743-1750.

[44] J.S. Waugh, L.M. Huber, Haeberle.U, Approach to High-Resolution Nmr in Solids, Phys Rev Lett, 20 (1968) 180-&.

[45] Mansfiel.P, Symmetrized Pulse Sequences in High Resolution Nmr in Solids, J Phys Part C Solid, 4 (1971) 1444-&.

[46] M. Lee, W.I. Goldburg, Nuclear-Magnetic-Resonance Line Narrowing by a Rotating Rf Field, Phys Rev, 140 (1965) 1261-&.

[47] E. Vinogradov, P.K. Madhu, S. Vega, High-resolution proton solid-state NMR spectroscopy by phase-modulated Lee-Goldburg experiment, Chem Phys Lett, 314 (1999) 443-450.

[48] P.K. Madhu, X. Zhao, M.H. Levitt, High-resolution H-1 NMR in the solid state using symmetry-based pulse sequences, Chem Phys Lett, 346 (2001) 142-148.

[49] M. Leskes, P.K. Madhu, S. Vega, Why does PMLG proton decoupling work at 65 kHz MAS?, J Magn Reson, 199 (2009) 208-213.

[50] P. Hodgkinson, Heteronuclear decoupling in the NMR of solids, Prog Nucl Mag Res Sp, 46 (2005) 197-222.

[51] A.E. Bennett, C.M. Rienstra, M. Auger, K.V. Lakshmi, R.G. Griffin, Heteronuclear Decoupling in Rotating Solids, J Chem Phys, 103 (1995) 6951-6958.

[52] B.M. Fung, A.K. Khitrin, K. Ermolaev, An improved broadband decoupling sequence for liquid crystals and solids, J Magn Reson, 142 (2000) 97-101.

[53] A. Detken, E.H. Hardy, M. Ernst, B.H. Meier, Simple and efficient decoupling in magic-angle spinning solid-state NMR: the XiX scheme, Chem Phys Lett, 356 (2002) 298-304.

[54] N.C. Nielsen, H. Bildsoe, H.J. Jakobsen, M.H. Levitt, Double-Quantum Homonuclear Rotary Resonance - Efficient Dipolar Recovery in Magic-Angle-Spinning Nuclear-Magnetic-Resonance, J Chem Phys, 101 (1994) 1805-1812.

[55] V. Chevelkov, K. Faelber, A. Schrey, K. Rehbein, A. Diehl, B. Reif, Differential line broadening in MAS solid-state NMR due to dynamic interference, J Am Chem Soc, 129 (2007) 10195-10200.

[56] http://nobelprize.org/, in.

[57] J.A. Mccammon, B.R. Gelin, M. Karplus, Dynamics of Folded Proteins, Nature, 267 (1977) 585-590.

[58] L.E. Kay, D.A. Torchia, A. Bax, Backbone Dynamics of Proteins as Studied by N-15 Inverse Detected Heteronuclear Nmr-Spectroscopy - Application to Staphylococcal Nuclease, Biochemistry-Us, 28 (1989) 8972-8979.

[59] H.J. Dyson, P.E. Wright, Unfolded proteins and protein folding studied by NMR, Chem Rev, 104 (2004) 3607-3622.

[60] F. Chiti, C.M. Dobson, Protein misfolding, functional amyloid, and human disease, Annu Rev Biochem, 75 (2006) 333-366.

[61] S. Akiyama, S. Takahashi, T. Kimura, K. Ishimori, I. Morishima, Y. Nishikawa, T. Fujisawa, Conformational landscape of cytochrome c folding studied by microsecond-resolved small-angle x-ray scattering, P Natl Acad Sci USA, 99 (2002) 1329-1334.

[62] M.H. Vos, F. Rappaport, J.C. Lambry, J. Breton, J.L. Martin, Visualization of Coherent Nuclear Motion in a Membrane-Protein by Femtosecond Spectroscopy, Nature, 363 (1993) 320-325.

[63] K.R. Rodgers, C. Su, S. Subramaniam, T.G. Spiro, Hemoglobin R-]T Structural Dynamics from Simultaneous Monitoring of Tyrosine and Tryptophan Time-Resolved Uv Resonance Raman Signals, J Am Chem Soc, 114 (1992) 3697-3709.

[64] B. Schuler, E.A. Lipman, W.A. Eaton, Probing the free-energy surface for protein folding with single-molecule fluorescence spectroscopy, Nature, 419 (2002) 743-747.

[65] Y.F. Wang, W.C. Yu, F.J. Zhou, Z.H. Xue, Applications of Terahertz(THz) Spectroscopy in Biological Macromolecules, Prog Biochem Biophys, 37 (2010) 484-489.

[66] A. Miranker, C.V. Robinson, S.E. Radford, R.T. Aplin, C.M. Dobson, Detection of Transient Protein-Folding Populations by Mass-Spectrometry, Science, 262 (1993) 896-900.

[67] M.S.Z. Kellermayer, S.B. Smith, H.L. Granzier, C. Bustamante, Folding-unfolding transitions in single titin molecules characterized with laser tweezers, Science, 276 (1997) 1112-1116.

[68] C. Cecconi, E.A. Shank, C. Bustamante, S. Marqusee, Direct observation of the three-state folding of a single protein molecule, Science, 309 (2005) 2057-2060.

[69] A. Krushelnitsky, D. Reichert, Solid-state NMR and protein dynamics, Prog Nucl Mag Res Sp, 47 (2005) 1-25.

[70] A.G. Krushelnitsky, Exchange NMR spectroscopy in solids: application in large-scale conformational biopolymer dynamics studies, Phys-Usp+, 48 (2005) 781-796.

[71] V. Chevelkov, Y. Xue, R. Linser, N.R. Skrynnikov, B. Reif, Comparison of Solid-State Dipolar Couplings and Solution Relaxation Data Provides Insight into Protein Backbone Dynamics, J Am Chem Soc, 132 (2010) 5015-+.

[72] J.L. Lorieau, A.E. McDermott, Conformational flexibility of a microcrystalline globular protein: Order parameters by solid-state NMR spectroscopy, J Am Chem Soc, 128 (2006) 11505-11512.

[73] D.A. Torchia, A. Szabo, Spin-Lattice Relaxation in Solids, J Magn Reson, 49 (1982) 107-121.

[74] S. Rozovsky, A.E. McDermott, The time scale of the catalytic loop motion in triosephosphate isomerase, J Mol Biol, 310 (2001) 259-270.

[75] M.S. Solum, K.W. Zilm, J. Michl, D.M. Grant, C-13 Line-Shape Study of 2-Site Exchange in Solid Dimethyl Sulfone, J Phys Chem-Us, 87 (1983) 2940-2944.

[76] C. Fares, J. Qian, J.H. Davis, Magic angle spinning and static oriented sample NMR studies of the relaxation in the rotating frame of membrane peptides, J Chem Phys, 122 (2005) 194908-194917.

[77] A. Krushelnitsky, R. Kurbanov, D. Reichert, G. Hempel, H. Schneider, V. Fedotov, Expanding the frequency range of the solid-state T-1rho experiment for heteronuclear dipolar relaxation, Solid State Nucl Mag, 22 (2002) 423-438.

[78] C.M. Quinn, A.E. McDermott, Monitoring conformational dynamics with solid-state R(1rho) experiments, J Biomol Nmr, 45 (2009) 5-8.

[79] C. Schmidt, B. Blumich, H.W. Spiess, Deuteron Two-Dimensional Exchange Nmr in Solids, J Magn Reson, 79 (1988) 269-290.

[80] E.R. deAzevedo, W.G. Hu, T.J. Bonagamba, K. Schmidt-Rohr, Principles of centerband-only detection of exchange in solid-state nuclear magnetic resonance, and extension to four-time centerband-only detection of exchange, J Chem Phys, 112 (2000) 8988-9001.

[81] W. Li, A.E. McDermott, Characterization of slow conformational dynamics in solids: dipolar CODEX, J Biomol Nmr, 45 (2009) 227-232.

[82] V.A. Higman, J. Flinders, M. Hiller, S. Jehle, S. Markovic, S. Fiedler, B.J. van Rossum, H. Oschkinat, Assigning large proteins in the solid state: a MAS NMR resonance assignment strategy using selectively and extensively C-13-labelled proteins, J Biomol Nmr, 44 (2009) 245-260.

[83] D.M. LeMaster, D.M. Kushlan, Dynamical mapping of E-coli thioredoxin via C-13 NMR relaxation analysis, J Am Chem Soc, 118 (1996) 9255-9264.

[84] S.P. Brown, H.W. Spiess, Advanced solid-state NMR methods for the elucidation of structure and dynamics of molecular, macromolecular, and supramolecular systems, Chem Rev, 101 (2001) 4125-4155.

[85] O.C. Andronesi, S. Becker, K. Seidel, H. Heise, H.S. Young, M. Baldus, Determination of membrane protein structure and dynamics by magic-angle-spinning solid-state NMR spectroscopy, J Am Chem Soc, 127 (2005) 12965-12974.

[86] N. Giraud, A. Bockmann, A. Lesage, F. Penin, M. Blackledge, L. Emsley, Site-specific backbone dynamics from a crystalline protein by solid-state NMR spectroscopy, J Am Chem Soc, 126 (2004) 11422-11423.

[87] D. Huster, L.S. Xiao, M. Hong, Solid-state NMR investigation of the dynamics of the soluble and membrane-bound colicin Ia channel-forming domain, Biochemistry-Us, 40 (2001) 7662-7674.

[88] J.J. Helmus, K. Surewicz, W.K. Surewicz, C.P. Jaroniec, Conformational Flexibility of Y145Stop Human Prion Protein Amyloid Fibrils Probed by Solid-State Nuclear Magnetic Resonance Spectroscopy, J Am Chem Soc, 132 (2010) 2393-2403.

[89] J.R. Lewandowski, J. Sein, H.J. Sass, S. Grzesiek, M. Blackledge, L. Emsley, Measurement of Site-Specific C-13 Spin-Lattice Relaxation in a Crystalline Protein, J Am Chem Soc, 132 (2010) 8252-+.

[90] N. Giraud, M. Blackledge, M. Goldman, A. Bockmann, A. Lesage, F. Penin, L. Emsley, Quantitative analysis of backbone dynamics in a crystalline protein from nitrogen-15 spin-lattice relaxation, J Am Chem Soc, 127 (2005) 18190-18201.

[91] V. Chevelkov, A. Diehl, B. Reif, Measurement of (15)N-T(1) relaxation rates in a perdeuterated protein by magic angle spinning solid-state nuclear magnetic resonance spectroscopy, J Chem Phys, 128 (2008).

[92] J.L. Lorieau, L.A. Day, A.E. McDermott, Conformational dynamics of an intact virus: Order parameters for the coat protein of Pf1 bacteriophage, P Natl Acad Sci USA, 105 (2008) 10366-10371.

[93] G. Lipari, A. Szabo, Model-Free Approach to the Interpretation of Nuclear Magnetic-Resonance Relaxation in Macromolecules .1. Theory and Range of Validity, J Am Chem Soc, 104 (1982) 4546-4559.

[94] R. Kurbanov, T. Zinkevich, A. Krushelnitsky, The nuclear magnetic resonance relaxation data analysis in solids: General R-1/R-1 rho equations and the model-free approach, J Chem Phys, 135 (2011).

[95] M. Tang, A.J. Waring, M. Hong, Arginine dynamics in a membrane-bound cationic beta-hairpin peptide from solid-state NMR, Chembiochem, 9 (2008) 1487-1492.

[96] J. Yang, M.L. Tasayco, T. Polenova, Dynamics of Reassembled Thioredoxin Studied by Magic Angle Spinning NMR: Snapshots from Different Time Scales, J Am Chem Soc, 131 (2009) 13690-13702.

[97] A. Krushelnitsky, R. Kurbanov, D. Reichert, G. Hempel, H. Schneider, V. Fedotov, Expanding the frequency range of the solid-state T-1p experiment for heteronuclear dipolar relaxation, Solid State Nucl Mag, 22 (2002) 423-438.

[98] J.R. Lewandowski, H.J. Sass, S. Grzesiek, M. Blackledge, L. Emsley, Site-Specific Measurement of Slow Motions in Proteins, J Am Chem Soc, 133 (2011) 16762-16765.

[99] C.M. Quinn, A.E. McDermott, Monitoring conformational dynamics with solid-state R (1 rho) experiments, J Biomol Nmr, 45 (2009) 5-8.

[100] A. Krushelnitsky, T. Zinkevich, D. Reichert, V. Chevelkov, B. Reif, Microsecond Time Scale Mobility in a Solid Protein As Studied by the N-15 R-1 rho Site-Specific NMR Relaxation Rates, J Am Chem Soc, 132 (2010) 11850-11853.

[101] A. Krushelnitsky, T. Zinkevich, N. Mukhametshina, N. Tarasova, Y. Gogolev, O. Gnezdilov, V. Fedotov, P. Belton, D. Reichert, C-13 and N-15 NMR Study of the Hydration Response of T4 Lysozyme and alpha B-Crystallin Internal Dynamics, J Phys Chem B, 113 (2009) 10022-10034.

[102] M. Tollinger, A.C. Sivertsen, B.H. Meier, M. Ernst, P. Schanda, Site-Resolved Measurement of Microsecond-to-Millisecond Conformational-Exchange Processes in Proteins by Solid-State NMR Spectroscopy, J Am Chem Soc, 134 (2012) 14800-14807.

[103] A.K. Mittermaier, L.E. Kay, Observing biological dynamics at atomic resolution using NMR, Trends Biochem Sci, 34 (2009) 601-611.

[104] P. Neudecker, P. Lundstrom, L.E. Kay, Relaxation Dispersion NMR Spectroscopy as a Tool for Detailed Studies of Protein Folding, Biophys J, 96 (2009) 2045-2054.

[105] E.R. deAzevedo, W.G. Hu, T.J. Bonagamba, K. Schmidt-Rohr, Centerband-only detection of exchange: Efficient analysis of dynamics in solids by NMR, J Am Chem Soc, 121 (1999) 8411-8412.

[106] A. Krushelnitsky, E. deAzevedo, R. Linser, B. Reif, K. Saalwachter, D. Reichert, Direct Observation of Millisecond to Second Motions in Proteins by Dipolar CODEX NMR Spectroscopy, J Am Chem Soc, 131 (2009) 12097-+.

[107] W.B. Li, A.E. McDermott, Characterization of slow conformational dynamics in solids: dipolar CODEX, J Biomol Nmr, 45 (2009) 227-232.

[108] J.J. Buffy, A.J. Waring, R.I. Lehrer, M. Hong, Immobilization and aggregation of the antimicrobial peptide protegrin-1 in lipid bilayers investigated by solid-state NMR, Biochemistry-Us, 42 (2003) 13725-13734.

[109] T.J. Bonagamba, F. Becker-Guedes, E.R. DeAzevedo, K. Schmidt-Rohr, Slow ester side-group flips in glassy poly(alkyl methacrylate)s characterized by centerband-only detection of exchange nuclear magnetic resonance, J Polym Sci Pol Phys, 39 (2001) 2444-2453.

[110] E.R. deAzevedo, R.W.A. Franco, A. Marletta, R.M. Faria, T.J. Bonagamba, Conformational dynamics of phenylene rings in poly(p-phenylene vinylene) as revealed by C-13 magic-angle-spinning exchange nuclear magnetic resonance experiments, J Chem Phys, 119 (2003) 2923-2934.

[111] T. Miyoshi, O. Pascui, D. Reichert, Slow chain dynamics in isotactic-poly(4-methyl-1-pentene) crystallites near the glass transition temperature characterized by solid-state C-13 MAS exchange NMR, Macromolecules, 37 (2004) 6460-6471.

[112] V. GerardyMontouillout, C. Malveau, P. Tekely, Z. Olender, Z. Luz, ODESSA, a new 1D NMR exchange experiment for chemically equivalent nuclei in rotating solids, J Magn Reson Ser A, 123 (1996) 7-15.

[113] D. Reichert, H. Zimmermann, P. Tekely, R. Poupko, Z. Luz, Time-reverse ODESSA. A 1D exchange experiment for rotating solids with several groups of equivalent nuclei, J Magn Reson, 125 (1997) 245-258.

[114] D.E. Favre, D.J. Schaefer, B.F. Chmelka, Direct determination of motional correlation times by 1D MAS and 2D exchange NMR techniques, J Magn Reson, 134 (1998) 261-279.

[115] A. Krushelnitsky, D. Reichert, G. Hempel, V. Fedotov, H. Schneider, L. Yagodina, A. Schulga, Superslow backbone protein dynamics as studied by 1D solid-state MAS exchange NMR spectroscopy, J Magn Reson, 138 (1999) 244-255.

Chapter 2

Biochemistry and Dynamics of Triosephosphate Isomerase

The biochemistry and dynamics of the protein trisosephosphate isomerase (TIM) are of particular interest to NMR spectroscopists both as a model system for developing methods to study protein dynamics, as well as to study the correlation between dynamics and catalysis in the so-called 'catalytically perfect' enzyme [1]. Particular features of TIM that make this an especially interesting enzyme to study include enantioselectivity of the catalytic cycle, the principle of transition state stabilization, and the catalytic power of TIM, in which k_{cat}/K_M values approach the diffusion encounter limit of 10^9 $M^{-1}s^{-1}$ [2, 3]. These features of TIM can be extended to improve biochemists' understanding of other enzymes as well.

2.1 The Glycolytic Pathway

The glycolytic pathway is the biochemical pathway through which glucose is converted to 2 molecules of pyruvate with the production of 2 molecules of adenosine triphosphate (ATP). Glycolysis (Figure 2.1) is a primary means of energy production for many organisms. The study of the glycolytic pathway and structure and dynamics of enzymes involved in the reactions along this pathway are important because these enzymes are being developed as targets for antibiotic drugs [4], targeting the glycolytic pathway of bacteria while not interfering with glycolysis of mammalian cells. Furthermore, it has been noted that cancer cells have up-regulation of glycolysis [5] and inhibition of glycolysis is being studied as a potential anti-cancer treatment [6]. TIM deficiency in humans is a rare, recessive disorder that leads to anemia, neuromuscular disfunction, and premature death [7].

The enzyme triosephosphate isomerase (TIM) performs a key step in this pathway, the reversible conversion of dihydroxyacetone phosphate (DHAP) into glyceraldehyde-3-phosphate (GAP). When the 6 carbon molecule fructose-1,6-biphosphate is cleaved into 2 three-carbon fragments, the two products are DHAP and GAP. TIM converts the DHAP that is produced into GAP, as shown in Figure 2.2, which then proceeds through the rest of the glycolytic pathway to produce ATP. The conversion of DHAP to GAP is the thermodynamically unfavorable but biologically relevant direction for this reversible isomerization. The k_{cat} for the conversion from DHAP to GAP is $7.5 \pm 0.2 \times 10^2$ s^{-1}. The reverse reaction has a k_{cat} of $8.7 \pm 0.3 \times 10^3$ s^{-1}. The Michaelis constant (K_M) for DHAP is 1.4 ± 0.1 mM, while the K_M for GAP is 0.055 ± 0.004 mM [8]. In the forward direction from DHAP to GAP, the rate-limiting step is believed to be product release mediated by a slow conformational change (i.e. the opening of loop 6) [9]. In the reverse direction from GAP to DHAP, the rate-limited step is a proton transfer step in the catalytic reaction mechanism [10].

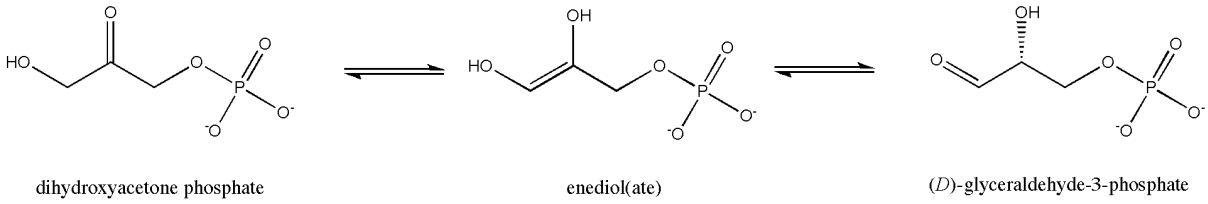

Figure 2.2 The reversible isomerization of dihydroxyacetone phosphate (DHAP) to glyceraldehyde-3-phosphate (GAP) by triosephosphate isomerase, showing the enediolate proposed intermediate or transition state.

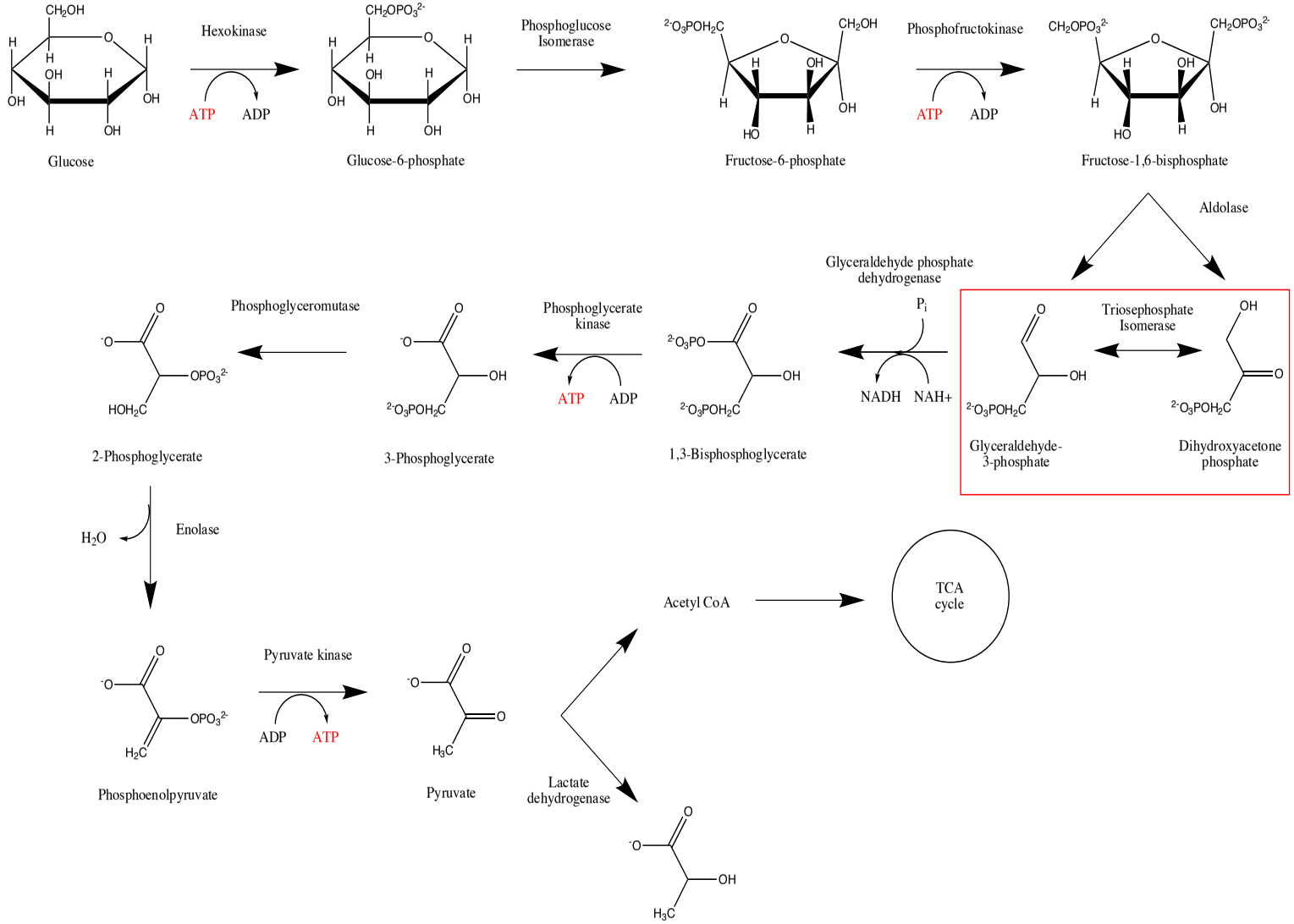

Figure 2.1 The glycolytic pathway showing the breakdown of glucose to pyruvate. The interconversion between dihydroxyacetone phosphate (DHAP) and glyceraldehyde-3-phosphate is highlighted in the red box. This interconversion, catalyzed by triosephosphate isomerase (TIM), is an essential reaction in glycolysis.

2.2 Topology of TIM

As shown in Figure 2.3, TIM is a prototypical 8-stranded α/β barrel. Also known as the TIM barrel, this fold consists of 8 α-helices surrounding 8 parallel β-strands that make up a cylindrical core. Each β-strand is connected to the subsequent α-helix by a loop; in TIM, these loops are critical for the biological activity of the enzyme. The first crystal structure of (chicken) TIM was solved in 1975 [11]. Figure 2.4 shows the correlation between sequence and structure for TIM (PDB ID: 1NEY), indicating the alternating α-helices and β-sheets. The TIM barrel is the most frequently observed enzyme structural fold [12, 13] and has evolved multiple times in nature. TIM is a dimeric enzyme; each monomer is 247 residues (for *S. cerevisiae*) with a mass of approximately 26 kDa. The amino acid composition of TIM is shown in Table 2.1. This amino acid composition and TIM's secondary structure are consistent with expected formation of β-sheet and α-helical features based on the properties of amino acids. There is a frequent occurrence of alanine (A), leucine (L), glutamic acid (E), and lysine (K) in helices, and most notably valine occurs with very high frequency in β-sheets. Prolines and glycines are generally found in unstructured regions. The large number of amino acids in TIM in correlation with the frequent occurrence in particular secondary structural elements can present challenges in NMR spectroscopy.

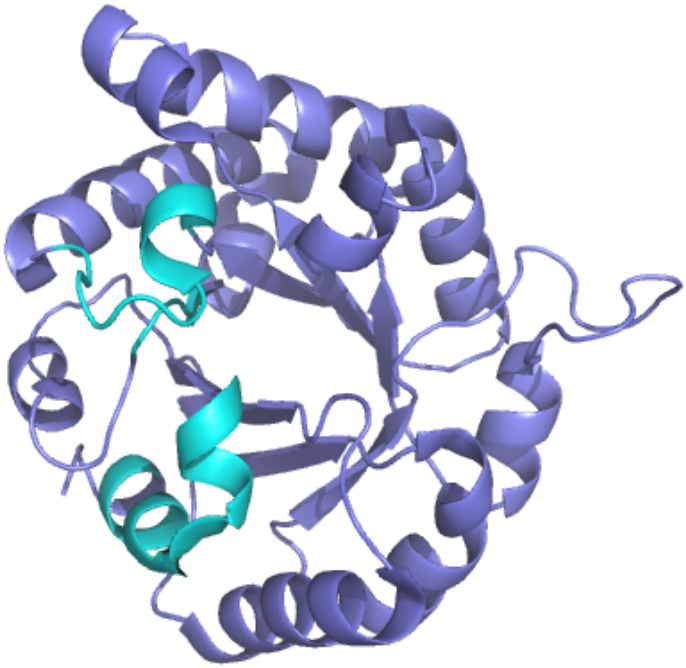

Figure 2.3 Overall structure of TIM, showing the α/β barrel structure of the protein. Loops 6, 7, and 8, the dynamics of which are critical for catalysis, are highlighted in teal. Figure made in PyMol with PDB ID 1NEY.

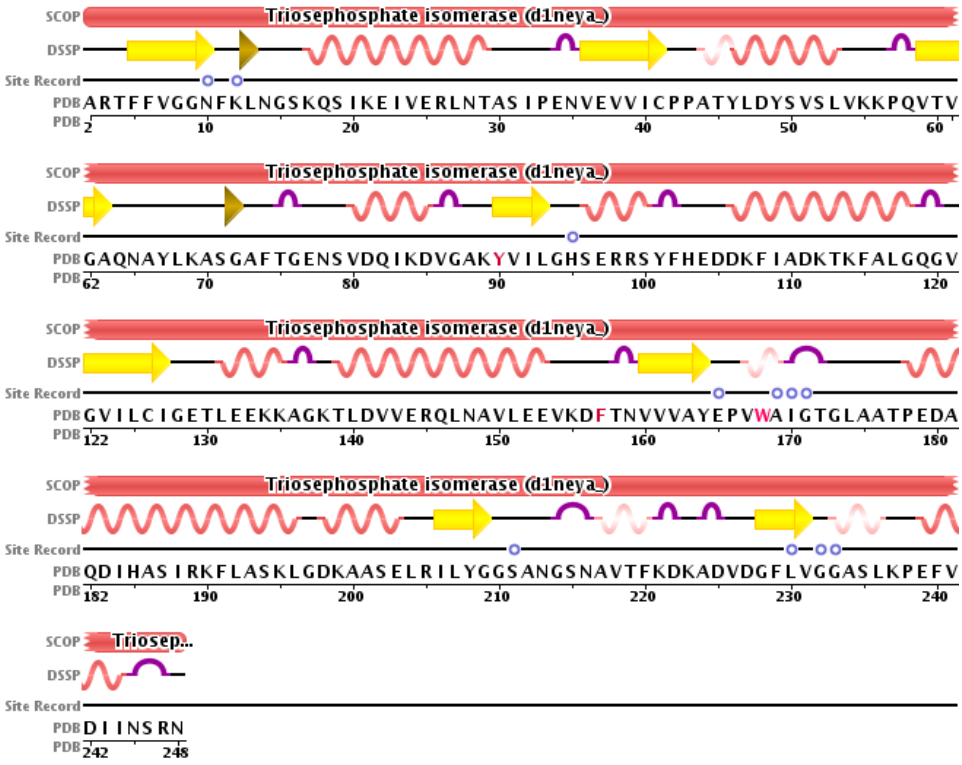

Figure 2.4 Sequence and secondary structure of TIM, showing the protein's α-helicies and β-sheets, connected by loops.

Amino acid	Occurrence
Alanine	25
Arginine	8
Asparagine	12
Aspartic Acid	15
Glutamine	7
Glutamic Acid	17
Glycine	22
Histidine	3
Isoleucine	15
Leucine	19
Lysine	21
Methionine	1
Phenylalanine	11
Proline	7
Serine	16
Threonine	12
Tyrosine	6
Valine	26
Tryptophan	2
Cysteine	2

Table 2.1 Occurrence of the 20 amino acids in *S. cerevisiae* TIM as determined from PDB IDs 1NEY and I145.

The dimerization of TIM is critical for its catalytic activity and is believed to rigidify the active site [2, 14, 15]. Many of the dimer interface residues are loop residues; as mentioned above, loops are critical for the biological activity in TIM [16]. Interestingly, one of the commonly observed point mutations that leads to TIM deficiency in humans is Glu 104. Glu 104 is located at the dimer interface and the E104D mutation leads to an 80-98% reduction in TIM activity [2]. Current studies are investigating the behavior of the mutated protein as a 'conformational disease,' related to formation of amyloid-like precipitates in the brain [2, 17].

2.3 Catalysis in TIM

The primary catalytic residues in *S. cerevisiae* TIM are lysine-12, histidine-95, and glutamic acid-165. The reaction mechanism for the isomerization has been studied for years and in fact is still being debated. The primary source of debate is the mechanism of proton transfer between the two DHAP/GAP oxygen atoms. Kinetic isotope studies [18, 19], mutagenesis studies [20-23], and crystallography [24-27] have been used to gain insight into the reaction mechanism; the crystal structure of TIM in complex with DHAP shown in Figure 2.6 indicates the proximity of the catalytic residues to the region of DHAP that undergoes the isomerization reaction, as well as the stabilization of the phosphate moiety by other residues in the protein [25]. The 'classic' reaction mechanism proposed in 1976 by Albery and Knowles [19] is still widely accepted and many more recent studies have supported this reaction mechanism [28-30] (Figure 2.5 A). The catalysis occurs by the abstraction of a proton from C1 of DHAP by the carboxylate group of Glu 165, with the neutral imidazole NH group of His 95 mediating the proton transfer between the oxygens, and the alkylammonium group of Lys 12 providing electrostatic interactions that promote stabilization of the reaction intermediate [31]. The dramatic mismatch between the pK_a of Glu 165 and the abstracted proton is compensated by the protonation of the neighboring carbonyl by His 95 [32]. The abstracted proton is transferred to C2 on an enediolate intermediate to give the product GAP. The neutral imidazole of His 95 was proposed to donate a proton to C2, forming an imidazolate anion ($R\text{-}N^-$), which abstracts a proton from C1 and Glu 165 is reprotonated. Malabanan et al recently proposed that these residues are activated in the TIM binding pocket relative to their electrostatics in water by the phosphate dianion moiety of the ligand [33]. Additional stabilization of the substrate is provided by hydrogen bonds to the

backbone amides of Gly 171, Ser 211, Gly 232, and Gly 233. Stabilization of the phosphate moiety of DHAP is essential to prevent the β-elimination, which leads to the formation of methyl glyoxyl, a toxic side product.

Other reaction mechanisms have been suggested by more recent work based upon computational and experimental studies. As shown in Figure 2.5 B, computational work has suggested that the enzyme residues in TIM merely act as stabilizing agents while the proton transfer is intramolecular, as indicated by movement of the proton between the two oxygen atoms [28]. A third mechanism proposes that not only does Glu 165 abstract the C1 proton, but also serves as the proton transfer agent between the two oxygen atoms through a low barrier hydrogen bond (Figure 2.5 C) [34].

In 2011, Samanta et al proposed a competing reaction mechanism based on mutagenesis and kinetic studies of glutamic acid 97 [35] (Figure 2.5 D). Glu 97 is not commonly cited as a catalytic residue but is one of 9 conserved residues among 503 different species of TIM (see Figure 2.8). In the classic reaction mechanism described above, the mediation of proton transfer by His 95 requires the formation of an imidazolate anion (N^-), which has a high pK_a (~14). Glu 97 is believed to contribute to the proper orientation of Lys 12, which is proposed to be key for catalytic activity of the enzyme. However mutations of Glu 97 (E97D), where Lys 12 has the same orientation as in the wild type enzyme, but a significant loss of catalytic activity suggest a direct role for Glu 97 in the catalysis. Samanta et al propose that the protonated alkylammonium group of Lys 12 donates a proton to C2 of the enediolate intermediate and extracts a proton from Glu 97. The potential for this mechanism is further supported by crystallographic work on

DHAP-bound TIM by Jogl et al [25]. Jogl et al noted that the close proximity of the Lys 12 alkylammonium group to the substrate oxygen may be an indicator of its role as a proton donor. The C1 proton is then extracted by the neutral imidazole of His 95. This reaction mechanism (or another alternative to the one described above) is supported by NMR data that shows the imidazole of His 95 is neutral over the entire range of pH values over which TIM is catalytically active. Follow-up work regarding this proposed mechanism has yet to be published.

The importance of understanding the TIM reaction mechanism is reinforced by the knowledge that other phosphate isomerases are believed to utilize the same mechanisms, and valuable insight into function by a wide range of key enzymes can be gained.

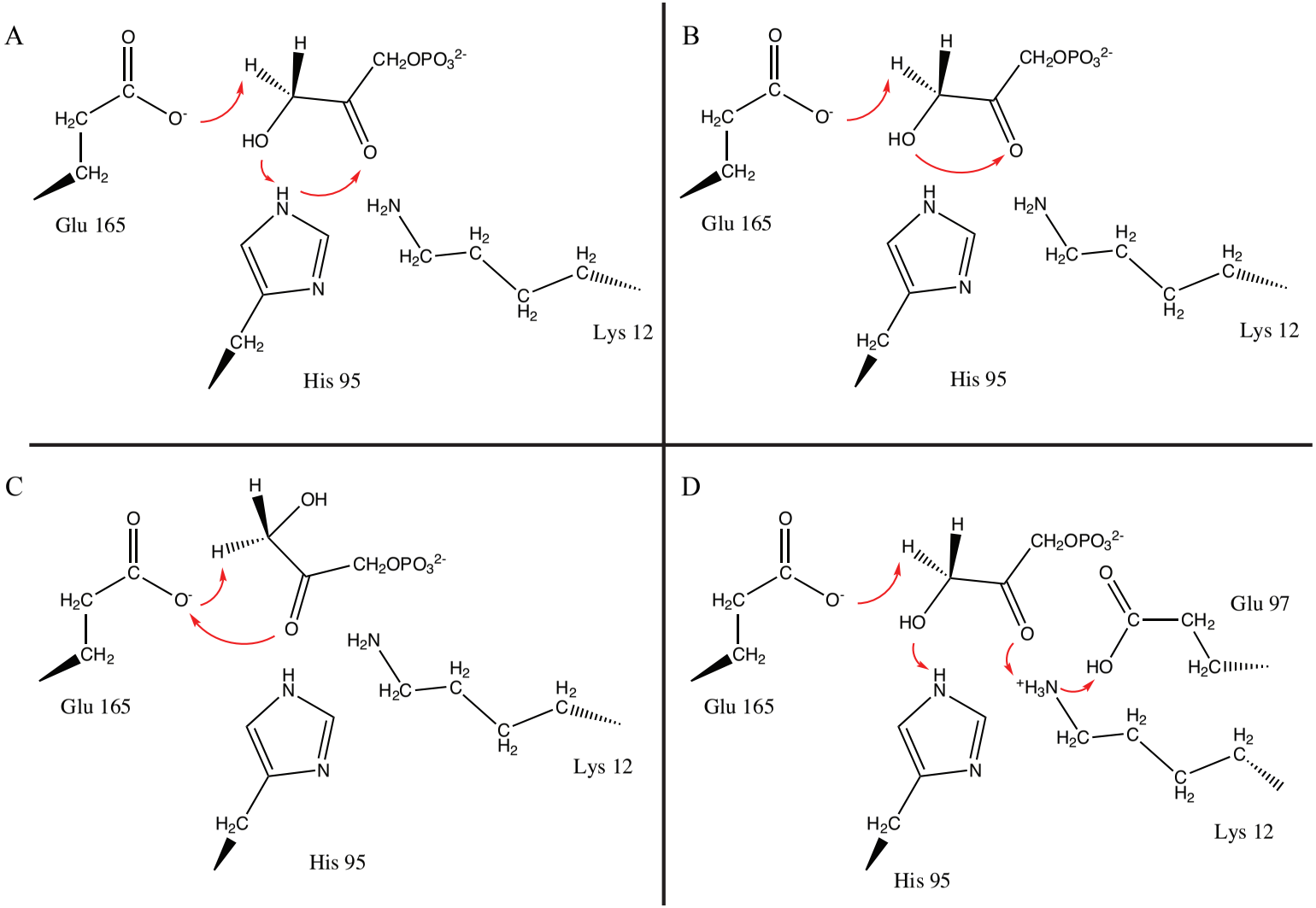

Figure 2.5 Proposed mechanisms for proton transfer in the isomerization of DHAP to GAP by TIM. (A) The classic mechanism proposed by Knowles et al. In this mechanism proton transfer is mediated by His 95. (B) Proposed mechanism in which proton transfer occurs through a direct internal transfer. (C) Mechanism in which the proton transferred comes from Glu 165 and His 95 merely helps stabilize the intermediate. (D) A new proposed mechanism of proton transfer, in which proton transfer is mediated by both Lys 12 and His 95. In all mechanisms, the first step is the proton abstraction by Glu 165.

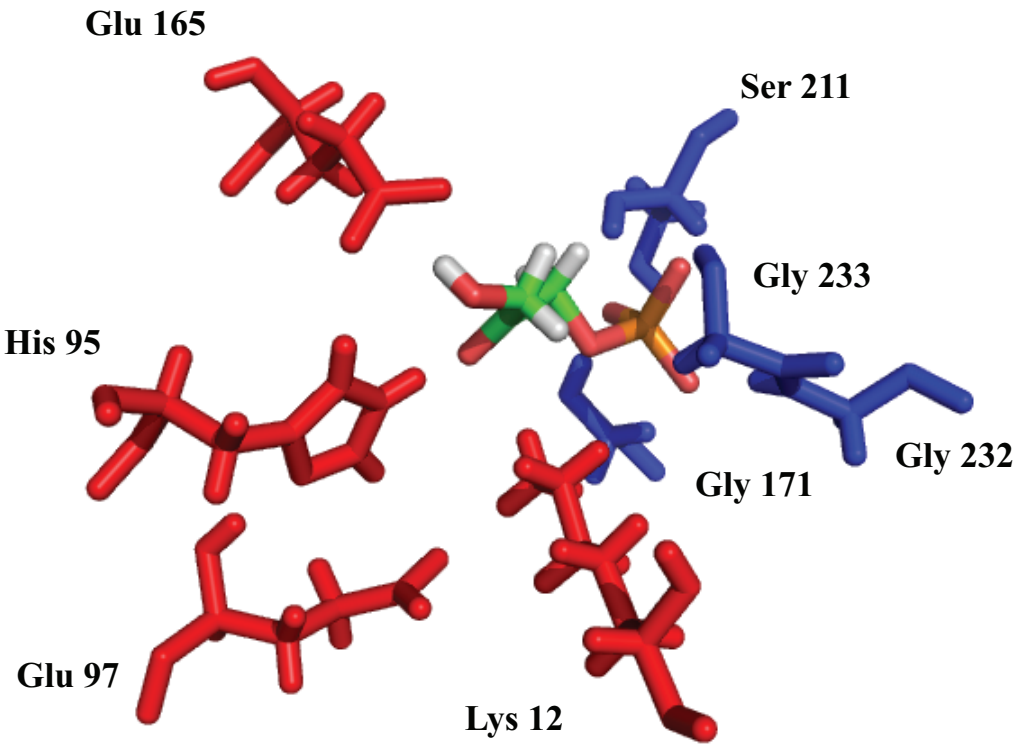

Figure 2.6 DHAP (green/orange/red) bound with the residues in TIM that are believed to play a role. Shown in red are the proposed catalytic residues, Lys 12, Glu 97, His 95, and Glu 165. In blue are additional residues that are believed to stabilize the substrate, Gly 171, Ser 211, Gly232, and Gly 233. Figure made in PyMOL with PDB structure 1NEY.

The key to preventing phosphate elimination during catalysis is believed to be the tight anchoring of the phosphate moiety by 4 N-H backbone sites of residues in loops 6, 7, and 8 [36]. These phosphate binding groups have very different conformations in the open and closed structures of the protein. In addition to the catalytic residues, the dynamics of these residues in loop 7 are important for catalysis.

2.4 Dynamics of TIM

As with many proteins, the dynamics of TIM are crucial for its function. The opening of loop 6 and release of product is the rate-limiting step in the DHAP to GAP reaction. Loop 6 is made up of residues 166 to 176 (166-PVWAIGTGLAA-176), directly next to the catalytic residue Glu 165. The rate limiting step in the GAP to DHAP direction is proton transfer to the reaction intermediate to form the product [37], $k_{cat} \sim 9 \times 10^3\ s^{-1}$, and is an example of diffusion controlled catalysis. In the metabolically crucial direction from DHAP to GAP, the rate-limiting step is the release of product from the enzyme, or the conformational change that allows product release. This conclusion is suggested by the fact that the rate of loop motion and the turnover rate closely match [37, 38]. The amino acid sequence of loop 6 is highly conserved among species (Figure 2.8), suggesting the importance of this feature in catalysis by the enzyme. When unligated, TIM is almost entirely in the open conformation as indicated by crystal structures of the protein without ligand [39], fluorescence measurements which indicated there are no appreciable kinetics for unligated protein [40], and NMR experiments [37, 38]. In this state, the carbonyl group of Glu 165 is held in place through hydrogen bonding to His 95 and Ser 96 [39]. Upon substrate binding, the loop closes (~ 7 Å movement), eliminating water from the active site. Loop 6 plays a key role in eliminating water from the active site as catalysis occurs. Limiting accessibility of the active site to bulk water is critical for preventing the toxic β-elimination reaction. Isotope exchange studies of mutated protein where 4 loop residues were deleted indicated weakened stabilization of the enediol intermediate and an increase in the production of the toxic side product, as the phosphate group is solvent exposed [41]. As the loop closes, glutamic acid 165 moves approximately 2 Å into its catalytic position, breaking the hydrogen

bond with Ser 96. In the catalytic position, Glu 165 can access both reactive carbons of DHAP/GAP, making both the forward and reverse reactions feasible. Several studies have shown that the dynamics of loop 6 are temperature-dependent and on the millisecond timescale, on the same timescale as catalysis by the enzyme, further suggesting a role for the loop dynamics in catalysis [42]. Studies of ligand binding have indicated that while the ligand does not induce loop opening and closing, it does affect the relative populations of the open and closed states of the protein.

A search for triosephosphate isomerase in the Protein Data Bank (PDB) returns 143 structures from 25 different species, including 7 from Saccharomyces cerevisiae, the protein used in these studies. The crystal structures of TIM include a wide range of mutants with a number of ligands, providing insight into the loop dynamics and potential reaction mechanism of the protein. Crystal structures have indicated that the open and closed structures of TIM are virtually identical across multiple species, further suggesting the key role of this loop in the catalytic mechanism [16].

Figure 2.7 The 7 crystal structures of *S. cerevisiae* triosephosphate isomerase showing both the open (red) and closed (blue) forms of the enzyme, with loop 6 highlighted in the black box. The PDB structures in the bound state are: 1NEY (1.2 Å resolution, ligand: DHAP), 7TIM (1.9 Å resolution, ligand: PGH), 2YPI (2.5 Å resolution, ligand: PGA), and 3YPI (2.8 Å resolution, ligand: PGH). The PDB structures in the open state are: 1NF0 (1.6 Å resolution, ligand: DHAP), 1YPI (1.9 Å resolution, ligand: none), and 1I45 (1.8 Å resolution, ligand: none).

Mutation studies have suggested several features of the loop's role in catalysis. When the loop is deleted, the protein is no longer able to form the enediol intermediate or product. The entire loop moves in a concerted manner, with the loop residues maintaining their relative ψ, Φ angles and simply translating through space, while the hinge residues move very little in space but undergo more dramatic changes in their ψ, ϕ angles [43-45]. Mutations of Glu 165 indicate that the proximity of the carboxylic acid group to the substrate carbons is essential to TIM's catalytic efficiency [20].

Correlated with the structural rearrangement of loop 6 upon ligand binding, loop 7 (208-YGGS-211) also undergoes conformational change. This amino acid sequence in loop 7 is highly conserved among species and appears to be correlated with the conserved loop 6 hinge residues 166-PVW [45]. These regions tend to co-mutate. Loop 7 stabilizes the closed conformation of loop 6 through hydrogen bonding between Ala 176 and Tyr 208, and Ser 211, Ala 169, and Gly 173. When loop 6 moves from the open state to the closed state, the Gly 209-Gly 210 peptide bond rotates 90° and Ser 211 flips out to allow Glu 165 to move into its catalytic position and form the hydrogen bonds between the 2 loops that stabilize the closed conformation.

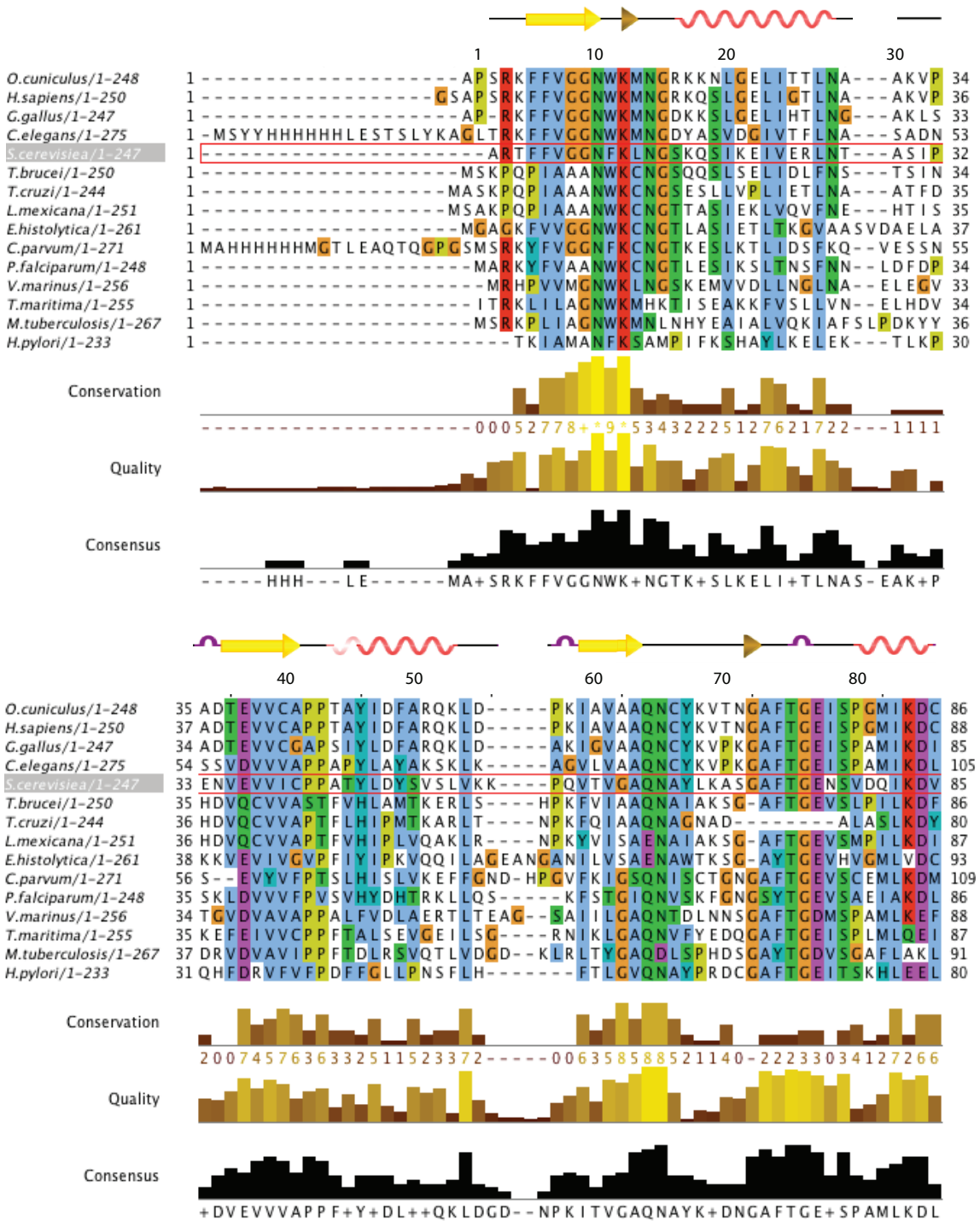
1 10 20 30
O.cuniculus/1-248 1 APSRKFFVGGNWKMNGRKKNLGELITTLNA---AKVP 34
H.sapiens/1-250 1 GSAPSRKFFVGGNWKMNGRKQSLGELIGTLNA---AKVP 36
G.gallus/1-247 1 AP-RKFFVGGNWKMNGDKKSLGELIHTLNG---AKLS 33
C.elegans/1-275 1 MSYYHHHHHHLESTSLYKAGLTRKFFVGGNWKMNGDYASVDGIVTFLNA---SADN 53
S.cerevisiea/1-247 1 ARTFFVGGNFKLNGSKQSIKEIVERLNT---ASIP 32
T.brucei/1-250 1 MSKPQPIAAANWKCNGSQQSLSELIDLFNS---TSIN 34
T.cruzi/1-244 1 MASKPQPIAAANWKCNGSESLLVPLIETLNA---ATFD 35
L.mexicana/1-251 1 MSAKPQPIAAANWKCNGTTASIEKLVQVFNE---HTIS 35
E.histolytica/1-261 1 MGAGKFVVGGNWKCNGTLASIETLTKGVAASVDAELA 37
C.parvum/1-271 1 MAHHHHHHMGTLEAQTQGPGSMSRKYFVGGNFKCNGTKESLKTLIDSFKQ--VESSN 55
P.falciparum/1-248 1 MARKYFVAANWKCNGTLESIKSLTNSFNN--LDFDP 34
V.marinus/1-256 1 MRHPVVMGNWKLNGSKEMVVDLLNGLNA--ELEGV 33
T.maritima/1-255 1 ITRKLILAGNWKMHKTISEAKKFVSLLVN--ELHDV 34
M.tuberculosis/1-267 1 MSRKPLIAGNWKMNLNHYEAIALVQKIAFSLPDKYY 36
H.pylori/1-233 1 TKIAMANFKSAMPIFKSHAYLKELEK---TLKP 30
Conservation
Quality
Consensus
-----HHH---LE------MA+SRKFFVGGNWK+NGTK+SLKELI+TLNAS-EAK+P
40 50 60 70 80
O.cuniculus/1-248 35 ADTEVVCAPPTAYIDFARQKLD-----PKIAVAAQNCYKVTNGAFTGEISPGMIKDC 86
H.sapiens/1-250 37 ADTEVVCAPPTAYIDFARQKLD-----PKIAVAAQNCYKVTNGAFTGEISPGMIKDC 88
G.gallus/1-247 34 ADTEVVCGAPSIYLDFARQKLD-----AKIGVAAQNCYKVPKGAFTGEISPAMIKDI 85
C.elegans/1-275 54 SSVDVVVAPPAPYLAYAKSKLK-----AGVLVAAQNCYKVPKGAFTGEISPAMIKDL 105
S.cerevisiea/1-247 33 ENVEVVICPPATYLDYSVSLVKK-----PQVTVGAQNAYLKASGAFTGENSVDQIKDV 85
T.brucei/1-250 35 HDVQCVVASTFVHLAMTKERLS-----HPKFVIAAQNAIAKSG-AFTGEVSLPILKDF 86
T.cruzi/1-244 36 HDVQCVVAPTFLHIPMTKARLT-----NPKFQIAAQNAGNAD---------ALASLKDY 80
L.mexicana/1-251 36 HDVQCVVAPTFVHIPLVQAKLR-----NPKYVISAENAIAKSG-AFTGEVSMPILKDI 87
E.histolytica/1-261 38 KKVEVIVGVPFIYIPKVQQILAGEANGANILVSAENAWTKSG-AYTGEVHVGMLVDC 93
C.parvum/1-271 56 S--EVYVFPTSLHISLVKEFFGND-HPGVFKIGSQNISCTGNGAFTGEVSCEMLKDM 109
P.falciparum/1-248 35 SKLDVVVFPVSVHYDHTRKLLQS-----KFSTGIQNVSKFGNGSYTGEVSAEIAKDL 86
V.marinus/1-256 34 TGVDVAVAPPALFVDLAERTLTEAG--SAIILGAQNTDLNNSGAFTGDMSPAMLKEF 88
T.maritima/1-255 35 KEFEIVVCPPFTALSEVGEILSG-----RNIKLGAQNVFYEDQGAFTGEISPLMLQEI 87
M.tuberculosis/1-267 37 DRVDVAVIPPFTDLRSVQTLVDGD--KLRLTYGAQDLSPHDSGAYTGDVSGAFLAKL 91
H.pylori/1-233 31 QHFDRVFVFPDFFGLLPNSFLH-------FTLGVQNAYPRDCGAFTGEITSKHLEEL 80
Conservation
Quality
Consensus
+DVEVVVAPPF+Y+DL++QKLDGD--NPKITVGAQNAYK+DNGAFTGE+SPAMLKDL

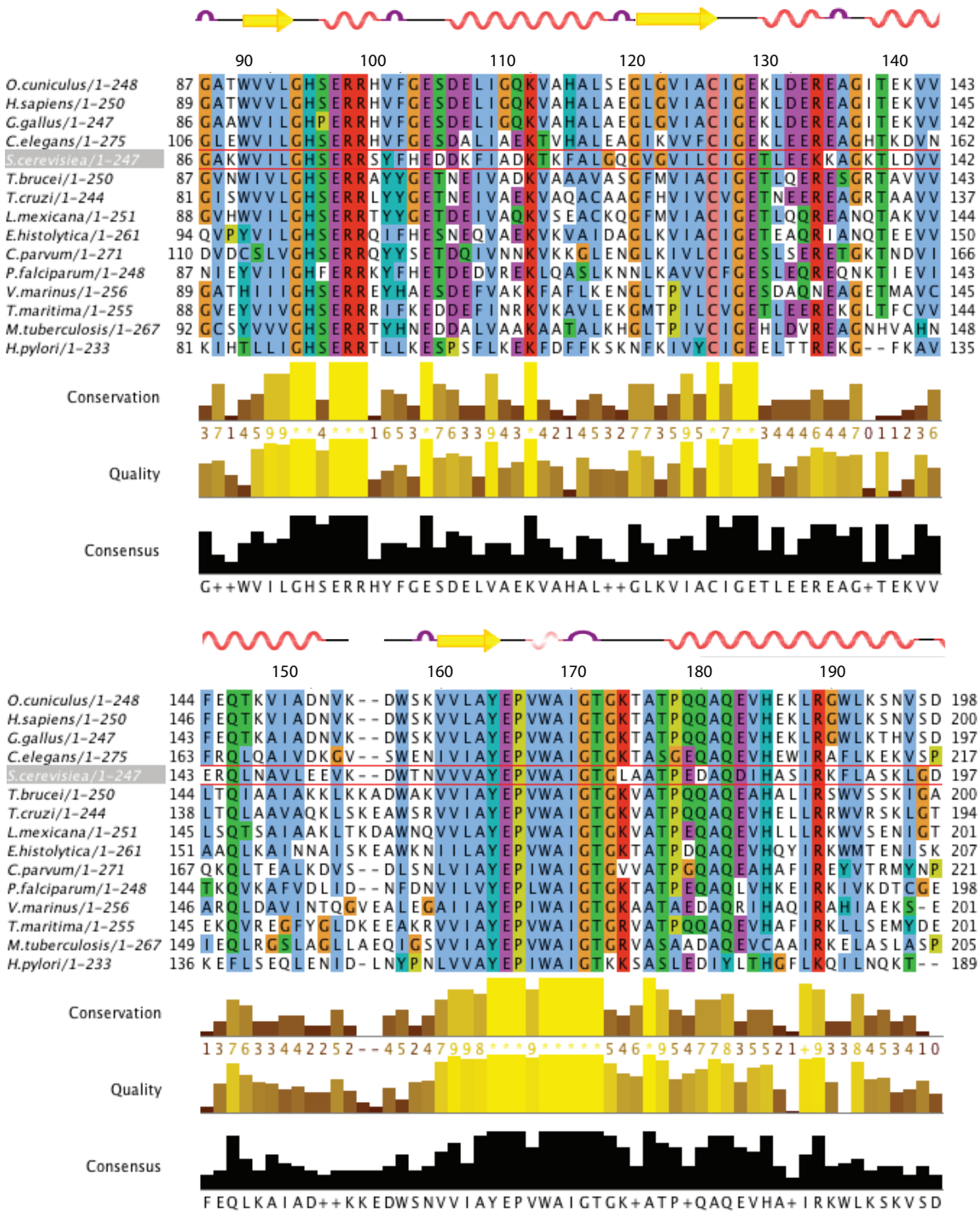
90 100 110 120 130 140
O.cuniculus/1-248 87 GATWVVLGHSERRHVFGESDELIGQKVAHALSEGLGVIACIGEKLDEREAGITEKVV 143
H.sapiens/1-250 89 GATWVVLGHSERRHVFGESDELIGQKVAHALAEGLGVIACIGEKLDEREAGITEKVV 145
G.gallus/1-247 86 GAAWVILGHPERRHVFGESDELIGQKVAHALAEGLGVIACIGEKLDEREAGITEKVV 142
C.elegans/1-275 106 GLEWVILGHSERRHVFGESDALIAEKTVHALEAGIKVVFCIGEKLEEREAGHTKDVN 162
S.cerevisiea/1-247 86 GAKWVILGHSERRSYFHEDDKFIADKTKFALGQGVGVILCIGETLEEKKAGKTLDVV 142
T.brucei/1-250 87 GVNWIVLGHSERRAYYGETNEIVADKVAAAVASGFMVIACIGETLQERESGRTAVVV 143
T.cruzi/1-244 81 GISWVVLGHSERRLYYGETNEIVAEKVAQACAAGFHVIVCVGETNEEREAGRTAAVV 137
L.mexicana/1-251 88 GVHWVILGHSERRTYYGETDEIVAQKVSEACKQGFMVIACIGETLQQREANQTAKVV 144
E.histolytica/1-261 94 QVPYVILGHSERRQIFHESNEQVAEKVKVAIDAGLKVIACIGETEAQRIANQTEEVV 150
C.parvum/1-271 110 DVDCSLVGHSERRQYYSETDQIVNNKVKKGLENGLKIVLCIGESLSERETGKTNDVI 166
P.falciparum/1-248 87 NIEYVIIGHFERRKYFHETDEDVREKLQASLKNNLKAVVCFGESLEQREQNKTIEVI 143
V.marinus/1-256 89 GATHIIIGHSERREYHAESDEFVAKKFAFLKENGLTPVLCIGESDAQNEAGETMAVC 145
T.maritima/1-255 88 GVEYVIVGHSERRIFKEDDEFINRKVKAVLEKGMTPILCVGETLEEREKGLTFCVV 144
M.tuberculosis/1-267 92 GCSYVVVGHSERRTYHNEDDALVAAKAATALKHGLTPIVCIGEHLDVREAGNHVAHN 148
H.pylori/1-233 81 KIHTLLIGHSERRTLLKESPSFLKEKFDFFKSKNFKIVYCIGEELTTREKG--FKAV 135
Conservation
37145994*4***1653*76339431*42145327735951*7**34446447011236
Quality
Consensus
G++WVILGHSERRHYFGESDELVAEKVAHAL++GLKVIACIGETLEEREAG+TEKVV
150 160 170 180 190
O.cuniculus/1-248 144 FEQTKVIADNVK--DWSKVVLAYEPVWAIGTGKTATPQQAQEVHEKLRGWLKSNVSD 198
H.sapiens/1-250 146 FEQTKVIADNVK--DWSKVVLAYEPVWAIGTGKTATPQQAQEVHEKLRGWLKSNVSD 200
G.gallus/1-247 143 FEQTKAIADNVK--DWSKVVLAYEPVWAIGTGKTATPQQAQEVHEKLRGWLKTHVSD 197
C.elegans/1-275 163 FRQLQAIVDKGV--SWENIVIAYEPVWAIGTGKTASGEQAQEVHEWIRAFLKEKVSP 217
S.cerevisiea/1-247 143 ERQLNAVLEEVK--DWTNVVVAYEPVWAIGTGLAATPEDAQDIHASIRKFLASKLGD 197
T.brucei/1-250 144 LTQIAAIAKKLKKADWAKVVIAYEPVWAIGTGKVATPQQAQEAHALIRSWVSSKIGA 200
T.cruzi/1-244 138 LTQLAAVAQKLSKEAWSRVVIAYEPVWAIGTGKVATPQQAQEVHELLRRWVRSKLGT 194
L.mexicana/1-251 145 LSQTSAIAAKLTKDAWNQVVLAYEPVWAIGTGKVATPEQAQEVHLLLRKWVSENIGT 201
E.histolytica/1-261 151 AAQLKAINNAISKEAWKNIILAYEPVWAIGTGKTATPDQAQEVHQYIRKWMTENISK 207
C.parvum/1-271 167 QKQLTEALKDVS--DLSNLVIAYEPIWAIGTGVVATPGQAQEAHAFIREYVTRMYNP 221
P.falciparum/1-248 144 TKQVKAFVDLID--NFDNVILVYEPLWAIGTGKTATPEQAQLVHKEIRKIVKDTCGE 198
V.marinus/1-256 146 ARQLDAVINTQGVEALEGAIIAYEPIWAIGTGKAATAEDAQRIHAQIRAHIAEKS-E 201
T.maritima/1-255 145 EKQVREGFYGLDKEEAKRVVIAYEPVWAIGTGRVATPQQAQEVHAFIRKLLSEMYDE 201
M.tuberculosis/1-267 149 IEQLRGSLAGLLAEQIGSVVIAYEPVWAIGTGRVASAADAQEVCAAIRKELASLASP 205
H.pylori/1-233 136 KEFLSEQLENID-LNYPNLVVAYEPIWAIGTKKSASLEDIYLTHGFLKQILNQKT-- 189
Conservation
13763344225 2--4524799 8***9*****546*954778355 21+9338453410
Quality
Consensus
FEQLKAIAD++KKEDWSNVVIAYEPVWAIGTGK+ATP+QAQEVHA+IRKWLKSKVSD

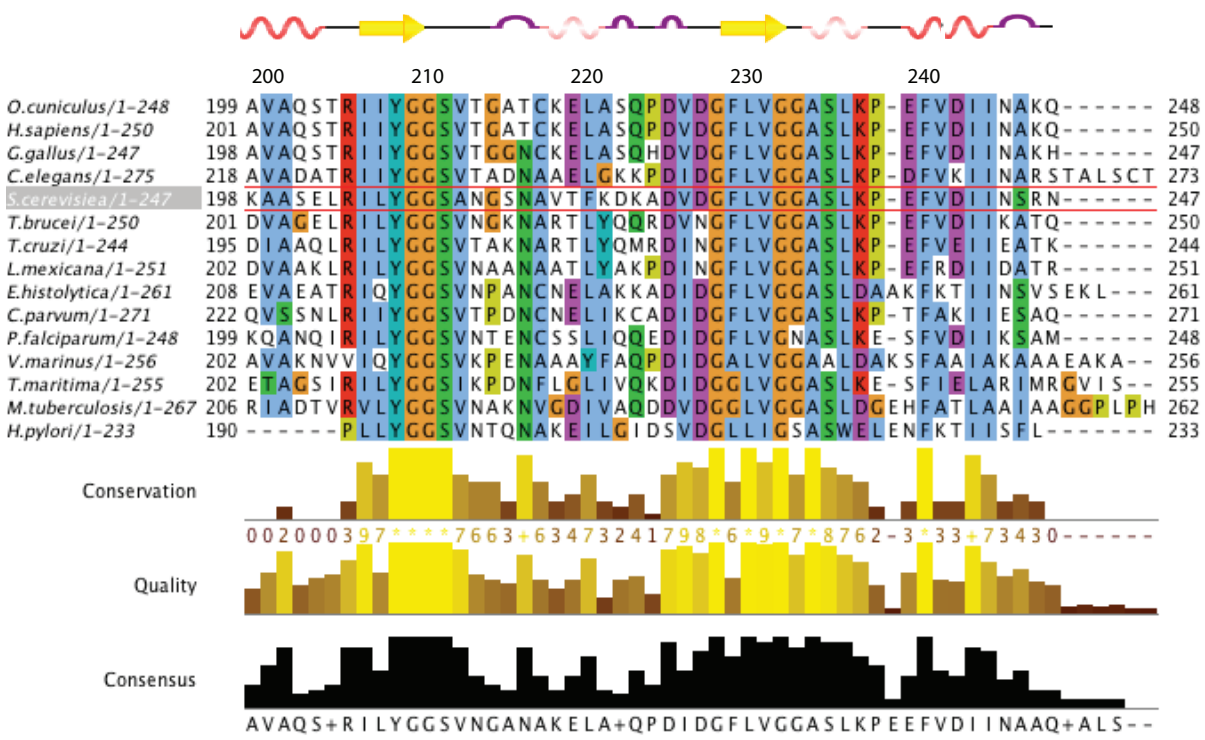

Figure 2.8 Sequence alignment of TIM from 15 different organisms, indicating highly conserved residues in the protein among species. Conserved residues of note include loop 6 as well as the catalytic residues Lys-12 and His-95 (sequence numbers from *S. cerevisiae*). Figure made using ClustalW2.

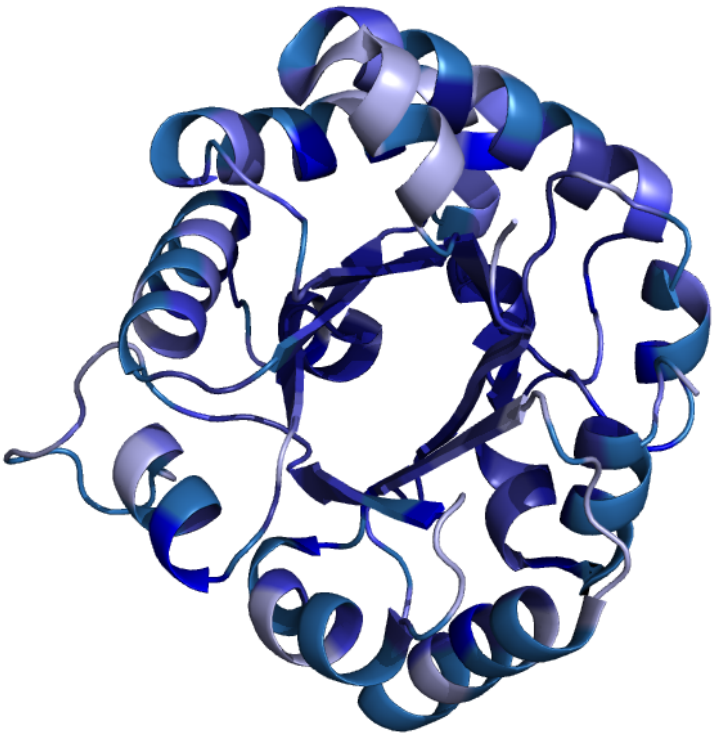

Figure 2.9 Degree of conservation of the among the residues of TIM from the 15 organisms in Figure 2.8 mapped onto the 3D structure of yeast TIM (PDB: 1NEY). The color scale ranges from light blue, not conserved, to dark blue, highly conserved. Many conserved residues appear in the hydrophobic core of β-sheets, along with loops 6 and 7.

2.5 Spectroscopic Studies of Dynamics in TIM

There is a limited temperature range over which the true substrate of TIM is stable. Furthermore, phosphate elimination by the enzyme leads to formation of methylglyoxal, a side product that causes enzyme modification [46]. Therefore to access a wider range of temperatures and allow for longer acquisition times, analogs of DHAP and GAP are often used in biochemical studies. DL-glycerol-3-phosphate (G3P) is a substrate analog, with a similar K_m to DHAP (1.4 ± 0.1 mM). 2-phosphoglycolate (PGA) is a tightly binding transition state analog with K_i = 30 μM. Phosphate is a loosely binding inhibitor of TIM. PGA and PO_4^{3-} induce the closed loop state of

TIM [40, 47]. Since Glu 165 interacts with the sugar portion of the ligand, PGA also induces Glu 165 into its 'swung in' active conformation [24, 48]. How PO_4^{3-} affects the conformation of Glu 165 is less clear. Crystallographic studies of PO_4^{3-} bound TIM (none of yeast TIM) have observed both the swung-in conformation [47], as well as alternative conformations, where the catalytic glutamic acid is interacting with other protein residues (but not the serine of the open conformation) [49]. The specific conformation of Glu 165 appears to be highly dependent on the protonation state of the phosphate ion.

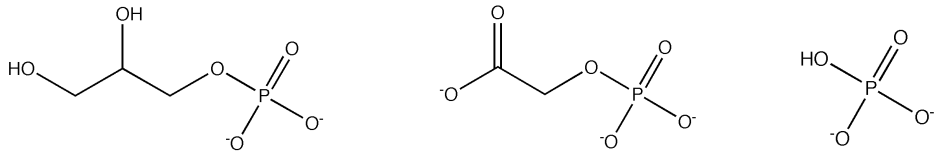

DL-glycerol-3-phosphate (G3P) 2-phosphoglycolate (PGA) phosphate

Figure 2.10 Three frequently used analogs for catalysis by TIM. DL-glycerol-3-phosphate is a substrate analog, with a similar K_D to DHAP (1.4 ± 0.3 mM). 2-phosphoglycolate (PGA) is a tightly binding transition state analog with K_i = 30 μM. Phosphate is a loosely binding inhibitor of TIM (K_i = 5.0 mM).

The dynamics of TIM have been studied through a wide range of techniques, including fluorescence spectroscopy [42], molecular dynamics [43, 50] and quantum mechanics/molecular mechanics (QM/MM, [8, 51]), and solution and solid state nuclear magnetic resonance [37, 38, 40, 45, 52-56]. Studies using this range of techniques have all indicated that dynamics of loop 6 occur on the μs to ms timescale, the same timescale as catalytic turnover by the enzyme, supporting the hypothesis that dynamics are (at least in part) rate-limiting in the catalysis [42]. Many NMR studies have focused on the dynamics of loops 6 and 7 and have provided a great deal of insight into catalysis by TIM. In solution NMR, the large size of TIM (26 kDa per monomer) requires the use of transverse relaxation optimized spectroscopy (TROSY) to obtain

narrower ^{15}N linewidths [57]. TROSY $R_{1\rho}$ measurements of loop 7 mutants of chicken TIM indicated the importance of hydrogen bonds between loop7 and loop 6 in the formation of the closed state of the enzyme [45, 54]. TROSY CPMG (Carr-Purcell-Meiboom-Gill) studies indicated the presence of dynamics in loop 6 (specifically Thr 172) on the millisecond timescale [55]. 5'-fluorotryptophan at W168 was also used to demonstrate the millisecond timescale dynamics [40]. Solid state deuterium NMR studies of ^{2}H-α W168 indicated that the dynamics of loop 6 are intrinsic to the protein and not due to ligand [38]. Complementary T-jump fluorescence and ^{19}F NMR further confirmed the timescale of the loop motion. Recently, extensive assignments of TIM in the solid-state were reported by Xu and McDermott [52]. Of great interest is the novel assignment of residues directly involved in catalysis and ligand stabilization. Such resonances include Gly 209, 210, and 233, as well as the sidechain carbon of the catalytic His 95.

In addition to spectroscopic studies on the protein itself, dynamics of TIM ligands have also been studied [40, 53, 58]. Fluorescence studies indicated that the choice of ligand affects the rate of loop opening [42]. G3P was shown to behave most closely to the natural ligand DHAP (both with dynamics occurring on the microsecond timescale), while PGA is an inhibitor, inducing slower than microsecond dynamics. Interestingly, the simple phosphate ligand was observed to have distributed dynamics, occurring on both the microsecond and millisecond timescales. This may be indicative of the loose fit of this ligand in the protein active site. (Crystallography suggests that hydrogen bonds between amino acid residues in the protein maintain its ordered structure when PO_4^{3-} is the ligand. [47, 49]) Very little work has been done utilizing phosphate

as the ligand of interest. ^{31}P NMR studies of G3P have shown that the rate of ligand release is on the same timescale as the loop motion, and further suggests the two processes are correlated [40].

2.6 Conclusions and Perspective

While triosephosphate isomerase is an extensively studied example of a highly evolved catalytic enzyme, there are still many opportunities to study this enzyme, to gain understanding of the reaction mechanism of catalysis and the correlation of biochemistry with dynamics. Advances in solid-state NMR, such as the development of selective labeling protocols with glycerol [59], as well as the recent extensive solid state assignment of TIM [52], notably the assignment of key residues involved in catalysis, including new resonances in Gly 209, 210, 232, and 233, as well His 95, have opened up great new opportunities to probe the dynamics and mechanism of proton transfer in this enzyme. Some of these key resonances are not visible in solution NMR, including Glu 97, and the key catalytic residue, Glu 165 (from BMRB 7216). Brownian tumbling of the protein in solution and exchange broadening often inhibit the observation of dynamics on the intermediate timescale. Static studies of the protein, such as crystallography, cannot gain the full insight into the role of dynamics in the catalysis. Hydrogen bonding plays a significant role in stabilizing the various conformations of the TIM loops along the catalytic path. Nuclear magnetic resonance is a very sensitive method for observing hydrogen bonds [60]. Solid state NMR has the power to potentially answer many additional open questions regarding the catalytic mechanism of TIM, and gain further insight into the correlation between catalysis and dynamics. In this work, questions that we hope to answer include

- Gaining further insight into the roles of various catalytic residues by detecting Glu 97 and 165 through low temperature measurements that slow the dynamics of the protein
- Measurements of dynamics of the protein and ligands to further correlate ligand binding and enzyme motion with chemistry
- Chemical shift anisotropy measurements of the ligand and/or protein residues which could provide information regarding protonation states and hydrogen bonds

These many opportunities to study TIM via solid state NMR can improve our understanding of both how this particular enzyme achieves such catalytic power, as well as more general principles of catalysis and dynamics that can be extended to other biomolecules. Furthermore, the extensive previous work on the dynamics of TIM, as well as the ability to tune these dynamics by choice of ligand and temperature, make it an ideal candidate for testing new methods of observing protein dynamics.

2.7 References

[1] J.R. Knowles, W.J. Albery, Perfection in Enzyme Catalysis - Energetics of Triosephosphate Isomerase, Accounts Chem Res, 10 (1977) 105-111.

[2] R.K. Wierenga, E.G. Kapetaniou, R. Venkatesan, Triosephosphate isomerase: a highly evolved biocatalyst, Cell Mol Life Sci, 67 (2010) 3961-3982.

[3] T.K. Harris, The mechanistic ventures of triosephosphate isomerase, Iubmb Life, 60 (2008) 195-198.

[4] C.L.M. Verlinde, V. Hannaert, C. Blonski, M. Willson, J.J. Perie, L.A. Fothergill-Gilmore, F.R. Opperdoes, M.H. Gelb, W.G.J. Hol, P.A.M. Michels, Glycolysis as a target for the design of new anti-trypanosome drugs, Drug Resist Update, 4 (2001) 50-65.

[5] R.A. Gatenby, R.J. Gillies, Why do cancers have high aerobic glycolysis?, Nat Rev Cancer, 4 (2004) 891-899.

[6] H. Pelicano, D.S. Martin, R.H. Xu, P. Huang, Glycolysis inhibition for anticancer treatment, Oncogene, 25 (2006) 4633-4646.

[7] A.S. Schneider, Triosephosphate isomerase deficiency: historical perspectives and molecular aspects, Best Pract Res Cl Ha, 13 (2000) 119-140.

[8] V. Guallar, M. Jacobson, A. McDermott, R.A. Friesner, Computational modeling of the catalytic reaction in triosephosphate isomerase, J Mol Biol, 337 (2004) 227-239.

[9] S.G. Maister, C.P. Pett, W.J. Albery, J.R. Knowles, Energetics of Triosephosphate Isomerase - Appearance of Solvent Tritium in Substrate Dihydroxyacetone Phosphate and in Product, Biochemistry-Us, 15 (1976) 5607-5612.

[10] E.B. Nickbarg, J.R. Knowles, Triosephosphate Isomerase - Energetics of the Reaction Catalyzed by the Yeast Enzyme Expressed in Escherichia-Coli, Biochemistry-Us, 27 (1988) 5939-5947.

[11] D.W. Banner, A.C. Bloomer, G.A. Petsko, D.C. Phillips, C.I. Pogson, I.A. Wilson, P.H. Corran, A.J. Furth, J.D. Milman, R.E. Offord, J.D. Priddle, S.G. Waley, Structure of Chicken Muscle Triose Phosphate Isomerase Determined Crystallographically at 2.5a Resolution Using Amino-Acid Sequence Data, Nature, 255 (1975) 609-614.

[12] G.K. Farber, G.A. Petsko, The Evolution of Alpha-Beta-Barrel Enzymes, Trends Biochem Sci, 15 (1990) 228-&.

[13] S. Janecek, Tracing the evolutionary lineages among alpha-amylases and cyclodextrin glycosyltransferases: The question of so-called "intermediary" enzymes, Biologia, 50 (1995) 515-522.

[14] S. Cansu, P. Doruker, Dimerization affects collective dynamics of triosephosphate isomerase, Biochemistry-Us, 47 (2008) 1358-1368.

[15] A.Q. Sun, K.U. Yuksel, R.W. Gracy, Interactions between the Catalytic Centers and Subunit Interface of Triosephosphate Isomerase Probed by Refolding, Active-Site Modification, and Subunit Exchange, J Biol Chem, 267 (1992) 20168-20174.

[16] R.K. Wierenga, M.E.M. Noble, R.C. Davenport, Comparison of the Refined Crystal-Structures of Liganded and Unliganded Chicken, Yeast and Trypanosomal Triosephosphate Isomerase, J Mol Biol, 224 (1992) 1115-1126.

[17] F.X. Guix, G. Ill-Raga, R. Bravo, T. Nakaya, G. de Fabritiis, M. Coma, G.P. Miscione, J. Villa-Freixa, T. Suzuki, X. Fernandez-Busquets, M.A. Valverde, B. de Strooper, F.J. Munoz, Amyloid-dependent triosephosphate isomerase nitrotyrosination induces glycation and tau fibrillation, Brain, 132 (2009) 1335-1345.

[18] S.V. Rieder, I.A. Rose, Mechanism of the Triosephosphate Isomerase Reaction, J Biol Chem, 234 (1959) 1007-1010.

[19] W.J. Albery, J.R. Knowles, Free-Energy Profile for Reaction Catalyzed by Triosephosphate Isomerase, Biochemistry-Us, 15 (1976) 5627-5631.

[20] D. Josephmccarthy, L.E. Rost, E.A. Komives, G.A. Petsko, Crystal-Structure of the Mutant Yeast Triosephosphate Isomerase in Which the Catalytic Base Glutamic-Acid-165 Is Changed to Aspartic-Acid, Biochemistry-Us, 33 (1994) 2824-2829.

[21] R.T. Raines, E.L. Sutton, D.R. Straus, W. Gilbert, J.R. Knowles, Reaction Energetics of a Mutant Triosephosphate Isomerase in Which the Active-Site Glutamate Has Been Changed to Aspartate, Biochemistry-Us, 25 (1986) 7142-7154.

[22] D. Straus, R. Raines, E. Kawashima, J.R. Knowles, W. Gilbert, Active-Site of Triosephosphate Isomerase - Invitro Mutagenesis and Characterization of an Altered Enzyme, P Natl Acad Sci USA, 82 (1985) 2272-2276.

[23] P.J. Lodi, L.C. Chang, J.R. Knowles, E.A. Komives, Triosephosphate Isomerase Requires a Positively Charged Active-Site - the Role of Lysine-12, Biochemistry-Us, 33 (1994) 2809-2814.

[24] E. Lolis, G.A. Petsko, Crystallographic Analysis of the Complex between Triosephosphate Isomerase and 2-Phosphoglycolate at 2.5-a Resolution - Implications for Catalysis, Biochemistry-Us, 29 (1990) 6619-6625.

[25] G. Jogl, S. Rozovsky, A.E. McDermott, L. Tong, Optimal alignment for enzymatic proton transfer: Structure of the Michaelis complex of triosephosphate isomerase at 1.2-angstrom resolution, P Natl Acad Sci USA, 100 (2003) 50-55.

[26] R.K. Wierenga, M.E.M. Noble, G. Vriend, S. Nauche, W.G.J. Hol, Refined 1.83-a Structure of Trypanosomal Triosephosphate Isomerase Crystallized in the Presence of 2.4 M-Ammonium Sulfate - a Comparison with the Structure of the Trypanosomal Triosephosphate Isomerase-Glycerol-3-Phosphate Complex, J Mol Biol, 220 (1991) 995-1015.

[27] M. Alahuhta, R.K. Wierenga, Atomic resolution crystallography of a complex of triosephosphate isomerase with a reaction-intermediate analog: New insight in the proton transfer reaction mechanism, Proteins-Structure Function and Bioinformatics, 78 (2010) 1878-1888.

[28] G. Alagona, C. Ghio, P.A. Kollman, The intramolecular mechanism for the second proton transfer in triosephosphate isomerase (TIM): A QM/FE approach, J Comput Chem, 24 (2003) 46-56.

[29] L.M. Fisher, W.J. Albery, J.R. Knowles, Energetics of Triosephosphate Isomerase - Nature of Proton-Transfer between Catalytic Base and Solvent Water, Biochemistry-Us, 15 (1976) 5621-5626.

[30] M. Perakyla, T.A. Pakkanen, Ab initio models for receptor-ligand interactions in proteins .4. Model assembly study of the catalytic mechanism of triosephosphate isomerase, Proteins, 25 (1996) 225-236.

[31] P.A. Bash, M.J. Field, R.C. Davenport, G.A. Petsko, D. Ringe, M. Karplus, Computer-Simulation and Analysis of the Reaction Pathway of Triosephosphate Isomerase, Biochemistry-Us, 30 (1991) 5826-5832.

[32] J.A. Gerlt, J.W. Kozarich, G.L. Kenyon, P.G. Gassman, Electrophilic Catalysis Can Explain the Unexpected Acidity of Carbon Acids in Enzyme-Catalyzed Reactions, J Am Chem Soc, 113 (1991) 9667-9669.

[33] M.M. Malabanan, A.P. Koudelka, T.L. Amyes, J.P. Richard, Mechanism for Activation of Triosephosphate Isomerase by Phosphite Dianion: The Role of a Hydrophobic Clamp, J Am Chem Soc, 134 (2012) 10286-10298.

[34] T.K. Harris, C. Abeygunawardana, A.S. Mildvan, NMR studies of the role of hydrogen bonding in the mechanism of triosephosphate isomerase, Biochemistry-Us, 36 (1997) 14661-14675.

[35] M. Samanta, M.R.N. Murthy, H. Balaram, P. Balaram, Revisiting the Mechanism of the Triosephosphate Isomerase Reaction: The Role of the Fully Conserved Glutamic Acid 97 Residue, Chembiochem, 12 (2011) 1885-1895.

[36] J.P. Richard, Acid-Base Catalysis of the Elimination and Isomerization-Reactions of Triose Phosphates, J Am Chem Soc, 106 (1984) 4926-4936.

[37] S. Rozovsky, A.E. McDermott, The time scale of the catalytic loop motion in triosephosphate isomerase, J Mol Biol, 310 (2001) 259-270.

[38] J.C. Williams, A.E. Mcdermott, Dynamics of the Flexible Loop of Triosephosphate Isomerase - the Loop Motion Is Not Ligand-Gated, Biochemistry-Us, 34 (1995) 8309-8319.

[39] E. Lolis, T. Alber, R.C. Davenport, D. Rose, F.C. Hartman, G.A. Petsko, Structure of Yeast Triosephosphate Isomerase at 1.9-a Resolution, Biochemistry-Us, 29 (1990) 6609-6618.

[40] S. Rozovsky, G. Jogl, L. Tong, A.E. McDermott, Solution-state NMR investigations of triosephosphate isomerase active site loop motion: Ligand release in relation to active site loop dynamics, J Mol Biol, 310 (2001) 271-280.

[41] D. Pompliano, A. Peyman, J.R. Knowles, Stabilization of a reaction intermediate as a catalytic device: definition of the functional role of the flexible loop in triosephosphate isomerase, Biochemistry-Us, 29 (1990) 3186-3194.

[42] R. Desamero, S. Rozovsky, N. Zhadin, A. McDermott, R. Callender, Active site loop motion in triosephosphate isomerase: T-jump relaxation spectroscopy of thermal activation, Biochemistry-Us, 42 (2003) 2941-2951.

[43] D. Joseph, G.A. Petsko, M. Karplus, Anatomy of a Conformational Change - Hinged Lid Motion of the Triosephosphate Isomerase Loop, Science, 249 (1990) 1425-1428.

[44] R.C. Wade, M.E. Davis, B.A. Luty, J.D. Madura, J.A. Mccammon, Gating of the Active-Site of Triose Phosphate Isomerase - Brownian Dynamics Simulations of Flexible Peptide Loops in the Enzyme, Biophys J, 64 (1993) 9-15.

[45] Y. Wang, R.B. Berlow, J.P. Loria, Role of Loop-Loop Interactions in Coordinating Motions and Enzymatic Function in Triosephosphate Isomerase, Biochemistry-Us, 48 (2009) 4548-4556.

[46] T.P. Degenhardt, S.R. Thorpe, J.W. Baynes, Chemical modification of proteins by methylglyoxal, Cell Mol Biol, 44 (1998) 1139-1145.

[47] C.L.M.J. Verlinde, M.E.M. Noble, K.H. Kalk, H. Groendijk, R.K. Wierenga, W.G.J. Hol, Anion Binding at the Active-Site of Trypanosomal Triosephosphate Isomerase - Monohydrogen Phosphate Does Not Mimic Sulfate, Eur J Biochem, 198 (1991) 53-57.

[48] R.C. Davenport, P.A. Bash, B.A. Seaton, M. Karplus, G.A. Petsko, D. Ringe, Structure of the Triosephosphate Isomerase Phosphoglycolohydroxamate Complex - an Analog of the Intermediate on the Reaction Pathway, Biochemistry-Us, 30 (1991) 5821-5826.

[49] C.H. Chu, Y.J. Lai, H.M. Huang, Y.J. Sun, Kinetic and structural properties of triosephosphate isomerase from Helicobacter pylori, Proteins-Structure Function and Bioinformatics, 71 (2008) 396-406.

[50] F. Massi, C.Y. Wang, A.G. Palmer, Solution NMR and computer simulation studies of active site loop motion in triosephosphate isomerase (vol 45, pg 10787, 2006), Biochemistry-Us, 45 (2006) 14232-14232.

[51] Q. Cui, M. Karplus, Quantum mechanics/molecular mechanics studies of triosephosphate isomerase-catalyzed reactions: Effect of geometry and tunneling on proton-transfer rate constants, J Am Chem Soc, 124 (2002) 3093-3124.

[52] Y.M. Xu, J. Lorieau, A.E. McDermott, Triosephosphate Isomerase: N-15 and C-13 Chemical Shift Assignments and Conformational Change upon Ligand Binding by Magic-Angle Spinning Solid-State NMR Spectroscopy, J Mol Biol, 397 (2010) 233-248.

[53] S. Rozovsky, A.E. McDermott, Substrate product equilibrium on a reversible enzyme, triosephosphate isomerase, P Natl Acad Sci USA, 104 (2007) 2080-2085.

[54] R.B. Berlow, T.I. Igumenova, J.P. Loria, Value of a hydrogen bond in triosephosphate isomerase loop motion, Biochemistry-Us, 46 (2007) 6001-6010.

[55] J.P. Loria, M. Rance, A.G. Palmer, A TROSY CPMG sequence for characterizing chemical exchange in large proteins, J Biomol Nmr, 15 (1999) 151-155.

[56] J.G. Kempf, J.Y. Jung, C. Ragain, N.S. Sampson, J.P. Loria, Dynamic requirements for a functional protein hinge, J Mol Biol, 368 (2007) 131-149.

[57] K. Pervushin, R. Riek, G. Wider, K. Wuthrich, Attenuated T-2 relaxation by mutual cancellation of dipole-dipole coupling and chemical shift anisotropy indicates an avenue to NMR structures of very large biological macromolecules in solution, P Natl Acad Sci USA, 94 (1997) 12366-12371.

[58] I.D. Campbell, R.B. Jones, P.A. Kiener, S.G. Waley, Enzyme-Substrate and Enzyme-Inhibitor Complexes of Triose Phosphate Isomerase Studied by P-31 Nuclear Magnetic-Resonance, Biochem J, 179 (1979) 607-621.

[59] V.A. Higman, J. Flinders, M. Hiller, S. Jehle, S. Markovic, S. Fiedler, B.J. van Rossum, H. Oschkinat, Assigning large proteins in the solid state: a MAS NMR resonance assignment strategy using selectively and extensively C-13-labelled proteins, J Biomol Nmr, 44 (2009) 245-260.

[60] C.L. Perrin, J.B. Nielson, "Strong" hydrogen bonds in chemistry and biology, Annu Rev Phys Chem, 48 (1997) 511-544.

Chapter 3

$R_{1\rho}$ Studies of Dimethyl Sulfone

Protein function and dynamics are closely linked; studying the dynamics of biological systems may provide insights into function that are not apparent through structure alone. Many biophysical methods have been developed to observe protein dynamics. Advantages of nuclear magnetic resonance (NMR) over other techniques to observe conformational changes include the wide range of accessible time scales of dynamics and the ability to monitor dynamics site-specifically. In solution NMR, techniques to study protein dynamics have been well-established, such as spin relaxation [1], amide proton exchange [2, 3], scalar coupling constants [4], and residual dipolar coupling constants (RDCs) [5-7]. These techniques have been used to observe dynamics and protein folding in a variety of biological systems, including cytochrome c [8], ubiquitin [9], and triosephosphate isomerase (TIM) [10].

As dramatic improvements in resolution and signal-to-noise have been made in recent years, the quantitative study of conformational dynamics using solid state NMR has become experimentally feasible [11-13]. Methods used to study conformational exchange in the solid state cover a broad range of timescales from picoseconds to seconds. Slow (millisecond-to-second) timescale methods include 2-dimensional exchange experiments [14] and newer 1-dimensional exchange techniques such as CODEX and dipolar CODEX [15, 16]. Intermediate timescale (microsecond-to-millisecond) experimental methods include rotating frame relaxation [17-19] and lineshape analysis [20, 21]. Fast (nanosecond-to-picosecond) timescale experiments include laboratory-frame relaxation [22] and measurements of order parameters [23, 24].

3.1 Introduction to $R_{1\rho}$ Experiments

Two-site chemical exchange between two conformations, A and B, can be modeled by the reaction

$$A \underset{k_{-1}}{\overset{k_1}{\rightleftharpoons}} B$$

in which k_1 is the rate constant for the forward reaction and k_{-1} is the rate constant for the reverse reaction. The exchange rate constant $k_{ex} = k_1 + k_{-1}$. If p_A and p_B are the populations of the 2 exchange sites, then $p_A k_1 = p_B k_{-1}$. The evolution of a system undergoing chemical exchange is further discussed in Section 1.1.1. Measuring spin relaxation due to chemical exchange is one means of obtaining information about the exchange process of interest [25].

Rotating frame relaxation ($R_{1\rho}$) experiments are sensitive to dynamics on the microsecond-to-millisecond timescale and is one of the few methods available to observe intermediate timescale dynamics [13]. Signals for sites undergoing intermediate exchange are often not observable due to exchange broadening. $R_{1\rho}$ experiments measure the rate of decay of magnetization parallel to the effect field in the rotating frame:

$$R_{1\rho} = R_1 \cos^2\theta + R_2^{\circ} \sin^2\theta + R_{ex} \sin^2\theta \qquad (1)$$

where R_1 is longitudinal relaxation, R_2^0 is transverse relaxation in the absence of a dynamic process, R_{ex} is transverse relaxation due to chemical exchange, and θ is the tilt angle between the static magnetic field and the effective field in the rotating frame. $R_{1\rho}$ measurements entail

irradiating the nucleus of interest with a continuous spin-lock pulse and observing the decay of magnetization as a function of spin-lock length.

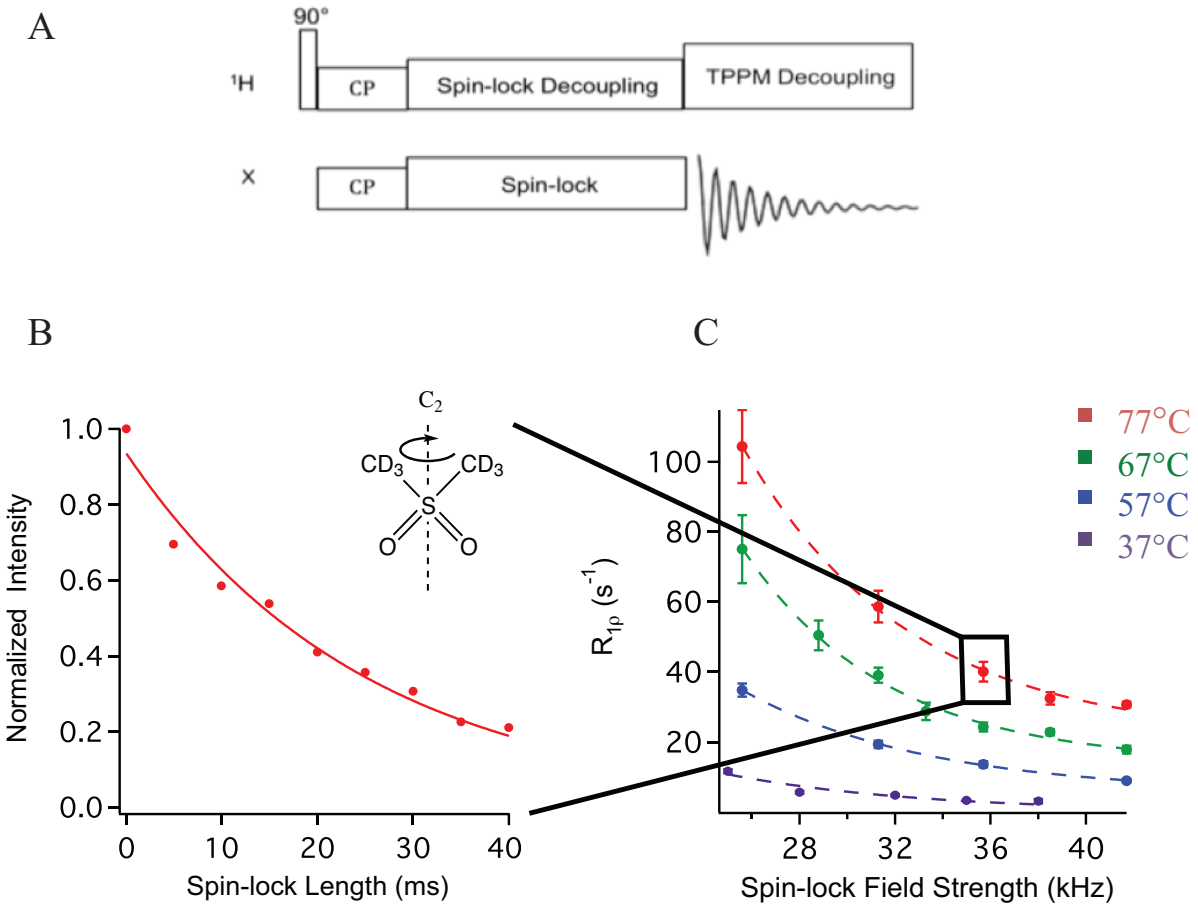

Figure 3.1 Illustration of how $R_{1\rho}$ experiments are done, using sample data on measurements of d_6-DMS (further discussed in Section 3.2.3. (A) Pulse sequence used for $R_{1\rho}$ measurements. The key element is the continuous wave spin-lock on the X channel. (B) The peak intensity or integral is recorded as a function of spin-lock length and fit to a single exponential decay (although this is not necessarily the true functional form of the decay curve). (C) The extracted relaxation rate, $R_{1\rho}$, corresponds to a single point on a dispersion curve. These measurements are repeated over a range of spin-lock field strengths and temperatures. The characteristic field strength and temperature dependence is indicative of the exchange process.

For intermediate timescale exchange processes, the exchange contribution to $R_{1\rho}$ is distinguished from the transverse and longitudinal relaxation terms by its characteristic spin-lock field strength dependence. Fast timescale dynamics, such as rotation of a methyl group, also contribute to $R_{1\rho}$. However under the condition that ω_e (the effective spin-lock field) << $1/k$, $R_{1\rho}$ due to fast

timescale dynamics is independent of the applied spin-lock field strength [26] and can be viewed as an R_2^0 process. This R_2^0 process can be considered the asymptote of an $R_{1\rho}$ dispersion curve. In order to quantify R_{ex} and k_{ex}, it is necessary to also quantify the R_2^0 contribution to relaxation, which is due to interactions other than chemical exchange. Accurately determining R_2^0 is necessary to fitting k_{ex} because of the covariance between the two parameters as expressed in Equation 1. In the solid state, R_2^0 may include fast rotation of methyl groups, as well as incomplete decoupling of dipolar interactions. These complications will be further discussed below.

The spin thermodynamics of $R_{1\rho}$ experiments have been described previously [17, 26, 27]. In the solid state, experimental $R_{1\rho}$ relaxation has both static (spin-spin) and dynamic (spin-lattice) contributions. Spin-spin relaxation (R_D) of the nucleus being studied arises from fluctuations of the local field due to spin fluctuations of other more abundant nuclei (i.e. protons) due to their mutual static dipolar interaction. These proton spin fluctuations modulate the proton-carbon dipolar interactions. Spin-lattice relaxation arises from chemical exchange of the site of interest. An additional relaxation mechanism that needs to be considered is relaxation from the proton reservoir to the lattice, although under MAS this relaxation rate is very fast. The spin thermodynamics of $R_{1\rho}$ experiments can be described by the schematic shown in Figure 3.2.

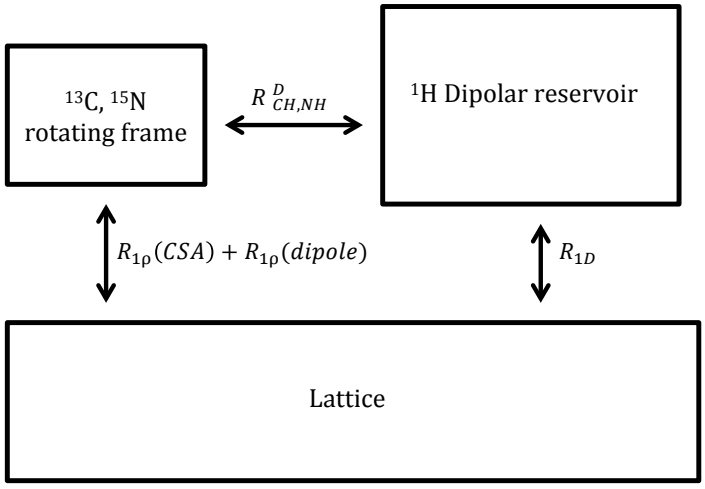

Figure 3.2 Spin thermodynamics of rotating frame relaxation. $R_{1\rho}$ relaxation due to reorientation of a dipolar or CSA tensor contains motional information. R^{D} is relaxation due to static spin-spin relaxation, which arises from dipolar fluctuations of protons adjacent to the nucleus of interest. R_{1D} is relaxation from the ^{1}H dipolar reservoir to the lattice.

Spin-spin relaxation is the dominant mechanism when low-to-moderate spin-lock fields are applied. A challenge of dynamics $R_{1\rho}$ measurements is to eliminate spin-spin relaxation while not interfering with spin-lattice relaxation [27]. Methods to minimize this term include off-resonance spin-locks and applying proton decoupling during the spin-lock [17].

In the solid state, dynamic rotating-frame relaxation (spin-lattice interactions) can be studied through 2 different interactions: monitoring reorientation of a dipole vector [17] or reorientation of a chemical shift anisotropy (CSA) tensor [19]. Using the CSA tensor to observe $R_{1\rho}$ relaxation can be useful as it provides a means for monitoring dynamics when the site of interest does not have a dipolar mechanism (i.e. no attached proton, for example a phosphate group or a carbonyl site in a sparsely labeled protein). Furthermore, a difference in isotropic chemical shift between the two exchange sites is not necessary as is required for solution NMR $R_{1\rho}$ measurements [28]. To observe relaxation purely due to reorientation of a chemical shift tensor,

both static and dynamic dipolar interactions need to be eliminated.

Farès et al and Kurbanov et al developed analytical expressions to describe relaxation due to both reorientation of a chemical shift tensor and a dipolar tensor under magic angle spinning [18, 29]. Greater detail regarding the derivation of these expressions through application of the master equation can be found in the Appendix, Section 8.1.

For a chemical shift tensor:

$$R_{1\rho}^{CS} \propto j(\omega_e + 2\omega_R) + j(\omega_e - 2\omega_R) + 2j(\omega_e + \omega_R) + 2j(\omega_e - \omega_R) \quad (2)$$

where $j(\omega)$ are the spectral density functions.

For reorientation of a dipolar tensor (I-S):

$$R_{1\rho}^{IS} \propto j(2\omega_e + 2\omega_R) + j(2\omega_e - 2\omega_R) + 2j(2\omega_e + \omega_R) + 2j(2\omega_e - \omega_R) \quad (3)$$

The spectral density functions $j(\omega)$ give rise to resonance conditions where the relaxation rate reaches a maximum. However, for solid-state rotating-frame relaxation studies, complications arise at these rotary resonance conditions (for the CSA, $\omega_1 = n\omega_R$, n = 1, 2). On these conditions, the CSA is recoupled [30, 31], leading to dramatically faster relaxation rates, which is by far the dominant effect and masks any dynamic information available. To allow for quantitative results, the rotary resonance conditions were avoided in these studies due to the challenges of quantifying the relaxation due to both CSA recoupling and CSA reorientation of a dynamic system on and near these conditions.

In the solid state, $R_{1\rho}$ studies have been used to gain insight into the general timescales of protein dynamics. Helmus et al used $R_{1\rho}$ relaxation (among other techniques) to investigate the dynamics of the amyloid core residues of Y145Stop human prion protein [32]. Lewandowski et al measured site-specific $R_{1\rho}$ values and modeled correlation times for GB1 [33, 34]. Krushelnitsky et al compared $R_{1\rho}$ values to order parameters to investigate microsecond timescale dynamics in the SH3 domain of α-spectrin [35]. The development of quantitative methods to interpret relaxation data and extract exchange rates has become increasingly important as site-specific measurements of $R_{1\rho}$ relaxation rates has become an increasing popular technique. Quantitative measurements of site-specific protein dynamics, specifically precise rates of molecular reorientation using $R_{1\rho}$ measurements, may be an important development to gain insight into protein function.

Analytical approaches to determining exchange rates from $R_{1\rho}$ relaxation for solid-state systems have been developed as discussed above. These analytical descriptions to calculating $R_{1\rho}$ and/or exchange rates are based upon solving the master equation for the density matrix. While these derivations provide insight into the mechanism of $R_{1\rho}$ relaxation, they have limitations. To our knowledge, little has been done in the way of applying these analytical expressions to experimental data. We chose a numerical approach to solving the problem of extracting exchange rates from $R_{1\rho}$ data. Using Spinevolution allows implementation for a wide range of spin systems and pulse sequences [36].

Here we will show that rotating-frame relaxation studies using reorientation of the CSA tensor as the probe of dynamics can be used to quantify the rate of molecular reorientation in a model

system, d_6-DMS. To our knowledge, this is the first example of $R_{1\rho}$ experiments being utilized to extract experimental exchange rates using the CSA tensor; the use of this model system serves to validate this new approach. Future extension of this method to biological systems may provide a new method to site-specifically quantify intermediate timescale dynamics with the novel advantages that dipolar interactions or differences in isotropic chemical shift between the two exchange sites are not necessary to still observe relaxation.

3.2 Results and Discussion

3.2.1 The System: Dimethyl Sulfone

Dimethyl sulfone (Figure 3.3) undergoes a 2-site hop around the molecule's C_2 symmetry axis, an exchange process that has been extensively studied using solid state NMR [14, 15, 17, 19, 20, 37-41]. The methyl groups of the molecule also undergo fast timescale rotation (~10^9) [42]. The 2-site hop is a slow-to-intermediate timescale activated process that R_{ex} is expected to report on. The fast methyl rotation is likely spin-lock field independent and captured in the R_2^0 component of the observed relaxation.

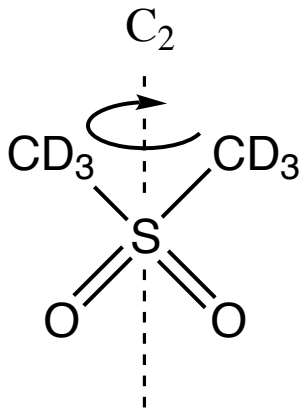

Figure 3.3 Structure and motional model of deuterated dimethyl sulfone (d_6-DMS). DMS undergoes a 180° flip around the molecule's C_2 axis, a motion that has been well-characterized in the solid-state NMR literature. In this study we have used both the protonated and deuterated forms of DMS.

Simulations of the reorientation of a carbon CSA tensor in DMS indicated the expected magnitude of $R_{1\rho}$ relaxation for this system. Figure 3.4 shows that consistent with theory, these experiments are most sensitive to intermediate timescale exchange processes. Enhanced relaxation on the rotary resonance conditions was also observed.

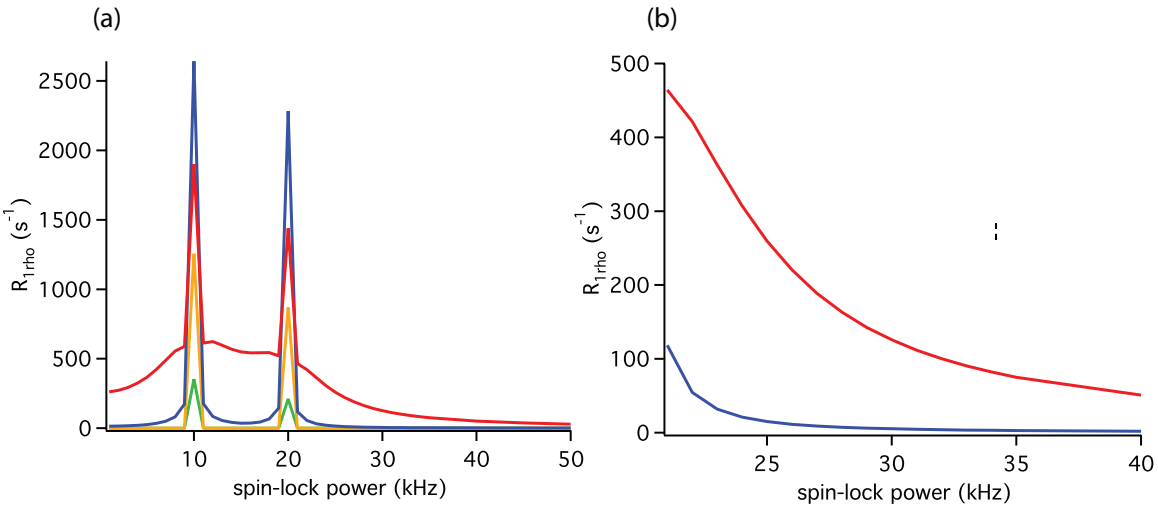

Figure 3.4 Simulations of DMS $R_{1\rho}$ relaxation, showing the dependence of $R_{1\rho}$ on the timescale of dynamics (a): k_{ex} = 1 Hz (green), 1 kHz (blue), 30 kHz (red), infinitely fast (yellow). (b) Expansion of intermediate exchange simulations in the region of 20-40 kHz applied spin-lock power. Parameters to model the reorientation of the DMS CSA tensor were δ = -36.77 ppm, η = 0.0625, β = 109° [38]. Simulations were performed using Spinevolution [36].

3.2.2 $R_{1\rho}$ Experiments and Simulations of ^{1}H-DMS

On-resonance carbon $R_{1\rho}$ measurements were performed on protonated DMS (^{1}H-DMS) over a range of spin-lock powers above the $\omega_1 = 2\omega_R$ condition at temperatures of 22°C, 37°C, and 65°C. Proton decoupling was applied during the spin-lock to reduce relaxation due to static and dynamic dipolar interactions. Peak integrals as a function of spin-lock length were fit to single exponentials to extract $R_{1\rho}$. A dispersion curve, $R_{1\rho}$ as a function of applied field strength, is presented in 3.5, which exhibits qualitative features consistent with the simulations in Figure 3.4 (B). Specifically, for elevated temperatures, where the motion is thermally activated, the relaxation rate $R_{1\rho}$ increases dramatically as the field strength approaches the $\omega_1 = 2\omega_R$ condition. The dependence of the dispersion curve on exchange rate (temperature) clearly illustrates that $R_{1\rho}$ is sensitive to the timescale of dynamics in a model exchange system, suggesting that the reorientation of a CSA tensor can be used to observe conformational exchange. A plot of $\ln(R_{1\rho})$ as a function of inverse temperature gives a slope of the order of 75 kJ/mol (Figure 3.5 inset), which is consistent with prior studies [37].

The β-methyl group of alanine was chosen as a static control system to confirm that the features of the dispersion curve are dependent on the presence and rate of chemical exchange rather than static dipolar interactions. The β-carbon of alanine has dipolar couplings to methyl protons and the methyl group undergoes fast rotation, analogous to DMS, but there is no chemical exchange process and thus no reorientation of the carbon CSA tensor occurs. Figure 3.6 (A) displays $R_{1\rho}$ for DMS and alanine as a function of applied spin-lock field strength. $R_{1\rho}$ for alanine has no

dependence on the applied field in this regime, leading to the conclusion that the feature above $\omega_1 = 2\omega_R$ in the $R_{1\rho}$ dispersion curve for DMS is due to reorientation of the carbon CSA tensor, not primarily static dipolar fluctuations of protons or fast rotation of the methyl group. Analogously, at low temperature, the chemical exchange process for DMS is suppressed (although the methyl rotation and couplings to the protons are still present); it is notable that the elevated relaxation above the rotary resonance condition is suppressed as expected.

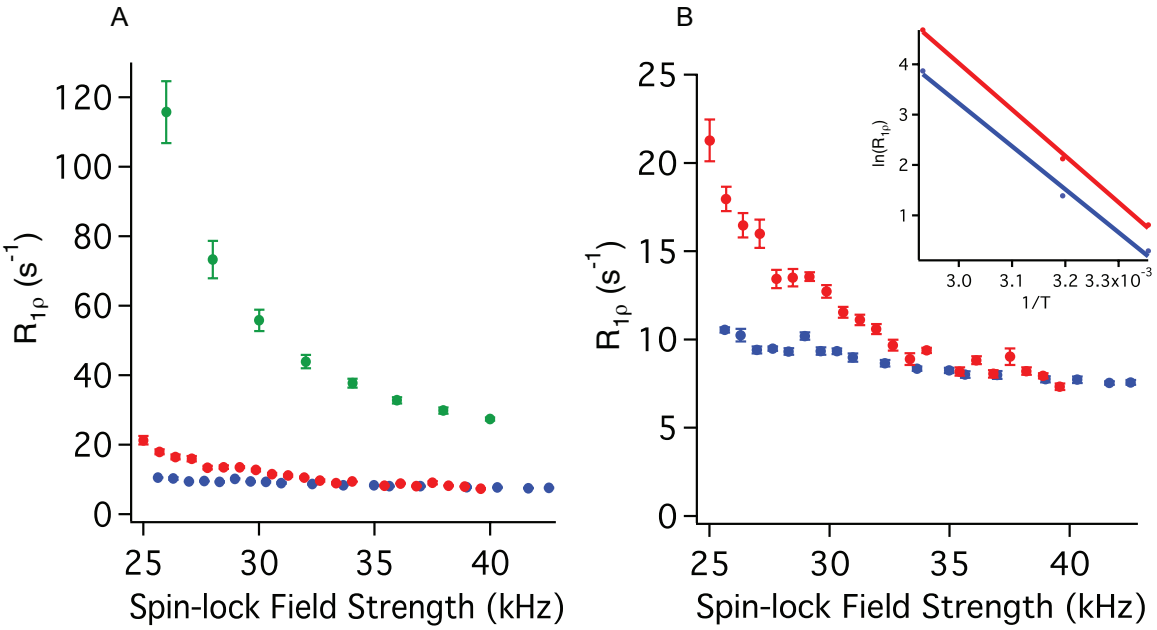

Figure 3.5 (A) Experimental $R_{1\rho}$ values for the methyl carbon of DMS as a function of on-resonance spin-lock powers, at 22°C (●), 37°C (●), and 65°C (●) collected with 100-125 kHz proton decoupling during the spin-lock. (B) Expansion of (A) highlighting the 22°C (●) and 37°C (●) data sets. In additional to the same spin-lock field strength dependence observed in (A), there is a notable and reproducible feature at ~ 29 kHz spin-lock field strength. It is hypothesized that this is a higher order rotary resonance feature not predicted by theory, and suggests the challenges of $R_{1\rho}$ experiments on protonated samples, which will be discussed further below. Error in the fit to a single exponential is indicated with error bars (~5-10%). (inset) The natural log of the $R_{1\rho}$ decay rate is plotted as a function of inverse temperature for spin lock field strengths of 25 and 30 kHz (red and blue traces respectively).

Control experiments were also performed with deuterated DMS (d_6-DMS) to observe the contribution of dipolar interactions to $R_{1\rho}$. Figure 3.6 (B) shows dispersion curves contrasting

deuterated and protonated DMS as a function of applied spin-lock field. Both protonated and detuerated DMS dispersion curves have a dependence on the applied spin-lock field strength. Thus the essential features in the dispersion curve appear to be largely independent of the presence or absence of proton couplings, confirming that the major contribution to $R_{1\rho}$ in these experiments is the chemical exchange of the CSA tensor.

Further controls utilized higher static magnetic fields to observe the effect on $R_{1\rho}$ relaxation rates. The magnitude of the CSA interaction is expected to scale as the square of the static magnetic field strength, B_0 [43, 44]. Due to the greater magnitude of the CSA tensor undergoing exchange, $R_{1\rho}$ relaxation rates are expected to be relatively higher at higher B_0 fields. This prediction was confirmed with both simulations and experiments as shown in Figure 3.6 (C). At a static field strength of 750 MHz, $R_{1\rho}$ relaxation is faster than observed at 400 MHz.

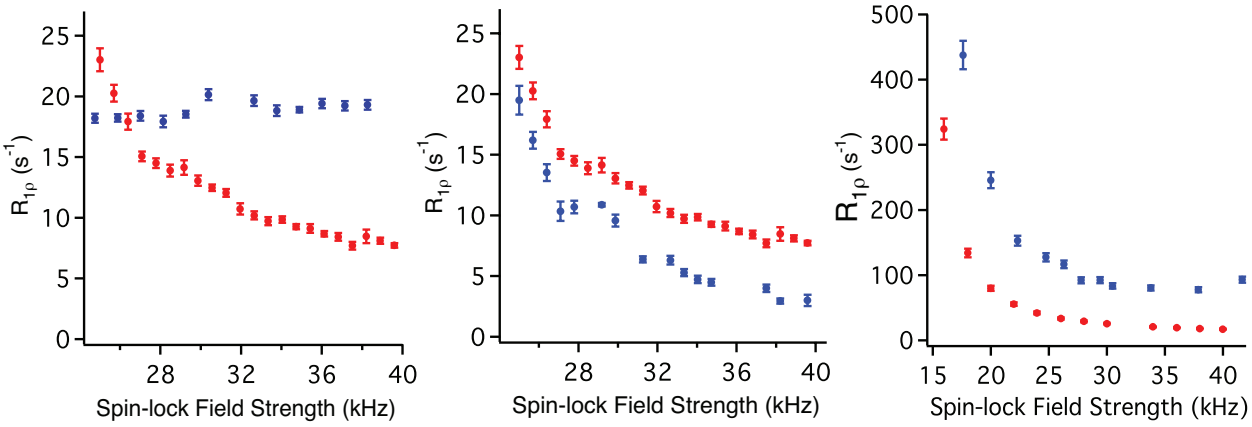

Figure 3.6 (A) (●) Dispersion curve for ^{1}H-DMS collected at 37°, 10 kHz MAS. (●) Dispersion curve for relaxation of the β-methyl carbon of protonated alanine collected at 37°, 10 kHz MAS. For alanine, which has no intermediate timescale exchange process, the dispersion curve has no dependence on the applied spin-lock field. (B) (●) Dispersion curve for ^{1}H-DMS collected at 37°, 10 kHz MAS. (●) Dispersion curve for d_6-DMS collected at 37°, 10 kHz MAS . The field-strength dependence in the absence of proton couplings indicates that CSA reorientation is the relaxation mechanism being utilized. (C) Dispersion curves for ^{1}H-DMS at B_0 field strengths of (•) 750 MHz and (•) 400 MHz. The expected B_0-field dependence was observed indicating that relaxation due to reorientation of the CSA tensor is the interaction being observed in these experiments. All data in (C) were collected at 65°C, 6 kHz MAS.

In addition to confirming that reorientation of the chemical shift tensor rather than the C-H dipole is the relaxation process observed, R_2^0 relaxation must also be taken into consideration. From the higher field strength $R_{1\rho}$ values for ^{1}H-DMS shown in Figure 3.5, the dispersion curve appears to be leveling out at an $R_{1\rho} \sim 8\ s^{-1}$. We attribute this residual relaxation to incomplete decoupling of protons, primarily arising from the fast rotation of the methyl group, which is expected to have a field-strength independent $R_{1\rho}$ value [26]. It is suggested that this is a spin-lattice contribution rather than a spin-spin contribution as a spin-spin relaxation term would be expected to have field-strength dependence under the conditions of our experiments. As shown in Figures 3.6 (A) and 3.7 for alanine, which we use as a static model for the DMS methyl group, there is no dependence of $R_{1\rho}$ on the applied spin-lock field strength. Thus for both compounds we conclude that this residual $R_{1\rho}$ relaxation arises from spin-lattice interactions. It can be seen in Figure 3.7 that $R_{1\rho}$ for alanine actually increases slightly with increased spin-lock field strengths. This may be due to Hartmann-Hahn effects as the spin-lock field strength becomes closer to the order of the proton decoupling, leading to unwanted magnetization transfer. Furthermore, as observed for DMS, alanine dispersion curves also show higher order rotary resonance effects not predicted by theory.

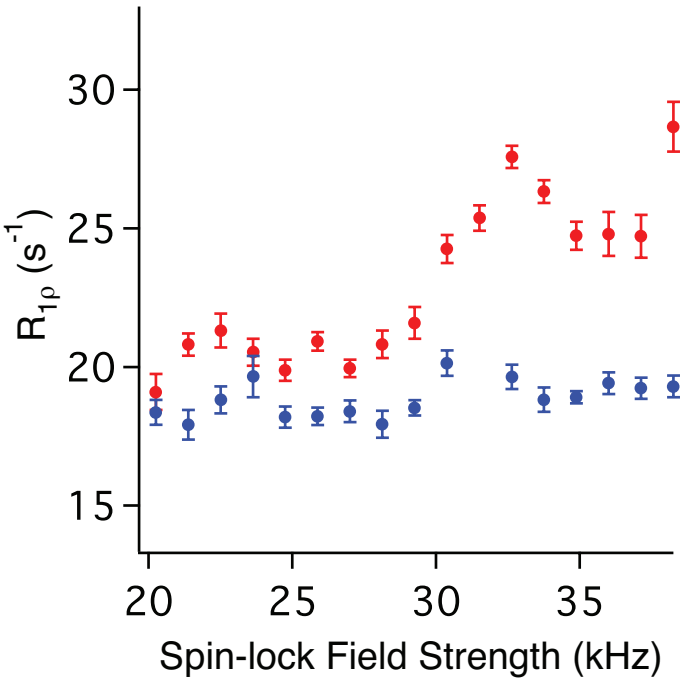

Figure 3.7 Dispersion curves for the β-methyl carbon of alanine at 37°C, 10 kHz MAS with (•) 86 kHz proton decoupling, and (•) 100 kHz proton decoupling. Higher order resonance effects not predicted by theory and observed in DMS are seen in this static molecule as well. There appears to be a field strength offset to the resonance conditions. A further observation is that $R_{1\rho}$ increases as a function of spin-lock field strength, possibly due to cross polarization-like effects.

Many experimental and simulated observations indicated the challenge that may be presented by using protonated compounds in these studies. At 37°C and 10 kHz MAS, DMS experiments were repeated using a range of decoupling powers during the spin-lock. As shown in Figure 3.8, while decoupling did have an effect on the relaxation rate relative to no decoupling, the strength of the ^{1}H decoupling in the range of 60 kHz to 125 kHz had virtually no impact on the relaxation rate. It would naively be predicted that higher decoupling would lead to slower relaxation due to more efficient decoupling of the protons. In fact, Figure 3.8 (B) indicates that relaxation rates are actually slower with 60 kHz decoupling than higher decoupling powers. This observation may be due to Hartmann-Hahn effects that occur while simultaneously irradiating the proton and carbon channels [45]. As the proton decoupling power is increased, a Hartmann-Hahn condition

is approached and there is actually increased magnetization transfer between proton and carbon, leading to faster relaxation. This idea is further supported by the observation that the method of decoupling during the spin-lock can also affect the observed relaxation rates. It was observed that both two pulse phase modulation (TPPM, [46]) and X-inverse X (XiX, [47]) proton decoupling during the spin-lock lead to faster relaxation than continuous wave decoupling. The apparent inability to completely eliminate relaxation due to dipolar interactions is consistent with what has been reported by other researchers [17, 26, 27]. Furthermore, the inefficiency of decoupling may be due to the dynamics of the molecule itself [48, 49]. This is further suggested by the fact that alanine $R_{1\rho}$ values shown in Figure 3.7 do appear to become lower with increased decoupling power.

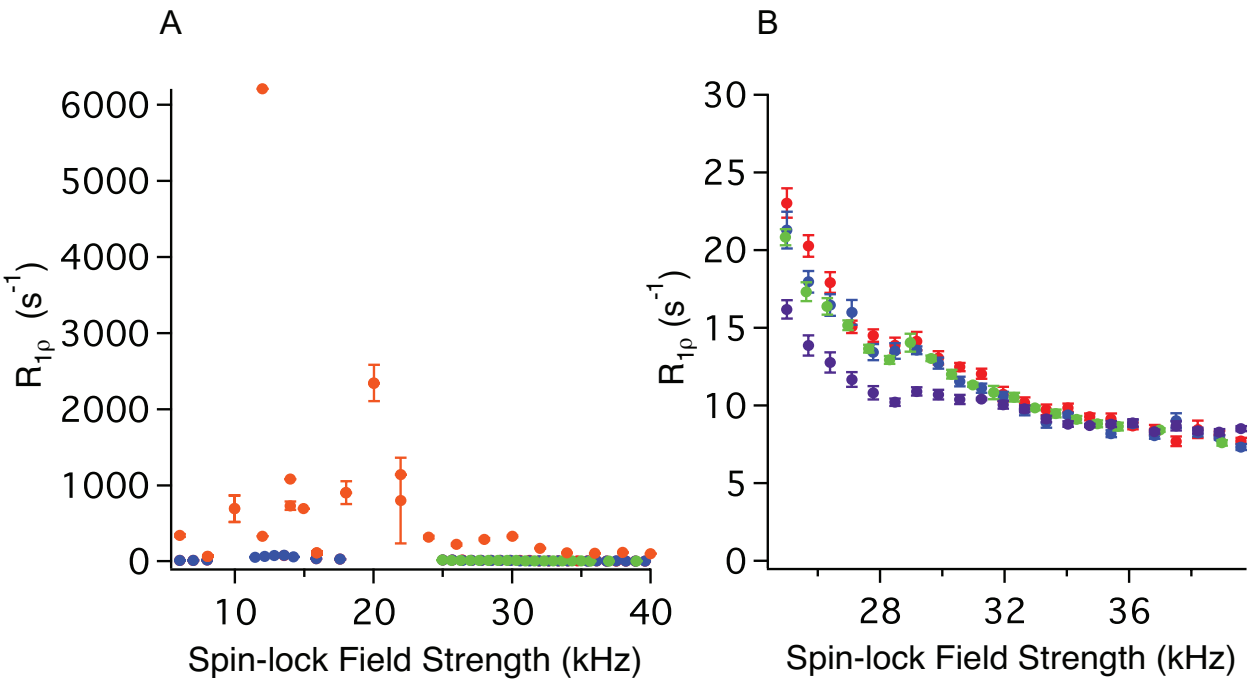

Figure 3.8 (A) Dispersion curves for ^{1}H-DMS with different decoupling powers: (•) 0 kHz ^{1}H decoupling, (•) 60 kHz ^{1}H decoupling, (•) 86 kHz ^{1}H decoupling, (•) 100 kHz ^{1}H decoupling, (•) 125 kHz ^{1}H decoupling. There is no observed dependence of relaxation on the decoupling field strength. In fact, relaxation is slower at 60 kHz decoupling, which may be due to more efficient relaxation at higher decoupling powers due to CP effects during the spin-lock. All data were collected at 37°C, 10 kHz MAS. (B) Expansion of (A) highlighting the minimal decoupling dependence from 60 -125 kHz.

A further challenge to obtaining quantitative exchange rates arises from the method of excitation. As shown in Figure 3.9, both simulations and experiments indicate that some relaxation occurs during cross-polarization, leading to erroneously low measured $R_{1\rho}$ relaxation rates for ^{1}H-DMS when excited using cross-polarization.

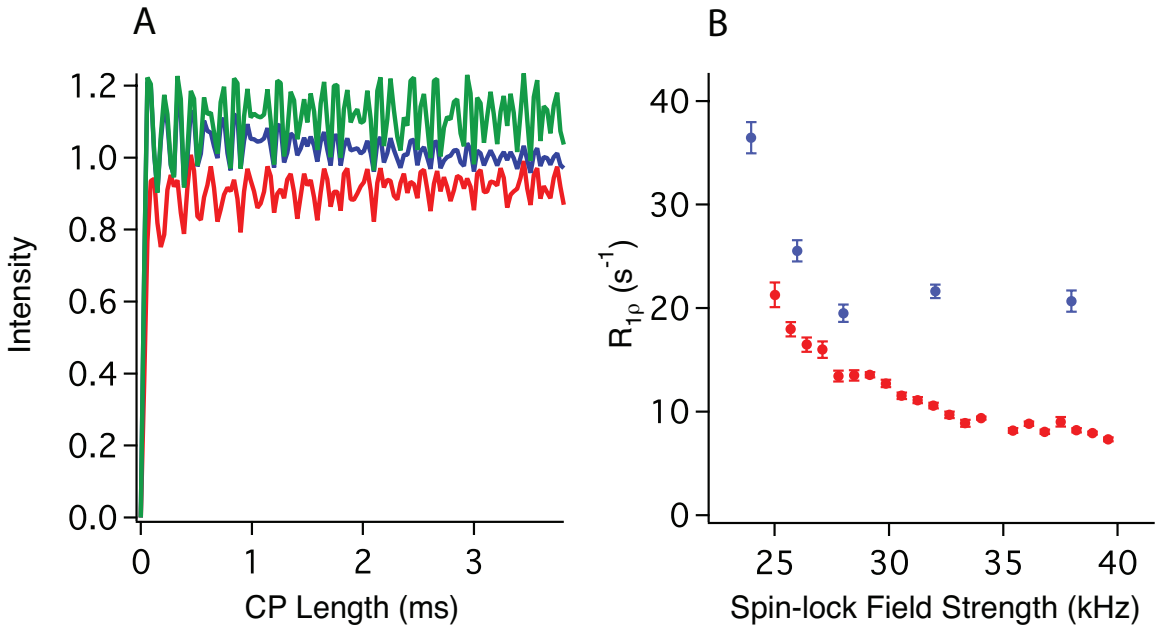

Figure 3.9 (A) Simulated build-up of intensity during cross polarization for a C-H group: green- static molecule, blue-1000 s^{-1} chemical exchange, red- infinitely fast chemical exchange. These simulations indicate that for a process undergoing intermediate exchange, there is actually some loss of magnetization during the H to C transfer of magnetization, particularly for longer CP times. (B) Experimental results: (•) $R_{1\rho}$ values measured with direct excitation of the carbon magnetization, (•) $R_{1\rho}$ values measured using cross polarization from proton to carbon. Both simulations and experimental results suggest that, particularly during longer CP times, transverse relaxation starts to occur, leading to erroneously low $R_{1\rho}$ values.

Simulations in Figure 3.9 (A) show that molecular dynamics have an effect on CP efficiency, particularly in the intermediate exchange regime. At a chemical exchange rate of 1000 s^{-1} (blue curve), carbon magnetization builds up, then starts to decay for CP lengths of longer than 1 ms. This decay of carbon magnetization was also confirmed with experiments comparing $R_{1\rho}$ using direct excitation versus cross polarization (Figure 3.9 (B)). The slower $R_{1\rho}$ values for

experiments done with cross polarization suggest that some carbon magnetization has decayed before the spin-lock and data acquisition.

Further evidence of the effects of relaxation during cross polarization, as well as B_1 inhomogeneity can be seen when the sample volume dependence of relaxation is studied (Figure 3.10). The volume-dependence of $R_{1\rho}$ for the data sets collected using direct excitation likely indicates that inhomogeneity of the spin-lock field produced by the coil leads to apparent faster relaxation for larger sample volumes. This phenomenon arises from portions of the sample away from the center of the coil receiving weaker spin-lock fields than near the center of the coil.

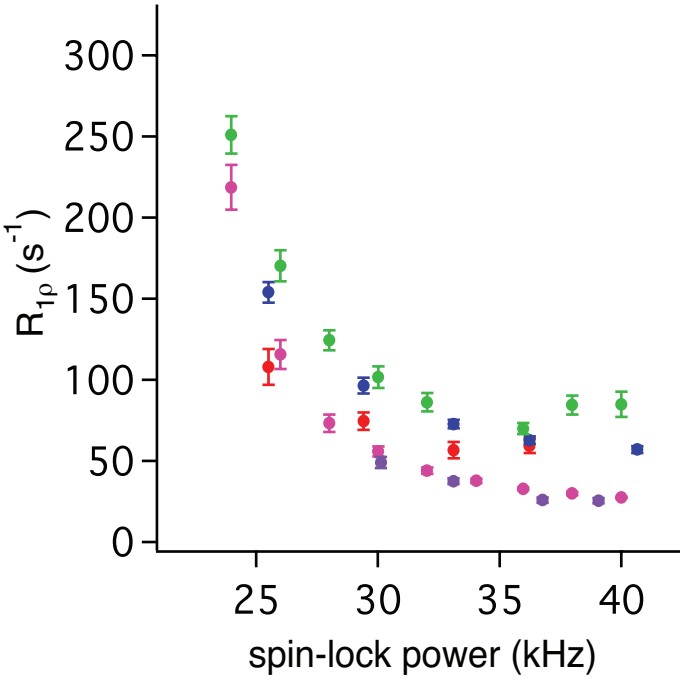

Figure 3.10 Volume-dependence of $R_{1\rho}$ relaxation for ^{1}H-DMS using both cross polarization and direct excitation at an MAS rate of 10 kHz and a temperature of 65°C. Direct excitation: (•) 68 µL volume, (•) 20 µL volume, (•) 5 µL volume. Cross polarization: (•) 68 µL volume, (•) 5 µL volume.

As a first attempt at quantifying exchange rates in DMS based on the decay curves for the protonated compound, data-fitting routines were used in both MINUET and Spinevolution. Given experimental decay trajectories, the fitting parameters of interest (in this case k_{ex} and R_2^0) were varied in Spinevolution to generate simulated decay curves. A root mean square (RMS) deviation between the simulated and experimental curves was calculated and this process was repeated until the RMS deviation was minimized. As was confirmed with data-fitting of deuterated DMS decay curves without R_2^0 as a free variable discussed later, the results obtained were generally in reasonable agreement with the true exchange rates. However, a few issues were encountered. Due to covariance between k_{ex} and R_2^0 as expressed in Equation 1, the fitting routine was not always able to distinguish between the different phenomena, at times ascribing all relaxation to one term or the other or being unable to reach convergence. Errors of up to 600% were observed. Final fitting results, including the ability to distinguish R_{ex} from R_2^0 relaxation were dependent on the initial values input by the user. In this system, based on exchange rates published in the literature and estimated R_2^0 values from dispersion curves, these values are better estimated for this model system than would likely be possible for more complicated systems. Furthermore, results from fitting a single data point were not reproduced when data sets were combined. As this method of data-fitting was not found to be robust, we sought other methods to eliminate covariance and fit the decay curves to exchange rates.

Parameter	Value	Error
k_1	0.11907	0.54919
T2SQpw3	124.84	46.420
T2SQpw5	126.22	130.78
T2SQpw8	48.886	8.3379

Table 3.1 Sample fitting results obtained from Spinevolution and MINUET for 3 data sets collected of protonated DMS at 30°C, fit to one exchange rate (k_1) and 3 different R_2^0 values (T2SQpw3, T2SQpw5, T2SQpw8). The values obtained from fitting are not unreasonable, but the large errors and absence of robust results over many data sets prompted the search for a better approach to quantifying exchange rates.

Because of the challenges that arise from attempting to account for the multitude of relaxation contributions present in the protonated compound, suggested by the many observations discussed above, including the absence of decoupling dependence, higher-order experimental rotary resonance conditions, cross polarization effects, and the absence of data-fitting convergence, we proposed that using deuterated DMS was necessary to obtain quantitative exchange rates, where these additional terms are minimized.

3.2.3 $R_{1\rho}$ Experiments and Simulations of d_6-DMS

Figure 3.11 shows dispersion curves collected for protonated and deuterated DMS at 77°C, 10 kHz MAS. As discussed above, these curves have two notable features. The first is that $R_{1\rho}$ for both compounds has a dependence on the applied spin-lock field strength, indicating that our method is probing relaxation due to reorientation of the CSA tensor. The second notable feature is that the relaxation rates are significantly higher for protonated DMS than deuterated DMS. We attribute this difference to the strong coupling of the carbon to its methyl protons, which could not be fully eliminated despite applying high-power proton decoupling during the spin-

lock. VanderHart and Garroway reported the dominant contribution of static dipolar interactions with protons to the observed carbon rotating-frame relaxation rate [27]. As suggested by the work on alanine described above, where the absence of an $R_{1\rho}$ spin-lock field dependence suggests the spin-spin contribution is being suppressed [50], the observed relaxation for DMS likely has a spin-lattice contribution from the reorientation of the CSA tensor. The additional relaxation due to the presence of protons appears to have a spin-lock field dependent component. This observation likely indicates that we are observing some relaxation due to reorientation of the C-H dipole vector, in addition to relaxation due to reorientation of the CSA tensor. For the deuterated DMS dispersion curve, control experiments showed that deuterium decoupling had no effect on the observed relaxation, suggesting that C-D dipolar relaxation is not a mechanism that contributes to relaxation in these experiments. While deuterated DMS is a very special case with an extremely limited number of relaxation mechanisms, we have chosen this simple model system to validate our method of extracting exchange rates from relaxation curves using numerical computations. Farès et al also commented on the challenges of accounting for residual strengths of existing interactions [18]. It is common practice to use deuteration to simplify relaxation measurements and eliminate undesired cross relaxation terms [35, 51, 52].

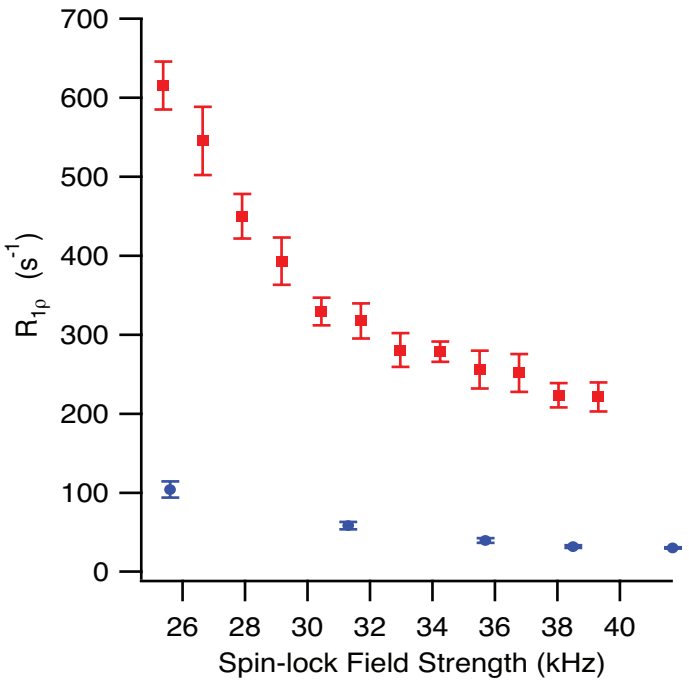

Figure 3.11 Dispersion curves for ^{1}H-DMS (■) and d_6-DMS (●) collected at 77°C, 10 kHz MAS. The field-strength dependence of both dispersion curves indicates that molecular reorientation of the carbon CSA tensor is being observed. The dramatically higher relaxation rates for protonated DMS are due to contributions from C-H dipolar interactions. The complexity of interactions occurring in the protonated compound suggests that deuteration is necessary to obtain quantitative exchange rates. The relative error for both data sets, generated from the error in the fit to a single-exponential decay, is the same, ~5-10%.

Dispersion curves were obtained for d_6-DMS at 4 different temperatures by measuring the decay of magnetization as a function of spin-lock length for a range of applied spin-lock fields, as shown in Figure 3.12. The field strength- and temperature-dependence of these curves are indicative of the exchange process. The multi-exponential behavior at lower spin-lock fields due to proximity to the $2\omega_R$ rotary resonance condition is reflected in the larger error bars when these data sets are fit to single exponentials.

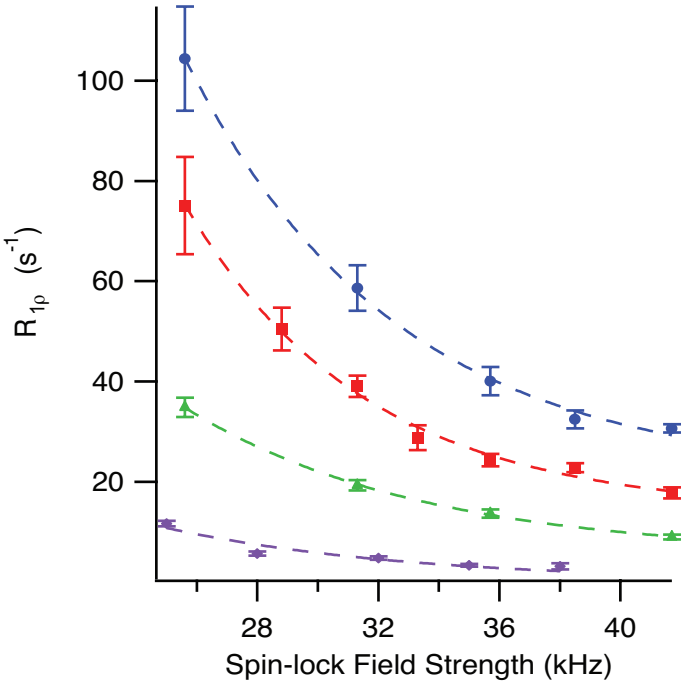

Figure 3.12 Dispersion curves collected at 4 different temperatures, (◆) 37°C, (▲) 57°C, (■) 67°C, and (●) 77°C for d_6-DMS. The greater dependence of $R_{1\rho}$ on spin-lock power at higher temperature indicates a faster exchange rate for the two-site hop. The larger error at low spin-lock field strengths is due to residual multi-exponential behavior near the rotary resonance condition.

To quantitatively analyze whether each decay curve is a better fit to a single or double exponential decay, an analysis-of-variance (ANOVA) test was done to determine F and P values given the χ^2 values determined from these fits.

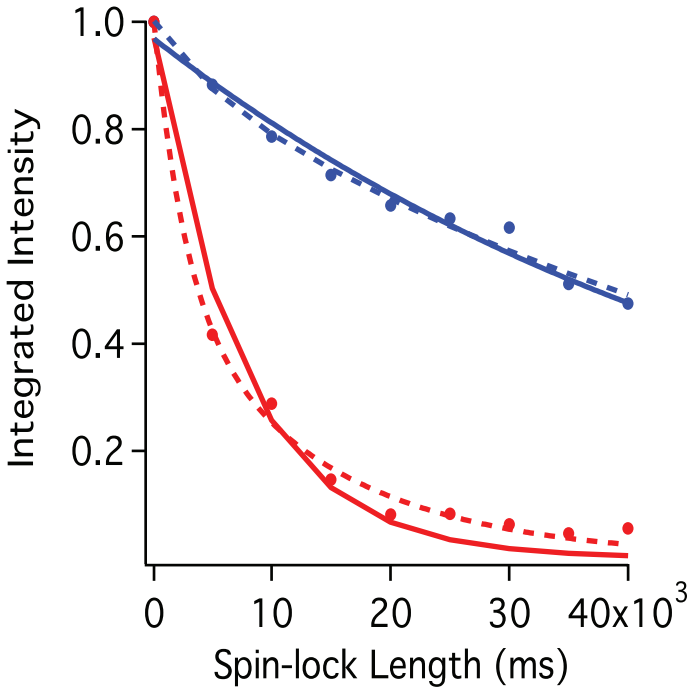

Figure 3.13 Decay curves for data at 67°C, 10 kHz MAS. Upper curve (blue): spin-lock field strength = 41.7 kHz. Lower curve (red): spin-lock field strength = 21.3 kHz. Solid lines are single-exponential fits; dotted lines are fits to double exponential decays. Qualitatively, it is apparent that there is little difference between single- and double-exponential fits at high spin-lock field strength, but the fits are different at low spin-lock field strength, with a double-exponential decay appearing to better capture the true decay of the data.

	χ^2	**Degrees of freedom**
Single-exponential	0.0414911	7
Double-exponential	0.00315725	5
Difference (single-exp – double-exp)	0.03833385	2
Relative Difference (difference/double-exp)	12.1415314	0.4
F ratio (Rel diff χ^2/ rel diff x dof)	30.3538	

Table 3.2 Sample ANOVA table, comparing fits to single-exponential and double-exponential for the decay curve collected at 25.6 kHz spin-lock, 67°C. From the resulting F ratio, a P value was determined.

The table below shows the results of this analysis for all 9 data points collected at 67°C.

Power (kHz)	χ^2 (single exp)	χ^2 (double exp)	F	P
18.5	0.0038076	0.00105059	6.560623078	0.027390865
21.3	0.0179041	0.00397422	8.762650281	0.014763497
25.6	0.0414911	0.00315725	30.35382849	0.000835533
28.8	0.0201234	0.00385417	10.55300493	0.009795148
31.3	0.00877997	0.00340356	3.949107699	0.074859779
33.3	0.017834	0.00799864	3.074072592	0.117296869
35.7	0.0059442	0.00461939	0.716983195	0.668164005
38.5	0.00293464	0.00082131	6.432802474	0.028536608
41.7	0.00553818	0.00309351	1.975644171	0.235498783

Table 3.3 χ^2 values for fits to single and double exponential decays, as well as calculated F and P values. Highlighted in yellow are the decay curves for which the analysis gave a P value of less than 0.05 indicating that for these curves, a double exponential decay is the better fit.

The results of this ANOVA analysis at other temperatures are consistent with the results shown in Table 3.3 for data at 67°C. This statistical approach indicates that for lower applied spin-lock powers, the curves are better fits to double-exponentials. This conclusion can also be seen qualitatively in Figure 3.13. At a spin-lock field strength of 21.3 kHz and 10 kHz MAS, there is notable difference between fitting the curve to a double or single exponential decay. At 41.7 kHz spin-lock field strength, there is virtually no difference between the decay models used. It is likely that the multi-exponential behavior at lower spin-lock field strengths is due to the experimental broadness of the rotary resonance conditions. However, we do not have a model at present to quantify this effect, thus spin-lock field strengths below ~ 25 kHz were generally avoided in data-fitting/ quantitative analyses.

The relaxation rate R_2^0 is independent of the conformational exchange rate but can contribute to the observed $R_{1\rho}$ relaxation rate through a number of processes. One challenge of this method

for quantifying rates of molecular reorientation is determining the R_2^0 contribution to $R_{1\rho}$. The accurate measurement of R_2^0 is critical to obtaining correct exchange rates due to the covariance between R_{ex} and R_2^0 as expressed in Equation 1. In order to determine the R_2^0 contribution to the observed relaxation, we determined where the $R_{1\rho}$ dispersion curves shown in Figure 3.12 reached an asymptotic temperature- and spin-lock independent $R_{1\rho}$ value, indicating that the R_{ex} component has been eliminated. $R_{1\rho}$ experiments were performed at very low temperatures and high spin-lock field strengths where the R_{ex} component to the relaxation (i.e. the intermediate exchange C_2 180° flip of DMS) is suppressed. At temperatures of -40°C and -25°C, we were able to obtain spin-lock and spinning speed independent relaxation rates, suggesting that R_2^0 is the process being observed. At these low temperatures, the exchange rate for the 180° flip is well below the timescale that $R_{1\rho}$ experiments are sensitive to. The average R_2^0 value from these measurements was $1.8 \pm 0.2\ s^{-1}$, shown in Figure 3.14.

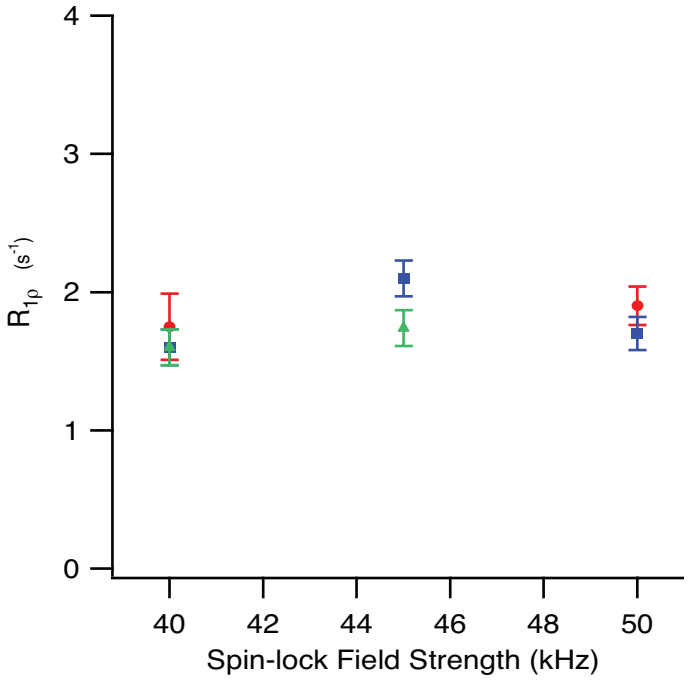

Figure 3.14 $R_{1\rho}$ values measured at low temperatures and high spin-lock fields are shown. The average $R_{1\rho}$ determined from these measurements was 1.8 ± 0.2 s^{-1}. The observed temperature and spin-lock field independence suggest that the minimum $R_{1\rho}$ value is being measured. Data was collected under the following conditions: (▲) -40°C, 10 kHz MAS; (■) -40°C, 5 kHz MAS; and (●) -25°C, 5 kHz MAS.

Two possible interpretations of the measured low-temperature $R_{1\rho}$ value are that this value corresponds to a temperature-dependent process, most likely rotation of the deuterated methyl groups, or temperature-independent dephasing processes, including pulse imperfections, field inhomogeneity, or deuterium spin diffusion. The choice of a temperature-dependent or –independent model has a small impact on the resulting exchange rates for the 180° flip of DMS. As we have no concrete reason to reject either model, we have presented both, showing that they agree within the error of the method.

To determine quantitative exchange rates from the observed relaxation, the R_2^0 values were then included in Spinevolution calculations using the program's optimization function to minimize the χ^2 difference between experimental relaxation curves and simulated curves which used the

exchange rate *k* as the sole fitting parameter as described in the Materials and Methods section. The exchange rates determined through this fitting procedure for both the temperature-dependent and temperature-independent models for R_2^0 are shown in Table 3.4 and an Arrhenius plot of the exchange rates obtained from this analysis are shown in Figure 3.16, along with data previously measured through a wide range of other techniques.

The low temperature $R_{1\rho}$ value, attributed to R_2^0 relaxation, may arise from the fast-limit, spin-lock field independent rotation of the deuterated methyl groups, which even at low temperatures is still in the fast limit for $R_{1\rho}$ experiments (~10^9) [42, 53, 54]. The value for R_2^0 determined in these low temperature experiments is consistent with the value that would be predicted for fast rotation of a deuterated methyl group as described by Akasaka et al [26]:

$$T_{1\rho}^{C} = \frac{1}{32} d^2 [4J_0(\omega_{1c}) + J_0(\omega_H - \omega_C) + 18J_1(\omega_c) + 36J_1(\omega_H) + 9J_2(\omega_H + \omega_c)] \quad (4)$$

$$J_m(\omega) = K_m \sum_i r_{CH_i}^{-6} N_i (3/4) (sin^2 2\beta_i + sin^4 \beta_i) \frac{2\tau_{c_i}}{1+\omega^2 \tau_{c_i}^2} \quad (5)$$

Here $d^2 = \gamma_C^2 \gamma_H^2 \hbar^2$, N_i is the number of equivalent protons undergoing rotation in the i^{th} group, β_i is the angle between the C-H vector and the axis of the group rotation, τ_C is the correlation time for the i^{th} group rotation, and the geometric factors are $K_0 = (4/5)$, $K_1 = (2/15)$, and $K_2 = (8/15)$.

Assuming an Arrhenius temperature-dependence for the methyl group rotation, with an activation barrier on the order of 20 – 30 kJ/mol and a pre-exponential factor of 10^{13} – 10^{15}, physically realistic and typical for a methyl group, we can estimate an $R_{1\rho}$ contribution from this

fast-limit process over the range of -40°C to +80°C according to the expressions in reference [26]. Both the small uncertainty in the true sample temperature (5-10° sample heating due to MAS) and activation barrier lead to a range of possible R_2^0 values for the methyl rotation at each temperature. The contribution to $R_{1\rho}$ would be expected to be relatively higher at -40°C and -25°C, and of the order of our experimentally derived value, 1.8 s^{-1}, and would be expected to be essentially negligible at 80°C. The exchange rates presented in Table 3.4 represent the middle of the range of sample temperature and activation energy with the errors indicating the exchange rates determined at the highest and lowest values in the range of both temperature and activation energy. It is important to note that the error due to the uncertainty in these experimental parameters is greater than the error due to data-fitting in Spinevolution.

Another possible explanation for the observed R_2^0 contribution to relaxation could be due to unidentified temperature-independent dephasing processes such as pulse imperfections, field inhomogeneity, or deuterium spin diffusion. The Spinevolution optimization to determine exchange rates was also done using the experimentally determined R_2^0 value of 1.8 s^{-1} at all temperatures. The exchange rates determined using this temperature-independent R_2^0 model agreed within error with the results using the temperature-dependent model described above, as shown in Table 3.4. The errors in the fit from Spinevolution are the same order of magnitude as the error introduced by the error in R_2^0.

It is significant to note that the exchange rates calculated using the 2 different models for R_2^0 are in agreement within the error of the method. The possible range of R_2^0 values in each model is the largest source of error expressed in the exchange rate (rather than the data-fitting). Over the

range of temperatures utilized in this study, these small R_2^0 contributions have little effect on the exchange rates determined in data-fitting.

Temperature	Temperature-independent Dephasing Model Exchange Rate (s^{-1})	R_2^0 Arrhenius Methyl Rotation Model Exchange Rate (s^{-1})
37°C	300 ± 30	350 ± 40
57°C	1600 ± 200	1800 ± 300
67°C	4500± 400	4500 ± 400
77°C	7500 ± 800	7900 ± 800

Table 3.4 Exchange rates determined for the C_2 180° flip in d_6-DMS using $R_{1\rho}$ relaxation and applying both temperature-independent and temperature-dependent models for the additional R_2^0 relaxation term. The errors in the exchange rates were determined by the error in the experimental R_2^0 measurement for the temperature-independent model and the error that arises from the choice of the methyl rotation activation energy in the range of 20 –30 kJ/mol for the temperature-dependent model. However at such small R_2^0 values the differences observed between these two models are small.

The errors on the exchange rates were determined as follows. For the temperature-independent model, simulations were repeated using the maximum and minimum R_2^0 values based on the error in the experimentally determined R_2^0 value, and the exchange rates determined from these calculations were used as the lower and upper limits of the exchange rate error. For the temperature-dependent model, the largest source of error arises from the choice of Arrhenius parameters for the methyl rotation, the uncertainty in the temperature, and the corresponding range of possible R_2^0 values. The upper and lower limits of the exchange rates were calculated by determining the R_2^0 values corresponding to activation energies of 20 kJ/mol and 30 kJ/mol for the methyl group rotation, extrapolated to the higher temperature range used (calibrated temperature ± ~2°C) and calculating corresponding exchange rates with Spinevolution.

Normalized decays in the integrated intensity of the DMS carbon peak as a function of spin-lock length are shown in Figure 3.15, along with fits to single exponential decays and the Spinevolution simulated curves using the exchange rates determined in data-fitting at temperatures of 37°C (A) and 77°C (B). These curves show that the quality of fits to single-exponentials at field strengths above ~25 kHz is good, as well as that the results from data-fitting in Spinevolution are able to reproduce experimental curves well.

Using the exchange rates determined from data-fitting shown in Table 3.4, an Arrhenius analysis of the exchange rates determined in this study was done and compared to previous studies of DMS dynamics, as shown in Figure 3.16.

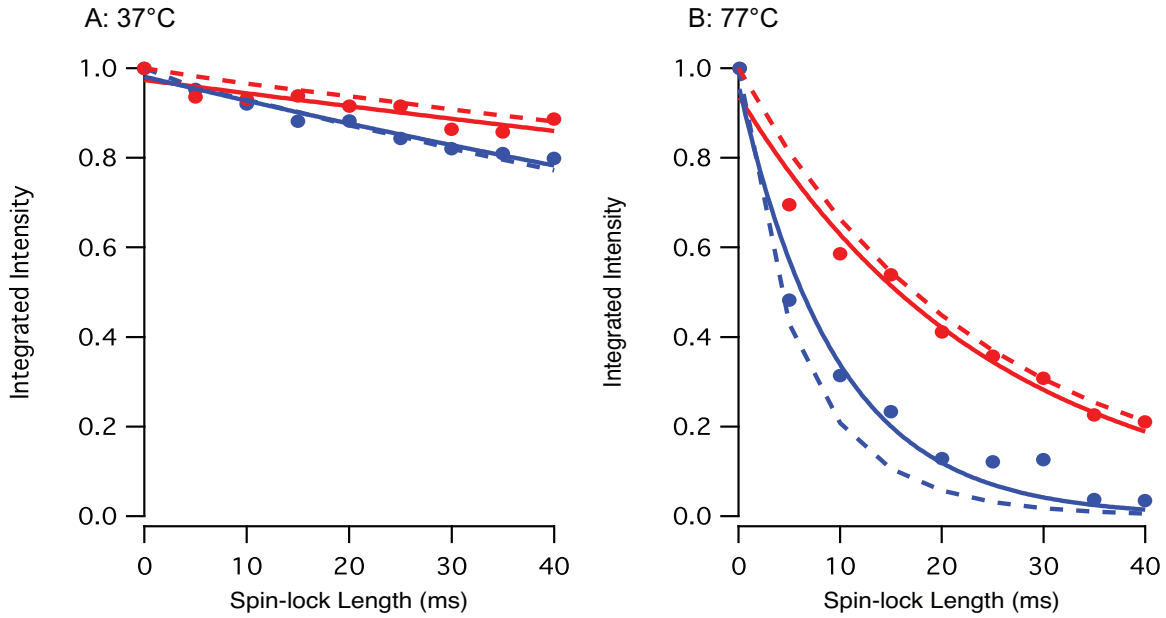

Figure 3.15 Normalized decay in integrated intensity of the DMS carbon peak as a function of spin-lock length, shown with fits to single exponential decays and the Spinevolution simulated curves using the exchange rate determined in data-fitting. (A) Raw decay curves collected at 37°C: (•) Raw decay curve collected at 38 kHz spin-lock field strength. (–) Fit of decay curve to a single exponential decay function, giving an $R_{1\rho}$ value of 3.3 ± 0.3 s^{-1}. (- -) Decay curve generated by fitting parameters given by fit in Spinevolution using the temperature-independent model, giving an $R_{1\rho}$ value of 3.1 ± 0.02 s^{-1}. (•) Raw decay curve collected at 28 kHz spin-lock field strength. (–) Fit of decay curve to a single exponential decay function, giving an $R_{1\rho}$ value of 5.6 ± 0.4 s^{-1}. (- -) Decay curve generated by fitting parameters given by fit in Spinevolution using the temperature-independent model, giving an $R_{1\rho}$ value of 6.4 ± 0.1 s^{-1}. (B) Raw decay curves collected at 77°C: (•) Raw decay curve collected at 36 kHz spin-lock field strength. (–) Fit of decay curve to a single exponential decay function, giving an $R_{1\rho}$ value of 40.1 ± 2.8 s^{-1}. (- -) Decay curve generated by fitting parameters given by fit in Spinevolution using the temperature-independent model, giving an $R_{1\rho}$ value of 39.5 ± 0.3 s^{-1}. (•) Raw decay curve collected at 26 kHz spin-lock field strength. (–) Fit of decay curve to a single exponential decay function, giving an $R_{1\rho}$ value 104.6 ± 10.5 s^{-1} (- -) Decay curve generated by fitting parameters given by fit in Spinevolution using the temperature-independent model, giving an $R_{1\rho}$ value of 158.2 s^{-1}.

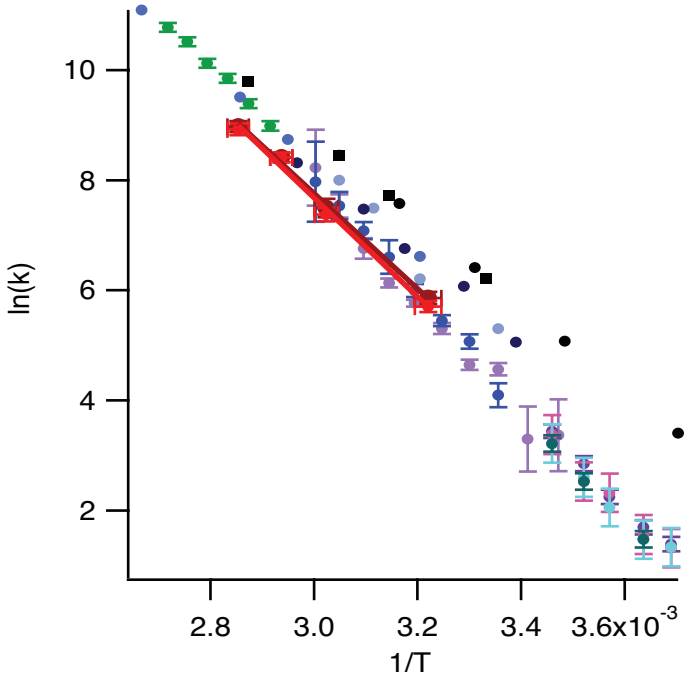

Figure 3.16 Arrhenius plot of exchange rates for the 180° C_2 flip of DMS measured using a wide range of solid-state NMR techniques highlighting the results for each individual technique. (●) $R_{1\rho}$ relaxation with a temperature-independent R_2^0 model (our data presented herein); (●) $R_{1\rho}$ relaxation with a temperature-dependent R_2^0 model (our data presented herein); (●) quadruploar echo [37]; (●) on-resonance selective inversion [37]; (●) off-resonance selective inversion [37]; (●) static 2D lineshape analysis [41]; (●) ODESSA [41]; (●) time-reverse ODESSA [41]; (●) exchange-induced sidebands [41]; (●) VACSY lineshape analysis [55]; (■) 1D static lineshape analysis [55]; (●) 1D MASS lineshape analysis [56]; (●) 2D MAS lineshape analysis [57]; (●) 1D static lineshape analysis [20]. Error bars are plotted when available. The Arrhenius parameters determined from each of these methods are reported in Table 3.5.

An Arrhenius analysis of the exchange rates from the temperature-independent R_2^0 model gave an activation energy of 74.7 ± 4.3 kJ/mol and an ln(A) value of 34.6 ± 1.6. Using the temperature-dependent model gave an activation energy of 71.7 ± 2.9 kJ/mol and an ln(A) value of 33.6 ± 1.0. These values are in excellent agreement with the Arrhenius parameters determined for DMS using other techniques and are presented for comparison in Table 3.5. The variation in these parameters among the various methods may be attributed to disagreement in the Arrhenius pre-factor A. From the crystal structure of DMS, the ln(A) value was calculated by Brown et al [37] to be 29.0 ($A \sim 10^{12}$), lower than that determined experimentally by all methods reported in Table 3.5. A common explanation for inaccurate ln(A) measurements is that the activation

energy is temperature-dependent. This disagreement could also be attributed to error propagation within the measurements such as systematic errors in the determination of R_2^0 or another methodological issue. It has also been noted that Arrhenius plots using NMR data (particularly over a small temperature range) can be intrinsically flawed [37, 41, 58].

Method	E_A (kJ/mol)	ln(A)
1D static lineshape analysis [20]	63.2 ± 3.0	30.9 ± 1.2
VACSY lineshape analysis [55]	64.3 ± 0.2	32.0 ± 0.1
1D static lineshape analysis [55]	64.6 ± 0.6	32.1 ± 0.2
2D MAS lineshape analysis [57]	69.2 ± 0.03	33.3 ± 0.01
Time-reverse ODESSA [41]	71.0 ± 7.2	32.7 ± 3.1
$R_{1\rho}$ relaxation (temperature-dependent R_2^0)	**71.7 ± 2.9**	**33.6 ± 1.0**
ODESSA [41]	74.0 ± 7.5	34.0 ± 3.2
$R_{1\rho}$ relaxation (temperature-independent R_2^0)	**74.7 ± 4.3**	**34.6 ± 1.6**
Quadrupolar echo [37]	75.7 ± 2.7	35.6 ± 0.9
1D MASS lineshape analysis [56]	75.7 ± 9.6	35.7 ± 3.7
Exchange induced sidebands [41]	76.1 ± 5.0	35.0 ± 2.2
Static 2D lineshape analysis [41]	81.3 ± 4.8	37.0 ± 2.0
On-resonance ^{2}H selective inversion [37]	86.1 ± 4.9	39.0 ± 1.9
Off-resonance ^{2}H selective inversion [37]	88.6 ± 3.0	40.1 ± 1.1

Table 3.5 Arrhenius parameters measured for protonated and deuterated DMS using our method, rotating-frame relaxation, and values obtained from linear fits of exchange rates from other solid-state NMR methods reported in the literature. Our values are in excellent agreement with previous measurements. The data indicate the wide range of Arrhenius parameters determined for this system, possibly due to the challenge that accurately measuring the pre-factor *A* presents in NMR experiments, particularly over a small temperature range [37, 41, 58].

As an alternative to measuring R_2^0 experimentally, we considered whether this value could be extracted by fitting the dispersion curve to a Lorentzian function, which is the expected functional form of the dispersion curve [18]. Using the experimentally determined exchange rates and R_2^0 values at 77°C for the temperature-independent R_2^0 model (R_2^0 = 1.8 s^{-1}, k = 7464 s^{-1}), the simulated dispersion curve shown in blue in Figure 3.17 was obtained. The points ± 1 kHz of the rotary resonance conditions were eliminated due to the non-dynamic components to the relaxation at these points. The dispersion curve was fit to a double Lorentzian function, fixing the centers of the Lorentzians at 10 kHz ($1\omega_R$) and 20 kHz ($2\omega_R$). From this fitting, we

were interested in extracting the offset of the Lorentzian from the baseline, which would be representative of the system's R_2^0 value. Despite simulating the dispersion curve with a broad range of spin-lock field strengths (out to 200 kHz), the R_2^0 value we obtained from fitting the dispersion curve was in error (R_2^0 = 4.12 ± 1.98 s^{-1}, compared to the true value of 1.8 s^{-1}). Practically we must restrict the range of spin-lock field strengths further to ν_1 < approximately 100 kHz due to probe limitations and ν_1 > about 25 kHz because the $\omega_1 = n\omega_R$ conditions are broad in practice. This indicates that although fitting a dispersion curve to a Lorentzian function can give an order-of-magnitude value for R_2^0, we believe that the experimental approach presented above can give more accurate results.

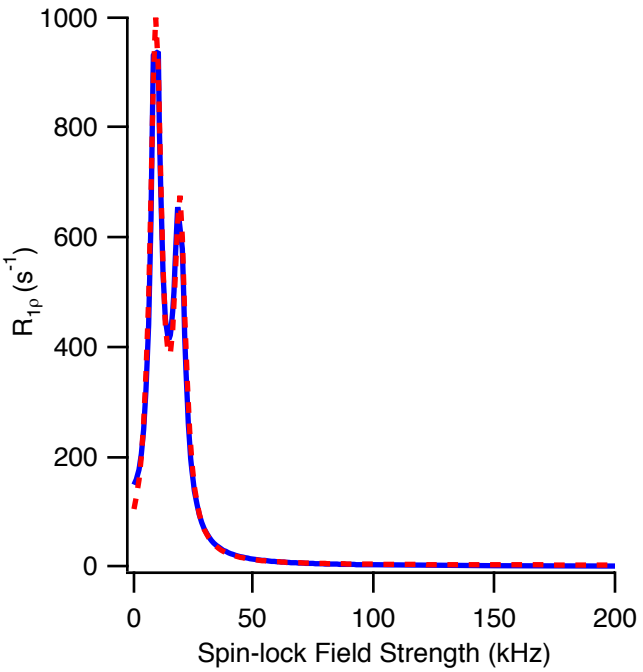

Figure 3.17 (–) Simulated dispersion curves using experimentally determined parameters at 77°C, 10 kHz MAS for the temperature-independent model (k = 7464 s^{-1}, R_2^0 = 1.8 s^{-1}). (- -) Fit of dispersion curve to a double Lorentzian function. The points ±1 kHz of the $1\omega_R$, $2\omega_R$ conditions were eliminated from the dispersion curve because of the non-dynamic contributions to $R_{1\rho}$ at these conditions. The R_2^0 value determined from the fit to a double Lorentzian was 4.12 ± 1.98 s^{-1}, compared to the true value of 1.8 ± 0.2 s^{-1}. Although this extrapolation method can determine order-of-magnitude R_2^0 fits, we believe that the experimental approach used in this paper gives a more accurate measure of R_2^0.

3.3 Conclusions

In conclusion, we have shown that the chemical shift anisotropy tensor can be used as a site-specific, quantitative probe of intermediate timescale conformational dynamics in $R_{1\rho}$ experiments to obtain exchange rates and activation energies. Performing these studies in the solid state is advantageous because in solution NMR, signals for sites undergoing intermediate exchange are often not observable due to exchange broadening. This method has unique advantages in that dipolar couplings and isotropic chemical shift differences between exchange sites are not necessary to observe dynamics. In the future this approach to extracting exchange rates may be applied to other mechanisms, such as reorientation of dipolar tensors. Our conclusions suggest important methodological considerations for the application of the method to more complicated systems such as proteins. The challenge of removing the strong dipolar coupling to protons indicates that deuteration is likely necessary to minimize this interaction. However deuteration of proteins to reduce undesired couplings is already common practice for the measurement of relaxation values [51, 52]. While DMS is an ideal case where the CSA parameters are well known, in more complicated systems the magnitudes and orientations of tensors may not be known, presenting an additional challenge. However techniques for the determination of CSA magnitudes and tensor orientations in proteins are readily available [59, 60]. When applying $R_{1\rho}$ techniques to quantify exchange rates, direct excitation is optimal to eliminate relaxation occurring during cross polarization to obtain accurate relaxation rates. As in any dynamics study, knowledge of sample temperature is important. Finally, the ability to minimize or quantify R_2^0 is a limiting factor in fitting accurate exchange rates using $R_{1\rho}$ relaxation, and may present an even greater challenge in more complicated systems than DMS.

3.4 Materials and Methods

3.4.1 Sample Preparation

Protonated DMS and Alanine were obtained from Fluka; d_6-DMS and β-d_3-Alanine were obtained from Cambridge Isotopes. Compounds were stored under vacuum for 24 hours to ensure they were dry, as hydration has been shown to affect observed dynamics in DMS [61]. L-Alanine was recrystallized as previously reported [62]. Powder diffraction was done to confirm the space group of the crystals and solution NMR was used to check the purity and % deuteration of the compounds (~99.5% ^{2}H for d_6-DMS). Approximately 35 mg of each DMS compound was doped with 1-2% KBr and packed into the center third of Varian 4 mm rotors. Alanine rotors were packed in the same manner, without KBr. Comparison with relaxation curves collected with no KBr indicated that this doping had no effect on the measurements.

3.4.2 NMR Experiments and Data Acquisition

NMR experiments were performed on a Varian 400 Infinity Plus spectrometer or Bruker Avance 750 MHz spectrometer using 4 mm probes at MAS rates of 6 or 10 kHz (±3 Hz) as noted for each particular experiment. $R_{1\rho}$ data was collected at thermocouple temperatures of 15°C, 30°C, and 58°C for ^{1}H-DMS; 30°C, 50°C, 60°C, and 70°C for d_6-DMS; and 30°C for alanine. The temperatures were measured at the end of the variable gas flow line. Sample temperatures are expected to be ~ 7° (± 2°) higher due to magic angle spinning, as shown in the temperature

calibrations below. The pulse sequences used for the on-resonance $R_{1\rho}$ experiments are shown in Figure 3.18. The variations in the $R_{1\rho}$ pulse sequence used in the different on-resonance experiments were as follows. ^{1}H-DMS: CP, ([$90^{H}(\phi_A)$]-[$CP^{H}(\phi_B)/CP^{C}(\phi_C)$]-[(CW dec)$^{H}(\phi_2)$/ $SL^{C}(\phi_C)$]-[(TPPM dec)^{H}/acq]) and direct excitation, ([$90^{C}(\phi_1)$]-[(CW dec)$^{H}(\phi_2)$/ $SL^{C}(\phi_3)$]-[(TPPM dec)^{H}/acq]); d_6-DMS ($R_{1\rho}$ and R_2^0 experiments): ([$90^{C}(\phi_1)$]-[$SL^{C}(\phi_3)$]-[acq]); d_6-DMS (^{2}H decoupling controls): ([$90^{C}(\phi_1)$]-[(CW dec)$^{D}(\phi_2)$/ $SL^{C}(\phi_3)$]-[acq]). The simple phase cycling scheme was ϕ_1=[x,-x, y, -y]; ϕ_2=[x]; ϕ_3=[-y, y, x, -x], ϕ_A=[x, x, -x, -x], ϕ_B=[y, y, y, y], ϕ_C=[x, y, x, y]. Typical ^{1}H 90° pulses were 2.2 μs and ^{13}C 90° pulse lengths were 5 μs. The spin-lock on the carbon channel was applied at fields of 25-40 kHz with continuous wave decoupling of 60-125 kHz on the proton channel during the spin-lock. The true field strength of the applied spin-lock was measured for each decay curve collected. ^{2}H decoupling field strengths for d_6-DMS experiments that used ^{2}H decoupling were 10-20 kHz during the spin-locks. On-resonance spin-lock pulses were applied for lengths of 100 μs, 1 ms – 9 ms or 5 ms, 10 ms, 15 ms, 20 ms, 25 ms, 30 ms, 35 ms, and 40 ms and at range of field strengths from 25-45 kHz for 22°-67°C experiments. For R_2^0 measurements at -25°C and -40°C, the on-resonance spin-lock pulses were applied for 100 μs, 10 ms, 20 ms, 30 ms, 40 ms, 50 ms, 60 ms, 70 ms, 80 ms, 90 ms, and 100 ms. For each scan, a 768 point FID was collected with a rotor-synchronized 100 μs dwell time.

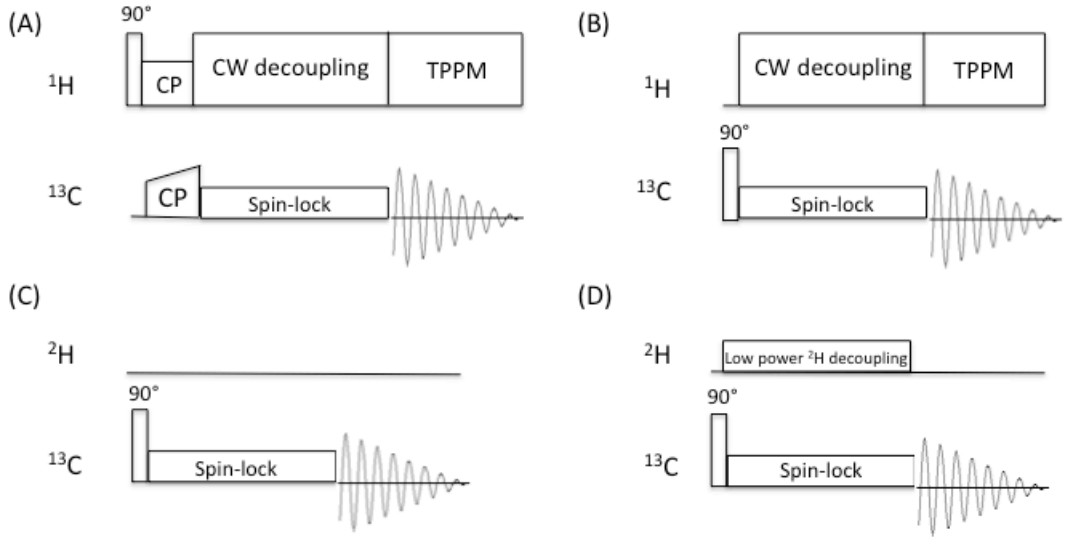

Figure 3.18 Variations of the $R_{1\rho}$ pulse sequences used in the studies of DMS dynamics reported here. Pulse sequences A and B were used for protonated DMS and alanine, while B and C were used for the deuterated compounds. (A) Cross polarization from ^{1}H to ^{13}C with high-power continuous wave decoupling during the spin-lock (the power of the decoupling was varied in different experiments as a control). (B) Direct excitation is used rather than cross polarization to excite carbon magnetization. (C) Direct excitation is used on the deuterated compounds, with no applied decoupling due to the absence of protons for d_6-DMS. (D) To ensure that there was no effect from the weak coupling of deuterons to the carbon of interest, control experiments with low power deuterium decoupling were also performed.

3.4.3 Temperature Calibrations

For studies of dynamics, accurate measurement of temperature is important, so temperature calibrations were performed using the ^{79}Br chemical shift of KBr-doped DMS [63]. A reference point was acquired with the thermocouple set to room temperature by spinning the rotor as slowly as possible (1-3 kHz). These resulting chemical shifts are shown in Table 3.6. Under these conditions, we assume that there is no heating due to magic angle spinning, and that the KBr chemical shift is representative of the true sample temperature.

Expt #	Sample volume (μL)	VT (°C)	MAS (Hz)	Chemical shift (Hz)
1	70	18	1000	-954.98
2	70	18	3000	-953.2
3	5	18	700	-954.68

Table 3.6 ^{79}Br chemical shifts recorded at very low spinning speeds and at ambient temperature. Under these conditions, the assumption is made that there is no sample heating due to magic angle spinning.

From the average chemical shifts reported in Table 3.6, the chemical shift of ^{79}KBr with no sample heating was approximated to an average of be -954 Hz. As reported by Thurber and Tycko, the ^{79}Br chemical shift changes by -0.0249 ± 0.0015 ppm per Kelvin (-2.475 ± 0.149 Hz per Kelvin on a 400 MHz spectrometer).

Spinning the sample up to 10 kHz and measuring the change in the ^{79}Br chemical shift allows the measurement of heating due to faster spinning. A 10 kHz MAS rate was found to contribute an additional 7 ± 2°C of heating as shown in Table 3.7; data analysis took this additional heating into account.

Expt #	Sample volume (μL)	VT (°C)	MAS (kHz)	Chemical shift (Hz)	Δ Chemical shift (Hz)	Chemical shift temp (°C)	ΔT (°C)
4	70	18	10	-970.447	-16.45	26	8
5	70	58	10	-1073.24	-119.24	68	10
6	70	70	10	-1096.7	-142.7	77	7

Table 3.7 Differences in chemical shift from the slow spinning speed average of -954 Hz determined as shown in Table 3.6 and the corresponding true sample temperatures.

It is interesting to note the other method for temperature calibration reported by Thurber and Tycko, the use of ^{79}Br T_1 relaxation to determine sample temperature, was not successfully implemented. This observation has also been previously reported in our lab [64].

We also investigated the dependence of sample heating on the volume of the rotor that was packing with DMS, as shown in Table 3.8. No temperature effects due to sample volume or the application of high power radio-frequency irradiation were observed.

Temperatures indicated in figures and discussions are true sample temperatures, based on this calibration data.

Expt #	Sample volume (μL)	VT (°C)	MAS (kHz)	Chemical shift (Hz)	Chemical shift temp (°C)
1	70	18	1	-954.98	20
3	5	18	0.7	-954.68	20
4	70	18	10	-970.447	26
7	5	18	10	-969.7	26
5	70	58	10	-1073.24	68
8	5	58	10	-1071.7	67

Table 3.8 Chemical shift measurements as a function of sample volume. No temperature-dependence on sample volume was observed.

3.4.4 Data Analysis

Data analysis was performed as follows. The decay in the normalized integrated intensity of the carbon peak as a function of spin-lock length was fit to a single-exponential decay to obtain $R_{1\rho}$. In some cases (particularly at lower spin-lock field strengths) the decay curves were better statistical fits to double exponential decays. Sample raw data showing these decay curves for DMS are seen in Figure 3.13. We do not have a model to explain this multi-exponential behavior and for this reason, spin-lock field strengths below 25 kHz were generally avoided. The observed $R_{1\rho}$ and R_2^0 values were plotted as a function of spin-lock field strength to generate

the dispersion curves. It should be noted that fitting the exchange rates as described below was done using raw data and therefore required no assumption regarding the single vs. multi-exponential behavior of the decay curves.

To obtain *k*, the optimization function in Spinevolution [20] was used to minimize the χ^2 difference between the raw decay curves and simulated decay curves with *k* and a scaling factor as the fitting parameters. In this data-fitting process, Spinevolution generates simulated decay curves (intensity as a function of spin-lock length, corresponding to the spin-lock lengths utilized in the experiments) at the specified spin-lock field strengths (i.e. the spin-lock field strengths used in the actual experiments). The difference between the experimental decay curves and these simulated decay curves was minimized using the NL2SOL non-linear least squares algorithm and exchange rate *k* as the fitting parameter, as this is the mechanism of decay in these experiments. Spinevolution performs calculations numerically by solving either the Liouville-von Nuemann equation or the Master equation using approximations such as the Chebyshev expansion to approximate the propagators of the Hamiltonian. Further detail can be found in reference [36]. The exchange process was modeled as a 2-site hop between 2 carbon atoms with a β angle of 109°. The CSA tensor parameters used were δ = -36.77 ppm and η = 0.0625 [20]. 538 crystallites were used for powder averaging. An additional R_2^0 relaxation term of was included to account for the measured R_2^0 relaxation as shown in Figure 3.14. All relaxation curves collected at a single temperature (different spin-lock field strengths) were combined into a single optimization and fit to a single *k*.

3.5 References

[1] A.G. Palmer, NMR characterization of the dynamics of biomacromolecules, Chem Rev, 104 (2004) 3623-3640.

[2] G. Hernandez, D.M. LeMaster, Reduced temperature dependence of collective conformational opening in a hyperthermophile rubredoxin, Biochemistry-Us, 40 (2001) 14384-14391.

[3] G. Hernandez, F.E. Jenney, M.W.W. Adams, D.M. LeMaster, Millisecond time scale conformational flexibility in a hyperthermophile protein at ambient temperature, P Natl Acad Sci USA, 97 (2000) 3166-3170.

[4] G. Bouvignies, P. Bernado, S. Meier, K. Cho, S. Grzesiek, R. Bruschweiler, M. Blackledge, Identification of slow correlated motions in proteins using residual dipolar and hydrogen-bond scalar couplings, P Natl Acad Sci USA, 102 (2005) 13885-13890.

[5] D. Shortle, M.S. Ackerman, Persistence of native-like topology in a denatured protein in 8 M urea, Science, 293 (2001) 487-489.

[6] O.F. Lange, N.A. Lakomek, C. Fares, G.F. Schroder, K.F.A. Walter, S. Becker, J. Meiler, H. Grubmuller, C. Griesinger, B.L. de Groot, Recognition dynamics up to microseconds revealed from an RDC-derived ubiquitin ensemble in solution, Science, 320 (2008) 1471-1475.

[7] M.W.F. Fischer, J.A. Losonczi, J.L. Weaver, J.H. Prestegard, Domain orientation and dynamics in multidomain proteins from residual dipolar couplings, Biochemistry-Us, 38 (1999) 9013-9022.

[8] H. Roder, G.A. Elove, S.W. Englander, Structural Characterization of Folding Intermediates in Cytochrome-C by H-Exchange Labeling and Proton Nmr, Nature, 335 (1988) 700-704.

[9] F. Massi, M.J. Grey, A.G. Palmer, Microsecond timescale backbone conformational dynamics in ubiquitin studied with NMR R-1p relaxation experiments, Protein Sci, 14 (2005) 735-742.

[10] F. Massi, C.Y. Wang, A.G. Palmer, Solution NMR and computer simulation studies of active site loop motion in triosephosphate isomerase, Biochemistry-Us, 45 (2006) 10787-10794.

[11] S.P. Brown, H.W. Spiess, Advanced solid-state NMR methods for the elucidation of structure and dynamics of molecular, macromolecular, and supramolecular systems, Chem Rev, 101 (2001) 4125-4155.

[12] O.C. Andronesi, S. Becker, K. Seidel, H. Heise, H.S. Young, M. Baldus, Determination of membrane protein structure and dynamics by magic-angle-spinning solid-state NMR spectroscopy, J Am Chem Soc, 127 (2005) 12965-12974.

[13] A. Krushelnitsky, D. Reichert, Solid-state NMR and protein dynamics, Prog Nucl Mag Res Sp, 47 (2005) 1-25.

[14] C. Schmidt, B. Blumich, H.W. Spiess, Deuteron Two-Dimensional Exchange NMR in Solids, J Magn Reson, 79 (1988) 269-290.

[15] E.R. deAzevedo, W.G. Hu, T.J. Bonagamba, K. Schmidt-Rohr, Principles of centerband-only detection of exchange in solid-state nuclear magnetic resonance, and extension to four-time centerband-only detection of exchange, J Chem Phys, 112 (2000) 8988-9001.

[16] W. Li, A.E. McDermott, Characterization of slow conformational dynamics in solids: dipolar CODEX, J Biomol Nmr, 45 (2009) 227-232.

[17] A. Krushelnitsky, R. Kurbanov, D. Reichert, G. Hempel, H. Schneider, V. Fedotov, Expanding the frequency range of the solid-state T-1rho experiment for heteronuclear dipolar relaxation, Solid State Nucl Mag, 22 (2002) 423-438.

[18] C. Fares, J. Qian, J.H. Davis, Magic angle spinning and static oriented sample NMR studies of the relaxation in the rotating frame of membrane peptides, J Chem Phys, 122 (2005) 194908-194917.

[19] C.M. Quinn, A.E. McDermott, Monitoring conformational dynamics with solid-state R(1rho) experiments, J Biomol Nmr, 45 (2009) 5-8.

[20] M.S. Solum, K.W. Zilm, J. Michl, D.M. Grant, C-13 Line-Shape Study of 2-Site Exchange in Solid Dimethyl Sulfone, J Phys Chem-Us, 87 (1983) 2940-2944.

[21] S. Rozovsky, A.E. McDermott, The time scale of the catalytic loop motion in triosephosphate isomerase, J Mol Biol, 310 (2001) 259-270.

[22] D.A. Torchia, A. Szabo, Spin-Lattice Relaxation in Solids, J Magn Reson, 49 (1982) 107-121.

[23] V. Chevelkov, Y. Xue, R. Linser, N.R. Skrynnikov, B. Reif, Comparison of Solid-State Dipolar Couplings and Solution Relaxation Data Provides Insight into Protein Backbone Dynamics, J Am Chem Soc, 132 (2010) 5015-5017.

[24] J.L. Lorieau, A.E. McDermott, Conformational flexibility of a microcrystalline globular protein: Order parameters by solid-state NMR spectroscopy, J Am Chem Soc, 128 (2006) 11505-11512.

[25] A.G. Palmer, C.D. Kroenke, J.P. Loria, Nuclear magnetic resonance methods for quantifying microsecond-to-millisecond motions in biological macromolecules, Method Enzymol, 339 (2001) 204-238.

[26] K. Akasaka, S. Ganapathy, C.A. Mcdowell, A. Naito, Spin Spin and Spin-Lattice Contributions to the Rotating Frame Relaxation of C-13 in L-Alanine, J Chem Phys, 78 (1983) 3567-3572.

[27] D.L. Vanderhart, A.N. Garroway, C-13 Nmr Rotating Frame Relaxation in a Solid with Strongly Coupled Protons - Polyethylene, J Chem Phys, 71 (1979) 2773-2787.

[28] A.G. Palmer, F. Massi, Characterization of the dynamics of biomacromolecules using rotating-frame spin relaxation NMR spectroscopy, Chem Rev, 106 (2006) 1700-1719.

[29] R. Kurbanov, T. Zinkevich, A. Krushelnitsky, The nuclear magnetic resonance relaxation data analysis in solids: General R-1/R-1 rho equations and the model-free approach, J Chem Phys, 135 (2011).

[30] Z.H. Gan, D.M. Grant, Rotational Resonance in a Spin-Lock Field for Solid-State Nmr, Chem Phys Lett, 168 (1990) 304-308.

[31] Z.H. Gan, D.M. Grant, R.R. Ernst, NMR chemical shift anisotropy measurements by RF driven rotary resonance, Chem Phys Lett, 254 (1996) 349-357.

[32] J.J. Helmus, K. Surewicz, W.K. Surewicz, C.P. Jaroniec, Conformational Flexibility of Y145Stop Human Prion Protein Amyloid Fibrils Probed by Solid-State Nuclear Magnetic Resonance Spectroscopy, J Am Chem Soc, 132 (2010) 2393-2403.

[33] J.R. Lewandowski, H.J. Sass, S. Grzesiek, M. Blackledge, L. Emsley, Site-Specific Measurement of Slow Motions in Proteins, J Am Chem Soc, 133 (2011) 16762-16765.

[34] J.R. Lewandowski, J. Sein, H.J. Sass, S. Grzesiek, M. Blackledge, L. Emsley, Measurement of site-specific 13C spin-lattice relaxation in a crystalline protein, J Am Chem Soc, 132 (2010) 8252-8254.

[35] A. Krushelnitsky, T. Zinkevich, D. Reichert, V. Chevelkov, B. Reif, Microsecond Time Scale Mobility in a Solid Protein As Studied by the (15)N R(1 rho) Site-Specific NMR Relaxation Rates, J Am Chem Soc, 132 (2010) 11850-11853.

[36] M. Veshtort, R.G. Griffin, SPINEVOLUTION: A powerful tool for the simulation of solid and liquid state NMR experiments, J Magn Reson, 178 (2006) 248-282.

[37] M.J. Brown, R.L. Vold, G.L. Hoatson, Selective inversion investigations of slow molecular motion in solid state deuteron NMR spectroscopy, Solid State Nucl Mag, 6 (1996) 167-185.

[38] V. Gerardy-Montouillout, C. Malveau, P. Tekely, Z. Olender, Z. Luz, ODESSA, a new 1D NMR exchange experiment for chemically equivalent nuclei in rotating solids, J Magn Reson Ser A, 123 (1996) 7-15.

[39] A. Schmidt, S. Vega, NMR Line-Shape Analysis for 2-Site Exchange in Rotating Solids, J Chem Phys, 87 (1987) 6895-6907.

[40] O. Weintraub, S. Vega, Dynamic H-2 Nuclear-Magnetic-Resonance of Rotating Solids, Solid State Nucl Mag, 4 (1995) 341-351.

[41] D.E. Favre, D.J. Schaefer, B.F. Chmelka, Direct determination of motional correlation times by 1D MAS and 2D exchange NMR techniques, J Magn Reson, 134 (1998) 261-279.

[42] R.L. Vold, G.L. Hoatson, Effects of jump dynamics on solid state nuclear magnetic resonance line shapes and spin relaxation times, J Magn Reson, 198 (2009) 57-72.

[43] O. Millet, J.P. Loria, C.D. Kroenke, M. Pons, A.G. Palmer, The static magnetic field dependence of chemical exchange linebroadening defines the NMR chemical shift time scale, J Am Chem Soc, 122 (2000) 2867-2877.

[44] J.W. Peng, G. Wagner, Frequency spectrum of NH bonds in eglin c from spectral density mapping at multiple fields, Biochemistry-Us, 34 (1995) 16733-16752.

[45] S.R. Hartmann, E.L. Hahn, Nuclear Double Resonance in Rotating Frame, Phys Rev, 128 (1962) 2042-&.

[46] A.E. Bennett, C.M. Rienstra, M. Auger, K.V. Lakshmi, R.G. Griffin, Heteronuclear Decoupling in Rotating Solids, J Chem Phys, 103 (1995) 6951-6958.

[47] A. Detken, E.H. Hardy, M. Ernst, B.H. Meier, Simple and efficient decoupling in magic-angle spinning solid-state NMR: the XiX scheme, Chem Phys Lett, 356 (2002) 298-304.

[48] J.R. Long, B.Q. Sun, A. Bowen, R.G. Griffin, Molecular-Dynamics and Magic-Angle-Spinning NMR, J Am Chem Soc, 116 (1994) 11950-11956.

[49] V. Chevelkov, K. Faelber, A. Schrey, K. Rehbein, A. Diehl, B. Reif, Differential line broadening in MAS solid-state NMR due to dynamic interference, J Am Chem Soc, 129 (2007) 10195-10200.

[50] J. Schaefer, E.O. Stejskal, R. Buchdahl, Magic-Angle C-13 Nmr Analysis of Motion in Solid Glassy Polymers, Macromolecules, 10 (1977) 384-405.

[51] V. Chevelkov, A. Diehl, B. Reif, Quantitative measurement of differential N-15-H-alpha/beta T-2 relaxation rates in a perdeuterated protein by MAS solid-state NMR spectroscopy, Magn Reson Chem, 45 (2007) S156-S160.

[52] V. Chevelkov, A. Diehl, B. Reif, Measurement of (15)N-T(1) relaxation rates in a perdeuterated protein by magic angle spinning solid-state nuclear magnetic resonance spectroscopy, J Chem Phys, 128 (2008).

[53] V. Copie, A. Mcdermott, K. Beshah, M. Spijker, J. Lugtenburg, J. Herzfeld, R. Griffin, Nmr-Studies of -Cd3 Group-Dynamics in Bacteriorhodopsin and Retinoic Acid Model Compounds - Evidence for a 6-S-Trans Retinal Chromophore in the Protein, Biophys J, 57 (1990) A360-A360.

[54] V. Copie, A.E. McDermott, K. Beshah, J.C. Williams, M. Spijkerassink, R. Gebhard, J. Lugtenburg, J. Herzfeld, R.G. Griffin, Deuterium Solid-State Nuclear-Magnetic-Resonance

Studies of Methyl-Group Dynamics in Bacteriorhodopsin and Retinal Model Compounds - Evidence for a 6-S-Trans Chromophore in the Protein, Biochemistry-Us, 33 (1994) 3280-3286.

[55] L. Frydman, S. Vallabhaneni, Y.K. Lee, L. Emsley, Solid-State Dynamic Processes in Complex-Systems Analyzed by 2-Dimensional Isotropic-Anisotropic Correlation Nuclear-Magnetic-Resonance, J Chem Phys, 101 (1994) 111-117.

[56] A. Schmidt, S.O. Smith, D.P. Raleigh, J.E. Roberts, R.G. Griffin, S. Vega, Chemical-Exchange Effects in the NMR Spectra of Rotating Solids, J Chem Phys, 85 (1986) 4248-4253.

[57] S. Kaufmann, S. Wefing, D. Schaefer, H.W. Spiess, 2-Dimensional Exchange Nuclear-Magnetic-Resonance of Powder Samples .3. Transition to Motional Averaging and Application to the Glass-Transition, J Chem Phys, 93 (1990) 197-214.

[58] A. Allerhand, H.S. Gutowsky, J. Jonas, R.A. Meinzer, Nuclear Magnetic Resonance Methods for Determining Chemical-Exchange Rates, J Am Chem Soc, 88 (1966) 3185-3194.

[59] G. Hou, S. Paramasivam, I.J.L. Byeon, A.M. Gronenborn, T. Polenova, Determination of relative tensor orientations by gamma-encoded chemical shift anisotropy/heteronuclear dipolar coupling 3D NMR spectroscopy in biological solids, Phys Chem Chem Phys, 12 (2010) 14873-14883.

[60] B.J. Wylie, L.J. Sperling, A.J. Nieuwkoop, W.T. Franks, E. Oldfield, C.M. Rienstra, Ultrahigh resolution protein structures using NMR chemical shift tensors, P Natl Acad Sci USA, 108 (2011) 16974-16979.

[61] J.B.D. de Lacaillerie, B. Jarry, O. Pascui, D. Reichert, "Cooking the sample": Radiofrequency induced heating during solid-state NMR experiments, Solid State Nucl Mag, 28 (2005) 225-232.

[62] B.J. Gross, A.E. McDermott, Locating hydrogen atoms in single crystal and uniaxially aligned amino acids by solid-state NMR, J Magn Reson, 185 (2007) 12-18.

[63] K.R. Thurber, R. Tycko, Measurement of sample temperatures under magic-angle spinning from the chemical shift and spin-lattice relaxation rate of (79)Br in KBr powder, J Magn Reson, 196 (2009) 84-87.

[64] A. Siemer, Personal Communication, in.

Chapter 4

Studies of Ligand Binding in Triosephosphate Isomerase

$R_{1\rho}$ measurements can be combined with other solid state NMR techniques to gain insight into both the timescale of ligand binding and properties of the ligand of interest. The timescale of ligand binding, in combination with understanding dynamics of the protein itself, can help deduce rate-limiting steps in catalysis. In this chapter, we utilized CSA tensor measurements and $R_{1\rho}$ studies of ligand dynamics to observe inorganic phosphate interacting with triosephosphate isomerase. Our measurements support a model of ligand binding in which the dianionic HPO_4^{2-} is interacting with loop 6, while the loop remains in the open state. These conclusions have implications for the catalytic mechanism.

4.1 NMR Spectroscopy as a Tool to Study Ligand Binding

The study of ligand binding and molecular recognition is critical for biochemical research. One of the main goals in the study of ligand binding is to gain insight into the interactions of pharmacologically active compounds with their targets. Much information on ligand binding is derived from x-ray crystallography. However given the cryogenic temperatures and static nature of crystallography studies, they may not provide a complete picture of ligand binding. NMR is a powerful method to study ligand binding over a wide range of affinities, molecular masses, and sample conditions [1]. NMR studies have shown dynamic properties of ligands, and structure determination has detected different conformations from those seen in crystal structures. In addition to studies of protein dynamics, behavior of ligands can provide insight into enzyme catalysis. Studies of ligands are extremely important in the drug discovery process. In addition to structure-activity relationships (SAR, [2]) which probe changes in protein resonances upon ligand binding, flexibility-activity relationships (FAR) have been used to observe how protein

binding affects ligand dynamics [3]. When considering ligand binding, the exchange process is determined by the off-rate of the binding process. When the off-rate is significantly faster than the chemical shift difference between the 2 states, the system is in fast exchange. When the off-rate is significantly slower than the chemical shift difference, the system is in slow exchange [1].

Frequently in solution NMR, binding is studied by observing changes in the chemical shifts of protein resonances near the ligand binding site(s) [4] or through solving the structure of the protein-ligand complex [5]. A solution NMR technique that is also used to study protein-ligand interactions via the spectroscopic behavior of the ligand is the transferred Nuclear Overhauser Effect (trNOE). The nuclear Overhauser effect (NOE) is a ubiquitous technique in nuclear magnetic resonance (NMR) and has been used for resonance assignments as well as to study both protein structure and dynamics [6-16]. For structure determination, ^{1}H-^{1}H homonuclear NOEs are generally used to extract distance constraints, while for dynamics studies, heteronuclear NOEs are utilized in conjunction with R_1 and R_2 relaxation rates.

The NOE is a dipolar, through-space interaction monitoring the cross relaxation between 2 spins (I and S), which arises due to the time-dependence of the dipolar coupling and is an intuitive tool for use in probing internuclear distances. A standard NOE experiment is executed by observing spin I during selectively irradiated perturbation of the S spin [17].

The NOE cross relaxation rate is proportional to correlation time, $\omega\tau_c$ (molecular tumbling), and therefore, molecular weight. At $\omega\tau_c$ just greater than 1, cross relaxation switches from positive to negative. For high molecular weight molecules with longer correlation times (such as

biomolecules), cross relaxation is fast and negative, leading to faster NOE build-up. For small molecules, NOE build-up is slow and cross relaxation is positive. Thus it is for medium sized molecules (i.e. ligands) that the cross over from negative to positive cross relaxation occurs, leading to small NOEs [16] and can be used to correlate protein-ligand residence times.

The transferred nuclear Overhauser effect (trNOE) is a technique commonly used in the study of ligand binding to macromolecules [18]. The concept of the trNOE is that NOEs build slowly for free ligand but more rapidly for bound ligand. The rapid exchange between free and bound ligand leads to free ligand, which can be easily detected but possesses NOEs characteristic of bound ligand [16]. The utility of the NOE to probe intermolecular interactions has been discussed [17, 19].

Halle and co-workers have applied the same overarching concept through magnetic relaxation dispersion. They utilize quadrupolar relaxation of non-exchanging ^{17}O and ^{14}N to observe the translational diffusion of water molecules, involving the transfer of magnetization between water populations with different relaxation times [20] (i.e. buried and bulk water). Due to the absence of exchange for O and N, the observed relaxation rates report on the dynamics of local water molecules. They apply this to the study of hydration dependence of dynamics for proteins including BPTI and ubiquitin [21].

Studies of Ligand Binding in the Solid State The advancement of solid state NMR as a technique to observe ligand binding is essential for the study of drug binding to membrane

proteins. Solid state NMR boasts the ability to study ligand binding in insoluble and non-crystalline environments [22]. A range of techniques using a range of nuclei has been used for studies of ligand binding in the solid state. Static deuterium experiments have been used to characterize the ligand orientation and gain insight into binding and dynamics for numerous systems, including the nicotinic acetylcholine receptor and rhodopsin [23, 24]. Carbon chemical shift differences have been used to characterize ligand binding to the GPCR (G-protein coupled receptor) nunerotensin [25]. Proton spin diffusion was used by Gallagher et al to quantify the membrane depth of the peptide Gramicidin A [26]. This experiment exploits the differential relaxation rates of the different water molecules within a sample: membrane associated protons having faster relaxation than the protons of surface waters [27, 28]. Differential relaxation has also been induced in membrane systems through the introduction of a paramagnetic surface ion, and taking advantage of paramagnetic relaxation enhancement (PRE) [29].

In Chapter 3, we demonstrated the power of $R_{1\rho}$ measurements as a probe of conformational exchange. Extending this work to biological systems provides a technique to observe site specific protein dynamics on the intermediate timescale. Furthermore, to our knowledge, $R_{1\rho}$ measurements have not been broadly applied to the study of ligand binding. This particular application could provide powerful knowledge with implications for drug discovery and other biomedical applications. $R_{1\rho}$ studies of chemical exchange in ligand binding can be thought of as utilizing the same concepts as the trNOE experiment and solid state spin diffusion. Analogous to faster cross relaxation for bound ligand, we expect a ligand in exchange between bound and free states to have faster $R_{1\rho}$ relaxation than free ligand, given the reintroduction of anisotropic properties upon binding, relative to the (presumably) isotropic free ligand. Like spin diffusion

experiments, $R_{1\rho}$ studies of ligands take advantage of the different relaxation properties of the free and bound states. The observed relaxation may indicate the off rate for ligand binding. Previous $R_{1\rho}$ studies of ligand binding by Krushelnitsky and co-workers observed the effects of ligand binding on the dynamics of the protein barstar [30]. In this chapter we will show the potential for utilizing $R_{1\rho}$ studies in the solid state as a novel technique for observing the dynamics of ligand binding. Additional CSA parameters also reveal characteristics of ligand binding in TIM.

4.2 Introduction to ^{31}P NMR Spectroscopy

Phosphorous NMR is a powerful technique in the study of biological systems. ^{31}P occurs with 100% natural abundance, eliminating the need for labeling schemes and allowing the study of interesting systems, including phosphorylated proteins, nucleic acids, and phospholipids. Line broadening in phosphorous spectra occurs largely due to 2 interactions—the chemical shift anisotropy and proton-phosphorous dipole-dipole interactions.

4.2.1 ^{31}P Chemical Shift Anisotropy

The sensitivity of phosphate ^{31}P CSAs arises from the degree of orbital overlap between phosphorous d-orbitals and oxygen p orbitals [31], affecting π-bonding character, which is reflected in the P-O bond length, and the sensitivity of the CSA to this bond length as well as deviations from tetrahedral geometry [32].

The chemical shift tensor of phosphate is extremely sensitive to additional properties of the phosphate group, most notably the protonation state of the oxygen atoms and number of phosphate groups (i.e. adenosine triphosphate vs adenosine diphosphate) or other attached functional groups [32-34]. The orientations of phosphate ^{31}P tensors have been shown to be generally similar [35]. A typical shielding tensor for a phosphate group is shown in Figure 4.1.

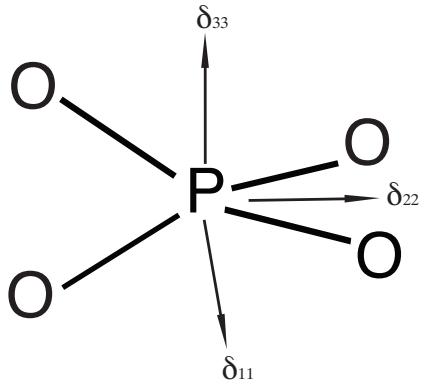

Figure 4.1 Average orientation of a phosphate ^{31}P chemical shielding tensor with respect to the molecular frame. The δ_{11} element is perpendicular to the δ_{22} and δ_{33} elements and is projected out of the page.

Protonated phosphates have significantly different CSAs from unprotonated phosphate ions [36], making the pH of the solution an important factor. For single unprotonated phosphate units, the isotropic chemical shift (δ_{iso}) can range from -30 to +12 ppm, while the anisotropy ($\Delta\delta$) is typically -60 to -15 ppm, and the asymmetry (η) can range from 0 to 1 [32]. For a monoprotonated phosphate group (1 P-OH or hydrogen bond, dianion), $\Delta\delta$ ranges from 76.7 to 107 ppm. Interestingly, the tensor parameters for a monoprotonated monophosphate are similar to the parameters for an unprotonated diphosphate. Monohydrogen monophosphates have approximate C_{3V} symmetry and thus small asymmetry parameters. Dihydrogen monophosphates can be separated into 2 groups with different CSA values, depending on their structure and symmetry. Highly symmetric groups have similar tensor properties to unprotonated phosphate

groups, as the P-OH bonds lengths are approximately equal. The chemical shift tensor parameters for a variety of phosphate groups as a function of protonation state are summarized in Table 4.1

	δ_{iso} (ppm)	$\Delta\delta$ (ppm)	η
Monophosphates Q^0	-30 to 12	-30 to -15	0 to 1
Diphospahtes Q^1	-33 to 4	-80 to 140	0 to 0.8
Polyphosphates Q^2	-53 to -18	-250 to -160	0.3 to 0.8
Monohydrogen Monosphosphates $Q^0(H^1)$	-7 to 6	75 to 105	0.1 to 0.6
Dihydrogen Monophosphates $Q^0(H^2)$	-6 to 4	-120 to -33	0 to 0.7
Dihydrogen Diphosphates $Q^1(H^1)$	-20 to -8	-180 to -110	0.8 to 1

Table 4.1 Summary of the chemical shift tensor parameters for phosphate groups given various degrees of protonation/hydrogen bonding and P-P condensation. Q^n indicates the number of phosphate groups connected by P-O-P bonds. (H^m) indicates the number of oxygens of the phosphate group that are protonated or involved in hydrogen bonding. Based on references [32, 36]. $\Delta\delta$ the is chemical shift anisotropy (not reduced anisotropy, the parameter described in most of the text) and η is the asymmetry. Only mono and dihydrogen phosphates are relevant for our work.

The phosphate-containing ligands of TIM are mono/dihydrogen monophosphates. Therefore the other classes of phosphates (i.e. diphosphates) will not be considered further.

4.2.2 ^{31}P Studies of Ligand Binding

Phosphate moieties are important functional groups in many pharmacologically active compounds, including drugs currently on the market to treat bone resorption diseases such as

osteoporosis [37], to kill parasites responsible for diseases such as malaria [38], and also stimulate T cell production to boost the immune system to kill tumor cells and bacterial pathogens [39]. Another purpose to the study of ligand binding via solid state NMR is to observe the effects of ligand binding on phospholipids, relevant to antibiotics as well [40].

For ligands that have both carbon and phosphate moieties, it can be advantageous to study the phosphorous rather than carbon moiety, as the background signal from the protein can make carbon measurements of ligands challenging [25]. ^{31}P 1D solid state NMR studies of Ras and GTP analogs by Iuga et al were able to detect two different conformations of the ligand and probed the 'on' and 'off' states of the protein [41]. They also approximated the proton $R_{1\rho}$s of the ligand through the dependence of CP efficiency on contact time at 2 temperatures, with faster relaxation observed at higher temperature.

Ligands of triosephosphate isomerase all contain a phosphate (PO_4^{3-}) moiety. The mechanism of catalysis in TIM can be modeled as

$$E + S \underset{k_{off}}{\overset{k_{on}}{\rightleftharpoons}} E \bullet S \underset{k_{-1}}{\overset{k_{1}}{\rightleftharpoons}} E \bullet P \underset{k_{on}}{\overset{k_{off}}{\rightleftharpoons}} E + P$$

Given the importance of the phosphate moiety of DHAP and GAP in the isomerization reaction, ^{31}P NMR has been used to study ligand binding in TIM. Previous solution ^{31}P studies have observed the phosphate group of the ligand G3P at a range of temperatures from 0°C to 70°C. Studies by Rozovsky et al [42] have indicated from chemical shift changes that ligand release is faster than 1000 s^{-1} at 30°C and slower than 1000 s^{-1} at 0°C, thus indicating the correlation between loop motion and product release. They reported a chemical shift difference of 1.3 ppm

between the bound and free states. At 30°C, it was found that the bound form of D-G3P is favored, while at 45°C, the unbound form is favored, and at 70°C, there is no evidence of bound G3P [43]. The phosphate group becomes more protonated and hydrogen bonds with protein residues are disrupted, favoring the unbound form of the ligand at higher temperatures.

Campbell et al investigated the differential binding of various ligand analogs as a function of pH [44], which is a reporter of the phosphate group's protonation state. The tightly binding inhibitor PGA was found to not change its phosphate ionization state over the pH range of 6.18 to 8.0, while G3P did have a pH dependence indicating that the binding mode of these two ligands is different.

Interesting studies of the native ligand DHAP and its hydrate by Knowles and co-workers indicated that the keto- form of the ligand binds as suggested from kinetics experiments and that the hydrate- form resonance is unaffected by protein concentration, and therefore does not bind to the protein as a non-competitive inhibitor. To our knowledge, all previous ^{31}P NMR studies of ligand binding in TIM have been done in solution.

For preliminary studies, we have chosen to observe ligand dynamics of the simple phosphate ion, PO_4^{3-}, although little work has been reported in the literature on this particular substrate. Analysis of PO_4^{3-} is simplified relative to G3P, which has both D- and L- conformers, but only the D- form binds appreciably, and potential issues of ligand decomposition are avoided. Potential challenges of using this ligand include the previous observation of multi-rate kinetics, indicating a loose fit in the TIM active site or disordered structure [45]. NMR is a powerful

technique for studying weak binding events that cannot be accessed well by other biophysical methods [1]. This advantage is valuable for the study of proteins like TIM, where even the native ligand DHAP has a K_d on the order of mM.

4.3 Slow Magic Angle Spinning One Dimensional ^{31}P Spectra

A great deal of information is contained in the chemical shift tensor of a resonance. Slow and fast spinning MAS spectra can be used to gain insight into phosphate binding in TIM. In solid state NMR, there are many techniques available to determine the value of a CSA tensor, including static powder pattern spectra, recoupling techniques, and spinning sideband analysis. Spinning sideband analysis is derived from the free induction decay (FID) of an anisotropic interaction having a series of rotational spin echoes [46]. The relative intensities of the isotropic peak and its spinning sidebands contain information from which the chemical shift tensors can be determined [47]. Herzfeld and Berger showed that the principle CSA values can be determined from a small number of spinning sidebands [48].

We hypothesize that in solid state NMR studies of phosphate ligand in TIM, at least two states of the ligand are present, a TIM-bound state and an unbound state, with ligand exchange occurring between these two states (Figure 4.2). Furthermore, it is expected that chelation of PO_4^{3-} by protein residues would introduce the anisotropic behavior of the chemical shift tensor, while unbound phosphate would only have an isotropic component. To test this hypothesis in the most straightforward manner, and to quantify the chemical shift tensor parameters of TIM-bound PO_4^{3-}, slow and fast one dimensional ^{31}P spectra were collected at multiple temperatures.

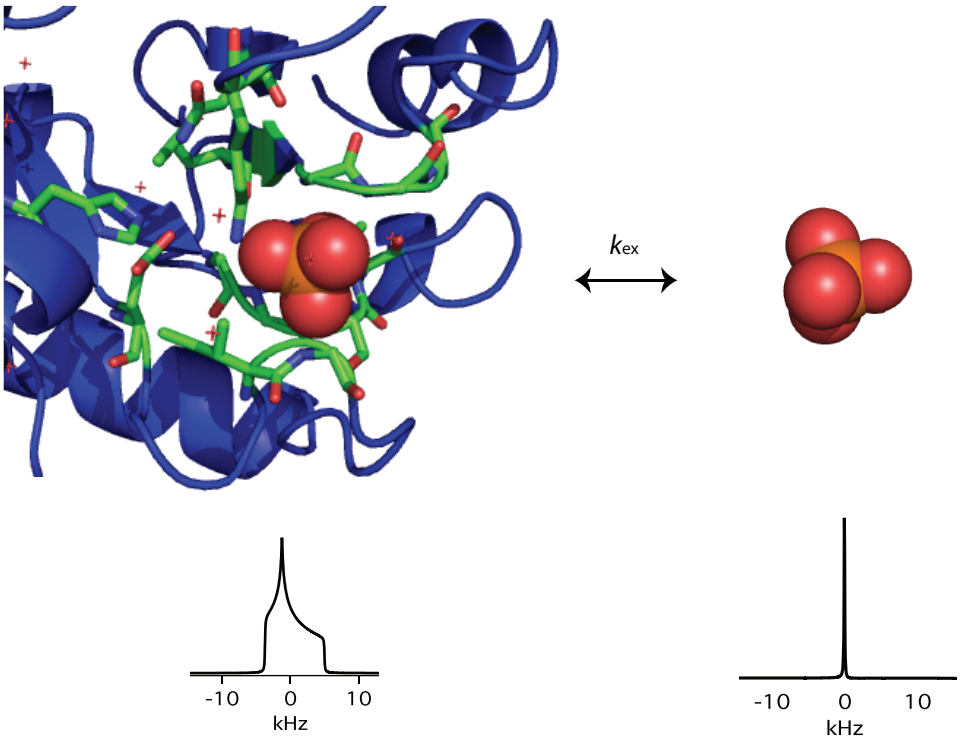

Figure 4.2 Hypothesized chemical shift tensor behavior for the binding of phosphate in TIM. While isotropic when unbound, binding to protein backbone resonances will reintroduce the anisotropy of the chemical shift tensor. (PDB ID: 1AG1)

Figure 4.3 shows one dimensional ^{31}P spectra of 50/50 TIM-bound/unbound PO_4^{3-} collected at -40°C, -20°C, and +20°C with 3 kHz magic angle spinning. These spectra have several notable features.

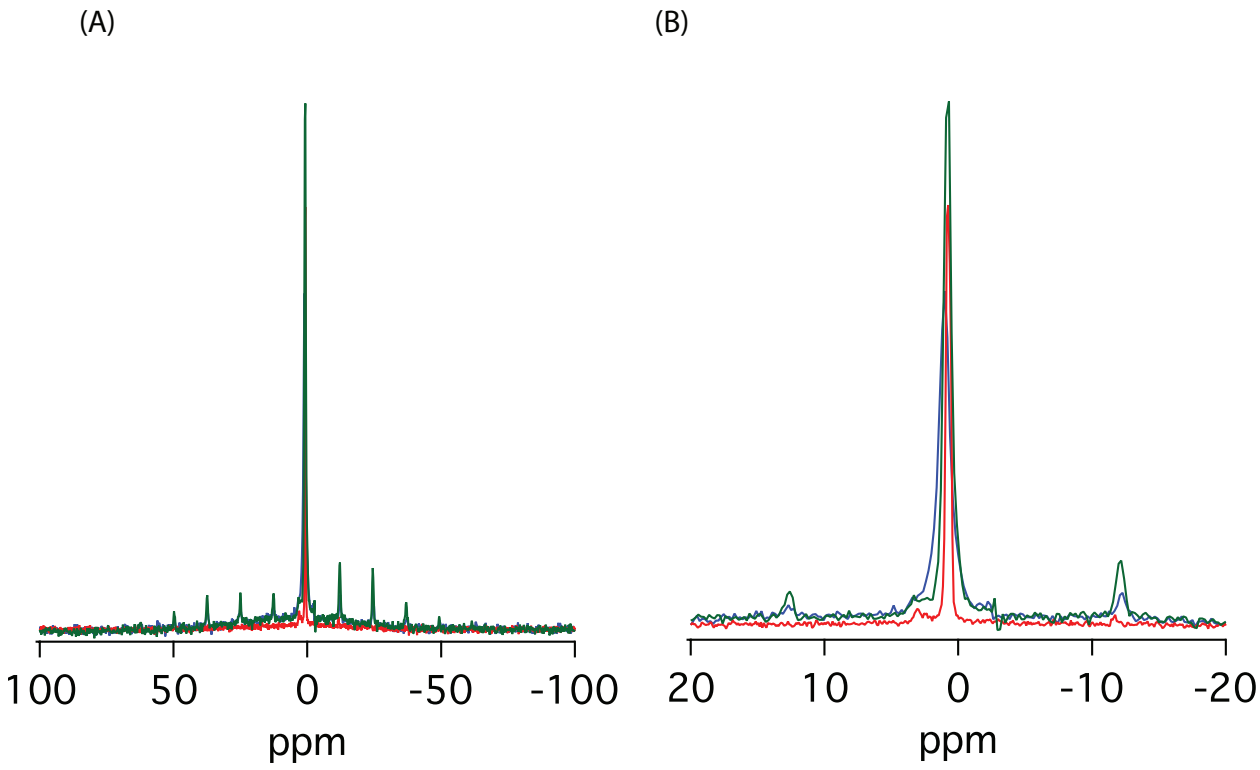

Figure 4.3 (A) One dimensional spectra of 50/50 TIM-bound/unbound PO_4^{3-} collected at (blue) -40°C, (green) -20°C, (red) +20°C at 3 kHz MAS. The presence of spinning sidebands indicates an anisotropic PO_4^{3-} species. The intensity of the centerband relative to the sidebands suggests there is a purely isotropic species present as well. The presence of only 1 sideband at +20°C suggests the species is isotropically averaged at this temperature. (B) Expansion of A to the centerband and first spinning sideband. The distance between the sidebands and centerbands indicated that the anisotropic species is expected to have a centerband upfield of the observed centerband. At high temperature, multiple PO_4^{3-} populations are observed.

Relative to a typical ^{31}P solid state NMR spectrum where the phosphorous atoms are all in the same state, the slow MAS spectrum of TIM-bound PO_4^{3-} exhibits a significantly more intense centerband relative to the sidebands. This observation suggests that the centerband intensity arises from both the isotropic (unbound) state(s) and the anisotropic (bound) state(s).

At low temperature (-20°C and -40°C), the spectra have spinning sidebands, while at higher temperature (+20°C), only the first upfield spinning sideband is visible. Furthermore, the

linewidth is significantly narrower at +20°C, and allows for the observation of multiple isotropic resonances where the broader centerband of the low temperature spectra appear.

Table 4.2 reports the chemical shifts of the centerband for the spectra collected at 3 kHz MAS. Given the spectral resolution, we can estimate a minimal chemical shift error of ± 0.2 ppm.

Temperature	δ_{iso} (ppm)	δ_{iso} (Hz)
-40°C	1.01	244.5
-20°C	0.79	192.4
+20°C	0.74	178.3

Table 4.2 Chemical shifts of the centerband observed at -20°C and -40°C, along with the dominant peak for the spectrum at +20°C, collected at 3 kHz MAS with direct excitation.

The weaker sidebands at higher temperature may indicate that the anisotropy is more dynamically averaged. It is not unexpected that linewidths become broader at lower temperature. Linewidth is determined by R_2 and becomes slower with lower temperatures. One dimensional control experiments of an Na_2HPO_4 solution in TIM buffer without protein had temperature-independent linewidths of ~ 90 Hz. The presence of protein-bound ligand causes linebroadening and the appearance of spinning sidebands (discussed further below, Section 4.5).

From closer analysis of the centerband and sidebands at low temperature, it can be seen that the observed centerband chemical shift is downfield of its predicted frequency based on the distance to the spinning sidebands at -20°C and -40°C (Figure 4.4). This is consistent with the hypothesis that the sample has both isotropic (presumably unbound) and anisotropic (presumably bound) PO_4^{3-} populations. The observed centerband frequency indicates that the purely isotropic chemical species has a downfield shift relative to the anisotropic species, leading to averaging of

the centerband frequency. The trend of the observed centerband frequency arising downfield of its predicted chemical shift is also seen at -40°C (not shown). In the slow MAS spectrum at +20°C, only the first upfield spinning sideband can be observed. The distance between this peak and the dominant isotropic peak is only 30 Hz, much less than the 130 Hz observed at -20°C or 210 Hz at -40°C. This provides evidence that this species is the one that gives rise to spinning sidebands.

Summing over the peak volume of the centerband and spinning sidebands, we observe that the total sideband volume is 57% of the centerband volume at -20°C, and 37% of the centerband volume at -40°C.

The observation of an isotropic species also is consistent with many experimental measurements that show hydration waters (the shell of solvent directly in contact with the protein) undergo a glass transition at significantly lower temperatures than bulk solvent (170-230 K) [49-51], and give a liquid-like signal above this temperature regime. Further experiments are necessary to conclusively rule out this possibility.

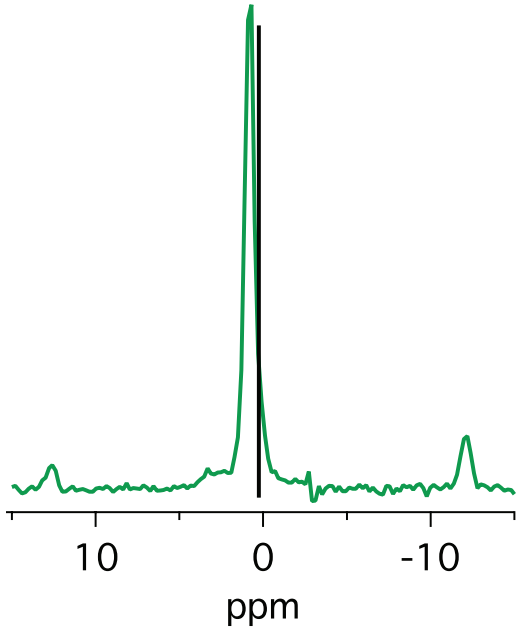

Figure 4.4 Expansion of the centerband of the slow MAS spectrum collected at -20°C and comparison of the observed centerband frequency with the expected frequency (black line) based on the distance to the sidebands. It is clear the observed intensity is downfield of the expected centerband frequency.

There does appear to be a shoulder on the upfield side of the observed centerband, which falls where the anisotropic centerband should appear. (The spectra were carefully phased and shimming should not give rise to a shoulder in peaks with such inherently broad linewidths.) It is possible that this upfield shoulder is from the anisotropic centerband. Determination of the CSA tensor parameters indicated that indeed the centerband of the anisotropic species is expected to be concealed by the larger isotropic peak (Figure 4.7).

While the isotropic and anisotropic components do have similar chemical shifts ($\Delta\delta_{iso} < 250$ Hz), possibly arising from the role of hydrogen bonding and/or ionization state in determining phosphate ^{31}P chemical shifts, the species *do* have slightly different chemical shifts. A downfield isotropic chemical shift indicates greater deshielding of a nucleus (electron withdrawing). While a bound phosphate ion is held somewhat in place by hydrogen bonds to

water molecules and protein backbone amides, a PO_4^{3-} ion that is free in solution would have neighboring phosphate and sodium ions, in addition to water molecules. Additional hydrogen bonding character causes downfield shifts in phosphate groups [32]. Cations including Na^+ have been shown to be influential at deshielding ^{31}P atoms in PO_4^{3-} [52]. Hydrogen bonds among phosphate groups are shorter than observed for bound PO_4^{3-} observed in crystal structures of TIM (~ 2.5Å for PO_4^{3-}-- PO_4^{3-} bonds vs ~ 3Å for PO_4^{3-}-- H_2O and PO_4^{3-}-- protein backbone hydrogen bonds [52, 53]). The closer proximity and general presence of these additional species may induce a downfield chemical shift in unbound PO_4^{3-} relative to TIM-bound PO_4^{3-}.

Somewhat in contradiction to our hypothesis that the unbound species has a downfield chemical shift relative to the unbound species is the previous observations in solution NMR ^{31}P studies in which the unbound ligand has an *upfield* chemical shift relative to the bound ligand [42, 44]. The difference may be that these studies observed DHAP, G3P, and PGA. These ligands all have a carbon moiety. The bridging oxygen is sterically hindered and less amenable to hydrogen bonding. The improved binding in the active site of these ligands relative to inorganic phosphate may explain why the observed ^{31}P shifts of the bound state are downfield relative to inorganic phosphate. Of course, an alternate hypothesis is that the anisotropic species we are observing is not the bound PO_4^{3-} ligand.

Cross Polarization vs Direct Excitation As direct excitation was observed to give ~50% improved signal-to-noise, the majority of data were collected with this polarization technique. Direct excitation is expected to more favorably excite and allow for detection of dynamic species. To better capture a less dynamic (i.e. the anisotropic) species, cross polarization may be

better. Figure 4.5 shows a spectrum of 50/50 TIM-bound/unbound PO_4^{3-} collected with cross polarization at 10 kHz MAS. (This CP spectrum was collected during instrument set-up and therefore used faster spinning and fewer scans.) Despite the faster spinning speed, the first spinning sidebands are still present.

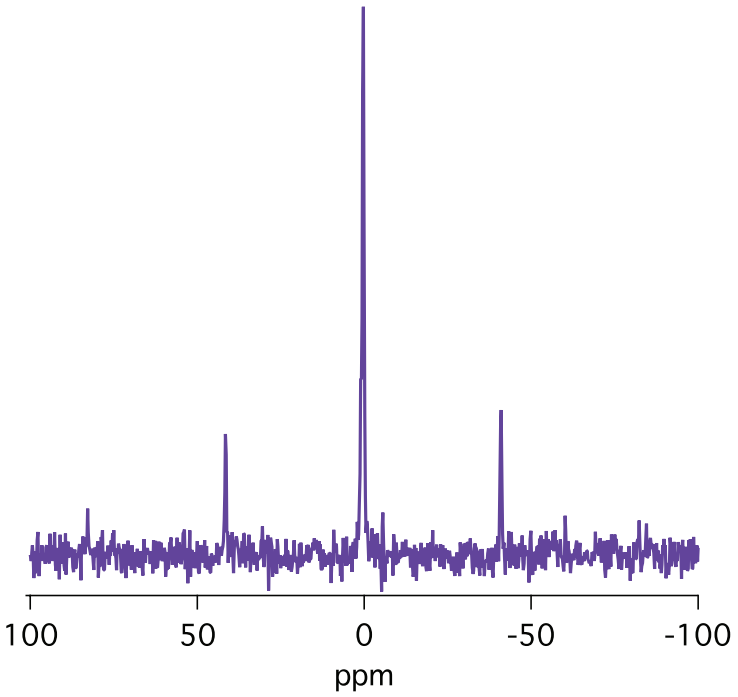

Figure 4.5 Spectrum of 50/50 TIM-bound/unbound PO_4^{3-} collected at -30°C, 10 kHz MAS with cross polarization as the method of excitation. The centerband exhibits greater anisotropic character than spectra collected with direct excitation.

As compared with the -20°C, 3 kHz MAS spectrum collected with direct excitation, the expected centerband matches the predicted central transition given the distance to the spinning sidebands when acquired with cross polarization (Figure 4.6). The better match between the observed and predicted centerband frequencies indicates that cross polarization gives improved detection of the anisotropic/static species relative to direct excitation. The chemical shift of the conterband for the spectrum collected with cross polarization is 0.3 ppm.

The spectrum collected with cross polarization also has a shoulder on the downfield side of the peak. This shoulder has a chemical shift of 1.1 ppm. This may be an additional species or the isotropic species, though how it exactly correlates to the slow MAS spectra is unclear.

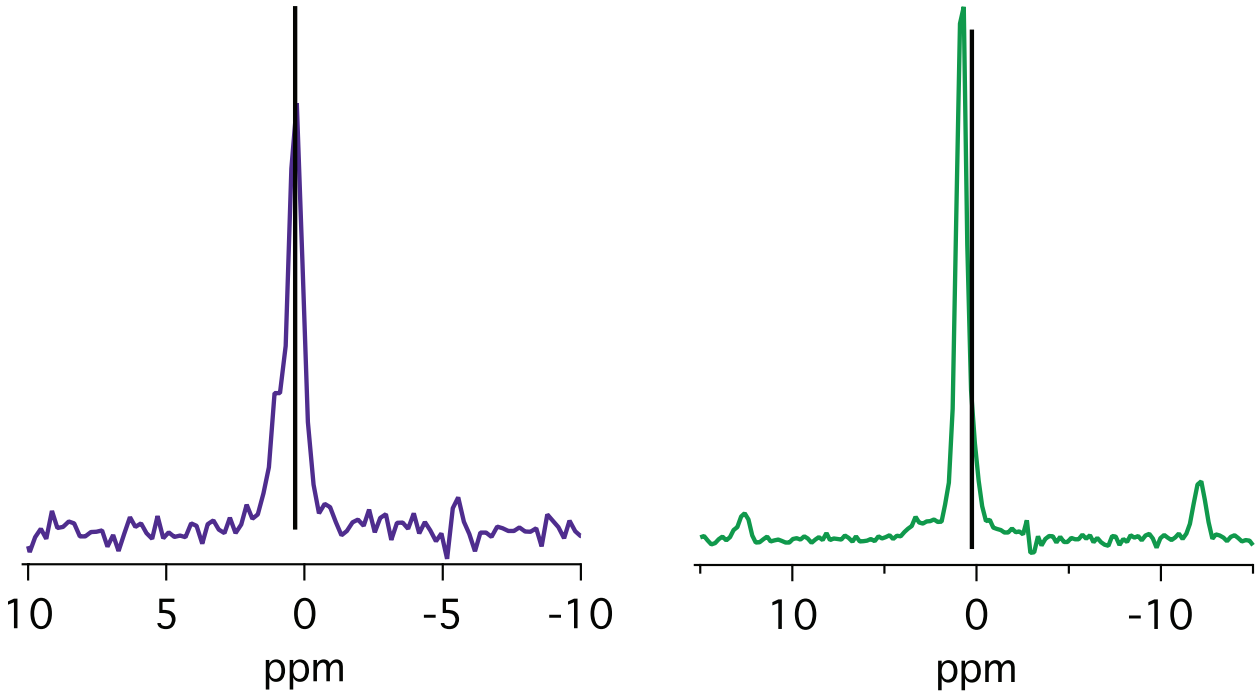

Figure 4.6 Side-by-side comparison of the centerband for 50/50 unbound/TIM-bound PO_4^{3-} collected at -30°C, 10 kHz MAS using CP (purple, left) and the spectrum collected with direct excitation, 3 kHz MAS at -20°C (green, right). Straight lines represent the expected centerband frequency based on the distance from the spinning sidebands. The expected centerband frequency is closer to the peak maximum when CP is used.

4.4 CSA Tensor Fitting and Implications for Catalysis

It was also of interest to extract CSA tensor parameters from the spinning sideband pattern of the low temperature spectrum using Spinevolution [54]. Determining these values may allow us to make conclusions regarding the protonation state and hydrogen bonding of TIM-bound PO_4^{3-}, as

well as to make estimates of expected relaxation rates using simulations. The reduced anisotropy (δ) and the asymmetry (η) were determined by fitting the spinning sideband intensities in Spinevolution from the data collected at -20°C, 3 kHz MAS. The sidebands were fit to a single ^{31}P atom, with the anisotropy, asymmetry, and a scaling factor as the fitting parameters. The apparent overlap of multiple phosphate populations at the centerband frequency necessitated that this peak is given zero weighting in the data-fitting, however excluding the centerband does cause the loss of significant information content. The best fit for the CSA tensor parameters determined from the slow MAS spectrum were $\delta = +74 \pm 8$ ppm (18 ± 2 kHz, $\Delta\delta = +111$ ppm), $\eta = 0.2 \pm 0.3$. In the standard convention, $\delta_{11} = 74$ ppm, $\delta_{22} = -30$ ppm, and $\delta_{33} = -44$ ppm.[1] The sideband intensities of the raw data and simulated sidebands based on the results of data-fitting are shown in Figure 4.7, along with the residuals. The RMSD between the predicted and experimental sideband intensities was 1.0. The maximum variance was on the order of the noise in the spectrum (~ 1.3).[2] The accuracy of the fit is highly dependent on correct sideband intensities. These values were determined by fitting the sidebands to Lorentzians with the baseline at the noise level immediately surrounding the peak. This was the best method to correct for the broad baseline underlying the spectrum.

---

[1] The tensor conventions are defined as follows. In the standard convention, $\delta_{11} > \delta_{22} > \delta_{33}$. $\delta_{iso} = (\delta_{11} + \delta_{22} + \delta_{33})/3$. In the Haeberlen convention, δ_{xx}, δ_{yy}, and δ_{zz} are defined such that $|\delta_{zz} - \delta_{iso}| \geq |\delta_{xx} - \delta_{iso}| \geq |\delta_{yy} - \delta_{iso}|$. $\delta = \delta_{zz} - \delta_{iso}$, $\Delta\delta = (3/2)\delta$, $\eta = (\delta_{yy} - \delta_{xx})/\delta$. [55] U. Haeberlen, High resolution NMR in solids : selective averaging, Academic Press, New York, 1976.

[2] Experimental data was scaled to simulated data. Variance = fit – experimental data. $RMSD = ((\Sigma(\text{fit-data})^2)/n)^{1/2}$

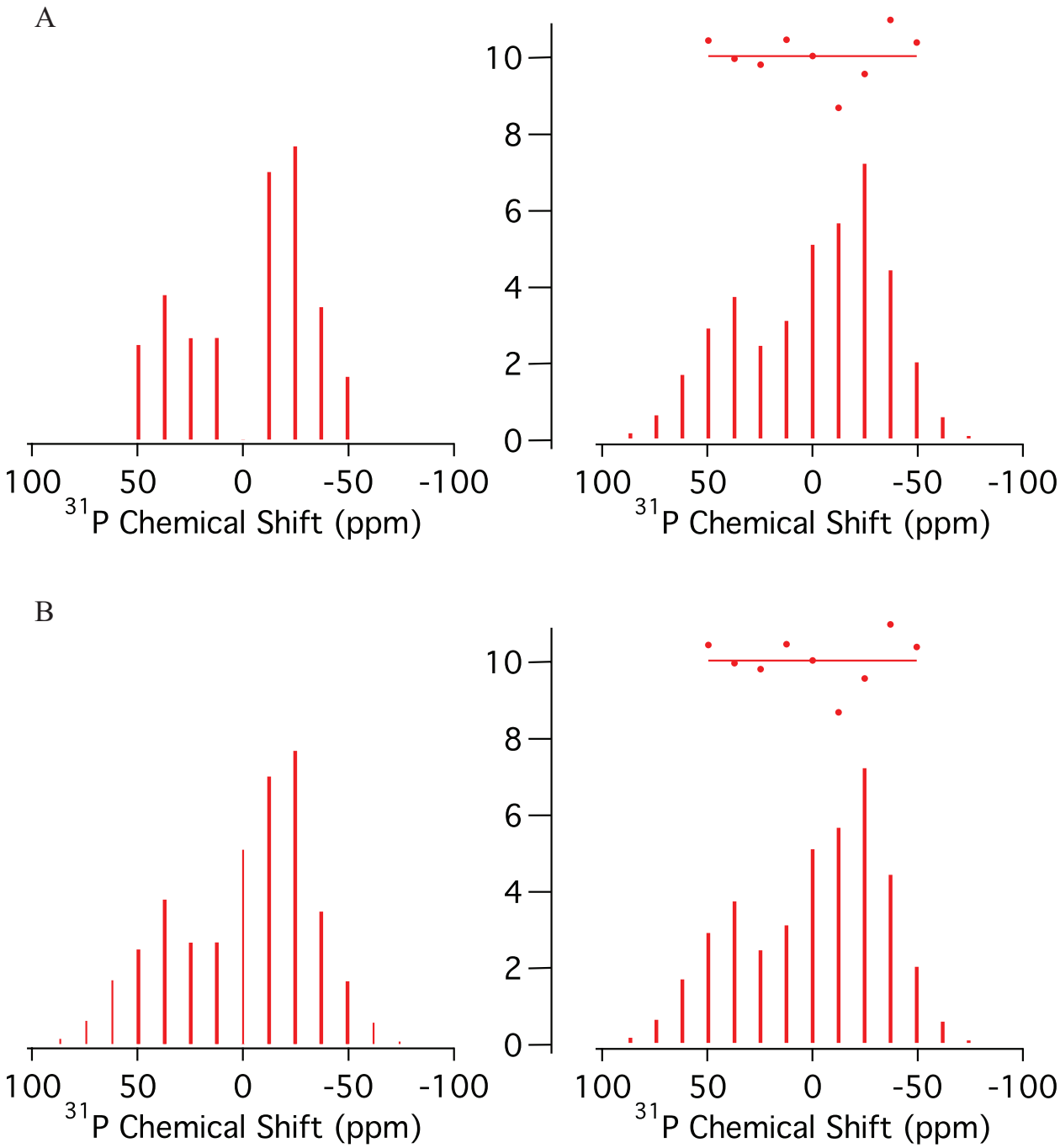

Figure 4.7 (A) Comparison of sideband intensities extracted from a ^{31}P 1D spectrum of 50/50 TIM-bound/unbound PO_4^{3-} collected at -20°C, 3 kHz MAS (left) and simulated sideband intensities generated from the CSA tensor parameters determined from data fitting, along with the residuals (right), δ = 74 ppm, η = 0.2. The RMSD was 1.0 and the maximum variance was on the order of the noise in the spectrum (~1.3). Both spectra are scaled to the center scale. The zero frequency centerband was not used in data fitting. (B) To clarify the agreement between simulations and experiments, the same spectra in A are shown, but the missing sidebands in the experimental spectrum are filled in with the sidebands determined from simulation (shown in narrower lines).

One important feature of TIM-bound ligands is their protonation state. The ionization state and hydrogen bonding of phosphate groups in biological systems can determine their role in catalysis or protein structure [52]. The interaction between the phosphate moiety and TIM is largely responsible for stabilization of the transition state [56]. Studies of G3P and DHAP have shown that both the monoanion and dianion of these ligands can bind to the enzyme, though it is thought the dianion binds better; the dianion is the ionization state for TIM-bound PGA [44]. Kinetics studies have indicated that interactions between the phosphate moiety and loop 6 activate TIM for catalysis [57]. In contrast to experimental data, QM/MM work by Friesner and co-workers has suggested that the monoanionic state of DHAP in the catalytically productive state. The ionization state may also influence the mechanism of catalysis. Specifically, for a monoanionc ligand, the catalytic mechanism is likely that described in Figure 2.5 (C) in which Glu 165 acts as both proton receptor and subsequent donor [58]. Crystal structures for various ligands of TIM indicate subtle differences in hydrogen bonding networks of the ligand phosphate moieties [53, 59, 60].

Characterization of the phosphate-protein interaction is central to understanding enzymatic rate acceleration in TIM; the protonation state of the ligand is likely a critical component of this interaction. The desired isomerization versus phosphate elimination with the formation of toxic methyl glyoxyl is dependent on the protonation state of the phosphate group; the phosphate monoanion increases the rate of phosphate elimination [61], thus study of phosphate ionization state can be very important in the TIM reaction mechanism.

Some broad statements regarding features of TIM-bound PO_4^{3-} based on the chemical shift tensor may be made as ^{31}P chemical shift tensors are particularly sensitive to the local environment and short/long range intermolecular interactions. Hartmann et al indicated that the sign of the anisotropy (δ) indicates whether a monophosphate is a monoanion or a dianion [32]; monoanions have a negative value for δ (the unique axis being lower in frequency than the isotropic shift), and dianions have a positive δ. Since for TIM, the PO_4^{3-} group exhibits a positive sign for δ, we conclude that the major species of PO_4^{3-} bound to TIM is the dianion. The asymmetry we determined is also consistent with a dianion, which tend to have a smaller asymmetry than a monoanion [32]. This conclusion does not preclude the reactive species being a minor species (the monoanion); nor is it necessarily true that the charge is the same for other ligands (DHAP, G3P, PGA, etc). The magnitude of the error on our asymmetry may be due to the small number of spinning sidebands, the lack of information at the centerband frequency, or the low signal-to-noise and broad background limiting the accuracy of the determined intensities. However, this parameter can have a broad range of values and is not as powerful an indicator as other tensor features. An additional weakness to our absolute conclusion that the ligand is a dianion, Tekely and co-workers reported that for phosphorserine, the spinning sideband manifold at pHs near the second pK_a was a mixture of the monoprotonated and diprotonated compounds [62]. This is an important consideration for our result, but more experiments are needed to evaluate this possibility in more detail.

For comparison with our values, the tensor parameters for multiple model compounds are presented in Table 4.3.

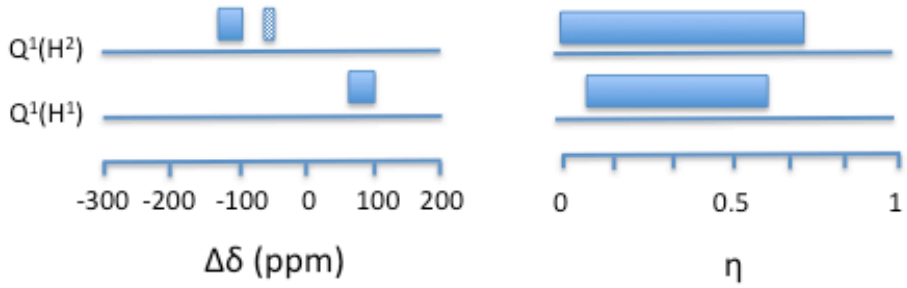

Figure 4.8 Average range of tensor values observed for monoanionic phosphate groups [$Q^1(H^2)$] and dianionic phosphate groups [$Q^1(H^1)$] of crystalline model compounds. For both groups, η can take on a relatively wide range of values, while δ is distinctly positive for dianions and distinctly negative for monoanions. Adapted from [32].

Compound	Ionization State	δ_{iso} (ppm)	δ (ppm)	Δδ (ppm)	η
TIM-bound HPO_4^{2-}	-2 (hypothesized)	0	74	111	0.2
$(NH_4)_2HPO_4$ [32]	-2	0.45	51.1	76.7	0.36
$(NH_4)_2$PThr [63]	-2	2.7	62.3	93.5	0.3
$COO^-/NH_3^+/PO_4^{2-}$ Ser [64]	-2	3.5	67	101	0.4
$NaH_2PO_4 \bullet H_2O$ [32]	-1	0.9	-67	-100	0.56
L-PThr [63]	-1	-3.7	-69.3	-104	0.75
$COOH/NH_3^+/PO_4H^-$ Ser [64]	-1	0.6	-56	-84	0.88

Table 4.3 Comparison of experimentally determined phosphate tensor parameters for TIM-bound PO_4^{3-} with model compounds in the Haeberlen convention. The values for TIM-bound PO_4^{3-} are consistent with a dianion given the sign of the anisotropy. The values in reference [63] were converted from the Hertzfeld-Berger convention. L-PThr is ortho-phospho-L-threonine. $(NH_4)_2$PThr is the diammonium salt of ortho-phospho-L-threonine.

Considerations for the ionization state we have determined include the role of hydrogen bonding and the subsequent influence on the geometry of the PO_4^{3-} group [63]. In the solid state literature of ^{31}P chemical shift tensors, it is not easy to distinguish ionization effects from hydrogen bonding effects. Campbell et al did suggest that the isotropic chemical shift (solution NMR studies) would report more on the ionization state of the ligand than the binding affinity (i.e.

hydrogen bonding) [44]. Phosphate chemical shift tensors are very sensitive to the P-O bond length [31]. The correlation between the chemical shift tensor and hydrogen bonding for phosphates in the -2 ionization state has not been addressed in the literature. In addition, there may be a mixture of the -1 and -2 ionization states within the sample [44, 64]. The temperature used for our measurements is very different from those used in solution NMR [44, 65].

Some insight into the hydrogen bonding network may be ascertained from analysis of ligand-bound TIM crystal structures (Figure 4.9). Comparison of crystal structures of PO_4^{3-} [53] and DHAP [59] bound TIM structures reveal a number of notable observations with implications for the significance of the ligand charge. The analysis was done for species within 3 Å of the phosphate oxygen atoms, representing the average hydrogen bond length. The phosphate moiety of both species is involved in an extensive hydrogen bonding network, with both direct protein-ligand hydrogen bonds and water-mediated hydrogen bonds with all oxygen atoms. In both structures, Gly171, Gly 232, and Gly 233 (numbering for yeast TIM) are hydrogen bonded to the phosphate moiety and their positions in the active site are virtually identical. Ser 211 is also involved for DHAP-bound TIM. HPO_4^{2-}bound TIM has a serine in the same position, but its angle is such that it is almost a full Å further from the ligand. There are 3 conserved water molecules.

In both structures, three oxygens of the phosphate groups are directly hydrogen-bonded to protein residues. Evaluating the HPO_4^{2-} bound TIM, the fourth oxygen atom is not ligated to any protein residues, only a non-conserved water molecule. This water is in the same position as the carbon moiety in DHAP-bound TIM; thus there are no protein residues to bind in that region.

Wierenga and co-workers attribute this oxygen atom as the protonated oxygen. Their comparison of the proton-deficient SO_4^{2-} with HPO_4^{2-} TIM structures indicated that this oxygen has no hydrogen bonds for SO_4^{2-}. They hypothesize that the presence of the proton in HPO_4^{2-}, allows this ligand to act as both a hydrogen bond donor and acceptor. DHAP-bound TIM does have more hydrogen bonds coordinating the amide group from Ser 211 and an additional water molecule. If the charge on the phosphate group of DHAP is monoanionic (has 2 protons), this may explain the additional hydrogen bonds relative to HPO_4^{2-} (though protein structure alone may explain the differences). Extending the analysis to TIM bound with the monoanion $H_2PO_4^-$, again we see the trend that 3 oxygens are directly coordinated with protein residues, with the 4th water-bound oxygen in approximately the same position. This indicates that the protein structure and ligand coordination is not significantly different regardless of the ligand charge.

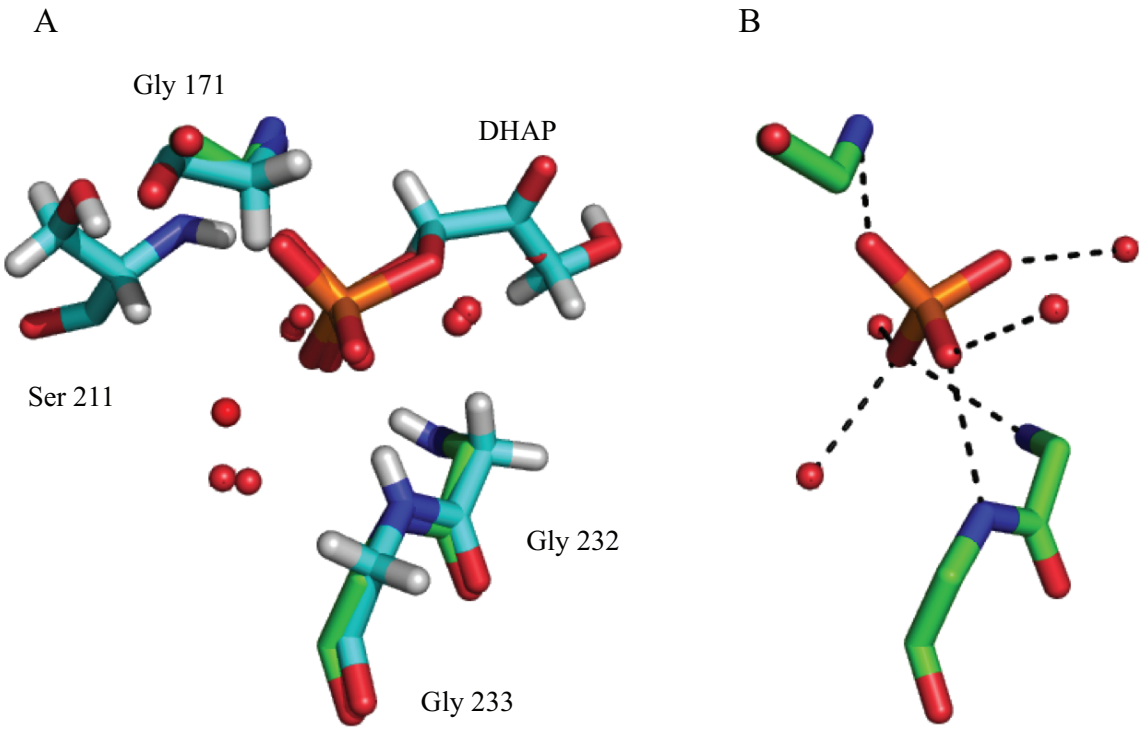

Figure 4.9 (A) Overlay of the PO_4^{3-} binding region for DHAP-bound TIM (blue, PDB ID: 1NEY, *S. cerevisiae*) and HPO_4^{2-} bound TIM (green, PDB ID: 1AG1, *t. brucei*). Glycines from loops 6 and 8 are involved in coordinating the phosphate moiety (loop 6 numbered Gly 171 for yeast TIM, and loop 8 Gly 232 and 233 numbered for yeast TIM). Ser 211 also binds to PO_4^{3-} in yeast TIM. There are 3 conserved waters involved in the ligand binding as well. (B) PO_4^{3-} binding region for HPO_4^{3-} region only. 3 oxygens of the phosphate group are coordinated to protein residues while the 4th is only coordinated to a water. This water appears in the same location that the carbon region of DHAP is located in 1NEY. Figure made in PyMol.

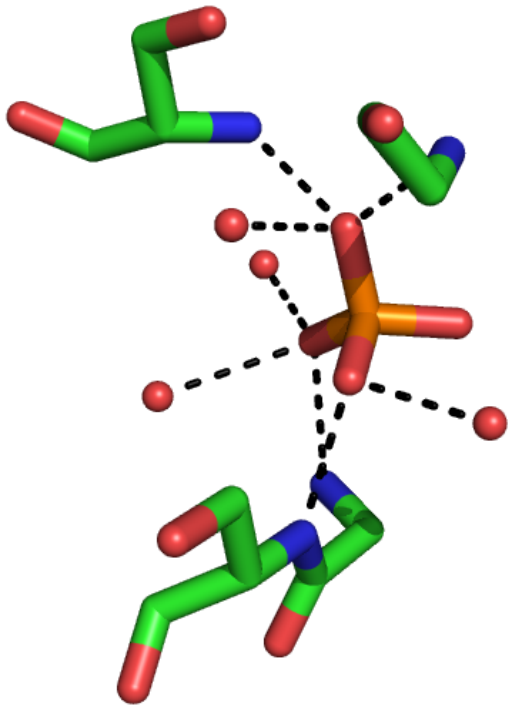

Figure 4.10 Monoanionic $H_2PO_4^-$ bound TIM from *H. pylori* (PDB ID: 2JGQ, [66]). Like DHAP and HPO_4^{2-} bound TIM, one phosphate oxygen atom in approximately the same position is not ligated to any protein residues. This suggests that at the very least, the protein structure is not affected by the phosphate charge.

PDB ID	Species	Resolution	R Factor	Ligand	pH
1NEY [59]	*S. cerevisiae*	1.2 Å	12.5%	DHAP	6.8
1AG1 [53]	*T. brucei*	2.4 Å	15%	HPO_4^{2-}	7.0
2JGQ [66]	*H. pylori*	2.3 Å	19%	$H_2PO_4^-$	8.0

Table 4.4 Summary of crystallography conditions for the proteins show in Figures 4.9 and 4.10 and discussed in the text.

An additional question arises in how to interpret our results in light of the computational work by Friesner and co-workers indicating that the monoanion is the catalytically active species [58]. Like the solution NMR work [44], we are only interpreting our data in terms of the species present with no indication of the catalytic chemistry.

There are weaknesses of our current conclusions that it is important to be aware of. Our η has a large error bar; there are many significant differences between our ligand and crystalline model compounds that we are interpreting our data based upon. A protein-ligated phosphate is going to be in a very different chemical environment. Furthermore, the bound ligand may undergo a dynamic process. Adding motion to the data-fitting (i.e. a 2 site hop of the phosphorous atom), η becomes 0. The magnitude of δ subsequently changes as well (the faster the motion, the greater the effect and the larger δ), but the sign of δ does not change. A static ligand such as PGA could provide a control for the presence of dynamics.

The tensor parameters determined from data-fitting were subsequently used to simulate the full experimental lineshape. Two ^{31}P atoms were included, one isotropic, the other with the CSA parameters determined in data-fitting; $\Delta\delta_{iso}$ was approximated to be 150 Hz. To reproduce the experimental linewidth, an R_2 or k_{ex} parameter was added to the simulation. The optimal values were $R_2 = 500\ s^{-1}$ or $k_{ex} = 1000\ s^{-1}$. This may indicate a low millisecond timescale dynamic process, though admittedly there is no concrete evidence for this hypothesis.

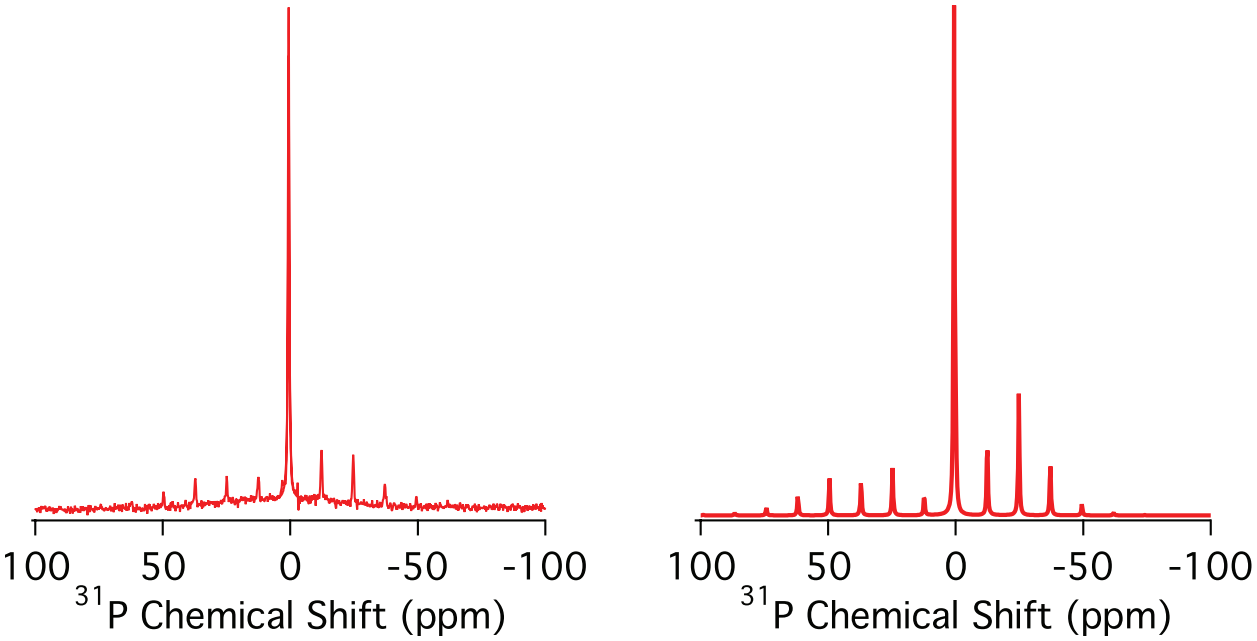

Figure 4.11 Experimental spectrum of 50/50 TIM-bound/unbound PO_4^{3-} collected at -20°C, 3 kHz MAS (left) and simulated spectrum using CSA parameters determined from fitting the full lineshape (left). The simulated spectrum had 2 ^{31}P atoms, one isotropic and one with the CSA tensor parameters. δ_{iso} = 150 Hz, δ = 17.7 kHz, η = 0.15. To match the experimental linewidths, either an R_2 or exchange parameter was added to the simulation. The optimal values were R_2 = 500 s^{-1} or k_{ex} = 1000 s^{-1}.

The simulated sideband manifold based on the tensor parameters determined and comparison to the experimental spectrum shows that the centerband would be expected to overlap with the dominant isotropic species and hence be buried under this peak.

4.5 Fast Magic Angle Spinning One Dimensional ^{31}P Spectra

Fast spinning MAS spectra where the CSA is averaged and linewidths are narrowed can provide information on the isotropic chemical shift of the system. Figure 4.12 shows fast spinning 1D spectra of TIM-bound PO_4^{3-} at -40°C and +20°C (VT temperature not true sample temperature). In the fast spinning spectra, no spinning sidebands are observed and up to 4 different phosphorous resonances are seen. At –40°C, 22 kHz MAS, two dominant peaks are observed at

~ 0 to 3 ppm. At +20°C, a third ^{31}P resonance becomes apparent in this chemical shift range along with the 2 observed at low temperature. In addition, the upfield peak loses intensity. These changes may suggest a change in the relative populations of the two species with temperature. The isotropic shift of the anisotropic (bound) species is expected to arise at the chemical shift of the dominant peak (peak 3 in Table 4.5). The loss in intensity of this peak may be due to a decrease in the population of bound PO_4^{3-}. A caveat to this statement is that intensities are not overly reliable in solid state NMR. The error in the intensities may be due to factors other than noise.

The features of the spectrum at +20°C, 22 kHz MAS has the same general features as the spectrum collected at +20°C, 3 kHz MAS. All resolved species in the fast MAS spectra would be hidden under the broader centerband with slow spinning. As shown in Table 4.5, the 2 dominant peaks (peaks 1 and 3) have chemical shift changes with temperature. The downfield shift with lower temperature is consistent with the small δ_{iso} shift changes observed in slow MAS spectra. This downfield shift may be indicative of increasing anionic behavior with increasing pH.

At present, we cannot make conclusions regarding the identities of these species. An important possibility may be that the different populations represent PO_4^{3-} with different ionization states or hydrogen bonding networks [64]. While they may be true PO_4^{3-} populations of interest, we should also consider possible sequestering of PO_4^{3-} solution as a result of fast magic angle spinning. In addition, further experiments will be done to determine if the observed temperature-dependence is due to a dynamic process.

The observed chemical shifts are reported in Table 4.5.

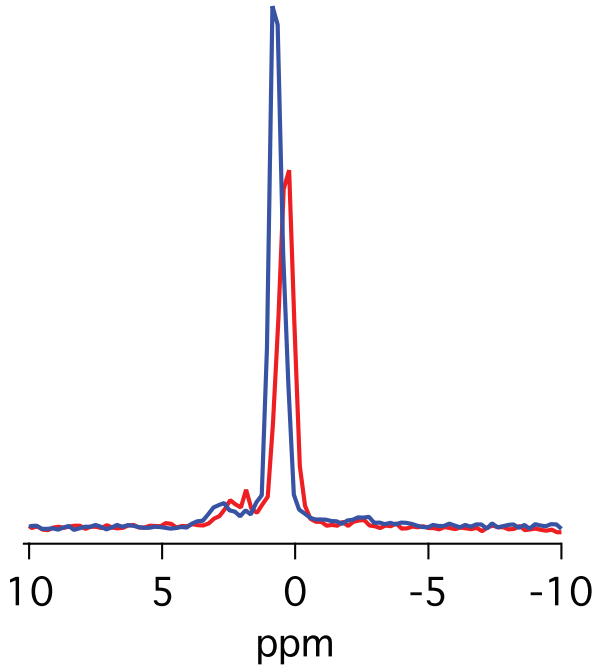

Figure 4.12 One-dimensional fast spinning spectra of TIM-bound PO_4^{3-} collected at (blue) -40°C and (red) +20°C, 22 kHz MAS. The anisotropic species is expected to arise at the chemical shift of the dominant peak. The loss of intensity of this peak with increased temperature may be explained by a decrease in the population of bound PO_4^{3-}.

Temperature	δ_{iso} (ppm) Peak 1	δ_{iso} (ppm) Peak 2	δ_{iso} (ppm) Peak 3	δ_{iso} (ppm) Peak 4
-40°C	2.75	1.81	0.78	-2.58
+20°C	2.42	1.84	0.32	-2.59

Table 4.5 Isotropic chemical shifts for the four phosphorous resonances observed in fast MAS spectra of 50/50 TIM-bound/unbound PO_4^{3-}collected at 22 kHz MAS. Peak one indicates the downfield most peak and peak 4 is the upfield most peak.

A summary of features of the ^{31}P one-dimensional spectra discussed in Sections 4.3 to 4.5 is reported in the Appendix, Section 8.2.

Previous measurements of $Pb(NO_2)_3$ in our group (Dr. Ansgar Siemer) observed that changing the spinning speed of a 3.2 mm rotor from 5 kHz to 20 kHz would lead to approximately 25°C of sample heating (measurements done on a T4 probe not the BioMAS probe used in these studies). The possibility of a significant temperature change with spinning speed must be considered.

4.6 Experimental $R_{1\rho}$ Studies of Ligand Binding in Triosephosphate Isomerase

A unique features of the $R_{1\rho}$ studies of ligand binding in TIM described below is that $R_{1\rho}$ relaxation is due to changes in the magnitude of the CSA tensor upon binding and release, rather than reorientation of the chemical shift tensor as was used for DMS studies in Chapter 3. Using changes in CSA tensor magnitude rather than tensor orientation for the study of dynamics with solid state NMR is a relatively novel concept. The transferred NOE and MRD experiments can be viewed as comparable experiments utilizing similar concepts (discussed in Section 4.1).

To execute $R_{1\rho}$ measurements of TIM-bound PO_4^{3-}, spin-locks were applied on-resonance with the isotropic centerband at an MAS rate of 7 kHz, over a range of spin-lock field strengths (20-32 kHz). All phosphorous resonances are close enough in frequency at the centerband that off-resonance effects for particular peaks are negligible. Direct excitation was used for phosphorous polarization. ^{31}P $R_{1\rho}$ dispersion curves of 50/50 TIM-bound/unbound PO_4^{3-} were collected under a range of experimental conditions on both 400 MHz and 600 MHz spectrometers.

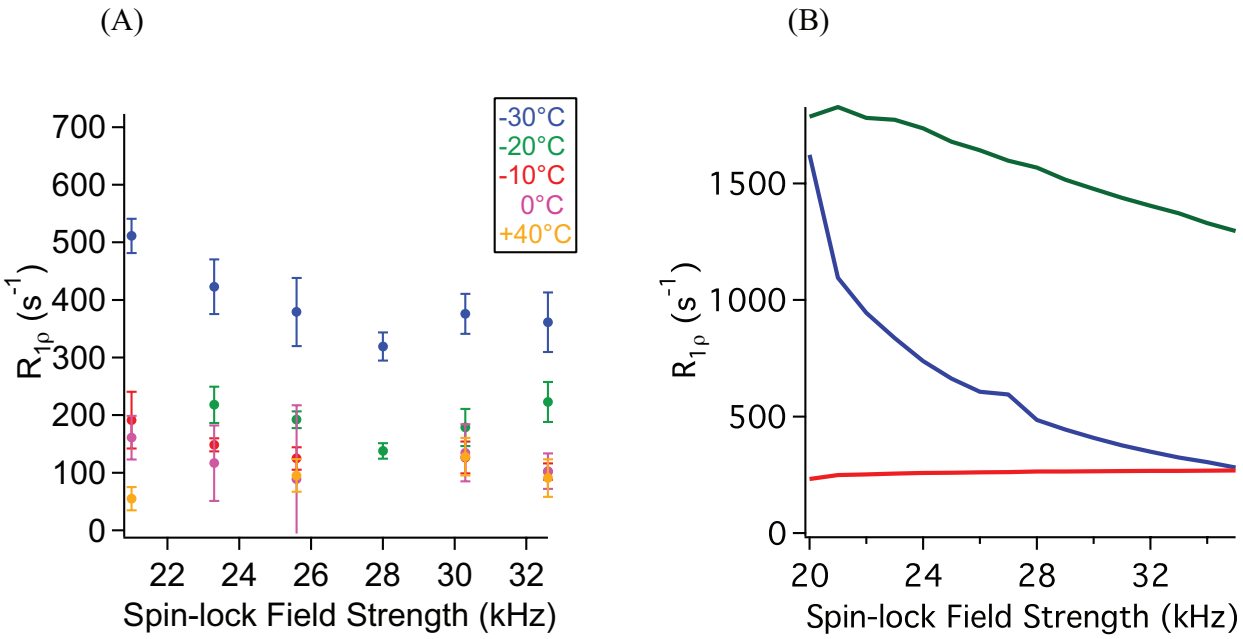

Figure 4.13 (A) On-resonance $R_{1\rho}$ dispersion curves for 50/50 TIM-bound to unbound PO_4^{3-} collected at 600 MHz ^1H B_0 frequency, 7 kHz magic angle spinning with direct excitation. (•) -30°C, (•) -20°C, (•) -10°C, (•) 0°C, (•) +40°C. At low temperature, the characteristic field-strength dependence due to a dynamic process is observed, while at higher temperature, $R_{1\rho}$ is relatively flat as a function of spin-lock field strength. This behavior is likely due to a fast timescale process that manifests as a flat R_2 contribution above -30°C, and slows to the $R_{1\rho}$-sensitive µs regime at low temperature. (B) Simulated dispersion curves showing the dependence of $R_{1\rho}$ on the exchange rate. (–) k_{ex} = 2 x 10^6 s^{-1}, (–) k_{ex} = 2 x 10^5 s^{-1}, (–) k_{ex} = 2 x 10^4 s^{-1}. For all simulations, exchange was between an isotropic and an anisotropic species, $\Delta\delta_{iso}$ = 150 Hz, δ = 18 kHz, η = 0.2, MAS = 7 kHz, $p_A = p_B = 0.5$.

Figure 4.13 shows experimental $R_{1\rho}$ values for 50/50 unbound/ TIM-bound PO_4^{3-} collected at a B_0 field strength of 600 MHz, an MAS rate of 7 kHz with direct excitation, and temperatures of -30°C (blue), -20°C (green), -10°C (red), 0°C (pink), and +40°C (orange). The notable trend is the $R_{1\rho}$ field strength dependence at low temperature, and a lower, relatively flat $R_{1\rho}$ dispersion at higher temperatures. This effect is consistent with a dynamic process which is above the µs timescale at warmer temperatures ($\omega_e << 1/k$) and at -30°C is slowed enough to be in the dynamic regime that $R_{1\rho}$ measurements are sensitive to. The flat dispersion at higher temperature is significantly faster than the R_2 of 0 s^{-1} for Na_2HPO_4 without TIM, indicating the presence of protein does play a role in the observed dynamic process.

The proposed dynamic process is supported by simulated relaxation curves shown in Figure 4.13 (B). These simulations used the CSA tensor parameters as determined from fitting the slow MAS spectra in Section 4.4. Exchange was assumed to be between an isotropic and an anisotropic species with the following tensor parameters: $\Delta\delta_{iso}$ = 150 Hz, δ = 18 kHz, η = 0.2, MAS = 7 kHz, $p_A = p_B = 0.5$. With an exchange rate of 10^6 s^{-1}, $R_{1\rho}$ is lower than at slower exchange rates and has an essentially flat dispersion. An interesting note is that while not necessarily apparent on the $R_{1\rho}$ scale shown, the simulated relaxation rate for fast exchange (red, 10^6 s^{-1}) actually increases with increasing spin-lock field strength, a trend that may also be occurring in experimental data.

The unanticipated dynamic behavior is likely not due to the on/off behavior of the ligand moving in and out of the binding pocket with loop opening and closing as initially hypothesized. The temperature dependence of $R_{1\rho}$ suggests a dynamic process that is faster than the timescale $R_{1\rho}$ experiments are sensitive to at temperatures above -30°C (above the microsecond timescale at physiological temperatures). While not the expected process, there is precedence in the literature for such dynamic behavior. Multiple hypotheses for the observed motion are proposed. Given an association rate constant of ~ 10^7 (k_{on}, [67]), we may be seeing an on/off process only associated with the open loop, rather than a slower off rate associated with loop opening. Fluorescence measurements of unligated TIM, along with DHAP, G3P, PGA, and PO_4^{3-} indicated that PO_4^{3-} has multi-exponential kinetics, while G3P and DHAP have mono-exponential kinetics, and unligated TIM and PGA show no kinetic or dynamic behavior [45]. Broadline deuterium studies of the loop dynamics of deuterated Trp 168 by Rozovsky and

McDermott indicate a low angle μs process at -15°C rather than the ms dynamics of k_{open} at higher temperatures [68].

The dynamics could also be explained by a phase transition related to the behavior of the solvation shell (slowing of dynamics of the solvent that forms the hydration shell), or rapid librations of the phosphate ion within the active site. Crystal structures of TIM bound with inorganic phosphate show multiple positions of the ion within the active site (Figure 4.14) [53, 59, 66, 69]. The orientation of the phosphate moiety for the native ligand is not in perfect alignment with any of these phosphate binding sites. Simulations suggest however that these small angle librations within the active site would have much lower $R_{1\rho}$ relaxation rates. The hydration shell of a protein freezes at significantly lower temperature than the bulk solvent (lower than -30°C vs ~5°C). The dynamics of the hydration shell ions slows from the nanosecond timescale as the temperature approaches the phase transition [49, 70, 71].

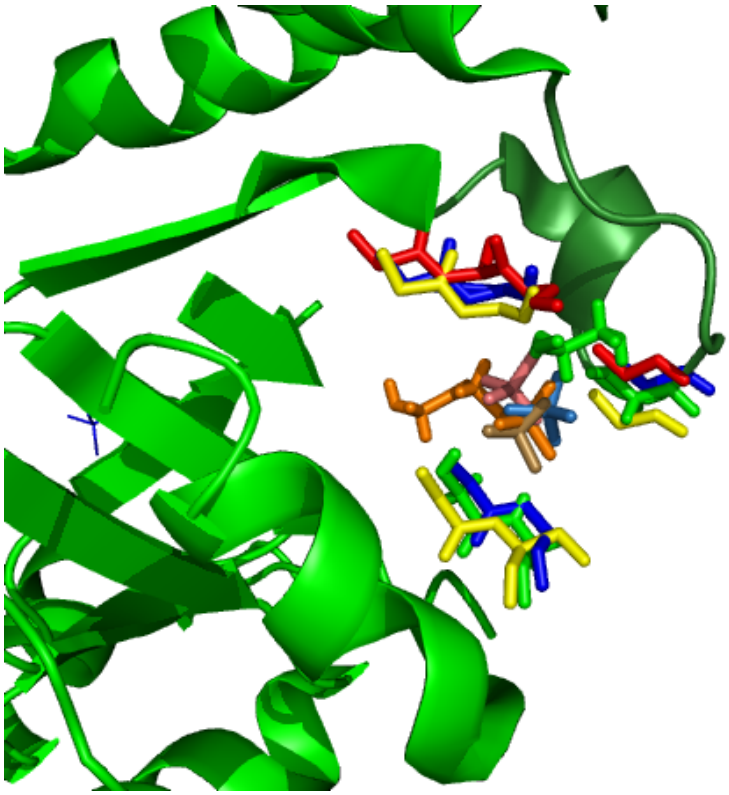

Figure 4.14 Overlay of 3 crystal structures of TIM with inorganic phosphate as the ligand (blue: *T. thermophilus*, 1YYA, 1.6Å; red: *T. tenax*, 1W0M, 2.5Å; yellow: *H. pylori*, 2JGQ, 2.3Å) and DHAP-bound TIM (green: 1NEY, *S. cerevisiae*, 1.2Å). The phosphate ligand associated with each structure is shown in a slightly lighter shade than the protein. The native ligand DHAP is shaded orange. The crystal structures indicate that the phosphate ligand may occupy multiple conformations within the active site. Librations among conformations of the phosphate ion may explain the faster timescale dynamic process.

As discussed in Section 4.4, lineshape simulations may suggest the possibility of an exchange process on the low millisecond timescale, while $R_{1\rho}$ experiments indicate a dynamic process ~ 100,000 s^{-1}. The fluorescence measurements described above may support this observation of dynamics on both fast and slow timescales for PO_4^{3-}.

The other possibility discussed in Section 4.4 is that the lineshape arises from an R_2 contribution. As discussed in Chapter 3, we would expect this R_2 contribution to lead to an offset in $R_{1\rho}$ measurements. Only at -30°C do the $R_{1\rho}$ rates measured have values at or above the ~ 500 s^{-1} determined as the approximate R_2 relaxation rate from lineshape simulations. This observation is

a further suggestion of the proposal for a slow exchange process reflected in the one-dimensional spectra.

The relaxation behavior of the spinning sidebands was also analyzed (albeit limitedly). At temperatures both above and below -20°C, the relaxation behavior of the sidebands could not be observed, due to either faster relaxation, lower signal-to-noise, or a combination of the two. At -20°C, the relaxation behavior of the spinning sidebands was faster than the relaxation of the centerband. This may be due to the more dominant contribution of the unaveraged CSA tensor to relaxation or may indicate different dynamic behavior (data not shown).

Different experimental conditions and/or methods need to be considered to capture the on-off process of ligand binding. Carr-Purcell-Meiboom-Gill (CPMG) experiments, which are more sensitive to ms timescale dynamics (as opposed to μs dynamics for $R_{1\rho}$), have recently been developed for the solid state [72]. Experiments at higher temperatures may move the dynamic process of interest into a range where it is detectable via $R_{1\rho}$ experiments. pH may be another important consideration. Mutations may provide another method to analyze the loop dynamics during ligand binding.

The Effect of Proton Decoupling Studies on the model compound dimethyl sulfone (DMS), discussed in Chapter 3, showed the role of decoupling during the spin-lock in $R_{1\rho}$ measurements of protonated compounds. This work indicated that proton decoupling did not have a significant impact on the measured $R_{1\rho}$ relaxation rates. In fact, at a certain threshold for the ^{1}H decoupling power during the spin-lock, weaker decoupling appeared to be more efficient than higher power

levels. This suggests a Hartmann-Hahn effect where simultaneous irradiation of the proton and X channels leads to magnetization transfer between the two, and thus unreliable relaxation rates. Dramatically lower relaxation rates were observed when deuterated rather than protonated DMS was used. This suggests not only that ^{13}C-^{1}H dipolar relaxation was occurring but also that the applied decoupling was not efficient, possibly due to the intermediate timescale dynamics of the system.

Two different decoupling controls for TIM-bound $^{31}PO_4^{3-}$ are shown in Figure 4.15. (A) was collected on a 600 MHz spectrometer, with an BioMAS probe. (B) was collected on a 400 MHz spectrometer with a standard probe at 10 kHz MAS with 60 kHz proton decoupling. In Figure 4.15 (A), the data in blue was collected at -40°C, 10 kHz MAS and the data in red was collected at +30°C, 7 kHz MAS. In both (A) and (B), closed circles indicate proton decoupling was applied during the spin-lock while open circles indicate no decoupling was used. It is indicated that applying proton decoupling during the spin-lock does decrease the relaxation rate, presumably by reducing ^{31}P-^{1}H couplings that lead to a dipolar contribution to relaxation. The effect is small however. In (B), an interesting trend of increasing relaxation with increasing spin-lock is observed. While this unexpected trend may be a true experimental effect of unknown origin, it may be introduced due to complications associated with proton decoupling. Higher spin-lock field strengths were used relative to Figure 4.15 (A), increasing the possibility of a Hartmann-Hahn like transfer of magnetization between the nuclei. In addition, unlike the BioMAS probe used for 600 MHz experiments, the probe used here delivers high power levels through the coil into the sample during the spin-lock. The increased spin-lock field strength may be causing sample heating that leads to faster relaxation. Due to the potential for sample heating,

further work was not done on this probe. On the 600 MHz spectrometer, the use of the BioMAS probe is an important experimental detail. This type of probe is specifically designed to reduce sample heating due to radio frequency irradiation. Unlike a crystalline sample such as dimethyl sulfone, biological samples have high salt concentrations and therefore are susceptible to heating. Accurate measurements of $R_{1\rho}$ require careful control of sample temperature.

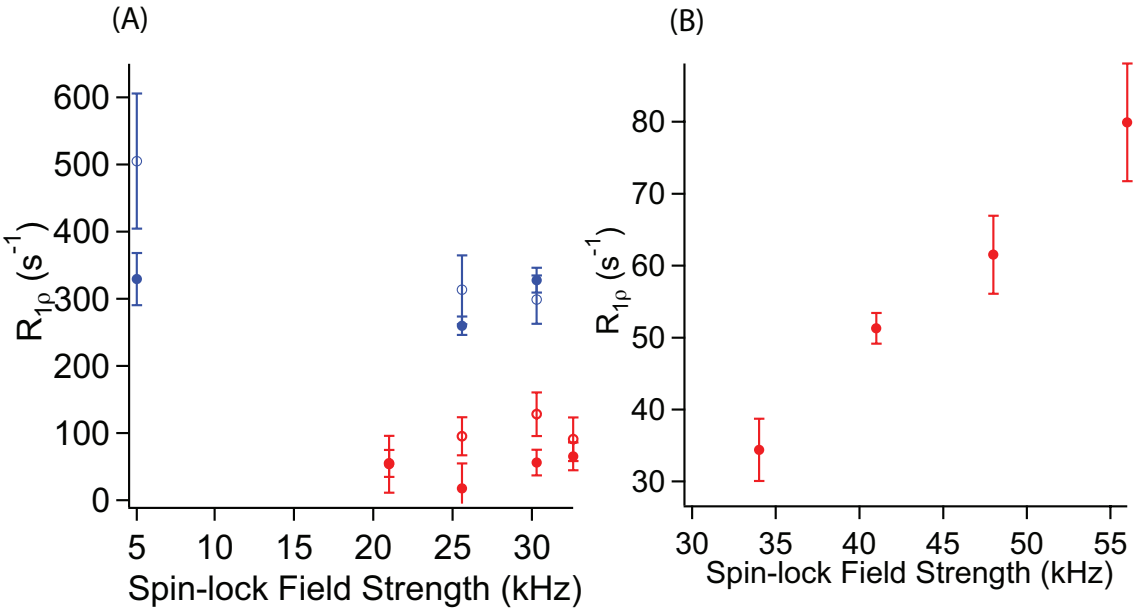

Figure 4.15 The effect of proton decoupling during the spin-lock in $R_{1\rho}$ experiments (A) Data collected at 600 MHz using a BioMAS probe. (Blue) -40°C, 10 kHz MAS; (Red) +30°C, 7 kHz MAS. Closed circles indicate 70 kHz proton decoupling was applied during the spin-lock while open circles indicate no decoupling was used. (B) Data collected at 400 MHz using a standard probe and 60 kHz proton decoupling during the spin-lock, 10 kHz MAS. With use of the BioMAS probe which helps reduce sample heating due to RF irradiation, $R_{1\rho}$ has little dependence on decoupling (left). At 400 MHz (right), the increase in $R_{1\rho}$ with increasing spin-lock field strengths is believed to be due to sample heating (and possibly Hartmann-Hahn effects).

Without the application of proton decoupling during the spin-lock, a question arises of what the influence of protons may be on the relaxation. Given the inefficiency of cross polarization, the H-P couplings are not strong, but may not be negligible. From the crystal structure of DHAP-bound TIM (Figure 4.16), it can be seen that the closest H-P distances are about 3-4 Å. This would give a dipolar coupling strength on the order of 1.5 kHz or less. This may only be a rough

approximation for phosphate-bound TIM, given inorganic phosphate is a smaller ligand. While $R_{1\rho}$ measurement discussed for protein-free Na_2HPO_4 suggest neighboring waters will likely not contribute any significant relaxation (Figure 4.17), the more fixed protons of proximal amino acids may.

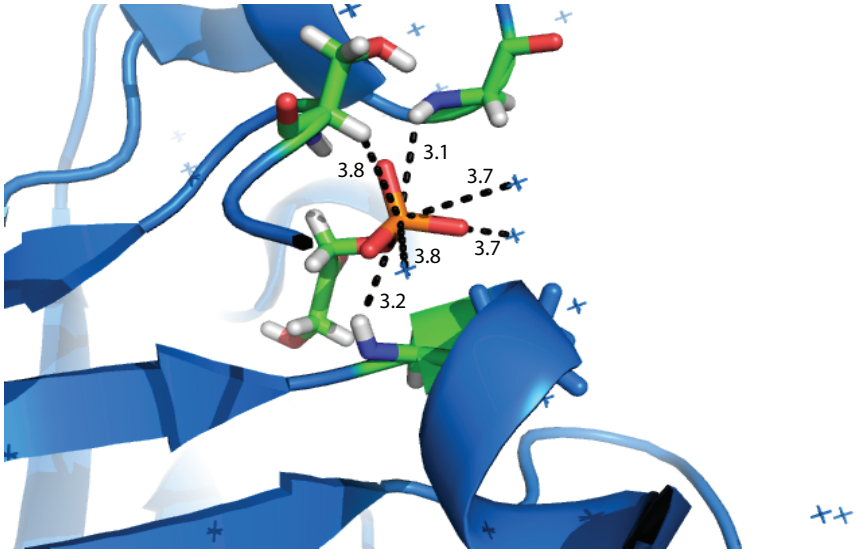

Figure 4.16 DHAP-bound TIM (PDB ID: 1NEY), showing the geometry of the phosphate moiety of the ligand, and neighboring atoms. The nearest protons to the phosphate group are 3-4 Å away. This would give dipolar couplings on the order of 1.5 kHz or less. Crosses represent water molecules. The amino acids highlighted are Gly 171, Gly 232, and Ser 211.

Unlike DMS, proton decoupling appears to have a small influence on the relaxation rate in this biological sample. It is important to realize that a hydrated protein sample with a complex network of protons may not have the same behavior as a crystalline model compound. There were both practical and theoretical reasons for using a protonated sample for initial experiments. While a deuterated sample is expected to give truer results, protonated samples were used for the first work on these new experiments to show that the experiments would work, given the increased expense and more intensive preparation of deuterated protein. The absence of attached protons to the phosphate atom suggested that dipolar couplings would be weak. Future studies

will use deuterated protein and buffer to reduce any residual ^{31}P-^{1}H couplings that may be present. As was shown for DMS, where decoupling did not have a significant effect on $R_{1\rho}$, utilizing deuteration will likely have a dramatic effect.

4.7 Control $R_{1\rho}$ Experiments of Na_2HPO_4

To confirm that observed $R_{1\rho}$ relaxation was due to protein-ligand interactions rather than phosphate spin-diffusion or fast timescale processes such as molecular tumbling seen in solution NMR, control experiments of a phosphate solution in TIM buffer was done.

$R_{1\rho}$ measurements of 50 mM Na_2HPO_4 in 50 mM Tris, 50 mMNaCl, and 1 mM EDTA, pH = 6.8 at 4°C (buffer for TIM NMR experiments) indicated that there was virtually no relaxation. The dispersion curves, shown in Figure 4.17 (A) show that there is no field strength or temperature dependence to the relaxation either.

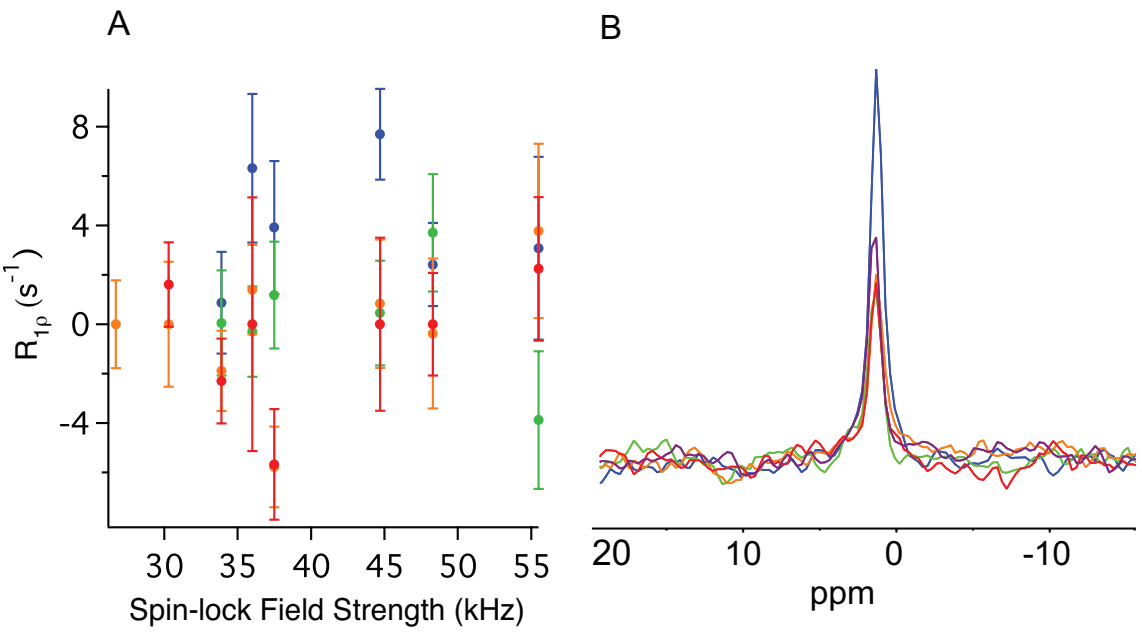

Figure 4.17 (A) ^{31}P $R_{1\rho}$ control experiments for a 50 mM PO_4^{3-} solution in 50 mMTris, 50 mM NaCl, 50 mM EDTA, pH = 6.8 at 4°C. Thermocouple temperatures were (•) +10°C, (•) 0°C, (•) -10°C, (•) -20°C. Relaxation measurements indicate that over the range of temperatures from -20°C to +10°C, unbound PO_4^{3-} is not expected to contribute to the observed relaxation. (B) One-dimensional spectra over the same range of temperatures, showing no spinning sidbands, no temperature-dependent chemical shift, and relatively constant linewidths. Data was collected on a 400 MHz spectrometer with 10 kHz MAS with direct excitation.

One dimensional ^{31}P spectra of the Na_2HPO_4 solution did not have spinning sidebands, suggesting that this species is largely isotropic. Furthermore, the temperature series indicated there was no evidence of chemical shift changes due to potential changes in pH, resulting from the temperature-dependence of Tris buffer and change of the phosphate ionization state (Figure 4.17 B). The chemical shift was 0.4 ppm at all temperatures. Linewidths were ~ 90 Hz at all temperatures as well. Over this range of temperatures from -20°C to +10°C, the pH is only expected to vary from 6.5 to 7.5, given that the pH of Tris buffer is expected to increase by 0.028 for every 1°C that sample temperature is lowered. In a solution NMR study of the ligand PGA, a 1.5 ppm (55 Hz) change was observed over a pH range from 6.2 to 8.0 [44]. Given the inherently broad linewidths of solid state NMR and smaller range of pH values expected in our experiments, it is likely that any pH/temperature-dependent chemical shift difference cannot be

observed. In Figure 4.17 (B), it is unclear why there is greater intensity to the spectrum collected at -20°C relative to the other temperatures.

As mentioned above, the chemical shift of the Na_2HPO_4/buffer frozen solution is 0.4 ppm. This better agrees with the chemical shift of the PO_4^{3-} species that gave rise to spinning sidebands in the slow MAS spectra of 50/50 TIM-bound PO_4^{3-}.

These control experiments of an Na_2HPO_4 solution in TIM buffer support the conclusion that the results of ^{31}P 1D spectra and $R_{1\rho}$ measurements of TIM-bound phosphate are due to protein-ligand interactions.

4.8 Practical Application of Solid State $R_{1\rho}$ Measurements for the Study of Biological Systems

An important question that needs to be considered in solid state $R_{1\rho}$ measurements is the sensitivity of $R_{1\rho}$ to the exchange rate. Over what range of timescales are $R_{1\rho}$ measurements useful? A dispersion curve is not sensitive to exchange rates that are too fast or too slow. What constitutes 'intermediate exchange' is not a simple question for $R_{1\rho}$ experiments. Many characteristics of the system, as well as experimental conditions, contribute to the exchange rate and spin-lock field strength dependence of $R_{1\rho}$. These features include the magnitude of the anisotropy and asymmetry, isotropic chemical shift differences, the hop angle between exchanging sites, as well as the spinning speed and static magnetic field strength. In general, a system with a larger $R_{1\rho}$ relaxation rate will be more sensitive to dynamic processes.

Dynamic processes on the millisecond to microsecond timescale are important for catalysis and allosteric regulation (among other biological functions). Realistic biological systems typically undergo small angle changes. Upon ligand binding, the allosteric protein aspartate transcarbamylase (ATCase) undergoes a 15° rotation of the two parts of the dimer [73]. The classic example hemoglobin undergoes a quaternary conformational change of approximately 15° with a rate of 5×10^4 s^{-1} [74]. Protein backbone chemical shift tensors are ~ 100 – 120 ppm for ^{15}N and ~ 70 – 90 ppm for carbon [75, 76]. The sensitivity of $R_{1\rho}$ for a typical case that may be encountered in a biological system is presented below to evaluate the dynamic range of $R_{1\rho}$ experiments.

$R_{1\rho}$ relaxation as a function of spin-lock field strength was simulated for a range of exchange rates, with reorientation of the chemical shift tensor of a single carbon atom as the probe of dynamics. The experimental and system parameters used were as follows: B_0 = 500 MHz, MAS = 10 kHz, $\Delta\delta_{iso}$ = 1 ppm, δ = 110 ppm, η = 0.6, β = 10°.

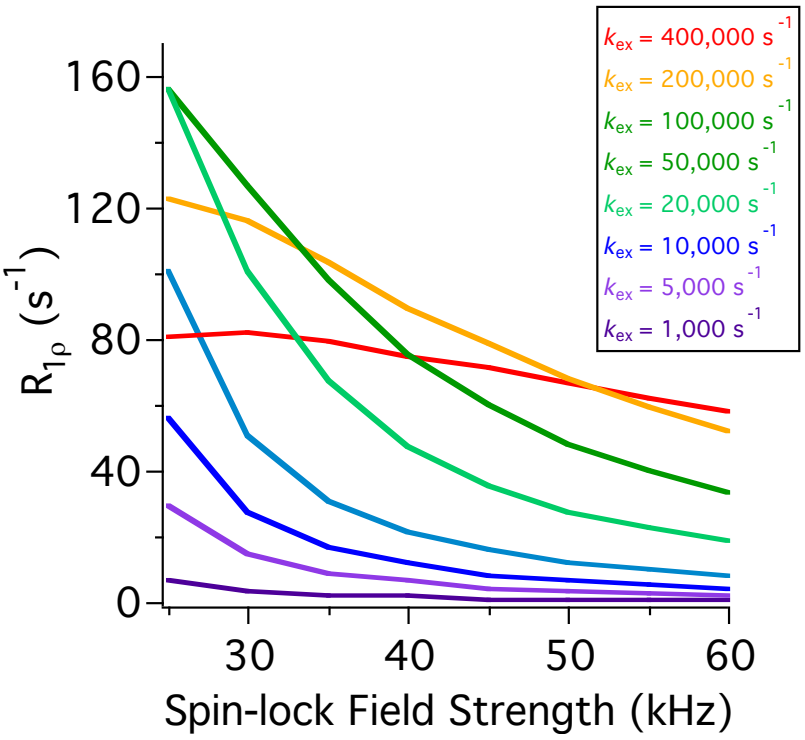

Figure 4.18 Exchange rate dependence of $R_{1\rho}$ dispersion for typical chemical shift tensors observed in backbone C_α atoms. The range of sensitivity for $R_{1\rho}$ is ~ 5000 s^{-1} to 200,000 s^{-1} with the greatest field strength sensitivity at 50,000 to 100,000 s^{-1}. The simulations assumed only a CSA tensor (no dipolar interaction) of 110 ppm and an asymmetry of 0.6. There is an isotropic shift difference of 1 ppm between the 2 exchanging sites with a hop angle of 10°. The MAS rate was 10 kHz

With a modest increase in exchange rate from 1000 s^{-1} to 5000^{-1}, the field strength dependence of $R_{1\rho}$ increases notably, into a range with reasonable rates to observe dynamics relatively reliably. As the exchange rate increases beyond this point, the dependence of $R_{1\rho}$ on the spin-lock field strength is more sensitive to the exchange rate. Even with variation of experimental and system parameters, the accessible regime changes very little; the optimal timescale for greatest sensitivity of $R_{1\rho}$ is ~ 10^4 s^{-1}. Higher spin-lock field strengths make somewhat faster timescales more accessible (i.e. 75,000 s^{-1} at field strengths over 30 kHz).

Exchange rates of 1000 s^{-1} and 400,000 s^{-1} have changes in $R_{1\rho}$ with increasing spin-lock field strength of less than 5 s^{-1}. These small changes are virtually undetectable within the error of the measurements. An additional consideration for the upper and lower limits of observable exchange rates is error bars on experimental $R_{1\rho}$ measurements. At the upper and lower limits of exchange, error bars will make trends in the spin-lock field strength even more difficult to observe.

The range of accessible exchange drops off relatively quickly. The optimal dynamic regime is ~ 10^4 s^{-1} but does extend to the lower end of 10^5 s^{-1}. As shown for a plot of $R_{1\rho}$ as a function of exchange rate (Figure 4.19, spin-lock field strength = 25 kHz), $R_{1\rho}^{MAX}$ is ~ 50,000 to 100,000 s^{-1}. This is the 'intermediate exchange' regime for $R_{1\rho}$ experiments, where $k_{ex} \sim \omega_{CSA}$ (rather than $\Delta\omega_{iso}$).

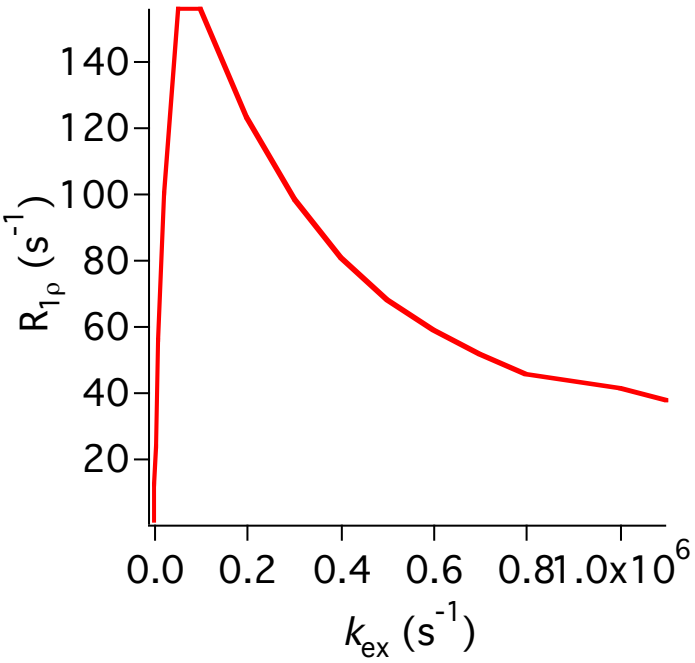

Figure 4.19 Exchange rate dependence of $R_{1\rho}$ at a constant spin-lock field strength of 25 kHz. $R_{1\rho}$ reaches a maximum in a relatively narrow range, making the optimal exchange rates for maximum $R_{1\rho}$ sensitivity in the relatively narrow regime of ~ 10^4 s^{-1}. The tensor and experimental conditions are the same as presented in Figure 4.18: CSA tensor reorientation (no dipolar interaction) of 110 ppm and an asymmetry of 0.6. $\Delta\delta_{iso}$= 1 ppm between the 2 exchanging sites with a hop angle of 10°. The MAS rate is 10 kHz.

With an isotropic chemical shift difference between exchanging sites of 125 Hz at 500 MHz B_0 field, linebroadening does occur at intermediate exchange on the chemical shift timescale (i.e. $k \sim \Delta\omega$). With this modest isotropic shift difference, linebroadening due to this phenomenon occurs at slower timescales than we are interested in for $R_{1\rho}$ experiments. However, there is linebroadening that occurs at the optimal exchange rates for $R_{1\rho}$ sensitivity. Both the maximum $R_{1\rho}$ relaxation rate and increased linebroadening occur under the condition $k_{ex} \sim \omega_{CSA}$.

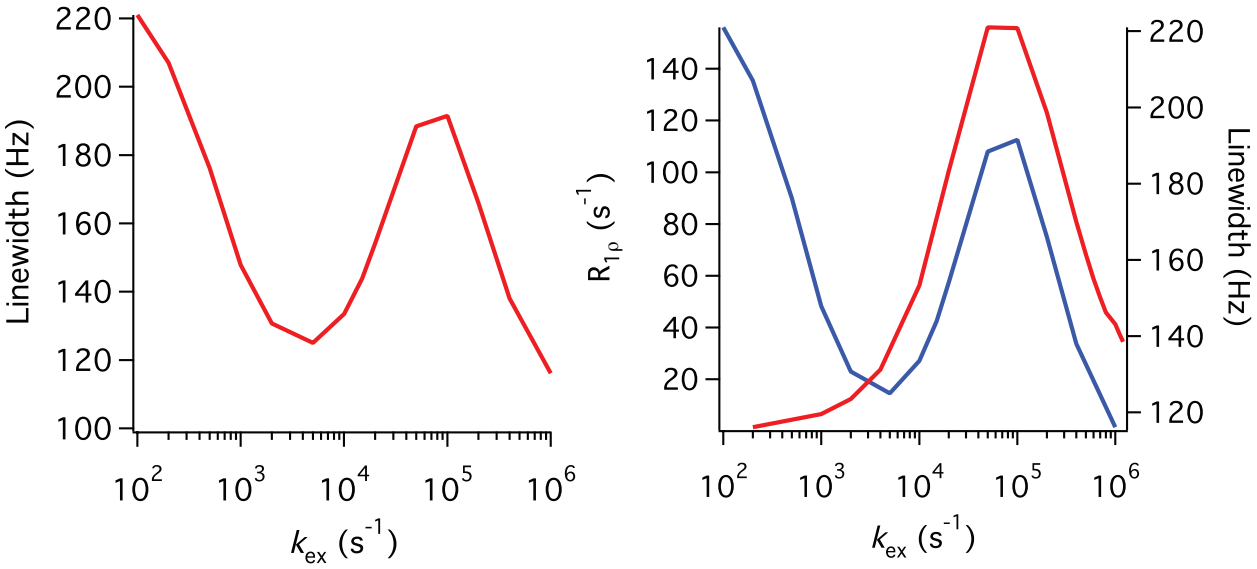

Figure 4.20 (Left) Dependence of linewidth on exchange rate. At the lowest exchange rates (~ 100 s^{-1}), linebroadening occurs due to intermediate exchange on the chemical shift timescale ($k_{ex} \sim \Delta\omega_{iso}$). At faster exchange rates, linebroadening has a second maximum (with less severe linebroadening) at the condition $k_{ex} \sim \omega_{CSA}$. (Right) Overlay of linebroadening and $R_{1\rho}$ as a function of k_{ex}, showing that both the maximum $R_{1\rho}$ and increased linebroadening occur at the same exchange rates. However, the extent of linebroadening will likely not completely eliminate signal. Simulated conditions were: a CSA tensor (no dipolar interaction) of 110 ppm and an asymmetry of 0.6. There is an isotropic shift difference of 1 ppm between the 2 exchanging sites with a hop angle of 10°. The MAS rate was 10 kHz (typical conditions for proteins).

Given an inherent linewidth of 100 Hz, and the specific simulation conditions above, the maximum linebroadening occurs at k_{ex} = 50,000 – 100,000 s^{-1} (ω_{CSA} ~ 86,000 s^{-1}). Therefore, maximum $R_{1\rho}$ sensitivity while minimizing linebroadening occurs just below regime, where $R_{1\rho}$ close to a maximum, at exchange rates slightly below or above the magnitude of the chemical shift tensor. It may not be that this linebroadening at maximum exchange rates significantly inhibits detection. Beyond non-exchange linebroadening, the additional contribution at the $k_{ex} \sim \omega_{CSA}$ condition is < 100 Hz, a less severe broadening than occurs at $k_{ex} \sim \Delta\omega_{iso}$.

4.9 Conclusions and Future Directions

We have made progress toward characterizing the nature of ligand binding and exchange in the enzyme triosephosphate isomerase utilizing the small inorganic phosphate ligand, PO_4^{3-}. Slow and fast spinning one-dimensional ^{31}P spectra complement $R_{1\rho}$ measurements by providing insight into ligand binding and features of NMR interactions in the system, such as the magnitude of the chemical shift anisotropy. These measurements indicate that there are multiple PO_4^{3-} populations present, with differing isotropic and anisotropic behavior. The change in spectra between low and high temperature may indicate a dynamic process is present.

The chemical shift tensor parameters of the anisotropic species suggest it is in a dianionic state. Ligand dynamics and/or a mixture of ionization states should be further considered. Complementary analysis of DHAP, $H_2PO_4^-$, and HPO_4^{2-} bound crystal structures may suggest that the protein structure is not affected by the ligand ionization state. The tensor parameters fit using Spinevolution are consistent with the appearance of spinning sidebands at 3 kHz MAS (and 7 kHz MAS used for $R_{1\rho}$ experiments) and the absence of this feature at 22 kHz MAS. In order to average out the anisotropy of the chemical shift tensor, the magic angle spinning rate needs to be faster than the magnitude of the tensor. If the CSA is on the order of 15 kHz, this condition is not met at 3 kHz spinning, but is at 22 kHz MAS.

The temperature dependence of $R_{1\rho}$ measurements indicates a dynamic process that is above the μs timescale at physiological temperature. A unique feature of these $R_{1\rho}$ experiments is that we are utilizing changes in the magnitude of the chemical shift tensor rather than reorientation. This

faster than expected dynamic process may be the ligand coming on and off the open loop, dynamics of the hydration shell, or librations of the ligand within the active site. Higher temperature $R_{1\rho}$ measurements may shift the sensitivity of the measurements to the slower timescale process by moving the faster dynamic process beyond the range that $R_{1\rho}$ measurements are sensitive to, and the slower dynamic process into this range. In order to confirm the identities of the various phosphate populations observed in the fast MAS spectra, correlations to other elements (i.e. ^{31}P ligand to ^{15}N protein backbone) through experiments such as TEDOR may provide evidence to assign the observed resonances. Appropriate choice of protein labels may allow the coordinated observation of loop and ligand dynamics.

In doing these experiments, it was found that using a direct 90° pulse on phosphorous as the method of excitation gave twice the signal-to-noise or better relative to magnetization transfer via cross polarization. The phosphorous atoms of interest do not have any attached protons. The improved signal with direct excitation of phosphorous may also be suggestive of dynamics in the system. It is likely that cross polarization will select for static resonances, while direct excitation will capture both static and dynamic components of the system. The combination of dynamics in the system and the relatively long distance between phosphorous atoms and their neighboring protons, which are either free in solution or bound to oxygen atoms, leads to a very weak dipolar coupling between proton and phosphorous. Using direct excitation is further ideal because previous model compound experiments had shown that relaxation can occur during cross polarization, leading to erroneously low $R_{1\rho}$ relaxation rates.

Protein-ligand interactions and molecular recognition are important fields of study for general biochemical research, drug discovery, as well as understanding the mechanisms of action for drugs currently on the market. Currently classes of proteins such as G-coupled protein receptors are being researched as drug targets. Furthering our understanding of how both native ligands and inhibitors and agonists interact with GPCRs can be greatly beneficial for medical research. The group of experiments presented here could contribute to this understanding. In particular, these membrane-bound proteins can be difficult to study with techniques that require the protein to be solubilized.

4.10 Materials and Methods

4.10.1 TIM/PO_4^{3-} Sample Preparation

Natural abundance TIM was prepared as described in Chapter 6.

To obtain the desired populations of bound-to-unbound phosphate ligand, the K_d of PO_4^{3-} in TIM, active site concentration, % bound TIM, and total [PO_4^{3-}] concentration must be taken into account.

From the expression given by Jones and Waley [77] for enzyme binding

$$K_d = \frac{1-y}{y}(L_t - S_t y) \quad (1)$$

where K_d is the dissociation constant for a particular ligand with the enzyme, y is the fraction of bound active sites, S_t is the total concentration of active sites, and L_t is the total ligand concentration, the total [PO_4^{3-}] necessary to attain 1:1 bound-to-unbound PO_4^{3-} can be calculated. Directly from equation 1, the fraction of bound active sites can be calculated for a given [PO_4^{3-}]. Since we want [free PO_4^{3-}] to equal ½ [total PO_4^{3-}] and [bound active sites] = [bound PO_4^{3-}], we can find the [total PO_4^{3-}] where this condition holds true for a known number of active sites.

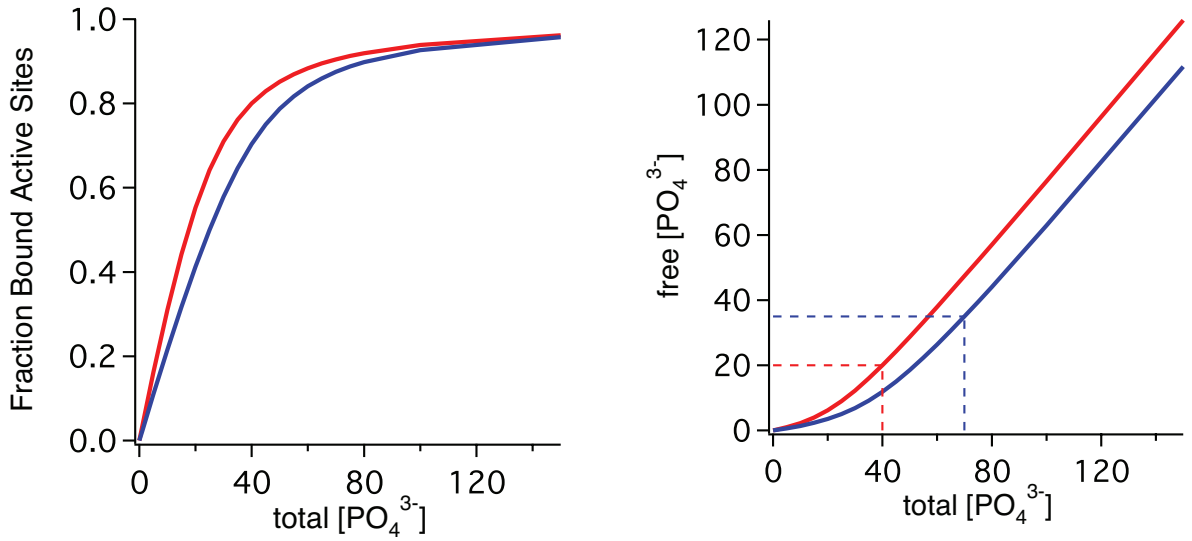

Figure 4.21 (A) Fraction of ligand-bound active sites as a function of total [PO_4^{3-}], given a K_d of 5 mM. (B) bound [PO_4^{3-}] as a function of total [PO_4^{3-}]. From simulations, the ratio of bound to free PO_4^{3-} for maximum relaxation effects is 1:1, which is obtained when the free [PO_4^{3-}] is half the total [PO_4^{3-}]. In both (A) and (B), red lines indicate a total active site concentration of 25 mM and blue lines are an active site concentration of 40 mM.

[active site]	20	25	30	35	40	45	50
Total [PO_4^{3-}]	30 mM	40 mM	50 mM	60 mM	70 mM	80 mM	90 mM

Table 4.6 Total [PO_4^{3-}] necessary to achieve 50% bound phosphate given particular active site concentrations.

The effect of precipitation, centrifugation, and rotor packing on the hydration of the protein pellet and the concentration of ligand in solution has not been characterized. Therefore to attain the desired concentrations as closely as possible, the protein was crystallized without any ligand,

and phosphate solution of the desired concentration was added to the protein once it was inside the rotor, and the final mass and volume of the pellet are better quantified. All parameters were carefully quantified to determine the TIM/PO_4^{3-} ratio as accurately as possible. The total number of active sites was determined by Bradford assay of the protein solution before crystallization to obtain a precise mass, as well as of the remaining supernatant after crystallization to estimate the amount of protein actually crystallized.

4.10.2 One Dimensional Spectra, CSA Measurements, and Data-Fitting

One-Dimensional Spectra One-dimensional ^{31}P spectra were collected on a Varian Chemagnetics 600 MHz spectrometer with a BioMAS probe. 30 mg TIM was packed into a 3.2 mm rotor. The sample was spun at 3000 ± 5 Hz and spectra were collected using a simple ^{31}P 90º pulse - detect with 90 kHz TPPM proton decoupling during acquisition at thermocouple temperatures of -40ºC, -20°C, and +20°C. 65,536 scans were collected at each temperature point. A spectrometer drift of 2.23 Hz/hour was accounted for in reported chemical shifts. Typical ^{31}P 90° pulse widths were 6.8 us. Fast spinning one-dimensional spectra were collected under the same conditions with a magic angle spinning speed of 22 kHz. To observe true linewidths, all spectra were processed with minimal 10 Hz exponential broadening.

CSA Data-Fitting Two different techniques were used in data-fitting to extract chemical shift tensor parameters from the slow MAS spectra. The sideband intensities were extracted after processing in MestReNova and scaled for fitting in Spinevolution. Only the intensities of the sidebands were used for fitting. The anisotropy and asymmetry parameters were fit using the

optimization function in Spinevolution. In this fitting routine, one atom was included in simulations. The central frequency was given a weighting of 0 in the data-fitting due to the overlap of the isotropic and anisotropic components that the simulation did not account for.

Examples of Spinevolution input files for data-fitting can be found in the Appendix, Section 8.3.

4.10.3 ^{31}P $R_{1\rho}$ Experiments

Spectra were collected on both a 600 MHz spectrometer with an E-free BioMAS probe and a 3.2 mm rotor and a 400 MHz spectrometer with a modified APEX probe and a 4 mm rotor. The pulse sequences used are shown in Figure 3.18; briefly this consisted of a ^{31}P 90° pulse, followed by a low power spin-lock on the phosphorous channel with or without simultaneous continuous wave proton decoupling. At 600 MHz, spinning speeds of 7 and 22 kHz were used. $R_{1\rho}$ data was collected at VT temperatures of -40°C, -30°C, -20°C, -10°C, +20°C, and +30°C (10° sample heating was added to account for MAS to approximate the true sample temperature). Some frictional heating due to magic angle spinning is expected but little to no RF heating. Typical ^{31}P 90° pulses were 6.7 μs. The spin-lock on the phosphorous channel was applied at fields of 5 – 33 kHz, depending on the spinning speed, to avoid the rotary resonance conditions. On-resonance spin-locks were applied for lengths of 100 μs, and 1-10 ms in 1.5-2 ms increments. Experiments were done both with and without 70 kHz continuous wave proton decoupling during the spin-lock. 90 kHz ^{1}H TPPM decoupling was used during acquisition.

At 400 MHz, spinning speeds of 10 and 14 kHz were used. Data was collected over a broad range of sample temperatures both with and without decoupling. Due to concerns over sample heating, most of this data is not presented.

$R_{1\rho}$ data analysis was performed as described for DMS in Chapter 3. No attempt has been made to extract quantitative exchange rates from the $R_{1\rho}$ data to date.

4.11 References

[1] M. Bieri, A.H. Kwan, M. Mobli, G.F. King, J.P. Mackay, P.R. Gooley, Macromolecular NMR spectroscopy for the non-spectroscopist: beyond macromolecular solution structure determination, Febs J, 278 (2011) 704-715.

[2] S.B. Shuker, P.J. Hajduk, R.P. Meadows, S.W. Fesik, Discovering high-affinity ligands for proteins: SAR by NMR, Science, 274 (1996) 1531-1534.

[3] A.T. Namanja, X.D.J. Wang, B.L. Xu, A.Y. Mercedes-Camacho, B.D. Wilson, K.A. Wilson, F.A. Etzkorn, J.W. Peng, Toward Flexibility-Activity Relationships by NMR Spectroscopy: Dynamics of Pin1 Ligands, J Am Chem Soc, 132 (2010) 5607-+.

[4] B. Meyer, T. Peters, NMR Spectroscopy techniques for screening and identifying ligand binding to protein receptors, Angew Chem Int Edit, 42 (2003) 864-890.

[5] S.B. Feng, J.K. Chen, H.T. Yu, J.A. Simon, S.L. Schreiber, 2 Binding Orientations for Peptides to the Src Sh3 Domain - Development of a General-Model for Sh3-Ligand Interactions, Science, 266 (1994) 1241-1247.

[6] D.G. Donne, J.H. Viles, D. Groth, I. Mehlhorn, T.L. James, F.E. Cohen, S.B. Prusiner, P.E. Wright, H.J. Dyson, Structure of the recombinant full-length hamster prion protein PrP(29-231): The N terminus is highly flexible, P Natl Acad Sci USA, 94 (1997) 13452-13457.

[7] L.E. Kay, D.A. Torchia, A. Bax, Backbone Dynamics of Proteins as Studied by N-15 Inverse Detected Heteronuclear Nmr-Spectroscopy - Application to Staphylococcal Nuclease, Biochemistry-Us, 28 (1989) 8972-8979.

[8] A. Kumar, G. Wagner, R.R. Ernst, K. Wuthrich, Buildup Rates of the Nuclear Overhauser Effect Measured by Two-Dimensional Proton Magnetic-Resonance Spectroscopy - Implications for Studies of Protein Conformation, J Am Chem Soc, 103 (1981) 3654-3658.

[9] A.M. Mandel, M. Akke, A.G. Palmer, Backbone Dynamics of Escherichia-Coli Ribonuclease Hi - Correlations with Structure and Function in an Active Enzyme, J Mol Biol, 246 (1995) 144-163.

[10] A.G. Palmer, M. Rance, P.E. Wright, Intramolecular Motions of a Zinc Finger DNA-Binding Domain from Xfin Characterized by Proton-Detected Natural Abundance C-12 Heteronuclear Nmr-Spectroscopy, J Am Chem Soc, 113 (1991) 4371-4380.

[11] R. Riek, S. Hornemann, G. Wider, R. Glockshuber, K. Wuthrich, NMR characterization of the full-length recombinant murine prion protein, mPrP(23-231), Febs Lett, 413 (1997) 282-288.

[12] A.A. Bothnerby, R.L. Stephens, J.M. Lee, C.D. Warren, R.W. Jeanloz, Structure Determination of a Tetrasaccharide - Transient Nuclear Overhauser Effects in the Rotating Frame, J Am Chem Soc, 106 (1984) 811-813.

[13] F.A.L. Anet, A.J.R. Bourn, Nuclear Magnetic Resonance Spectral Assignments from Nuclear Overhauser Effects, J Am Chem Soc, 87 (1965) 5250-&.

[14] W. Hohlweg, S. Kosol, K. Zangger, Determining the Orientation and Localization of Membrane-Bound Peptides, Curr Protein Pept Sc, 13 (2012) 267-279.

[15] S.P. Babailov, NMR studies of photo-induced chemical exchange, Prog Nucl Mag Res Sp, 54 (2009) 183-194.

[16] M.P. Williamson, Applications of the NOE in Molecular Biology, Annual Reports on Nmr Spectroscopy, Vol 65, 65 (2009) 77-109.

[17] T. Brand, E.J. Cabrita, S. Berger, Intermolecular interaction as investigated by NOE and diffusion studies, Prog Nucl Mag Res Sp, 46 (2005) 159-196.

[18] G.M. Lippens, C. Cerf, K. Hallenga, Theory and Experimental Results of Transfer-Noe Experiments .1. The Influence of the Off Rate Versus Cross-Relaxation Rates, J Magn Reson, 99 (1992) 268-281.

[19] H.P. Mo, T.C. Pochapsky, Intermolecular interactions characterized by nuclear Overhauser effects, Prog Nucl Mag Res Sp, 30 (1997) 1-38.

[20] B. Halle, V.P. Denisov, Magnetic relaxation dispersion studies of biomolecular solutions, Method Enzymol, 338 (2001) 178-201.

[21] E. Persson, B. Halle, Nanosecond to microsecond protein dynamics probed by magnetic relaxation dispersion of buried water molecules, J Am Chem Soc, 130 (2008) 1774-1787.

[22] S. Luca, H. Heise, A. Lange, M. Baldus, Investigation of ligand-receptor systems by high-resolution solid-state NMR: Recent progress and perspectives, Arch Pharm, 338 (2005) 217-228.

[23] P.T.F. Williamson, J.A. Watts, G.H. Addona, K.W. Miller, A. Watts, Dynamics and orientation of N+(CD3)(3)-bromoacetylcholine bound to its binding site on the nicotinic acetylcholine receptor, P Natl Acad Sci USA, 98 (2001) 2346-2351.

[24] A.V. Struts, G.F.J. Salgado, K. Martnez-Mayorga, M.F. Brown, Retinal dynamics underlie its switch from inverse agonist to agonist during rhodopsin activation, Nat Struct Mol Biol, 18 (2011) 392-394.

[25] S. Luca, J.F. White, A.K. Sohal, D.V. Filippov, J.H. van Boom, R. Grisshammer, M. Baldus, The conformation of neurotensin bound to its G protein-coupled receptor, P Natl Acad Sci USA, 100 (2003) 10706-10711.

[26] G.J. Gallagher, M. Hong, L.K. Thompson, Solid-state NMR spin diffusion for measurement of membrane-bound peptide structure: Gramicidin A, Biochemistry-Us, 43 (2004) 7899-7906.

[27] K.K. Kumashiro, K. Schmidt-Rohr, O.J. Murphy, K.L. Ouellette, W.A. Cramer, L.K. Thompson, A novel tool for probing membrane protein structure: Solid-state NMR with proton spin diffusion and X-nucleus detection, J Am Chem Soc, 120 (1998) 5043-5051.

[28] A. Bockmann, C. Gardiennet, R. Verel, A. Hunkeler, A. Loquet, G. Pintacuda, L. Emsley, B.H. Meier, A. Lesage, Characterization of different water pools in solid-state NMR protein samples, J Biomol Nmr, 45 (2009) 319-327.

[29] M. Hong, Y.C. Su, Structure and dynamics of cationic membrane peptides and proteins: Insights from solid-state NMR, Protein Sci, 20 (2011) 641-655.

[30] A.G. Krushelnitsky, G. Hempel, D. Reichert, Simultaneous processing of solid-state NMR relaxation and 1D-MAS exchange data: the backbone dynamics of free vs. binase-bound barstar, Bba-Proteins Proteom, 1650 (2003) 117-127.

[31] S. Un, M.P. Klein, Study of P-31 Nmr Chemical-Shift Tensors and Their Correlation to Molecular-Structure, J Am Chem Soc, 111 (1989) 5119-5124.

[32] P. Hartmann, J. Vogel, B. Schnabel, The Influence of Short-Range Geometry on the P-31 Chemical-Shift Tensor in Protonated Phosphates, J Magn Reson Ser A, 111 (1994) 110-114.

[33] G.L. Turner, K.A. Smith, R.J. Kirkpatrick, E. Oldfield, Structure and Cation Effects on P-31 Nmr Chemical-Shifts and Chemical-Shift Anisotropies of Ortho-Phosphates, J Magn Reson, 70 (1986) 408-415.

[34] Y. Zhang, E. Oldfield, Solid-state P-31 NMR chemical shielding tensors in phosphonates and bisphosphonates: A quantum chemical investigation, J Phys Chem B, 108 (2004) 19533-19540.

[35] J. Herzfeld, R.G. Griffin, R.A. Haberkorn, P-31 Chemical-Shift Tensors in Barium Diethyl Phosphate and Urea-Phosphoric Acid - Model Compounds for Phospholipid Head-Group Studies, Biochemistry-Us, 17 (1978) 2711-2718.

[36] A. Iuga, C. Ader, C. Groger, E. Brunner, Applications of solid-state P-31 NMR spectroscopy, Annu Rep Nmr Spectro, 60 (2007) 145-189.

[37] S. Harada, G.A. Rodan, Control of osteoblast function and regulation of bone mass, Nature, 423 (2003) 349-355.

[38] H. Jomaa, J. Wiesner, S. Sanderbrand, B. Altincicek, C. Weidemeyer, M. Hintz, I. Turbachova, M. Eberl, J. Zeidler, H.K. Lichtenthaler, D. Soldati, E. Beck, Inhibitors of the nonmevalonate pathway of isoprenoid biosynthesis as antimalarial drugs, Science, 285 (1999) 1573-1576.

[39] M. Wilhelm, V. Kunzmann, S. Eckstein, P. Reimer, F. Weissinger, T. Ruediger, H.P. Tony, gamma delta T cells for immune therapy of patients with lymphoid malignancies, Blood, 102 (2003) 200-206.

[40] B. Bechinger, Detergent-like properties of magainin antibiotic peptides: A P-31 solid-state NMR spectroscopy study, Bba-Biomembranes, 1712 (2005) 101-108.

[41] A. Iuga, M. Spoerner, H.R. Kalbitzer, E. Brunner, Solid-state P-31 NMR spectroscopy of microcrystals of the Ras protein and its effector loop mutants: Comparison between crystalline and solution state, J Mol Biol, 342 (2004) 1033-1040.

[42] S. Rozovsky, G. Jogl, L. Tong, A.E. McDermott, Solution-state NMR investigations of triosephosphate isomerase active site loop motion: Ligand release in relation to active site loop dynamics, J Mol Biol, 310 (2001) 271-280.

[43] Y. Xu, Solid State NMR Approach to Conformational Change and Chemical Exchange of Triosephosphate Isomerase, in: Department of Chemistry, Columbia University, New York, 2009.

[44] I.D. Campbell, R.B. Jones, P.A. Kiener, S.G. Waley, Enzyme-Substrate and Enzyme-Inhibitor Complexes of Triose Phosphate Isomerase Studied by P-31 Nuclear Magnetic-Resonance, Biochem J, 179 (1979) 607-621.

[45] R. Desamero, S. Rozovsky, N. Zhadin, A. McDermott, R. Callender, Active site loop motion in triosephosphate isomerase: T-jump relaxation spectroscopy of thermal activation, Biochemistry-Us, 42 (2003) 2941-2951.

[46] H. Saito, I. Ando, A. Ramamoorthy, Chemical shift tensor - The heart of NMR: Insights into biological aspects of proteins, Prog Nucl Mag Res Sp, 57 (2010) 181-228.

[47] M.M. Maricq, J.S. Waugh, Nmr in Rotating Solids, J Chem Phys, 70 (1979) 3300-3316.

[48] J. Herzfeld, A.E. Berger, Sideband Intensities in Nmr-Spectra of Samples Spinning at the Magic Angle, J Chem Phys, 73 (1980) 6021-6030.

[49] A.B. Siemer, K.Y. Huang, A.E. McDermott, Protein Linewidth and Solvent Dynamics in Frozen Solution NMR, Plos One, 7 (2012).

[50] W. Doster, The protein-solvent glass transition, Bba-Proteins Proteom, 1804 (2010) 3-14.

[51] K. Tompa, P. Banki, M. Bokor, P. Kamasa, L. Gyorgy, P. Tompa, Interfacial Water at Protein Surfaces: Wide-Line NMR and DSC Characterization of Hydration in Ubiquitin Solutions, Biophys J, 96 (2009) 2789-2798.

[52] C. Gardiennet-Doucet, B. Henry, P. Tekely, Probing the ionisation state of functional groups by chemical shift tensor fingerprints, Prog Nucl Mag Res Sp, 49 (2006) 129-149.

[53] C.L.M.J. Verlinde, M.E.M. Noble, K.H. Kalk, H. Groendijk, R.K. Wierenga, W.G.J. Hol, Anion Binding at the Active-Site of Trypanosomal Triosephosphate Isomerase - Monohydrogen Phosphate Does Not Mimic Sulfate, Eur J Biochem, 198 (1991) 53-57.

[54] M. Veshtort, R.G. Griffin, SPINEVOLUTION: A powerful tool for the simulation of solid and liquid state NMR experiments, J Magn Reson, 178 (2006) 248-282.

[55] U. Haeberlen, High resolution NMR in solids : selective averaging, Academic Press, New York, 1976.

[56] J.P. Richard, A Paradigm for Enzyme-Catalyzed Proton Transfer at Carbon: Triosephosphate Isomerase, Biochemistry-Us, 51 (2012) 2652-2661.

[57] D.L. Pompliano, A. Peyman, J.R. Knowles, Stabilization of a Reaction Intermediate as a Catalytic Device - Definition of the Functional-Role of the Flexible Loop in Triosephosphate Isomerase, Biochemistry-Us, 29 (1990) 3186-3194.

[58] V. Guallar, M. Jacobson, A. McDermott, R.A. Friesner, Computational modeling of the catalytic reaction in triosephosphate isomerase, J Mol Biol, 337 (2004) 227-239.

[59] G. Jogl, S. Rozovsky, A.E. McDermott, L. Tong, Optimal alignment for enzymatic proton transfer: Structure of the Michaelis complex of triosephosphate isomerase at 1.2-angstrom resolution, P Natl Acad Sci USA, 100 (2003) 50-55.

[60] E. Lolis, G.A. Petsko, Crystallographic Analysis of the Complex between Triosephosphate Isomerase and 2-Phosphoglycolate at 2.5-a Resolution - Implications for Catalysis, Biochemistry-Us, 29 (1990) 6619-6625.

[61] J.P. Richard, Acid-Base Catalysis of the Elimination and Isomerization-Reactions of Triose Phosphates, J Am Chem Soc, 106 (1984) 4926-4936.

[62] C. Gardiennet, B. Henry, P. Kuad, B. Spiess, P. Tekely, Straightforward detection of the secondary ionisation of the phosphate group and pK determinations by high-resolution solid-state P-31 NMR, Chem Commun, (2005) 180-182.

[63] J. Gajda, S. Olejniczak, I. Bryndal, M.J. Potrzebowski, Elucidation of Structural Restraints for Phosphate Residues with Different Hydrogen Bonding and Ionization States, J Phys Chem B, 112 (2008) 14036-14044.

[64] C. Gardiennet-Doucet, X. Assfeld, B. Henry, P. Tekely, Revealing successive steps of deprotonation of L- phosphoserine through C-13 and P-31 chemical shielding tensor fingerprints, J Phys Chem A, 110 (2006) 9137-9144.

[65] S. Rozovsky, A.E. McDermott, Substrate product equilibrium on a reversible enzyme, triosephosphate isomerase, P Natl Acad Sci USA, 104 (2007) 2080-2085.

[66] C.H. Chu, Y.J. Lai, H.M. Huang, Y.J. Sun, Kinetic and structural properties of triosephosphate isomerase from Helicobacter pylori, Proteins-Structure Function and Bioinformatics, 71 (2008) 396-406.

[67] W.J. Albery, J.R. Knowles, Free-Energy Profile for Reaction Catalyzed by Triosephosphate Isomerase, Biochemistry-Us, 15 (1976) 5627-5631.

[68] S. Rozovsky, A.E. McDermott, The time scale of the catalytic loop motion in triosephosphate isomerase, J Mol Biol, 310 (2001) 259-270.

[69] H. Walden, G.L. Taylor, E. Lorentzen, E. Pohl, H. Lilie, A. Schramm, T. Knura, K. Stubbe, B. Tjaden, R. Hensel, Structure and function of a regulated archaeal triosephosphate isomerase adapted to high temperature, J Mol Biol, 342 (2004) 861-875.

[70] A.B. Siemer, K.Y. Huang, A.E. McDermott, Protein-ice interaction of an antifreeze protein observed with solid-state NMR, P Natl Acad Sci USA, 107 (2010) 17580-17585.

[71] A.B. Siemer, A.E. McDermott, Solid-State NMR on a Type III Antifreeze Protein in the Presence of Ice, J Am Chem Soc, 130 (2008) 17394-17399.

[72] M. Tollinger, A.C. Sivertsen, B.H. Meier, M. Ernst, P. Schanda, Site-Resolved Measurement of Microsecond-to-Millisecond Conformational-Exchange Processes in Proteins by Solid-State NMR Spectroscopy, J Am Chem Soc, 134 (2012) 14800-14807.

[73] O. Roche, M.J. Field, Simulations of the T <-> R conformational transition in aspartate transcarbamylase, Protein Eng, 12 (1999) 285-295.

[74] J. Hofrichter, E.R. Henry, A. Szabo, L.P. Murray, A. Ansari, C.M. Jones, M. Coletta, G. Falcioni, M. Brunori, W.A. Eaton, Dynamics of the Quaternary Conformational Change in Trout Hemoglobin, Biochemistry-Us, 30 (1991) 6583-6598.

[75] N. Tjandra, A. Szabo, A. Bax, Protein backbone dynamics and N-15 chemical shift anisotropy from quantitative measurement of relaxation interference effects, J Am Chem Soc, 118 (1996) 6986-6991.

[76] B.J. Wylie, L.J. Sperling, H.L. Frericks, G.J. Shah, W.T. Franks, C.M. Rienstra, Chemical-shift anisotropy measurements of amide and carbonyl resonances in a microcrystalline protein with slow magic-angle spinning NMR spectroscopy, J Am Chem Soc, 129 (2007) 5318-+.

[77] R.B. Jones, S.G. Waley, Spectrophotometric Studies on the Interaction between Triose Phosphate Isomerase and Inhibitors, Biochem J, 179 (1979) 623-630.

Chapter 5

$R_{1\rho}$ Studies of Loop Dynamics in Triosephosphate Isomerase

In addition to the dynamics of the ligand, it is of interest to study the dynamics of a protein itself. Correlation between the dynamics of the loop and ligand can provide insight into the catalytic mechanism, and particularly its rate-limiting steps. Detection and dynamics studies of the catalytic residues can be invaluable in achieving this goal. Assignment of these previously unassigned residues may be accomplished through selective labeling and low temperature measurements. In the protein triosephosphate isomerase, it has been shown that the exchange of the ligand in and out of the active site is on the same timescale as loop opening (with G3P) [1], suggesting that loop opening or ligand release is the rate-limiting step. $R_{1\rho}$ measurements of valine 167 in TIM have been done with solution NMR and agree with other dynamics measurements that the loop undergoes dynamics on the millisecond timescale [2]. In addition to the insight that can be gained into ligand binding, we are interested in utilizing solid state $R_{1\rho}$ measurements for loop 6 in TIM as a model biological system for quantifying exchange rates.

5.1 Introduction

As discussed in previous chapters, understanding the dynamics of a protein can greatly contribute to understanding its biological function. Nuclear magnetic resonance (NMR) is one of many biophysical techniques used to observe protein dynamics [3-5]. Relative to other biophysical methods, nuclear magnetic resonance possesses both advantages and disadvantages. NMR techniques can monitor dynamics over a broad range of timescales, from picoseconds to seconds [5]. However, intermediate timescale processes can sometimes be difficult to detect due to exchange broadening. When the difference in the isotropic chemical shift between the two

exchanging sites is on the same timescale as the exchange rate (~10^3 to 10^5 s^{-1}), the resonance can be broadened into the baseline and therefore not visible in an NMR spectrum [6].

NMR is one of the few techniques that can monitor dynamics site specifically over numerous sites of a protein simultaneously. A complementary challenge is obtaining the resolution necessary to study the sites of interest; lack of spectral resolution also puts a limit on the size of proteins that can be studied [7]. Alternative isotopic labeling schemes have been developed to improve this issue. Within the field of NMR, both solution and solid state techniques are available for the study of protein dynamics. While greater resolution is generally attained in solution, solid state NMR can achieve a greater range of temperatures, with fewer limitations on protein size and system type (i.e. membrane proteins or amyloids) [8, 9]. The combination of labeling schemes for high resolution, the ability to limit spin diffusion, as well as a wide range of accessible temperatures and observable dynamic timescales make solid state NMR an increasingly powerful technique for the study of protein dynamics.

Many methods to study dynamics via solid state nuclear magnetic resonance utilize the reorientation of a dipole vector to observe chemical exchange, among them rotating frame ($R_{1\rho}$) relaxation [10, 11]. However, there are advantages to utilizing the chemical shift anisotropy (CSA), and in certain situations may be necessary [12, 13]. The two interactions can also be complementary in dynamics studies. As discussed in Chapter 3, monitoring reorientation of a chemical shift tensor with $R_{1\rho}$ measurements allows the quantification of exchange processes [12]. The chemical shift anisotropy is very sensitive to the local chemical environment and orientation of the chemical shift tensor and hence is a superior probe of changes in that

environment due to dynamics. When dynamics are present in a system, the local environment can change due to various factors, including hydrogen bonding, secondary structure, and the presence of ligands [14, 15].

The coordination between ligand binding and loop dynamics is of great interest in the enzyme triosephosphate isomerase [16, 17]. A particular site of interest is the catalytic carbonyl of glutamic acid 165. NMR assignments of TIM have been reported in both the solid state and solution [18, 19]. None of this work has been able to detect the catalytic carbonyl carbon resonance. It may be that the site cannot be resolved due to overlap with other resonances or that the absence of this peak is due to intermediate exchange. Crystal structures show Glu 165 moves ~ 2 Å upon ligand binding [20, 21]. Other residues in the region of Glu 165 have been reported to undergo intermediate timescale dynamics [22, 23]. Furthermore, assignment and study of the terminal carbonyl of Glu 97 may provide insight into the disputed catalytic mechanism in this protein [24]. These important carbonyls have no attached protons. For dynamics studies of sites like these, using $R_{1\rho}$ relaxation due to reorientation of the carbonyl CSA tensor may allow the study of an intermediate timescale process that other methods cannot capture. Furthermore, in solution NMR, rotating frame relaxation studies of TIM loop 6 only captured an exchange contribution to relaxation for hinge residues (Val167 and T177 in chicken TIM) [23], despite the fact that the loop residues undergo a large conformational change ~ 7 Å upon ligand binding [20, 21]. This is believed to be due to the absence of a change in isotropic chemical shift for residues in the middle of the loop. To complement studies of ligand binding in triosephosphate isomerase, we have pursued studies of loop dynamics via rotating frame relaxation. Furthmore, given the previous characterization of the loop motion with other techniques [17, 22], TIM is an

excellent model protein for preliminary application of quantitative $R_{1\rho}$ studies to biological systems.

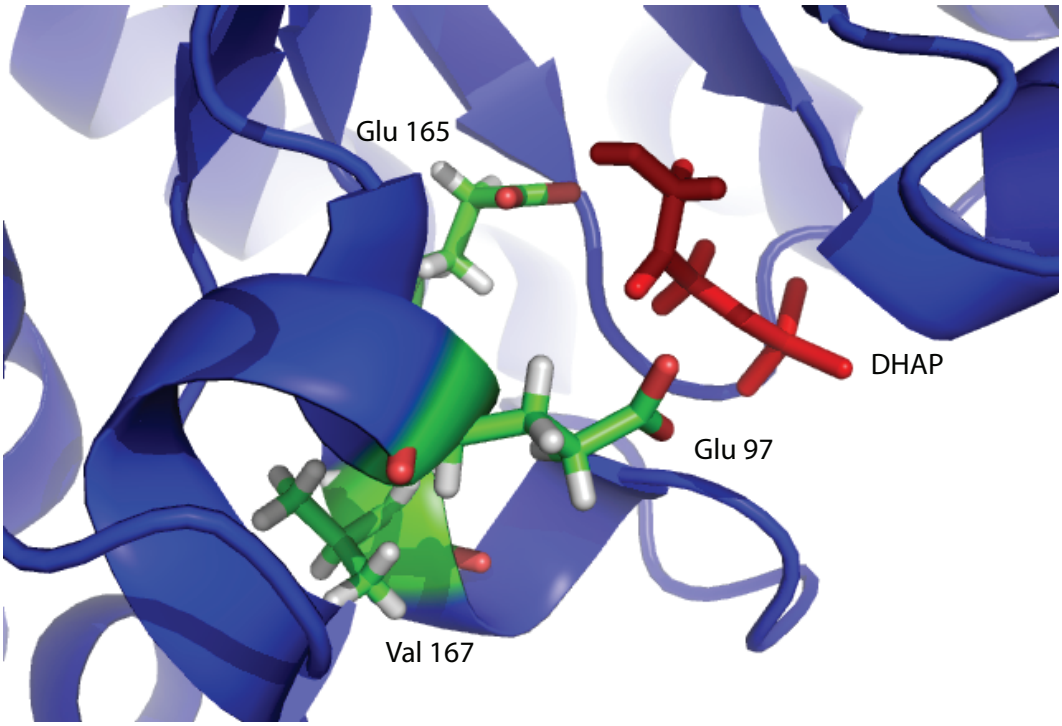

Figure 5.1 DHAP-bound TIM. The key catalytic residue, Glu 165 is believed to be dynamic and the catalytic carbonyl responsible for proton transfer possesses no protons attached to the site of interest. Glu 97 also has no attached protons and its role in the catalytic mechanism is disputed. Valine 167 is a dynamic hinge residue. DHAP is colored red while the protein residues of interest are highlighted in green. (PDB ID:1NEY)

While many previous solid state studies of loop dynamics in TIM, have focused on Trp 168 [22], in solution NMR, marker peaks used include Val 167, particularly for $R_{1\rho}$ studies [23]. This residue is in the hinge of loop 6 and undergoes intermediate timescale dynamics. Due to its presence in the hinge, Val 167 also has an isotropic chemical shift change between the open and closed states of the protein. The reorientation of the chemical shift tensor for this residue during ligand binding makes it an excellent marker peak to observe loop dynamics.

In hopes of detecting and assigning these residues of interest, several experimental approaches were utilized. These include (1) sparse labeling schemes to reduce spectral crowding, (2) deuteration to narrow linewidths and reduce spin diffusion, (3) direct excitation as the method of polarization, (4) very low temperatures, (5) attention to carrier location to detect specific resonances. Preliminary $R_{1\rho}$ studies were done to assess the feasibility of the technique.

5.2 Toward Detection of Dynamic Residues and Assignment of TIM with Selective Labeling Schemes

In the solid state, *S. cerevisae* TIM has been approximately 70% assigned [18]. Selective isotopic labeling schemes have been developed which can significantly reduce spectral crowding. One of the key advantages of these sparser labeling schemes relative to uniform carbon labeling is the ability to study larger systems. Labeling schemes that are used in nuclear magnetic resonance include 'spectral simplification' with labeled lactate, combinations of labeled and unlabeled glucose for labeling of Val and Leu sidechains (statistical labeling), broadly used methyl group labeling, and alternate site labeling, of particular interest here [25]. These labeling schemes are produced from the biochemical pathways that synthesize particular amino acids.

Alternate site labeling has been described by LeMaster and Kushlan and Higman et al [26, 27]. The method utilizes [1,3-^{13}C] or [2-^{13}C] glycerol to improve spectral resolution. In general, [1,3-^{13}C] glycerol will label backbone carbonyl carbons and C_β. Growth with [2-^{13}C] glycerol gives much more C_α labeling, but the specific labeling scheme is unique for each amino acid. In addition to the decreased spectral crowding relative to uniform carbon labeling, this method has

an additional advantage in that the general elimination of neighboring labeled carbons leads to a greatly attenuated dipolar coupling and reduced interference due to carbon-carbon spin diffusion. This is of particular importance in studies of protein dynamics, particularly for spin relaxation techniques. A further consideration for both spectral resolution and the elimination of undesired spin diffusion is the presence of protons. As discussed in Chapter 3, C-H dipolar spin diffusion can lead to difficulty monitoring relaxation processes of interest. Perdeuteration of proteins is becoming an increasingly common practice in solid state NMR, particularly for studies of protein dynamics [28]. Deuteration of proteins can lead to significantly narrower linewidths as well.

To study the dynamics of sites of interest in TIM via spin relaxation, as well as to make progress toward assigning resonances that may be in crowded regions of the spectrum, selective carbon labeling with 1,3- and 2-glycerol and perdeuteration (of the 1,3-glycerol sample) were employed and series of carbon-carbon and carbon-nitrogen correlation spectra were collected.

Uniform Labeling vs Extensive Labeling Figure 5.2 shows the comparison between 2D DARR spectra of uniform ^{13}C, ^{15}N TIM (green) and ^{2}H, [1,3-glycerol] ^{13}C, ^{15}N TIM (blue) and illustrates the success of the ^{2}H, [1,3-glycerol] ^{13}C labeling scheme. Expression of protein with [1,3-glycerol] ^{13}C or ^{2}H labels is more difficult than expression with traditional uniform labeling, but we were able to incorporate both these labeling schemes into a single sample while still achieving moderately high yields. The protocol for protein expression using this labeling scheme as well as for other selective labeling schemes described below is given in Chapter 6.

Given that the 1,3-glycerol spectrum is deuterated and was collected using direct excitation, the signal-to-noise is predictably lower than a uniformly labeled sample. The success of the [1,3-^{13}C] glycerol incorporation is confirmed by the appearance of particular spin systems in the sparsely labeled sample, while other correlations are absent. The 1,3-glycerol labeling scheme preferentially labels C_β and CO for most amino acids. Resonances that are absent in the 1,3-glycerol sample include many C_α-C_β correlations, while C_β to sidechain correlations are present. Some groups of unique resonances, particularly in the range of 55 to 65 ppm in both dimensions may arise from inter-residue C_α-C_α correlations. The appearance of these resonances could be due to the longer mixing times used in acquisition of the sparsely labeled protein spectra (25 ms for U-TIM vs 200 ms for [1,3-glycerol] TIM). In addition to sparser labeling and deuteration, improved resolution may be due to the use of direct excitation (made necessary in the 1,3-glycerol sample by deuteration). Direct excitation can polarize residues that may not be efficiently polarized with cross polarization due to dynamics.

There is evidence suggestive of scrambling however. There appear to be alanine C_α-C_β and valine C_β-C_γ cross peaks, neither of which should arise in the expected 1,3-glycerol labeled spectrum. But the absence of overlap of these resonances with other amino acids labeled with this scheme decreases the significance of this scrambling.

Figure 5.3 highlights some of the resonances that can be resolved in a 1.3-glycerol spectrum due to the combination of sparser labeling and deuteration, which reduce spin diffusion, and are assigned to their likely spin systems given the expected carbon labeling. In dark blue is the data as processed for high signal-to-noise shown in Figure 5.2. Overlayed in lighter blue is the same

data set, processed to achieve greater resolution, which leads to a loss in signal-to-noice. Analyzing the data with high resolution and high signal-to-noise processing in tandem is useful to determine peaks that are both well resolved and above the noise level.

Extensive vs Selective Labeling As mentioned above, protein expression with [1,3-^{13}C] glycerol and [2-^{13}C] glycerol are expected to have different carbon labeling patterns. This is readily apparent in Figure 5.4, which shows an overlay of spectra from the protein with the two different labeling schemes ([2-^{13}C] glycerol in magenta, [1,3-^{13}C] glycerol in blue). The spectrum of the [2-^{13}C] glycerol sample has significantly fewer cross peaks overall. The resonances and spin systems that appear in the two different spectra are by and large unique. There is overlap between the 2 spectra for spin systems that are expected to appear in both labeling schemes, such as Lys C_α-C_γ and -C_δ cross peaks. Along with nitrogen-carbon correlation spectra, the two labeling schemes can complement each other for sequential assignment of proteins. The spin systems that are expected to arise in the [2-^{13}C] glycerol sample are labeled in Figure 5.5, which compares cross polarization with direct excitation as the method of polarization.

The two spectra have notably different linewidths. There are multiple possible explanations. The 1,3-glycerol labeled TIM sample was also perdeuterated. The resulting reduction in carbon-deuterium dipolar coupling relative to protons leads to a reduction in linewidth. However, comparing the 2-glycerol sample to previously collected uniform ^{13}C, ^{15}N but protonated shows that the 2-glycerol spectrum still has broader lines. This suggests additional factors, such as

sample inhomogeneity. Despite the broad linewidths of the 2-glycerol sample, many individual resonances were still resolved and are discussed in the following section.

As compared to uniformly labeled TIM, the fewer number of resonances and improved resolution attained with sparser labeling schemes may allow further assignment of this large protein, as well as dynamics studies with reduced spin diffusion.

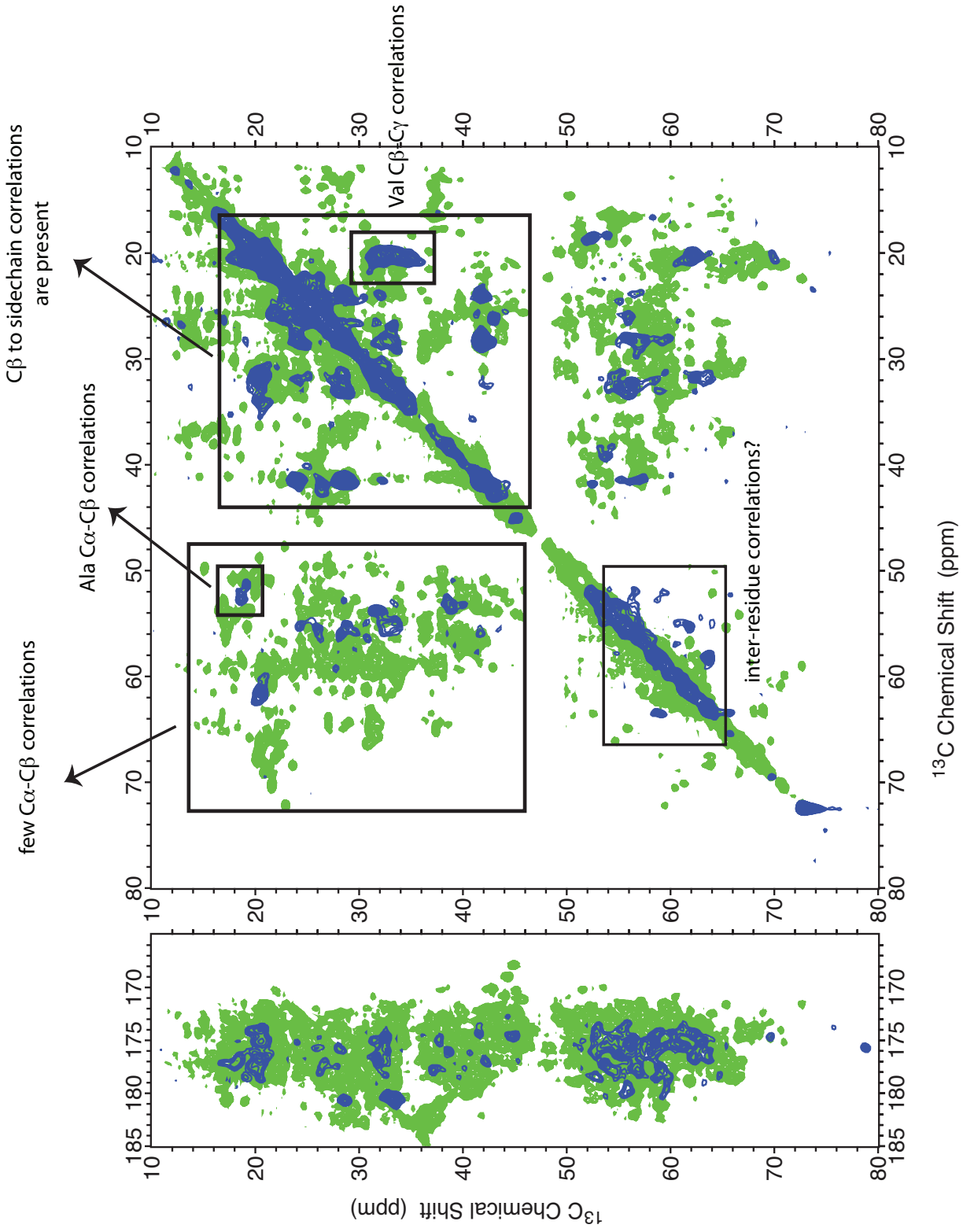

Figure 5.2 2D DARR spectra comparing U-^{13}C, ^{15}N TIM (green) with ^{2}H, [1,3-^{13}C] glycerol, ^{15}N TIM (blue). The differences between the spectra indicate the success of this selective labeling scheme. Both spectra were collected at 750 MHz. Mixing time: U-TIM, 25 ms; 1,3-gly TIM, 200 ms. MAS: U-TIM, 14 kHz; 1,3-gly TIM, 12 kHz. Temperature: U-TIM, 263 K; 1,3-gly TIM, 248 K.

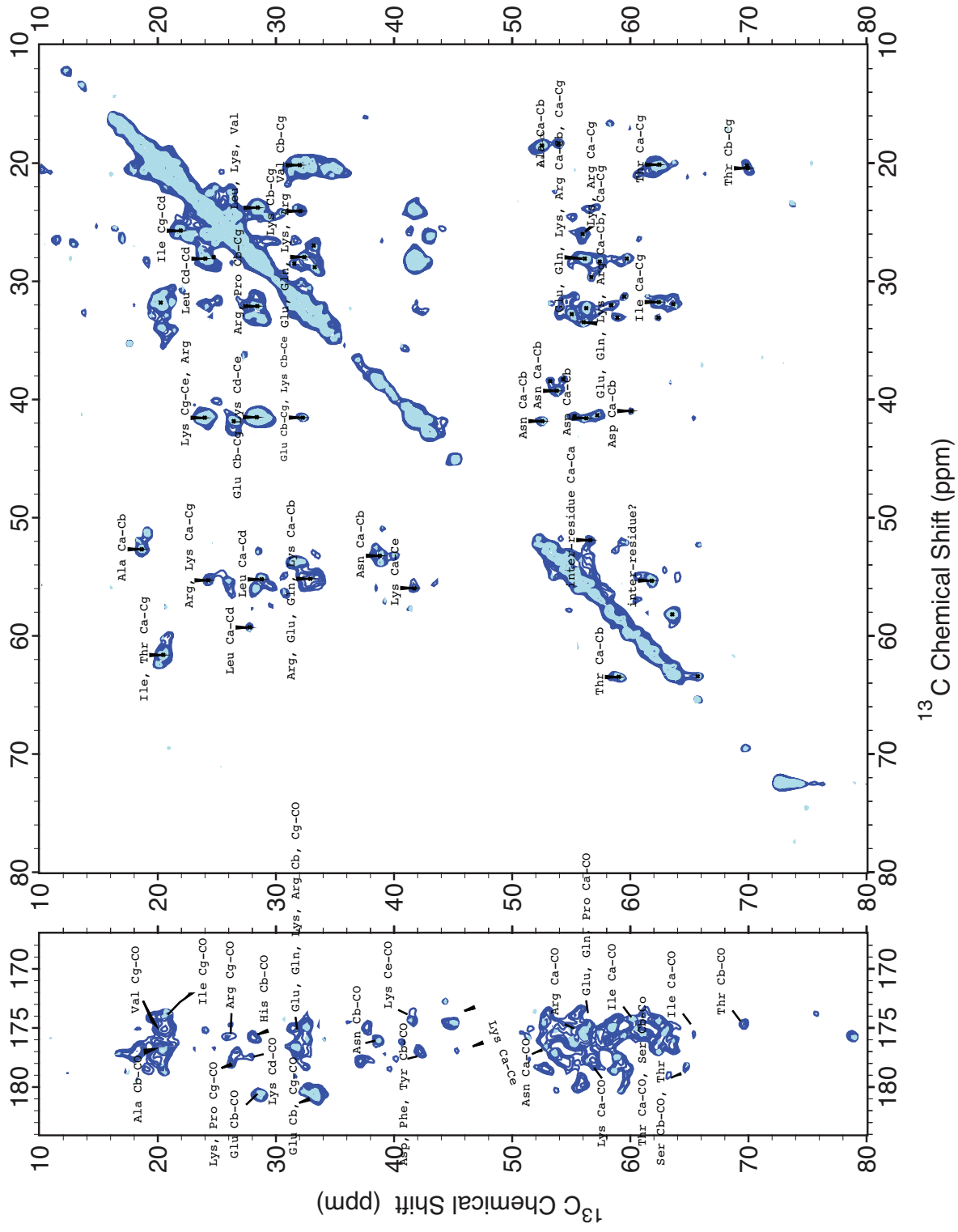

Figure 5.3 2D DARR spectrum of ^{2}H, [1,3-^{13}C] glycerol, ^{15}N TIM processed two different ways to achieve high signal-to-noise (darker blue) and high resolution (lighter blue). Several expected spin systems for this labeling scheme are labeled.

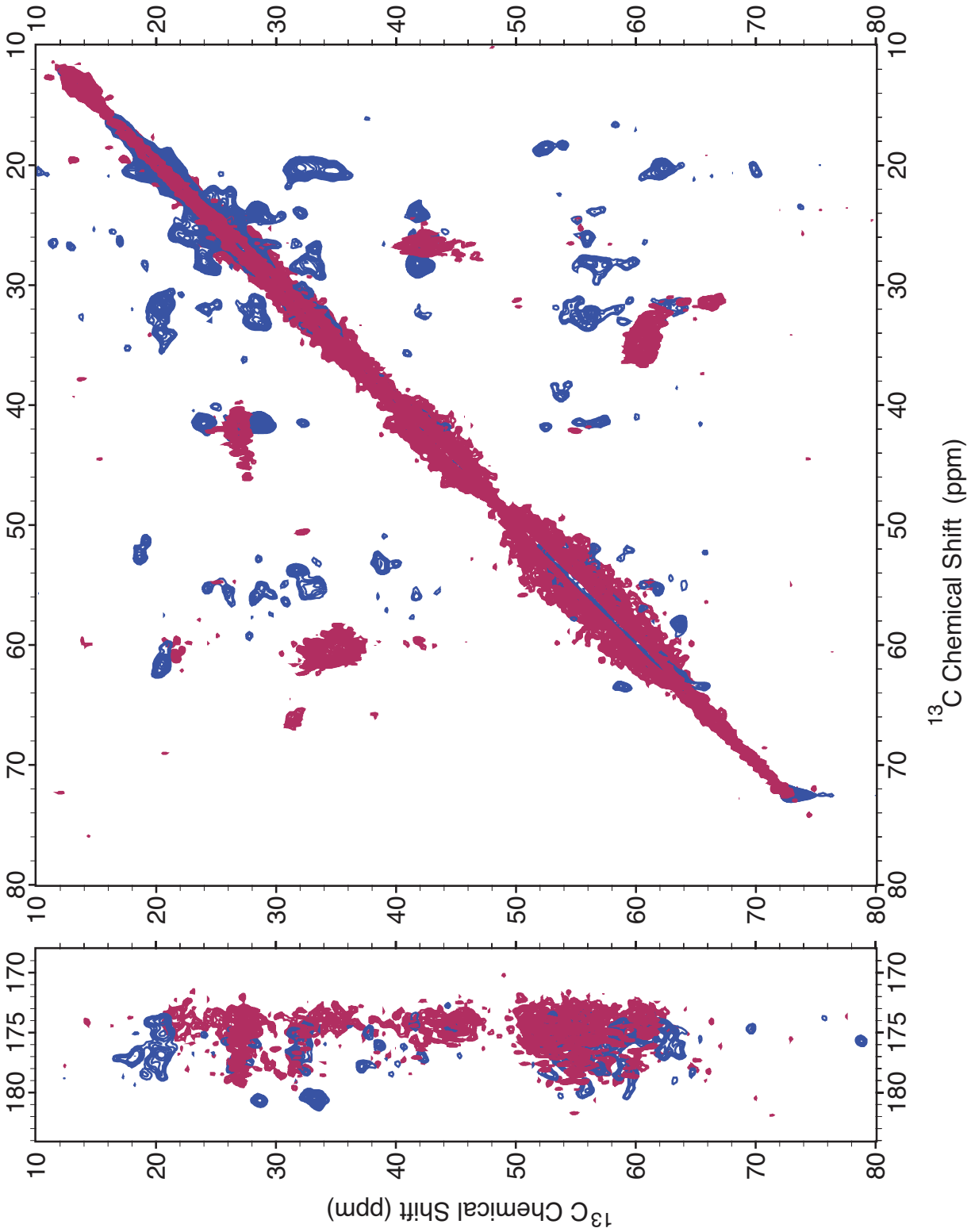

Figure 5.4 Overlay of ^{2}H, [1,3-^{13}C] glycerol, ^{15}N TIM (blue) and [2-^{13}C] glycerol, ^{15}N TIM (magenta), both collected with direct excitation. Different resonances occur in the two spectra due to the different labeling schemes.

Cross Polarization vs Direct Excitation For relaxation studies, the method and efficiency are important considerations. As mentioned in discussion of 1,3-glycerol labeled TIM, cross polarization and direct excitation can select for different resonances in a sample. Direct excitation can polarize residues that CP does not polarize efficiently due to dynamics. Furthermore, we showed that in relaxation studies, direct excitation is optimal for accurate measurements of relaxation rates. Figure 5.5 compares spectra of [2-glycerol] ^{13}C, ^{15}N TIM collected with cross polarization (purple) and direct excitation (pink). As expected from the polarization enhancement gained with CP, this spectrum has higher signal to noise and many more resonances appear. However, some distinct resonances are seen from using direct excitation. Certain resonances are well polarized while the bulk is not, leading to better resolved peaks. Threonine C_α-C_γ, arginine Cα-C_δ, and His C_α-C_ε cross peaks are have significantly greater intensity with cross polarization. Proline C_β-C_δ peaks are only detected with direct excitation. The spectrum with direct excitation shows better resolution, notably in the region of Lys and Pro C_β-CO, as well as Lys C_α-C_ε. Given the catalytic role of Lys 12 and His 95, and the presence of Pro 166 in the loop 6 hinge and its proximity to the catalytic Glu 165, these may be important observations for future dynamic and enzymatic studies.

High Temperature vs Low Temperature Many dynamic processes of interest in proteins occur on an intermediate exchange timescale, and can be invisible via NMR due to exchange broadening. An advantage of solid state NMR in the study of dynamics is the ability to achieve a wide range of temperatures. As numerous residues of interest are expected to be dynamic, a carbon-carbon 2D DARR spectrum of ^{2}H, ^{15}N, [1,3-^{13}C] glycerol TIM was collected at -93°C to

slow dynamics of the protein. As compared to a higher temperature spectrum, there are numerous notable differences (Figure 5.6, high temperature: blue, low temperature: teal).

While low temperature and spectral artifacts (which caused phasing issues) lead to line broadening, there are many unique, well-resolved resonances at low temperature. Overall, the intensity is greater as well. The combination of low temperature, selective labeling, and deuteration may allow the resolution of sites that could not be observed at higher temperature. Particularly of note are downfield shifted C_α-CO resonances that are not observed in other spectra. Sidechain carbonyls, particularly for Glu and Gln, have significantly downfield shifted chemical shifts, thus further assignment may be valuable, although in practice the sidechain carbonyls are not expected to be labeled with [1,3-^{13}C] glycerol. Alanines also have downfield shifted backbone carbonyls. The C_α chemical shifts are too high to be attributed to Ala, and may be inter-residue C_α-CO contacts. Outlying resonances upfield in the aliphatic region may be Ile C_γ-C_δ cross peaks. Additional resolved Thr C_α-C_γ peaks appear, along with other C_α-C_β resonances.

Despite poorer resolution, the increase in signal-to-noise and appearance of different resonances makes further experiments at low temperature worthwhile.

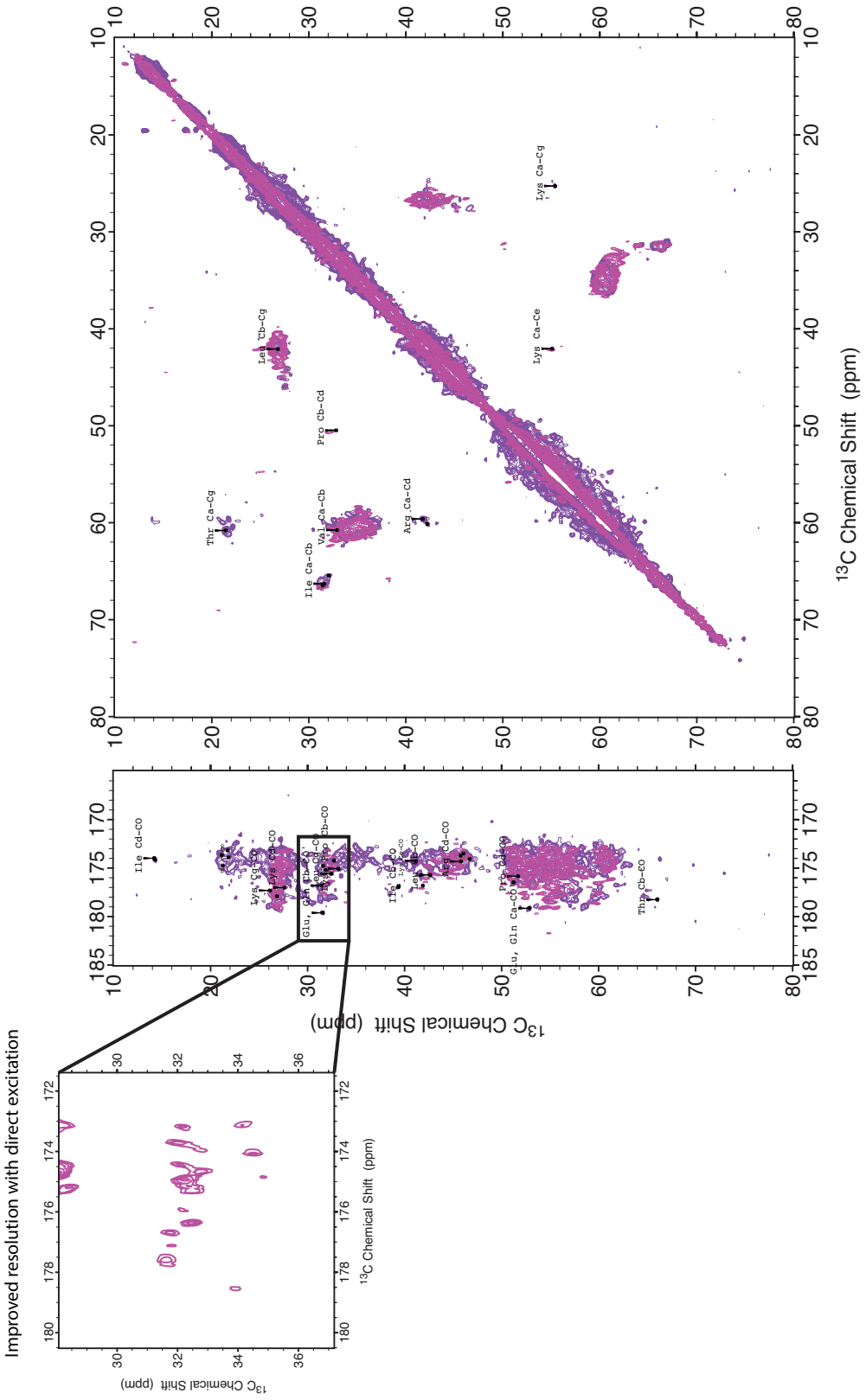

Figure 5.5 Comparison of data collected with cross polarization (purple) and direct excitation (magenta) for [2-^{13}C] glycerol, ^{15}N TIM. Particular resonances are favored with the different polarization methods and greater resolution is achieved with direct excitation.

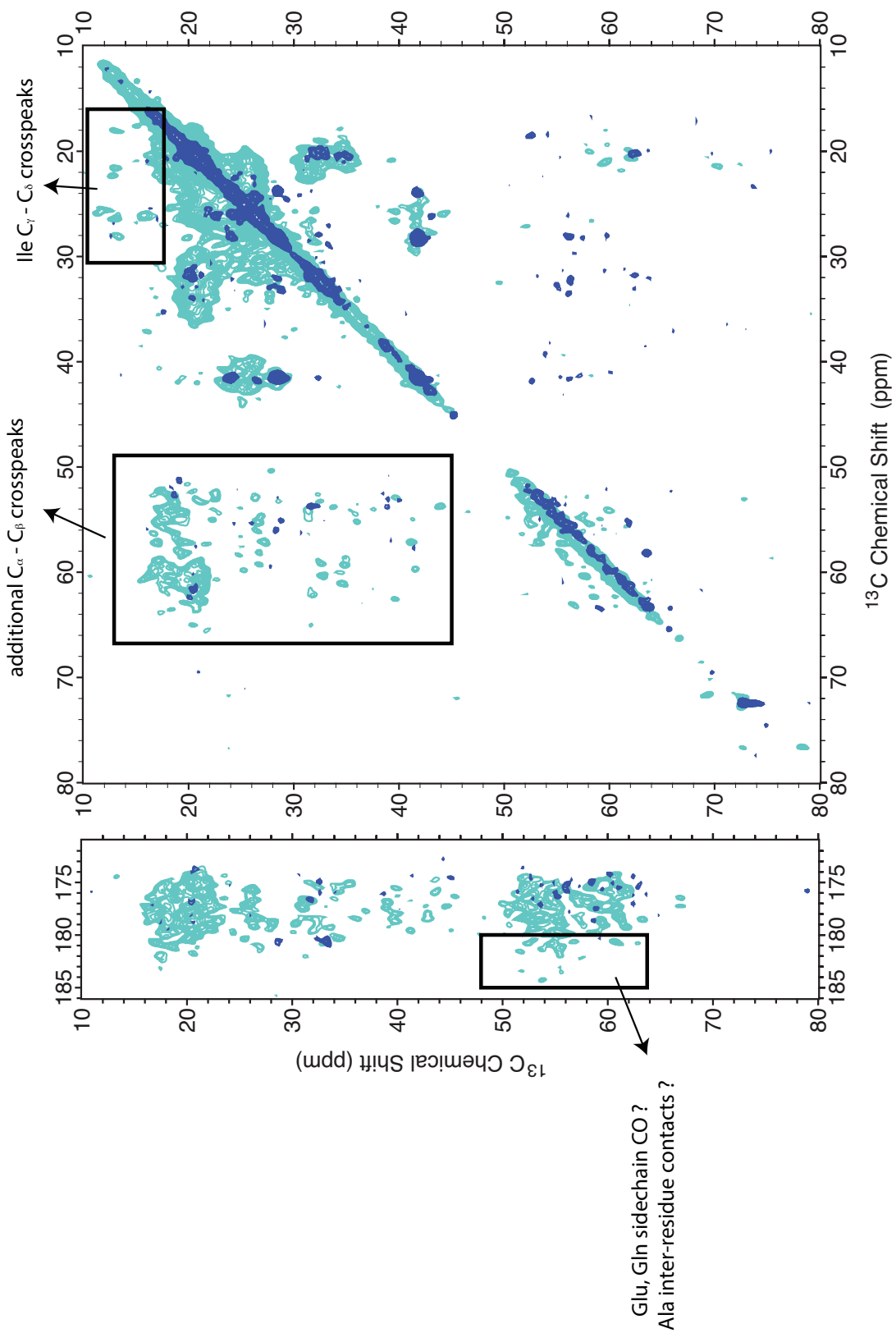

Figure 5.6 Overlay of spectra of ^{2}H, [1,3-^{13}C] glycerol, ^{15}N TIM collected at 248 K (blue) and 180 K (teal). Resolution is poorer at low temperature (due in part to spectral artifacts), but signal-to-noise is better and numerous unique resonances appear. Particularly of interest are downfield shifted resonances in the carbonyl region.

Carbon-Nitrogen Correlation Spectra Of particular interest in TIM is glutamic acid-165. This is a key catalytic residue that is responsible for abstracting a proton from the C2 carbon of the substrate DHAP. This resonance has not been assigned in either solution or the solid state. Detection is likely inhibited by intermediate exchange, as well as the challenges of spectral crowding in a large protein like TIM. Previous assignments in our group indicated that neighboring proline 166 has a nitrogen frequency of 141 ppm, shifted significantly downfield from other prolines in TIM [18]. With this in mind, NCO and NCA correlation spectra were collected with the nitrogen carrier shifted downfield relative to previous data collected in our group. Glutamic acid has a somewhat mixed labeling pattern with 1,3- and 2-glycerol (Figure 5.7). N-C correlation spectra were collected of [2-^{13}C] glycerol, ^{15}N TIM. The specific inter-residue correlation of interest would be Pro 166 N to Glu 165 backbone CO.

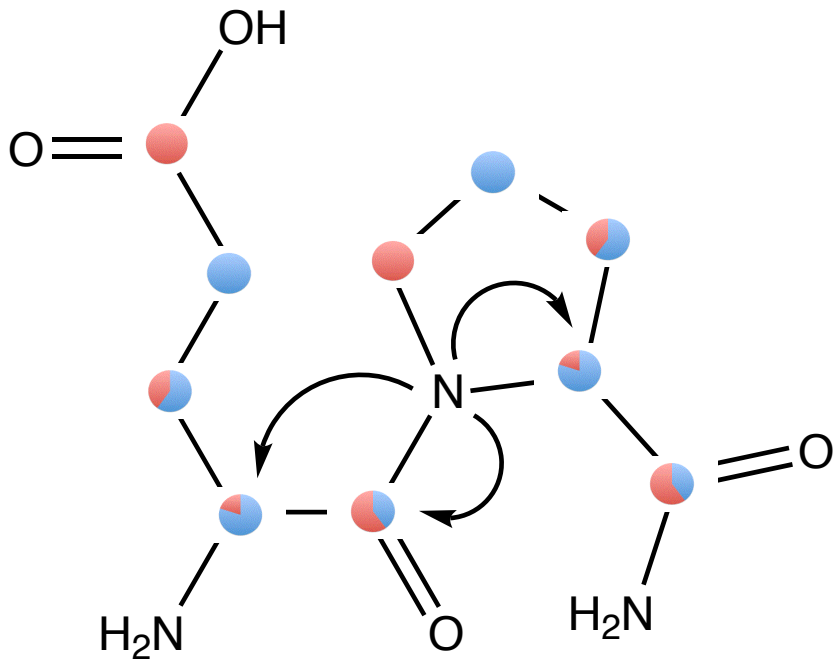

Figure 5.7 Proline-Glutamic acid peptide fragment showing expected labeling of carbon atoms with (blue) 1,3-^{13}C glycerol and (red) 2-^{13}C glycerol. From the labeling patterns, it is apparent that C_α and C_β of Glu-165 would be best detected with 1,3-glycerol while CO and the catalytic site, C_δ, would be better detected with 2-glycerol. Arrows show the expected one-bond NCO correlation from Pro 166 to Glu 165 and possible longer range NCA correlation as well as the Pro NCA intra-residue correlation.

Overall resolution in the NCO and NCA spectra may be inhibited by the presumable sample heterogeneity seen in the 2D DARR spectra. However numerous resolved peaks are still seen, notably outliers that may be useful for assignments. With the nitrogen transmitter set to 139 ppm, notable downfield intensity is apparent that is not seen with the transmitter set to 120 ppm, particularly in the NCO spectrum (Figure 5.8). With the exception of Pro 166, no other assigned nitrogen resonances in the solid state are shifted this downfield, however only about 50% of the nitrogens have been assigned. In addition, none of the 180 nitrogen resonances assigned in solution appear above ~ 131 ppm. From average chemical shifts in the BMRB, it is apparent that prolines are one of the most notable amino acids with downfield nitrogen chemical shifts. TIM has 7 prolines, of which only 2 in addition to Pro 166 have been assigned in the nitrogen dimension. SPARTA chemical shift predictions [[29], PDB ID: 1YPI] do predict all prolines to have chemical shifts of 136 to 141 ppm, several ppm higher than any other amino acid.

[2-^{13}C] glycerol labeling labels the C_α of many amino acids, therefore many amino acids can be detected in the NCA experiment. The broad nitrogen-carbon CP matching condition also allows for the detection of nitrogen-sidechain carbon correlations.

In the C_α region, there is notable intensity up to 140 ppm in the NCA spectrum shown in Figure 5.8. There is no remarkable difference between this region of the spectrum and previously collected NCACX 3D spectra of uniformly labeled TIM. However, there are a number of well-resolved resonances that appear upfield in the carbon dimension (20-32 ppm). Given the selective labeling scheme, there are only a few spin systems that these peaks may be attributed

to, including Glu, Gln, Pro, and Val C_β or Leu or Thr C_γ. The frequencies range from 120 to 128 ppm in the nitrogen dimension.

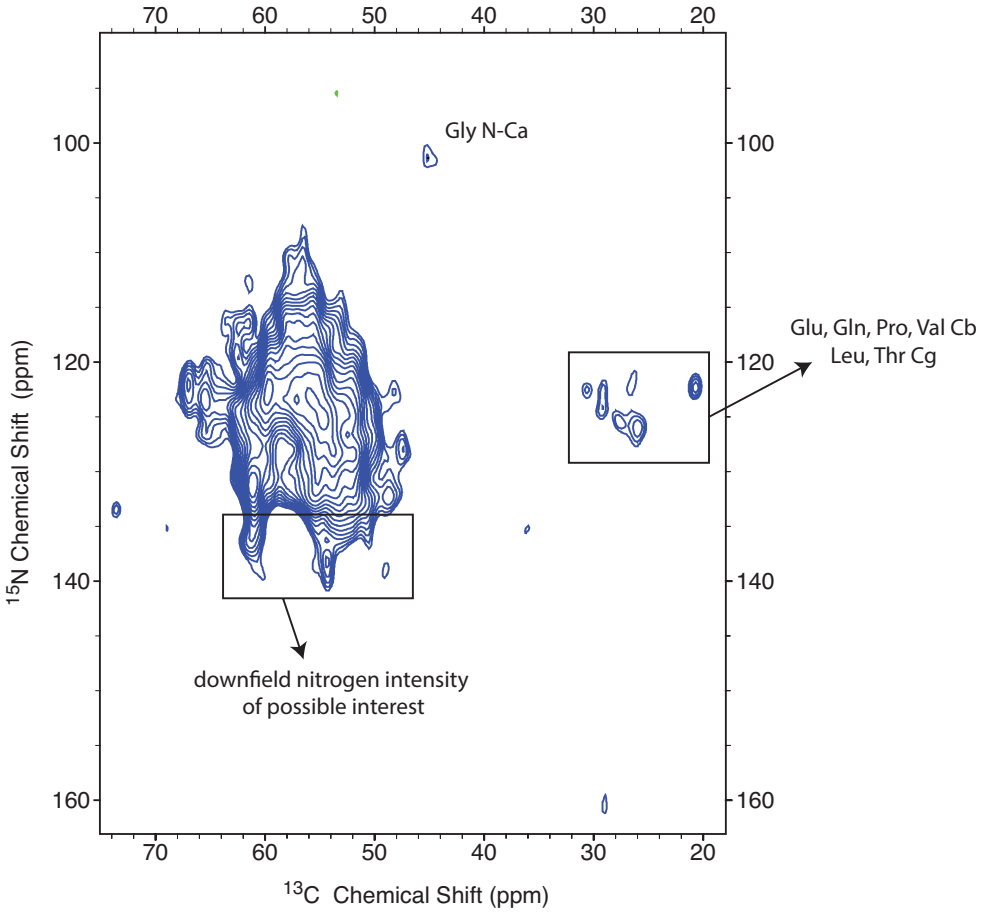

Figure 5.8 NCA nitrogen-carbon correlation spectrum of [2-^{13}C] glycerol, ^{15}N TIM collected with the nitrogen carrier at 139 ppm. The C_α and C_β resonances that appear may help with extending assignments of the protein.

In an NCO spectrum the dominant correlation is expected to be N_i to CO_{i-1}. Given the expected backbone carbonyl labeling of [2-^{13}C] glycerol, CO_{i-1} amino acids that are expected to appear are Thr, Lys, Glu, Gln, Pro, Ile, Leu, Arg, Asp, and Asn.

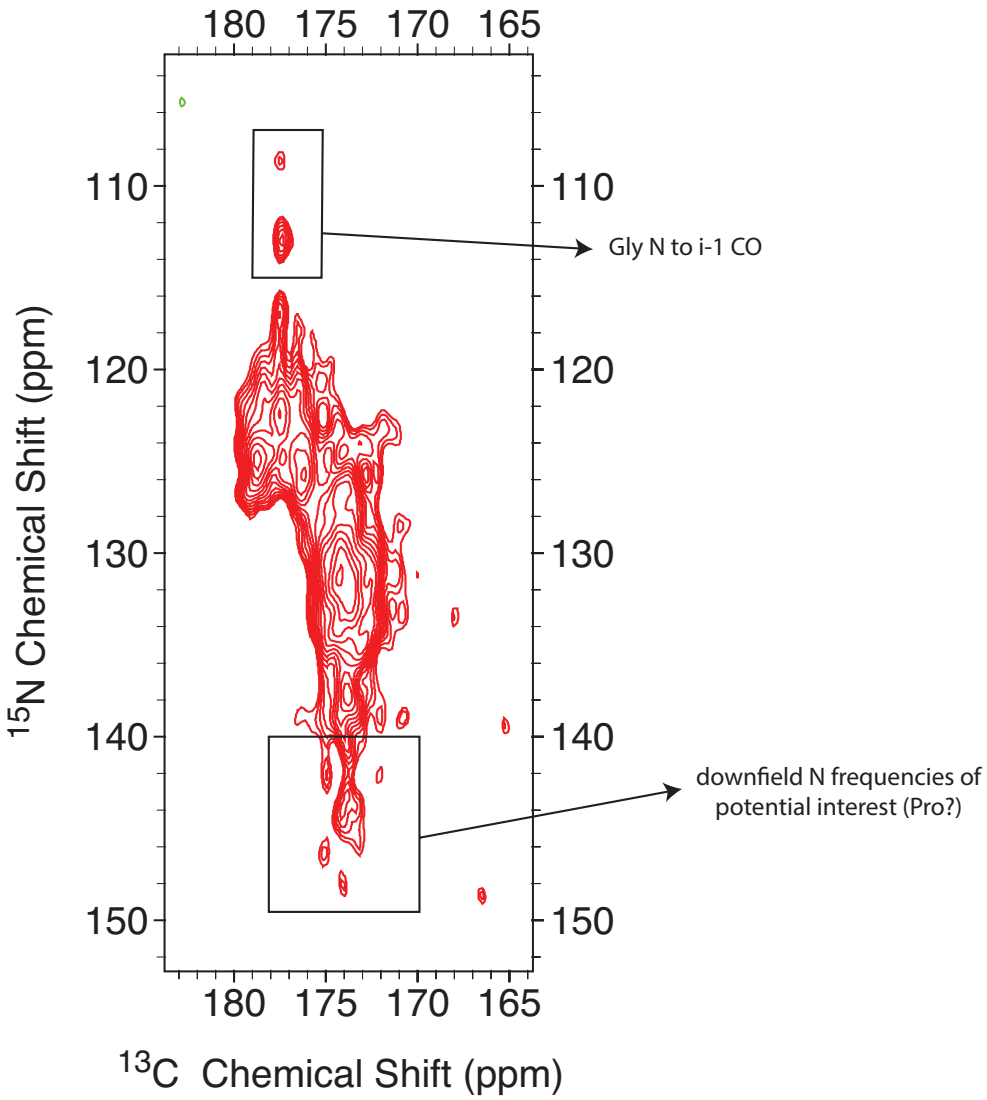

Figure 5.9 NCO nitrogen-carbon correlation spectrum of [2-^{13}C] glycerol, ^{15}N TIM collected with the nitrogen carrier shifted downfield to 139 ppm. There is significant intensity that appears downfield in the nitrogen dimension compared to previous spectra collected with the nitrogen transmitter at 120 ppm.

A notable observation in the NCO spectrum is significant intensity downfield in the nitrogen dimension (up to 148 ppm). This is much higher than previously assigned nitrogen resonances in TIM. Only 55% of backbone nitrogens have been assigned in the solid state and only 73% in solution for *S. cerevisiae* TIM ([30], BMRB: 7216, 15064, 15065). It may be that unassigned nitrogens are unassigned because their resonance frequencies are too downfield to have been reliably or optimally detected in previous experiments. Previous 3-dimensional NCOCX spectra

of U-TIM collected in our lab did not have sufficient signal-to-noise or use sufficiently downfield nitrogen frequencies to determine if observed peaks at these downfield nitrogen frequencies are real. As noted in Chapter 1, nitrogen chemical shifts are extremely sensitive to (1) the preceding residue type [31], (2) backbone torsion angles and secondary structure [32, 33], (3) and hydrogen bonding [34], among other parameters. Additional experiments are necessary to determine the identity of these resonances, but the carbonyl chemical shifts of 174-175 ppm are consistent with the amino acids that precede Pro in the TIM sequence and would be ^{13}C labeled: Glu, Ile, Lys, and Thr.

In addition to prolines, alanines can also have somewhat downfield shifted nitrogen frequencies. It may be suggested that the 'unusual' chemical shifts that are observed in the NCO spectrum are due to a referencing issue; while this cannot be conclusively eliminated, the spectrum was referenced carefully to reduce this possibility. These observed NCO nitrogen frequencies are several ppm downfield of those seen in the NCA experiment and it is true that if the downfield nitrogen intensity in the NCO spectrum arises from Pro residues that we would expect to see proline intra-residue correlations at these same N frequencies in the NCA spectrum. Therefore more work is necessary to evaluate these resonances.

A challenge of determining site specific assignments from the selective labeling data collected to date is the large number of correlations to C_γ and C_δ; very few of these sidechain resonances have been previously assigned. Without 3-dimensional experiments and because there are unique resolved sites relative to uniformly labeled TIM, it is almost impossible to make more

conclusive statements regarding the identities of resonances observed in the spectra discussed above.

5.3 $R_{1\rho}$ Studies of the Loop Residue Valine 167

As model compound studies have shown the importance of reducing spin diffusion, as well as to reduce the experimental time necessary, approaches that allow the measurement of relaxation in TIM with 1-dimensional spectra were considered. Previous chemical shift measurements indicated that valine 167, the nitrogen resonance in one of the dynamic loop residues, is shifted 1.8 ppm downfield from other assigned valines in the protein [18, 19]. This provides an opportunity to monitor Val 167 in one dimension with selectively labeled protein. Spin relaxation of valine 167 has previously been studied by Wang et al. They observed R_{ex} values of 38.2 ± 2.3 s^{-1} in WT chicken TIM (without ligand). From the temperature-dependence of this exchange contribution to relaxation, they determined an activation energy of 57.6 ± 7.7 kJ/mol for loop closing and quantified the exchange rate to k_{ex} = 9000 ± 1500 s^{-1}. This intermediate timescale dynamic process, as well as the possible resolution in one dimension, is ideal for initial solid state $R_{1\rho}$ experiments.

^{15}N Simulations of Loop Dynamics in TIM To assess the feasibility of solid state $R_{1\rho}$ measurements of loop dynamics, Spinevolution [35] simulations were performed. Isotropic shift data was taken from BMRB files 7216 (solution), 16565 (solid), and 16566 (solid), as well as reference [19]. From these isotropic chemical shift values, the $\Delta\omega$ between the bound and unbound forms of the protein were estimated. Being in loop 6, valine 167 is not in a portion of

the protein with well-defined secondary structure. Few statements have been made in the literature regarding trends in CSA values for sites that are not clearly α-helical or β-sheet. Furthermore, these sites are frequently dynamic and therefore more difficult to detect. Therefore CSA values were approximated based on CSA measurements from GB1, chosen based on residue type and secondary structure [36]. (I.e. to represent dynamic residues in TIM, loop or other residues without well-defined secondary structure in GB1 were chosen.) Simulations were done both on-resonance, and 0.6 kHz off-resonance because as shown in Figure 5.11, to simultaneously obtain measurements for Val 167 and a control site, the nitrogen carrier must be placed in the center of the two sites, so that one site is not affected by a greater off-resonance effect. Simulations indicated that this change in the frequency of the carrier does not have a notable effect on the relaxation rate.

Given the 2 site chemical exchange between the open and bound forms of TIM, simulation parameters were as follows: k_{ex} = 20,000 s^{-1}, $p_A = p_B = 0.5$, δ = -3.2 kHz, η = 0.1, β (angle hop) = 30°.

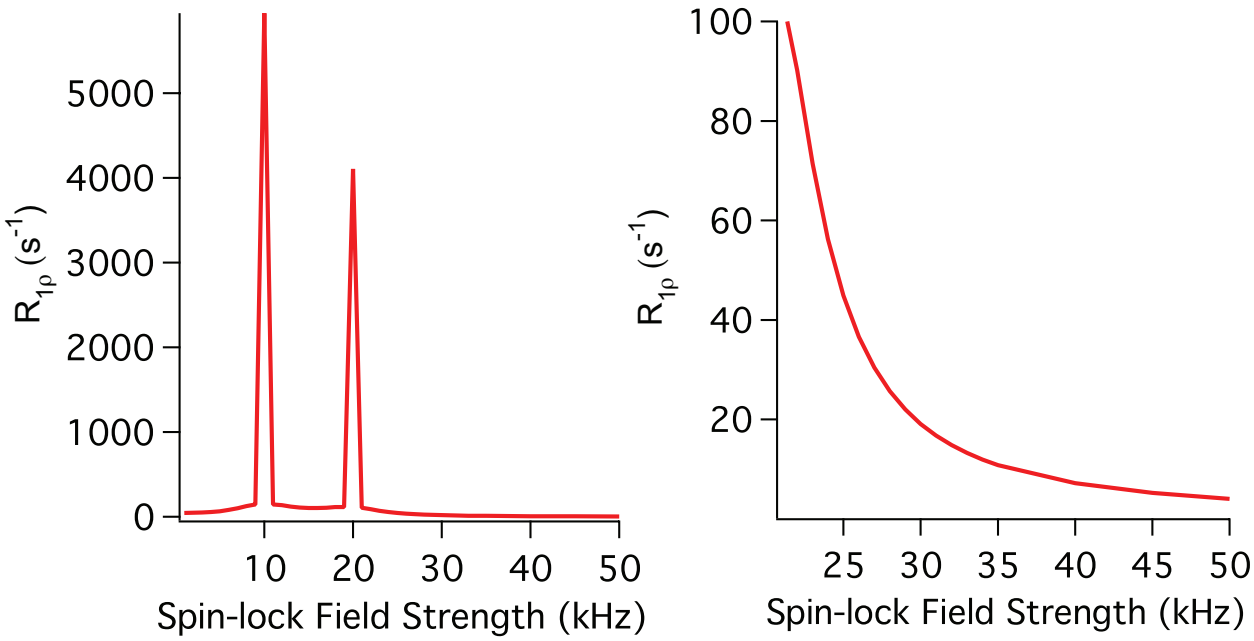

Figure 5.10 $R_{1\rho}$ dispersion curve simulated for TIM valine 167, a dynamic residue of interest. The dispersion curves were developed using Spinevolution to simulate relaxation given estimated CSA tensors. Isotropic chemical shifts that have been reported were also included in the Spinevolution simulations. On the right is the full dispersion curve, showing the rotary resonance conditions, while on the left is an expansion indicating the range of spin-lock field strengths that solid state NMR experiments would access.

These simulations indicate that with an exchange rate ~ 20,000 s^{-1}, the expected relaxation trend should be accessible with solid state NMR techniques. Thus in theory, experimental $R_{1\rho}$ measurements of Val 167 should be possible.

Experimental $R_{1\rho}$ Studies of Dynamics in Valine 167 For initial application of $R_{1\rho}$ studies to biological systems, we prepared ^{15}N-valine labeled TIM. With this labeling scheme, the protein is perdeuterated and only valine nitrogen resonances appear in an NMR spectrum. Figure 5.11 shows a 1-dimensional spectrum of ^{15}N-valine labeled TIM. There are resonances that are shifted both upfield and downfield from the bulk valine nitrogen signal. These peaks are believed to be valine 167 at 131 ppm and valine 86 at 104 ppm. The resolution of these 2 resonances provides an opportunity to study the dynamic residue and a static control residue

simultaneously in a 1-dimensional spectrum. Val 86 would be expected to have no relaxation due to an exchange process, though it is possible that relaxation could be observed due to R_2^0 processes as discussed for dimethyl sulfone in Chapter 3. The presence of this control peak may be superior for providing a direct measure of an R_2^0 contribution to measured $R_{1\rho}$ relaxation rates. The spectrum shown in Figure 5.11 is 1024 scans of 25 mg of protein with G3P in a ratio of ~ 50/50 open/closed loop conformation, collected at a proton frequency of 400 MHz with ^{1}H-^{15}N cross polarization and 85 kHz proton decoupling

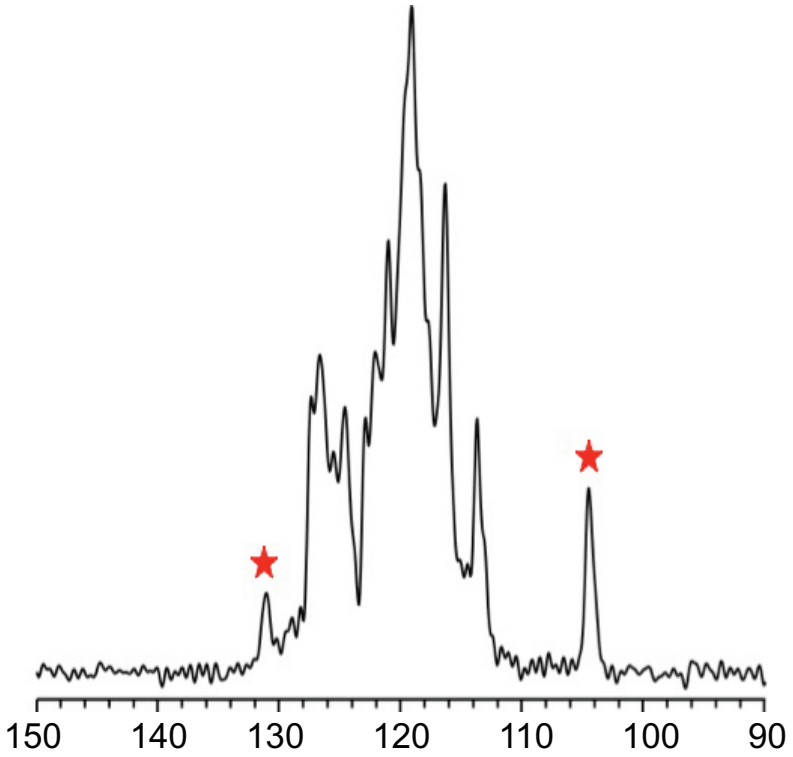

Figure 5.11 1-Dimensional nitrogen spectrum of selectively ^{15}N-valine labeled TIM collected at 400 MHz proton frequency. The peak around 131 ppm is presumably valine 167, a dynamic loop residue of interest. The peak around 104 ppm is likely valine 86, a valine residue in a static region of TIM that could serve as an excellent control residue.

$R_{1\rho}$ studies of these TIM resonances were also performed. As can be seen in Figure 5.12, there was no conclusive relaxation behavior in the ^{15}N-valine labeled sample. Differences in peak intensity at ~ 131 ppm do not follow the expected trend of decreasing peak intensity with

increasing spin-lock length. The differences in intensity are within the signal-to-noise of the sample. Figure 5.12 (B) plots the integrated intensity of 3 regions of the spectrum as a function of spin-lock length: 1) 128—131 ppm, where Val 167 appears, 2) 109—128 ppm, the bulk ^{15}N valine signal, and 3) 100—105 ppm, where Val 86 appears. The integrated intensity was normalized to 1 at the first spin-lock length point, 1 ms. Although the expected trend of intensity decay with increasing spin-lock length was not observed, there are trends that can be discerned which may or may not be significant. Changes in intensity appear to be dependent on the spectra themselves rather than a function of spin-lock length. For example, peak intensity is greater under a 10 ms spin-lock, rather than decaying away; however this behavior seems less pronounced for valine 167, perhaps due to an underlying $R_{1\rho}$ process.

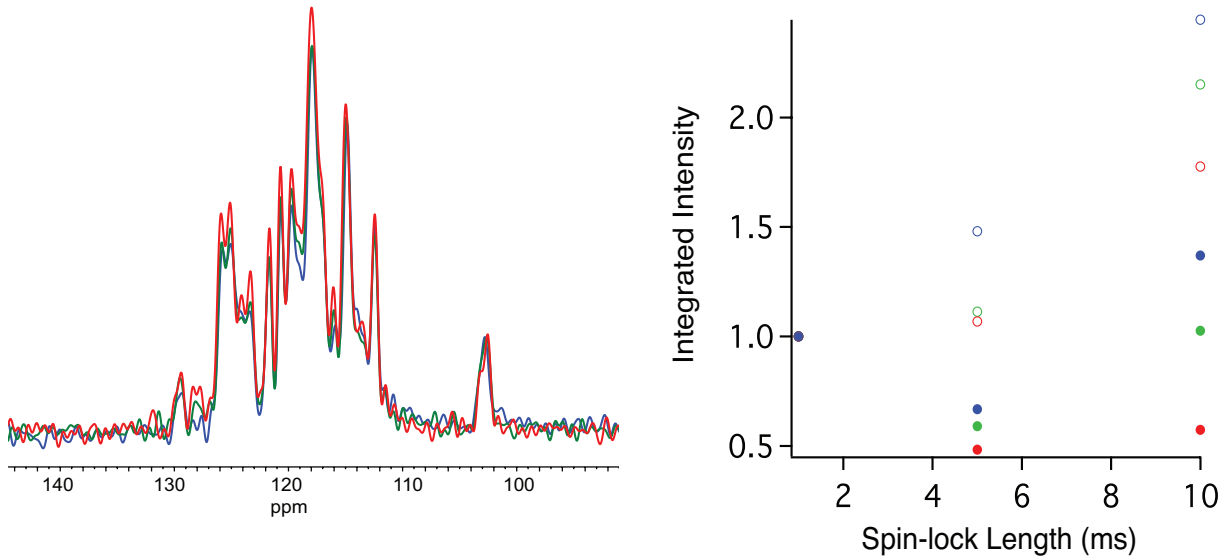

Figure 5.12 (A) Spectra of G3P-bound ^{15}N-valine labeled TIM collected at spin-lock lengths of (red) 1 ms, (green) 5 ms, and (blue) 10 ms at a field strength of 25 kHz. (B) Integrated intensity for 3 regions of the spectrum plotted as a function of spin-lock length at spin-lock field strengths of (●) 25 and (❍) 30 kHz. Red is the spin-lock length dependent relaxation behavior of the region of interest: 128—131 ppm, green is the control region of valine-86 from 100—105 ppm, and blue is the integral of the bulk nitrogen signal from 109—128 ppm. MAS = 10 kHz

These $R_{1\rho}$ studies were done on a protonated sample using cross polarization before DMS studies indicated the importance of deuteration and direct excitation for dynamics studies. Later studies

on a duterated sample presented a great challenge in signal-to-noise due to the loss of polarization efficiency from direct excitation.

There are several possible reasons for the observation of increasing peak intensity with increasing spin-lock length. The behavior of increasing intensity with increasing spin-lock length may be attributed to a Hartmann-Hahn cross polarization effect, due to the simultaneous irradiation of the carbon and proton channels. Proton spin diffusion or other processes may be masking a relatively small $R_{1\rho}$ contribution. Furthermore, the ligand utilized in these studies was G3P. G3P induces ligand dynamics on the ms timescale [1, 17, 37], which may be too slow for the somewhat faster dynamics that $R_{1\rho}$ is most sensitive to (Chapter 3, [13]). Later work in our lab also indicated the challenges of using G3P as the ligand for dynamics studies in TIM [30]. It is also possible given that only three spin-lock length data points were collected, the differences between these points are due to the small sampling size.

In addition, higher signal-to-noise may also be necessary to observe the relaxation effect; or if the $R_{1\rho}$ relaxation is very slow, longer spin-lock lengths will be necessary to see changes in the spectrum. It is also important to note that TIM has 26 valines, of which only 18 have been assigned in the nitrogen dimension [18, 19]. If unassigned valines also lie downfield in the spectrum, their non-relaxing behavior may make relaxation from a single residue difficult to detect. These preliminary experiments were also done using spin-locks that are not significantly off the second rotary resonance condition (MAS = 10 kHz). It might be expected that any $R_{1\rho}$ effect has decayed away very rapidly.

A first control for these $R_{1\rho}$ experiments would be to use ^{15}N direct excitation with faster spinning or higher field strengths. A further complication has indicated that care must be taken to minimize sample heating as discussed in Chapter 4.

5.4 Conclusions

In this chapter we have investigated selective labeling schemes for the study of relaxation in triosephosphate isomerase. [1,3-^{13}C] and [2-^{13}C] glycerol were successfully incorporated into protein expression, along with deuteration. These labeling schemes and various methods of data acquisition indicated possible protein sites for future relaxation studies of key residues in the protein. Direct excitation provides improved resolution and detection of different spin systems relative to cross polarization. Low temperature measurements detected different resonances and showed improved signal to noise. Unique resolved resonances and downfield peak intensity in carbon-nitrogen correlation spectra may provide opportunities for extending the assignment of TIM.

Simulations and previous solution NMR studies indicate that the loop residue valine 167 may provide a good marker for $R_{1\rho}$ studies of loop dynamics in triosephosphate isomerase. Initial rotating-frame ($R_{1\rho}$) relaxation studies did not capture the expected relaxation behavior. These unsuccessful measurements may be due to labeling scheme, signal-to-noise, and/or parameters used for data acquisition.

This work provides preliminary concepts that can be built upon for further site-specific assignment of TIM and the study of dynamic and catalytic sites in the protein.

5.5 Materials and Methods

All protein samples were prepared as described in Chapter 6.

DARR Carbon-Carbon Correlation Spectra 2-Dimensional Dipolar Assisted Rotational Resonance (DARR) ^{13}C-^{13}C homonuclear correlation spectra of [2-^{13}C] glycerol, ^{15}N-TIM and ^{2}H, [1,3-^{13}C] glycerol, ^{15}N-TIM were collected on a Bruker Avance DRX-750 spectrometer (New York Structural Biology Center) in a 4 mm rotor. Due to interest in dynamic residues, spectra of [2-^{13}C] glycerol TIM were collected using direct ^{13}C excitation as well as cross polarization. For spectra collected using cross polarization, DARR mixing times of 25, 100, and 200 ms were used. In these sparsely labeled samples, longer mixing times were found to give a greater number of correlations; therefore this mixing time was used for all subsequent experiments. Spectra were processed in NMRPipe and analyzed with SPARKY.

Experiment	Carbon-Carbon 2D DARR with direct excitation
Spectrometer	Bruker Avance 750 MHz
Sample	Unligated ^{2}H, [1,3-^{13}C] glycerol, ^{15}N TIM
Data Acquisition Parameters	MAS: 12 kHz VT: 248 K Mixing time: 200 ms NS: 16 TD: F2- 2818, F1-943 SW: F2-500 ppm, F1-250 ppm
Data Processing Parameters	Zero filling to double points *High signal-to-noise* Lorentz-to-Gauss window function, 40 Hz line narrowing, 100 Hz line broadening *High resolution* Lorentz-to-Gauss window function, 30 Hz line narrowing, 60 Hz line broadening

Experiment	Carbon-Carbon 2D DARR with direct excitation
Spectrometer	Bruker Avance 750 MHz
Sample	Unligated [2-^{13}C] glycerol, ^{15}N TIM
Data Acquisition Parameters	MAS: 12 kHz VT: 243 K Mixing time: 200 ms NS: 48 TD: F2-1536, F1-512 SW: F2-265 ppm, F1-265 ppm (50 kHz)
Data Processing Parameters	16 points back linear prediction Lorentz-to-Gauss window function, 60 Hz line narrowing, 100 Hz line broadening Zero filling to double points

Experiment	Carbon-Carbon 2D DARR with cross polarization
Spectrometer	Bruker Avance 750 MHz
Sample	Unligated [2-^{13}C] glycerol, ^{15}N TIM
Data Acquisition Parameters	MAS: 12 kHz VT: 240 K Mixing time: 25, 100, 200 ms NS: 32 TD: F2-2048, F1-1024 SW: F2-250 ppm, F1-250 ppm
Data Processing Parameters	8 points back linear prediction Lorentz-to-Gauss window function, 30 Hz line narrowing, 60 Hz line broadening Zero filling to double points

Experiment	Carbon-Carbon 2D DARR with direct excitation
Spectrometer	Bruker Avance 750 MHz
Sample	Unligated ^{2}H, [1,3-^{13}C] glycerol, ^{15}N TIM
Data Acquisition Parameters	MAS: 12 kHz VT: 180 K Mixing time: 250 ms NS: 32 TD: F2-1498, F1-471 SW: F2- 500 ppm, F1-250 ppm
Data Processing Parameters	16 points back linear prediction Lorentz-to-Gauss window function, 30 Hz line narrowing, 60 Hz line broadening Zero filling to double points

Table 5.1 Experimental parameters for C-C 2D DARR spectra of selectively labeled TIM.

NCO and NCA Correlation Spectra NCO and NCA correlation spectra of [2-^{13}C] glycerol, ^{15}N labeled triosephosphate isomerase were collected on a Bruker Avance 400 MHz spectrometer in a 3.2 mm rotor spinning at 16 kHz with double cross polarization (DCP). The thermocouple temperature was set to -15°C. To detect downfield peaks, the nitrogen carrier was set to 139 ppm. The NCO spectrum had 1024 points in the direct dimension, 81 points in the indirect dimension, and 384 scans were acquired. The NCA had 1152 and 81 points in the direct and indirect dimensions respectively. 329 scans were acquired. Spectra were processed in NMRPipe with Lorentz-to-Gauss window functions, 35 Hz line narrowing, and 90 Hz line broadening, and zero filling to double points.

^{15}N-Valine TIM Nitrogen 1D The 1-dimensional nitrogen spectrum (Figure 5.11) was collected on a Varian Chemagnetics 400 MHz spectrometer, with a 4 mm rotor and T3 probe spinning at 6.67 kHz. The temperature at the thermocouple was set to -10°C. Ramped ^{1}H-^{15}N cross polarization used 42 kHz on proton and 43 kHz on nitrogen. Contact time was 2.0 ms. 1024 points were collected with 85 kHz ^{1}H TPPM decoupling during acquisition, with optimized

decoupling pulse length (6.25 μs) and phases (40°). 20480 scans were collected in 8 hours. The spectrum was processed in Spinsight with 20 Hz Gaussian line broadening, 2 points back linear prediction, and zero filling to 2048 points.

^{15}N-Valine TIM Nitrogen $R_{1\rho}$ Measurements Nitrogen $R_{1\rho}$ relaxation spectra of ^{15}N-valine TIM were collected on a Bruker Avance DRX-750 spectrometer (New York Structural Biology Center) with a 4 mm rotor spinning at 10 kHz. The temperature was set to -8°C. The nitrogen carrier was set to the center of the spectrum, ~ 1 kHz off-resonance of the peaks at 131 and 107 ppm. The ^{1}H 90° pulse was 3.1 μs. The H-N CP conditions were as follows. Cross polarization field strengths were 49 kHz on proton and 36 kHz on nitrogen. The contact time was 1.5 ms. Spectra were collected at 2 spin-lock field strengths: 25 and 30 kHz at spin-lock lengths of 1, 5, and 10 ms. 1024 points were collected per spectrum. 4096 scans were collected per spin-lock length and field strength. Spectra were processed with 50 Hz exponential line broadening and zero filling to 16384 points.

5.6 References

[1] S. Rozovsky, G. Jogl, L. Tong, A.E. McDermott, Solution-state NMR investigations of triosephosphate isomerase active site loop motion: Ligand release in relation to active site loop dynamics, J Mol Biol, 310 (2001) 271-280.

[2] J.P. Loria, R.B. Berlow, E.D. Watt, Characterization of enzyme motions by solution NMR relaxation dispersion, Accounts Chem Res, 41 (2008) 214-221.

[3] D.D. Boehr, H.J. Dyson, P.E. Wright, An NMR perspective on enzyme dynamics, Chem Rev, 106 (2006) 3055-3079.

[4] A.J. Baldwin, L.E. Kay, NMR spectroscopy brings invisible protein states into focus, Nat Chem Biol, 5 (2009) 808-814.

[5] A. Krushelnitsky, D. Reichert, Solid-state NMR and protein dynamics, Prog Nucl Mag Res Sp, 47 (2005) 1-25.

[6] A.G. Palmer, C.D. Kroenke, J.P. Loria, Nuclear magnetic resonance methods for quantifying microsecond-to-millisecond motions in biological macromolecules, Method Enzymol, 339 (2001) 204-238.

[7] M. Rance, J.P. Loria, A.G. Palmer, Sensitivity improvement of transverse relaxation-optimized spectroscopy, J Magn Reson, 136 (1999) 92-101.

[8] S. Luca, H. Heise, M. Baldus, High-resolution solid-state NMR applied to polypeptides and membrane proteins, Accounts Chem Res, 36 (2003) 858-865.

[9] A.T. Petkova, Y. Ishii, J.J. Balbach, O.N. Antzutkin, R.D. Leapman, F. Delaglio, R. Tycko, A structural model for Alzheimer's beta-amyloid fibrils based on experimental constraints from solid state NMR, P Natl Acad Sci USA, 99 (2002) 16742-16747.

[10] A. Krushelnitsky, R. Kurbanov, D. Reichert, G. Hempel, H. Schneider, V. Fedotov, Expanding the frequency range of the solid-state T-1p experiment for heteronuclear dipolar relaxation, Solid State Nucl Mag, 22 (2002) 423-438.

[11] W.B. Li, A.E. McDermott, Characterization of slow conformational dynamics in solids: dipolar CODEX, J Biomol Nmr, 45 (2009) 227-232.

[12] C.M. Quinn, A.E. McDermott, Quantifying conformational dynamics using solid-state R-1 rho experiments, J Magn Reson, 222 (2012) 1-7.

[13] C.M. Quinn, A.E. McDermott, Monitoring conformational dynamics with solid-state R (1 rho) experiments, J Biomol Nmr, 45 (2009) 5-8.

[14] M.A. McCoy, D.F. Wyss, Spatial localization of ligand binding sites from electron current density surfaces calculated from NMR chemical shift perturbations, J Am Chem Soc, 124 (2002) 11758-11763.

[15] J. Meiler, D. Baker, ROSETTALIGAND: Protein-small molecule docking with full side-chain flexibility, Proteins, 65 (2006) 538-548.

[16] J.C. Williams, A.E. Mcdermott, Dynamics of the Flexible Loop of Triosephosphate Isomerase - the Loop Motion Is Not Ligand-Gated, Biochemistry-Us, 34 (1995) 8309-8319.

[17] R. Desamero, S. Rozovsky, N. Zhadin, A. McDermott, R. Callender, Active site loop motion in triosephosphate isomerase: T-jump relaxation spectroscopy of thermal activation, Biochemistry-Us, 42 (2003) 2941-2951.

[18] Y.M. Xu, J. Lorieau, A.E. McDermott, Triosephosphate Isomerase: N-15 and C-13 Chemical Shift Assignments and Conformational Change upon Ligand Binding by Magic-Angle Spinning Solid-State NMR Spectroscopy, J Mol Biol, 397 (2010) 233-248.

[19] F. Massi, C.Y. Wang, A.G. Palmer, Solution NMR and computer simulation studies of active site loop motion in triosephosphate isomerase (vol 45, pg 10787, 2006), Biochemistry-Us, 45 (2006) 14232-14232.

[20] E. Lolis, T. Alber, R.C. Davenport, D. Rose, F.C. Hartman, G.A. Petsko, Structure of Yeast Triosephosphate Isomerase at 1.9-a Resolution, Biochemistry-Us, 29 (1990) 6609-6618.

[21] E. Lolis, G.A. Petsko, Crystallographic Analysis of the Complex between Triosephosphate Isomerase and 2-Phosphoglycolate at 2.5-a Resolution - Implications for Catalysis, Biochemistry-Us, 29 (1990) 6619-6625.

[22] S. Rozovsky, A.E. McDermott, The time scale of the catalytic loop motion in triosephosphate isomerase, J Mol Biol, 310 (2001) 259-270.

[23] Y. Wang, R.B. Berlow, J.P. Loria, Role of Loop-Loop Interactions in Coordinating Motions and Enzymatic Function in Triosephosphate Isomerase, Biochemistry-Us, 48 (2009) 4548-4556.

[24] M.M. Malabanan, A.P. Koudelka, T.L. Amyes, J.P. Richard, Mechanism for Activation of Triosephosphate Isomerase by Phosphite Dianion: The Role of a Hydrophobic Clamp, J Am Chem Soc, 134 (2012) 10286-10298.

[25] C.G. Hoogstraten, J.E. Johnson, Metabolic labeling: Taking advantage of bacterial pathways to prepare spectroscopically useful isotope patterns in proteins and nucleic acids, Concept Magn Reson A, 32A (2008) 34-55.

[26] D.M. LeMaster, D.M. Kushlan, Dynamical mapping of E-coli thioredoxin via C-13 NMR relaxation analysis, J Am Chem Soc, 118 (1996) 9255-9264.

[27] V.A. Higman, J. Flinders, M. Hiller, S. Jehle, S. Markovic, S. Fiedler, B.J. van Rossum, H. Oschkinat, Assigning large proteins in the solid state: a MAS NMR resonance assignment strategy using selectively and extensively C-13-labelled proteins, J Biomol Nmr, 44 (2009) 245-260.

[28] B. Reif, Ultra-high resolution in MAS solid-state NMR of perdeuterated proteins: Implications for structure and dynamics, J Magn Reson, 216 (2012) 1-12.

[29] Y. Shen, A. Bax, SPARTA plus : a modest improvement in empirical NMR chemical shift prediction by means of an artificial neural network, J Biomol Nmr, 48 (2010) 13-22.

[30] Y. Xu, Solid State NMR Approach to Conformational Change and Chemical Exchange of Triosephosphate Isomerase, in: Department of Chemistry, Columbia University, New York, 2009.

[31] Y. Shen, A. Bax, Protein backbone chemical shifts predicted from searching a database for torsion angle and sequence homology, J Biomol Nmr, 38 (2007) 289-302.

[32] H.B. Le, E. Oldfield, Correlation between N-15 Nmr Chemical-Shifts in Proteins and Secondary Structure, J Biomol Nmr, 4 (1994) 341-348.

[33] B.J. Wylie, W.T. Franks, C.M. Rienstra, Determinations of N-15 chemical shift anisotropy magnitudes in a uniformly N-15, C-13-labeled microcrystalline protein by three-dimensional magic-angle spinning nuclear magnetic resonance spectroscopy, J Phys Chem B, 110 (2006) 10926-10936.

[34] Y.F. Wei, A.C. de Dios, A.E. McDermott, Solid-state N-15 NMR chemical shift anisotropy of histidines: Experimental and theoretical studies of hydrogen bonding, J Am Chem Soc, 121 (1999) 10389-10394.

[35] M. Veshtort, R.G. Griffin, SPINEVOLUTION: A powerful tool for the simulation of solid and liquid state NMR experiments, J Magn Reson, 178 (2006) 248-282.

[36] B.J. Wylie, L.J. Sperling, H.L. Frericks, G.J. Shah, W.T. Franks, C.M. Rienstra, Chemical-shift anisotropy measurements of amide and carbonyl resonances in a microcrystalline protein with slow magic-angle spinning NMR spectroscopy, J Am Chem Soc, 129 (2007) 5318-+.

[37] R.B. Desamero, S. Rozovsky, A. McDermott, R.H. Callender, Ligand dependence and thermal activation of active site loop motion in triosephosphate isomerase, Biophys J, 84 (2003) 499A-499A.

Chapter 6

Expression and Purification of Triosephosphate Isomerase for Various Labeling Schemes

For nuclear magnetic resonance experiments, choice of labeling scheme is an important consideration. $R_{1\rho}$ experiments require sparse isotropic labeling to limit spin diffusion. For site-specific assignment in a large protein such as TIM, labeling with [1,3-^{13}C] and [2-^{13}C] glycerol can reduce the number of labels and thus reduce spectral overlap. By eliminating proton spin diffusion via deuteration, narrower linewidths in protein spectra can be attained. Deuteration is also a critical feature for $R_{1\rho}$ experiments.

6.1 TIM Expression

The expression vector for the wild-type protein was freshly transformed into competent BL21(DE3)-T1^{R} cells following the protocol provided by Sigma-Aldrich and plated onto 25 g/L Luria broth (LB) and 15 g/L agar plates with 50 mg/L final ampicillin concentration. The plates were incubated at 37°C for approximately 7 hours. Single colonies were selected from the plates to inoculate several 5 mL starter cultures of 25 g/L LB and 50 mg/L ampicillin. Starter cultures were incubated with shaking at 37°C, 240 rpm to an OD_{600} of 0.2 (2-3 hours).

6.2 Growth of Natural Abundance TIM

Natural abundance protein was prepared from starter cultures as described above and transferred to 1 L LB with 50 mg/L ampicillin. The cells were incubated at 37°C, 240 rpm to a cell density of 0.8 — 1.0 (~ 3-5 hours), monitored by UV approximately every hour. The media was refreshed by spinning the cells down at 5000 g for 15 minutes and resuspending the cells in 1 L of fresh LB. After 1 hour, protein expression was induced with IPTG (0.4 mM final

concentration). Cells were harvested after 22.5 hours via centrifugation at 5000 g, 4°C for 30 minutes.

6.3 Growth of [1,3-] and [2-^{13}C] glycerol, ^{15}N TIM

Approximately 2 mL of the starter cultures was transferred to each of 4 1 L volumes of LB (25 g/L) with 50 mg/L ampicillin. These cultures were incubated at 37°C, 240 rpm to a cell density (OD_{600}) of 0.5 (~ 3 hours), monitored with UV every hour. When OD_{600} reached 0.5, the cells were spun down at 5000 g, 4°C for 15 minutes. The cells were then finely resuspended in 25°C M9 (1x) buffer then centrifuged again at 5000 g, 4°C for 15 minutes and this process was repeated to ensure the elimination of unlabeled carbon and nitrogen sources. The cells were then resuspended in 1 L of the growth media described in Table 6.1. This 4:1 transfer ratio had previously been optimized for expression of triosephosphate isomerase. It is important to note that growth with [2-^{13}C] glycerol also uses carbon-labeled $NaH^{13}CO_3$, while growth with [1,3-^{13}C] glycerol uses natural abundance $NaH^{12}CO_3$.

M9 buffer (10x) // autoclaved (Table 5.2)	100 mL
H_2O // autoclaved	860 mL
1 M $MgSO_4$ // autoclaved	2 mL
1 M $CaCl_2$ // autoclaved	100 μL
100 mg/mL ampicillin stock	500 μL
Solution C (Table 5.3)	20 mL
Vitamin stock (Table 5.5)	500 μL
Thiamin solution (0.01 g in 20 mL H_2O, freshly made, sterile filtered)	200 μL
$^{15}NH_4Cl$	3 g
[2-^{13}C] glycerol or [1,3-^{13}C] glycerol	2 g
$NaH^{13}CO_3$ or $NaH^{12}CO_3$	2 g

Table 6.1 Labeled growth media for expression of TIM using glycerol as the carbon source

$Na_2HPO_4•7H_2O$	128 g
KH_2PO_4	30 g
NaCl	5 g

Table 6.2 Recipe for 1 L 10x M9 buffer, autoclaved and stored at 25°C

KOH	7.3 g
Metals 44 (Table 5.4)	50 mL
Nitrilotriacetic acid	10 g
$MgCl_2•6H_2O$	24 g
$CaCl_2•2H_2O$	3.335 g

Table 6.3 Recipe for 1 L of Solution C, pH = 7.8, sterile filtered and stored at 4°C

$K_2EDTA•2H_2O$	0.327 g
$ZnCl_2$	0.522 g
$FeCl_2•4H_2O$	0.502 g
$MnCl_2•4H_2O$	0.180 g
$(NH_4)_6Mo_7O_{24}•6H_2O$	0.0185 g
$CuCl_2•2H_2O$	0.0156 g
$Co(NO_3)_2•6H_2O$	0.0248 g
Boric acid	0.0114 g

Table 6.4 Recipe for 100 mL of Metals 44 solution, sterile filtered and stored away from light at 4°C

Nicotinic acid	0.5 g
4-Aminobenzoic acid	0.05 g
D-Biotin	0.005 g

Table 6.5 Recipe for 50 mL vitamin stock, sterile filtered and stored away from light at 4°C

Particularly for cell growth using glycerol as the carbon source, previous work has shown that good aeration and fast shaking give optimal protein yields. For this reason, the culture was divided into 5 2 L baffled flasks each containing 200 mL M9 labeled media and cells. The cells were incubated in labeled M9 media at 37°C, 400 rpm for 1 hour to allow recovery of cell growth. Protein expression was then induced with 0.4 mM isopropyl-β-D-1-thiogalactopyranoside (IPTG). The expression of TIM at 37°C, 400 rpm proceeded for 22-23 hours with aliquots for monitoring expression via UV and SDS-page gel taken every 2-4 hours.

After 22-23 hours, the cells were harvested via centrifugation at 5000 g, 4°C for 30 minutes. The yield from this growth was approximately 10 g of wet cells.

6.4 Growth of ^{2}H, [1,3-^{13}C] glycerol, ^{15}N TIM

Deuterated protein was prepared with the following changes to the protocol described above. To allow optimal growth of cells and expression of protein, the cells must be adapted to D_2O gradually over multiple tranfers to higher D_2O concentrations.

A 25 mL LB pre-culture with 50 mg/L ampicillin was inoculated from freshly plated cells. The cells were grown at 37°C, 240 rpm to an OD_{600} = 0.7. The cells were centrifuged at 5000 g for 15 minutes at room temperature and resuspended in 175 mL pre-warmed ^{1}H-minimal media (Table 5.6). The cells were grown at 37°C, 240 rpm to an OD_{600} = 0.7. The entire 175 mL culture was transferred into 1 L 65% ^{2}H-minimal media (Table 6.7). The cells were again grown to an OD_{600} = 0.7. The cells were then centrifuged at 5000 g for 15 minutes at room temperature, and resuspended/washed with 1 X M9 solution in D_2O (Table 6.9) to eliminate all unlabeled proton, carbon, and nitrogen sources. The cells were centrifuged again at 5000 g for 15 minutes at room temperature and re-suspended in 500 mL pre-warmed 100% ^{2}H-minimal media (Table 6.8). The cells were divided into 2 baffled flasks with 250 mL solution each, and incubated with shaking for 1 hour at 37°C. 25 mg IPTG per 250 mL solution was then added to induce protein expression. After 22.5 hours, the cells were harvested by centrifugation at 5000 g, 4°C for 30 minutes.

M9 buffer (10x) // autoclaved (Table 5.2)	17.5 mL
H_2O // autoclaved	150 mL
1 M $MgSO_4$ // autoclaved	350 μL
1 M $CaCl_2$ // autoclaved	17.5 μL
100 mg/mL ampicillin stock	87.5 μL
Solution C (Table 5.3)	3.5 mL
Vitamin stock (Table 5.5)	87.5 μL
Thiamin solution (0.01 g in 20 mL H_2O, freshly made, sterile filtered)	35 μL
NH_4Cl (natural abundance)	0.525 g
Glycerol (natural abundance)	0.35 g
$NaHCO_3$ (natural abundance)	0.35 g

Table 6.6 Formula for 175 mL ^{1}H-minimal media for growth and expression of deuterated protein

M9 buffer (10x) // autoclaved (Table 5.2)	100 mL
H_2O // autoclaved	35 mL
D_2O	650 mL
1 M $MgSO_4$ // autoclaved	2 mL
1 M $CaCl_2$ // autoclaved	100 μL
100 mg/mL ampicillin stock	500 μL
Solution C (Table 5.3)	20 mL
Vitamin stock (Table 5.5)	500 μL
Thiamin solution (0.01 g in 20 mL H_2O, freshly made, sterile filtered)	200 μL
NH_4Cl (natural abundance)	3 g
Glycerol (natural abundance)	2 g
$NaHCO_3$ (natural abundance)	2 g

Table 6.7 Formula for 1 L 65% ^{2}H-minimal media for growth and expression of deuterated protein

M9 buffer (10x) in D_2O with $MgSO_4$, $CaCl_2$, and $CuCl_2$ (Table 5.9)	50 mL
D_2O	430 mL
100 mg/mL ampicillin in D_2O	250 μL
Biotin	0.23 g
Thiamin	0.5 g
$^{15}NH_4Cl$	1.5 g
^{2}H, [1,3-^{13}C] glycerol	1 g
$NaHCO_3$ (natural abundance)	1 g

Table 6.8 Recipe for 500 mL 100% deuterated minimal media for the growth of ^{2}H, [1,3-^{13}C] glycerol, ^{15}N-TIM

Na_2HPO_4 (anhydrous)	6.8 g
KH_2PO_4	3 g
NaCl	0.5 g
$MgSO_4$ (anhydrous)	0.24 g
$CaCl_2$ (anhydrous)	11 mg
$CuCl_2 \bullet 2H_2O$ (anhydrous not available)	8.5 mg

Table 6.9 Recipe for 100 mL 10x M9 buffer in D_2O

6.5 Growth of ^{2}H, ^{15}N-Valine TIM

For growth of ^{2}H, ^{15}N-valine labeled TIM, the protocol above for ^{2}H, ^{13}C-glycerol, ^{15}N TIM was modified as follows. For 500 mL 100% deuterated media, the following recipe was used:

M9 buffer (10x) in D_2O with $MgSO_4$, $CaCl_2$, and $CuCl_2$ (Table 5.9)	50 mL
D_2O	450 mL
100 mg/mL ampicillin in D_2O	250 μL
Biotin	0.23 g
Thiamin	0.5 g
NH_4Cl (natural abundance)	1.5 g
^{2}H-glucose	2 g
^{2}H, ^{15}N-valine	0.5 g

Table 6.10 Recipe for 500 mL 100% deuterated media for the growth of ^{3}H, ^{15}N-valine TIM

6.6 TIM Purification

TIM purification (all labeling schemes) was performed as follows:

All solutions, including ruptured cells were kept on ice. After every step, aliquots were collected for monitoring purification via UV (absorbance at 280 nm vs 260 nm) and gel electrophoresis.

After harvesting, the cells were resuspended in ~ 30 mL resuspension buffer (pH = 7.8 at 4°C, Table 6.11). The more dilute this cell suspension, the more efficient the purification. Cells were lysed using the French press, run through 2-3 times. The lysate was centrifuged at 10000 g, 4°C for 20 minutes to remove cell debris. The solution is then equilibrated with ammonium sulfate (45% saturation, 258 g/L solution) at 4°C for 1-2 hours to precipitate membrane proteins. The solution was then centrifuged at 12000 g, 4°C for 20 minutes to remove precipitant. The solution was dialyzed extensively (12-24 hours) against 3.5 L of buffer: 50 mM Tris-HCl, 300 mM NaCl, 1 mM ETDA (pH = 7.8 at 4°C). Enough dialysis tubing was allowed for the volume of the solution to double.

50 mM Tris	0.303 g
150 mM NaCl	0.4383 g
20 mM KH_2PO_4	0.136 g
1 mM EDTA	0.0202 g
1 mM DTT (dithiothreitol)	0.0077 g
1 μM PMSF (phenylmethylsulfonyl fluoride)	0.0001 g
protease inhibitor cocktail	1 mL

Table 6.11 Recipe for 50 mL resuspension buffer (pH = 7.8 at 4°C). Tris, NaCl, KH_2PO_4, and EDTA are added and the pH is adjusted to 7.8 at 4°C. The remaining chemicals are then added.

The solution was equilibrated with protamine sulfate for 1 hour for the precipitation of nucleic acids at a concentration of 1.5 mg of protamine sulfate per mL protein solution. The solution was then centrifuged at 14000 g, 4°C for 15 minutes. (The original protocol called for 12000 g for 10 minutes, but this was not efficient enough.) The solution was dialyzed extensively (12-24 hours) against 3.5 L of buffer: 50 mM Tris-HCl, 150 mM NaCl, 1 mM EDTA (pH=7.8 at 4°C). Nucleic acids were then removed using a Q-sepharose fast flow column, run using the same buffer as used for dialysis. The solution was dialyzed against 10 mM Tris-HCl (pH=7.8 at 4°C).

This dialysis can be done by ultrafiltration if concentration is needed. The enzyme was further purified using a Q-sepharose fast flow column with a linear gradient of 0-150 mM KCl. Fractions containing protein, as confirmed with gel electrophoresis and UV-vis spectroscopy, were combined and an activity assay was performed.

Sample gels of the purification process are shown in Figure 6.1. The mass of protein at each step can be estimated through the following formula: A_{280} x 2.015 x volume of solution (based on TIM extinction coefficient).

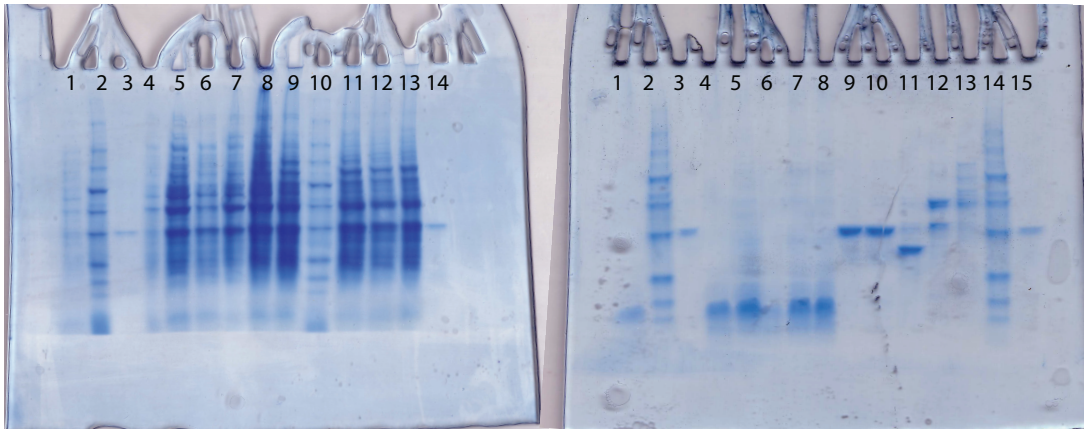

Figure 6.1 Sample gels monitoring the purification process. The left gel is aliquots collected over the course of TIM growth. Lanes 2 and 10 contain protein marker, lanes 3 and 4 contain purified TIM for reference. Lanes 1 and 4 are the growth before induction of protein expression. There is a very notable increase in the intensity of the TIM band (as well as other bands) from lane 4 to 5, which is one hour after induction of protein expression. The right gel is fractions of a KCl gradient Q-sepharose column. Lanes 2 and 14 contain protein marker, lanes 3 and 15 contain purified TIM for reference, pure TIM from the column appears in lanes 9 and 10. Other lanes are other fractions from the column that contain impurities.

For the activity assay, the following solutions were prepared: 100 mM TEA (triethanolamine-HCl) solution (pH = 7.6 at room temperature), 5.6 mg NADH (β-Nicotinamide adenine dinucleotide, reduced dipotassium salt) in 2 mL TEA solution, 75 μL GDH/GHP (glycerol-3-phosphate dehydrogenase, α-glycerophosphate dehydrogenase) in 675 μL TEA solution, and approximately 4 commercial TIM/TEA diluted solutions (i.e. 1 μL TIM + 100 μL TEA solution

(solution 1), 10 μL solution 1 + 2351.2 μL TEA solution, 10 μL solution 1. + 1000 μL TEA solution, 10 μL solution 1 + 500 μL TEA solution, 10 μL solution 1. + 250 μL TEA solution). Dilutions needed may vary depending on observed UV absorbances.

Control assays were run, being sure to 'practice' until reproducible slopes could be obtained using a constant TIM concentration. Solutions were added in the following order with the cuvettes already in the UV spectrometer: 891 μL TEA solution, 17 μL GAP (D-glyceraldehyde 3-phosphate), 66.7 μL NADH solution, 15 μL GDH solution, and 10 μL diluted TIM solution. These volumes were chosen such that the final volume in the cuvette was always exactly 1 mL. The solution was quickly mixed 3 times using a 1 mL pipette and the UV measurement was started as quickly as possible. The length of each run was 60 seconds, recording the absorbance at $\lambda = 340$ nm every 10 seconds. 4-5 runs were performed for each TIM concentration, recording time and absorbance to get an average slope (i.e. Δ Abs) for each TIM concentration. Often, only the last 30 s (out of 1 min of UV data per run, recording every 10 s) was used for calculations because first 30 s of data tended to be non-linear. The activity assay was then performed as described above using the labeled TIM sample, diluted as necessary.

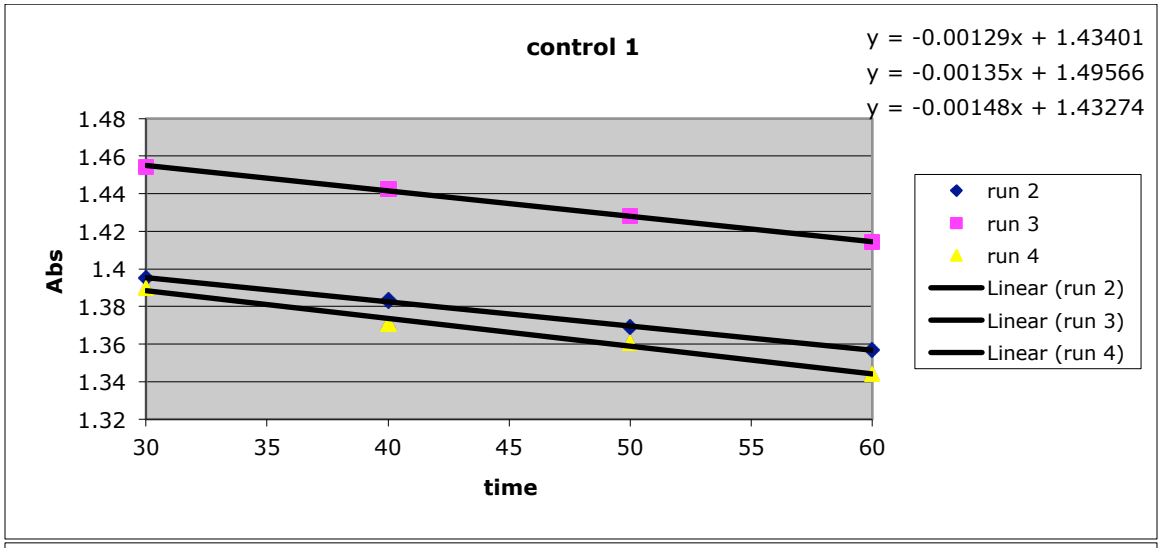
control 1
y = -0.00129x + 1.43401
y = -0.00135x + 1.49566
y = -0.00148x + 1.43274
Abs
time
run 2
run 3
run 4
Linear (run 2)
Linear (run 3)
Linear (run 4)

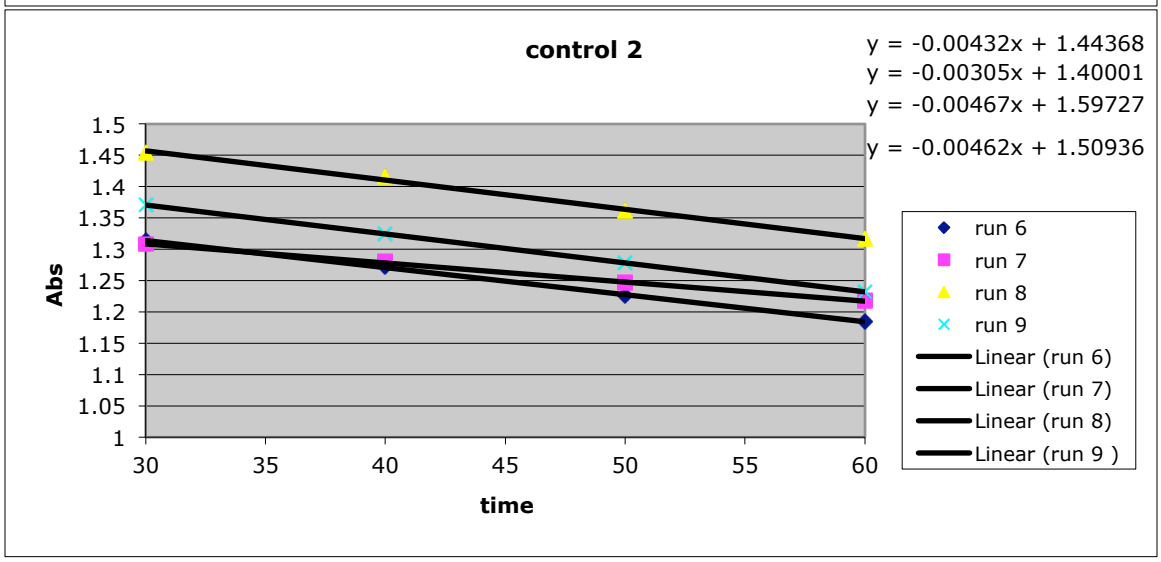
control 2
y = -0.00432x + 1.44368
y = -0.00305x + 1.40001
y = -0.00467x + 1.59727
y = -0.00462x + 1.50936
Abs
time
run 6
run 7
run 8
run 9
Linear (run 6)
Linear (run 7)
Linear (run 8)
Linear (run 9)

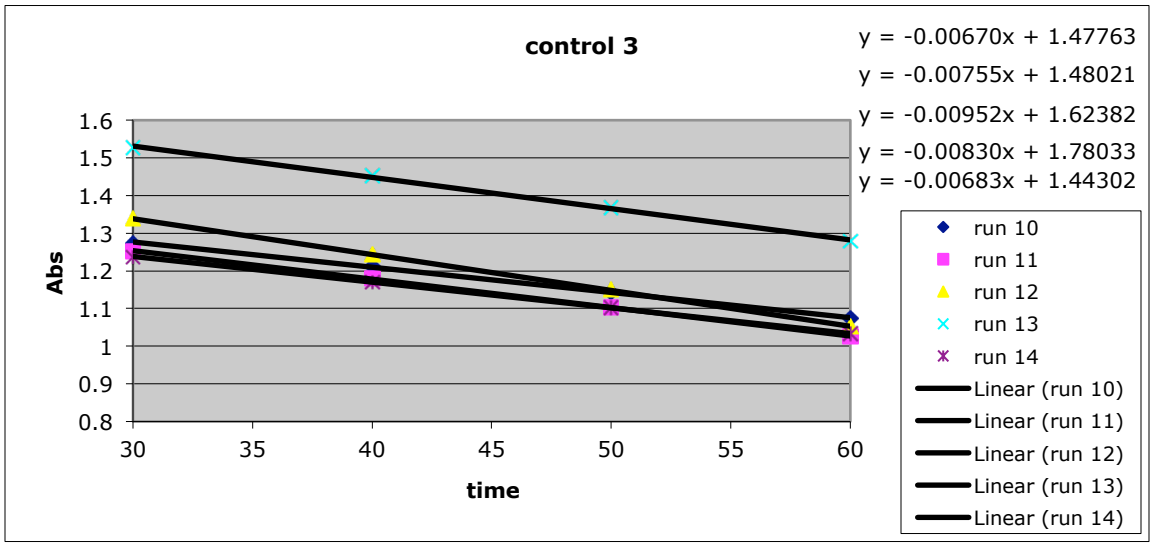
control 3
y = -0.00670x + 1.47763
y = -0.00755x + 1.48021
y = -0.00952x + 1.62382
y = -0.00830x + 1.78033
y = -0.00683x + 1.44302
Abs
time
run 10
run 11
run 12
run 13
run 14
Linear (run 10)
Linear (run 11)
Linear (run 12)
Linear (run 13)
Linear (run 14)

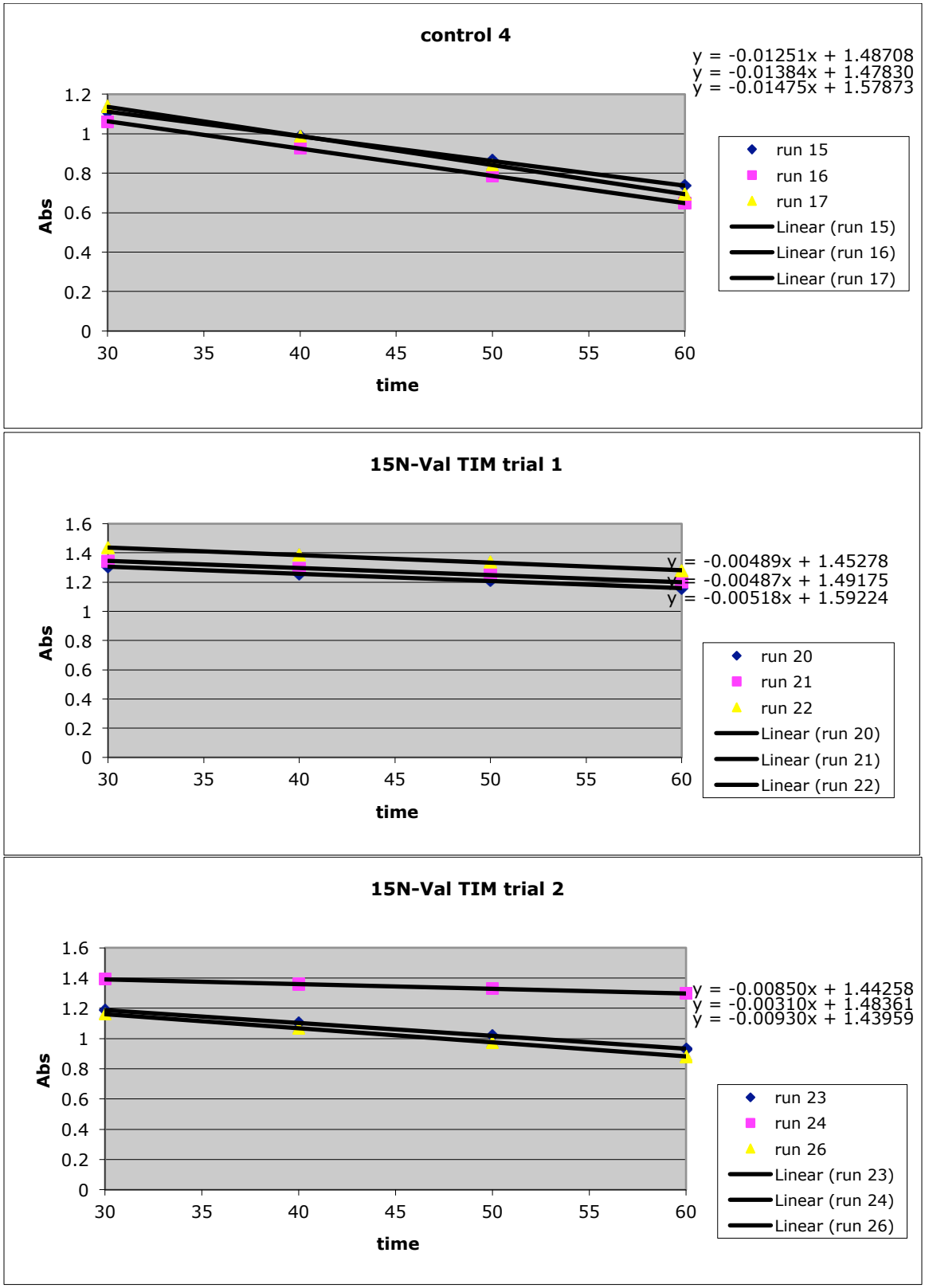

Figure 6.2 Sample ΔAbs curves for ^{15}N-Valine labeled TIM activity assay.

TIM activity was calculated as follows according to Beer's law.

$$\frac{d}{dt} Abs_{NADH} = l \cdot \varepsilon \cdot \frac{d}{dt}[NADH] \quad (1)$$

where $\frac{d}{dt} Abs_{NADH}$ is the slope from the ΔAbs curves like those in Figure 6.2, l (the path length) = 1 cm, ε (the TIM extinction coefficient) = 6.22 x 10^3 $M^{-1}cm^{-1}$ and $\frac{d}{dt}[NADH]$ is the activity. Therefore,

$$activity = \frac{avg\ slope}{\varepsilon} \quad (2)$$

converted to units of μM per minute.

$$\frac{d}{dt}[NADH] = \frac{\mu mol}{L \cdot min} = \frac{units}{L} \times \frac{1\ L}{1000\ mL} = units\ in\ cuvette \quad (3)$$

given the final volume of 1 mL for the solutions in the cuvette. The mass of TIM added to each cuvette is then calculated given the concentration of the original protein solution and any dilutions (i.e. 10 μL of protein solution is diluted to 1 mL of solution in the cuvette). The specific activity is units in cuvette per mg TIM added to each cuvette. Ideal TIM activity is ~ 9000, however activities typically attained in these measurements were ~ 4000, which has been previously observed in our group as well.

Once enzyme activity was confirmed, the protein solution was dialyzed against 1.4 M $(NH_4)_2SO_4$, 50 mM $Na_3(PO_4)_2$ and run through a phenyl-sepharose column with a linear gradient of 1.4-0 M $(NH_4)_2SO_4$. Purity was confirmed via gel electrophoresis and UV-vis spectroscopy (A_{280}/A_{260} > 1.7). Purity and labeling scheme were also confirmed with mass spectrometry (Figure 6.3). Typical yields were ~ 100 mg, with deuterated protocols giving somewhat lower yields. Final protein concentrations and yields were determined through UV and Bradford assay.

The protein was finally concentrated and dialyzed into the NMR buffer: 50 mM Tris, 50 mM NaCl, 1 mM EDTA, pH = 6.8 at 4°C (TIM buffer). For deuterated samples, this buffer was prepared with 90% D_2O, 10% H_2O.

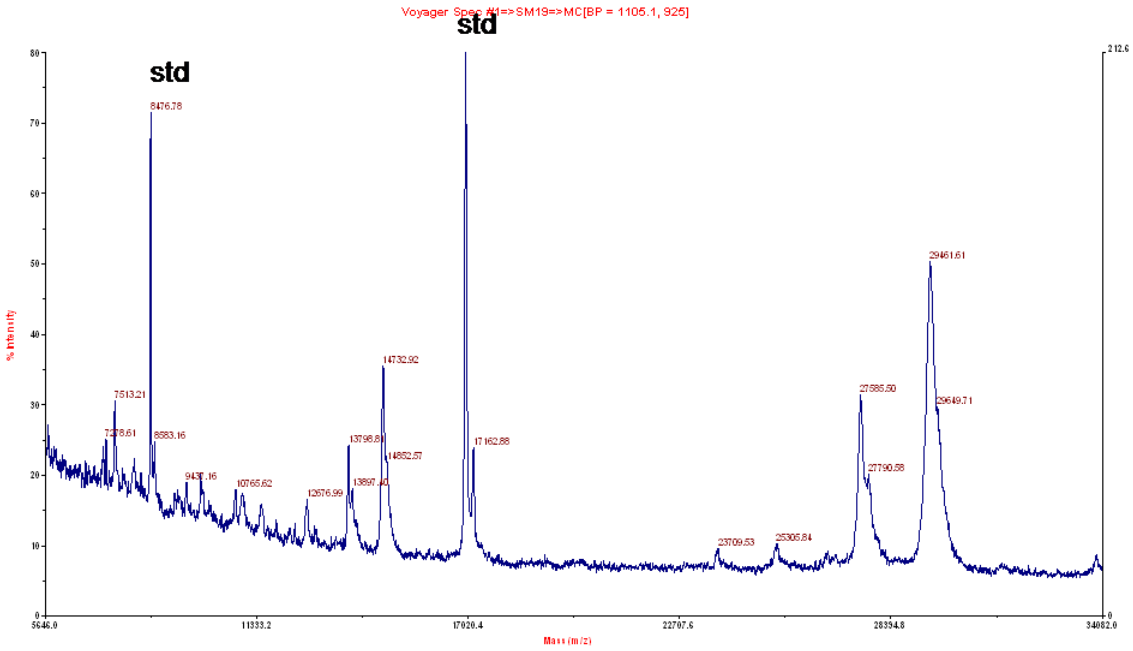

Figure 6.3 Sample mass spectrometry results for ^{2}H, [1,3-^{13}C] glycerol, ^{15}N-TIM. The peaks at 29,500 and 27,500 m/z are TIM protein. The peak with the higher m/z is deuterated protein while the lower peak is protein that is largely still protonated.

6.7 Crystallization and Ligand Binding

The protein was crystallized and particular care was taken to ensure the desired ratio of ligand to protein in samples where ligand was added. Ideal crystallization conditions were found to be ~ 200 mg/mL concentrated TIM solution and a final PEG concentration of 15%.

As utilized in experiments in Chapter 4, to obtain the desired populations of bound to unbound phosphate, the K_d of PO_4^{3-} in TIM, active site concentration, % bound TIM, and total [PO_4^{3-}] concentration must be taken into account.

From the expression given by Jones and Waley [1] for enzyme binding

$$K_d = \frac{1-y}{y}(L_t - S_t y) \quad (4)$$

where K_d is the dissociation constant for a particular ligand with the enzyme, y is the fraction of bound active sites, S_t is the total concentration of active sites, and L_t is the total ligand concentration, the total [PO_4^{3-}] necessary to attain 1:1 bound-to-unbound PO_4^{3-} can be calculated.

The effect of precipitation, centrifugation, and rotor packing on the hydration of the protein pellet and the concentration of ligand in solution has not been characterized. Therefore to attain the desired concentrations as closely as possible, the protein was crystallized without any ligand, and phosphate solution of the desired concentration was added to the protein once it was inside the rotor.

The same expression was used to determine desired G3P concentrations for studies of TIM loop dynamics when the desired ratio was 50/50 open-to-closed loop conformation. In these samples, the approximate pellet volume was estimated based upon the mass of protein before crystallization and G3P in TIM buffer was added at a concentration which given dilution in the precipitation solution would have the desired final volume in the pellet.

6.8 References

[1] R.B. Jones, S.G. Waley, Spectrophotometric Studies on the Interaction between Triose Phosphate Isomerase and Inhibitors, Biochem J, 179 (1979) 623-630.

Chapter 7

Conclusions and Future Directions

7.1 Conclusions

Within the available array of NMR techniques to observe protein dynamics, spin relaxation has a broad range of applicability. Rotating frame ($R_{1\rho}$) relaxation is sensitive to dynamics on the microsecond (μs) timescale. $R_{1\rho}$ measurements in the solid state are a powerful technique to observe intermediate timescale dynamic processes in proteins. In contrast to solution NMR, where $R_{1\rho}$ relaxation requires changes in isotropic chemical shift among exchanging conformational states, this is not a limitation in the solid state.

$R_{1\rho}$ measurements in the solid state can utilize either the reorientation of a chemical shift tensor or dipolar vector as a probe of dynamics. We have pursued using the chemical shift tensor to observe dynamics. This method has the additional advantages in that sites of interest do not need to have attached protons, or even undergo an angular change. Analysis of $R_{1\rho}$ relaxation due to the CSA is simplified relative to dipolar vector reorientation. The strong dipolar couplings among spins in a typical NMR sample make it difficult to isolate individual spin pairs for quantitative analysis [1]. Despite this challenge, $R_{1\rho}$ measurements of dipolar systems have been done with techniques to reduce spin-diffusion (deuteration and fast MAS) with semi-quantitative results [2, 3].

Through model compound studies of dimethyl sulfone (DMS), discussed in Chapter 3, we have shown that $R_{1\rho}$ relaxation due to CSA tensor modulation is a large effect in the solid state. Rates of chemical exchange were quantified through numerical simulations and quasi-global analysis with Spinevolution [4]. The exchange rates and activation energies obtained for DMS over a

range of temperatures from 40-80°C are in excellent agreement with values previously reported in the literature from many other solid state NMR dynamics techniques. Quantitative results required deuteration of the methyl sites to reduce dipolar contributions. Low temperatures and high spin-lock field strengths, where the exchange contribution to relaxation is suppressed, were utilized to distinguish the non-dynamic (R_2^0) contribution to the observed relaxation rate. Additional experimental considerations include avoiding the rotary resonance conditions ($\omega_1 = \omega_R, 2\omega_R$) where relaxation becomes multi-exponential, using direct excitation rather than cross polarization, and determining true sample temperature.

We extended these $R_{1\rho}$ measurements to the study of ligand binding in triosephosphate isomerase. TIM is a key protein in the glycolytic pathway, responsible for the interconverstion of dihydroxyacetone phosphate (DHAP) and glyceraldehyde-3-phosphate (GAP). The phosphate moiety of the substrate is essential for proper positioning in the active site, preventing formation of the toxic side product, methyl glyoxyl, and is largely responsible for the rate acceleration of the catalytic mechanism.

In contrast to the model compound studies where the CSA tensor modulation effect was reorientation of the tensor relative to the static magnetic field (B_0), in the ligand binding work, the effect was the change in the magnitude of the ligand chemical shift tensor as it binds and releases from the protein. We hypothesize that when the ligand is unbound, it has isotropic behavior, but when bound, chelation to protein residues will reintroduce the anisotropic component of the chemical shift tensor. Utilizing the change in tensor magnitude rather than tensor orientation to observe dynamics is a relatively novel concept in solid state NMR.

The chemical shift tensor from slow MAS spectra was measured with $\delta = 74 \pm 8$ ppm and $\eta = 0.2 \pm 0.3$. The positive sign of the anisotropy suggests the ligand is a dianion (HPO_4^{2-} rather than $H_2PO_4^-$) and/or involved in extensive hydrogen bonding, as is suggested by PO_4^{3-} ligated crystal structures [5-7]. The relatively small η is also consistent with a dianion. Caveats of this conclusion include the possible influence of ligand dynamics, and the absence of interpretation in terms of hydrogen bonding.

$R_{1\rho}$ measurements of PO_4^{3-} dynamics indicated that at physiological temperatures, the observed dynamic process is above the μs timescale. This is much faster than the expected ms to μs timescale process associated with ligand binding upon loop opening and closing. The anticipated timescale was approximated from fluorescence t-jump measurements of TIM with PO_4^{3-} as well as the mM K_d also seen for DHAP and G3P [8]. While the kinetics measured with fluorescence were multi-exponential, dynamics on the μs and ms timescales were observed. We hypothesize that we are observing the ligand moving in and out of the active site on a rapid timescale that does not allow time for the loop to close. This rapid process may be dominating the measured $R_{1\rho}$ relaxation even if the slower dynamic processes are present. Going to higher temperatures could test this hypothesis, but is not appropriate for a temperature-sensitive biological sample. A secondary hypothesis is that the observed dynamics are related to a phase transition of the hydration shell. It may be that the phosphate tensor is reporting on the dynamics of the solvent, if the ^{31}P resonance we are observing are non-specifically bound to the protein surface [9-11]. As the temperature is lowered, the solvent dynamics, including PO_4^{3-} ions, are no longer a fast

timescale, isotropic process. Measurements of protein-ligand correlations can help rule out this possibility.

Another interest was in extending the resonance assignments of TIM and assigning key catalytic residues such as Glu 165. To achieve this goal, selective labeling with [1,3-^{13}C] and [2-^{13}C] glycerol were employed, along with deuteration. New resonances were observed in low temperature spectra, likely from slowed dynamics. NCO spectra with the nitrogen carrier placed at 139 ppm observed downfield nitrogen resonances, which may include the Pro 166 N to Glu 165 CO correlation.

$R_{1\rho}$ measurements of ^{15}N-valine TIM were inconclusive. There was no discernable trend in the spin-lock field strength dependence of any regions of the ^{15}N 1D spectra. It is likely that the sample and experimental conditions were not optimal to detect the dynamic process with $R_{1\rho}$. The absence of deuteration and use of proton decoupling, the sample temperature, and/or low signal-to-noise may have limited the sensitivity of the measurements.

To summarize, we have shown that the reorientation of a chemical shift tensor can be used as a quantitative probe of dynamics through $R_{1\rho}$ measurements in the solid state. The success of the method relies on the elimination of dipolar interactions. The application of $R_{1\rho}$ measurements to biological systems can be combined with other techniques to observe dynamics in these systems.

7.2 Future Directions

7.2.1 Future Studies of TIM Ligand Binding

As described in Chapter 4, progress has been made toward characterizing the ionic state and dynamics of the inorganic phosphate ligand (PO_4^{3-}) interacting with TIM. Future work will seek to confirm the observation of a dianionic state for the ligand, as well as to gain further insight into the interactions of the ligand with the protein (hydrogen bonding etc). The roles of Lys 12, His 95, and Glu 165 in catalysis by TIM have been extensively debated in the literature. The ionic state of the phosphate moiety of TIM ligands has important implications for the catalytic mechanism. Richard and co-workers have also shown that the phosphate moiety of the ligand is largely responsible for rate acceleration of the isomerization by the enzyme. The binding energy of this group enables the large scale conformational change of loop 6 [12]. Friesner and co-workers discussed the importance of the singly charged phosphate moiety in the catalytic process and concluded that Glu 165 is responsible for proton transfer, rather than His 95; their work emphasized the importance of the proximity of Lys 12 to the carbon moiety of the ligand. This proposed catalytic mechanism has also been supported by crystallographic and NMR studies [13, 14]. Other NMR studies have observed a mixture of mono- and dianions for TIM-bound DHAP and G3P [15]. Given the continuing debate in the literature over the ionization state of the TIM ligand and the true catalytic pathway, it is of great interest to further pursue work that can address these questions.

Tensor fittings may be improved by using samples that are under-titrated (i.e. the sample is prepared such that 100% ligand is bound) reducing interference at the centerband frequency from the isotropic unbound PO_4^{3-} species. The true sample pH must be carefully considered given the

temperature-dependent pK_as for both Tris and $HPO_4^{2-}/H_2PO_4^-$ and the additional dependence of pH on the ionic strength of the buffer. The effect that changes in pH may have on the crystal form is uncertain. From a survey of TIM structures in the PDB, there is not enough consistency among other experimental factors (mutations, ligands, buffers, etc) to make any confident assertions regarding the dependence of the crystal form on pH, but it is a factor to be considered.

Slow MAS CSA tensor measurements at different pHs may provide valuable insight into the ligand ion state and its role in catalysis. This is particularly interesting given that alternative catalytic mechanisms to that originally proposed by Albery and Knowles [16] have recently been published. It has been suggested that the catalytic mechanism is not altered in the pH regime of ~ 5 to 9 [17], therefore we would expect to observe a dianionic ligand over this range of pHs (assuming we are observing ionic state rather than hydrogen bonding character). Studying the pH dependence is important given that our data collected to date was in the pH range of 7.5 to 7.8, above the anticipated pK_a value. On the other hand, if we are observing a mixture of mono- and dianion as has been suggested from solution NMR experiments [15, 18], this would be reflected in changes in the tensor with pH. Another consideration that may be reflected in spectra is the ligand affinity as a function of pH [15, 19]. Given the sensitivity of the tensor parameters to bond length, these changes may affect the tensor. As P-O bonds become shorter with weaker protein affinity, δ_{33} shifts upfield and δ_{11} shifts downfield [20, 21]. The effect on the sign of the overall tensor would depend on the relative magnitudes of these changes. Interpretation of the tensor in terms of bond length would be more reflective of the hydrogen bonding network than the ionization state. Overall, the interpretation of the pH dependence of the chemical shift tensor may be complicated but is a worthwhile endeavor.

Of great interest would be to measure the CSA tensor of the native ligand DHAP. Solution NMR studies have shown that both the monoanion and dianion bind [15]. QM/MM computional work has suggested that the monoanion is the catalytically productive ionization state. A challenge to working with this particular ligand is that it is prone to hydrolysis over the extended periods of time that are generally necessary for solid state NMR experiments. This effect can be reduced by using low temperatures [15].

Tensor measurements of the tightly binding ligand PGA may provide complementary results. PGA is significantly more stable than DHAP. The tensors of these 2 ligands with significantly different dynamics are worth comparing for multiple reasons. The magnitude of the ^{31}P tensor for static PGA may indicate if there is a degree of dynamic averaging of the observed CSA tensor for PO_4^{3-}. Comparison of the ionic states of these ligands may provide further insight into the catalytic mechanism, and a possible correlation between ionization state and dynamics. The pH dependence of the ^{31}P chemical shift for PGA has suggested that this ligand is a dianion over the pH range of 5.5 to 8.5, while DHAP appears to have a mixture of mono- and dianion [15]. Thus we expect PGA to have a positive value for δ. Both solid state and solution NMR measurements have concluded that the carbonyl carbon of PGA is also deprotonated [15, 22]. Wojciechowski et al have shown that the pK_a of a phosphate group depends on other charged residues in the vicinity of the PO_4^{3-} moiety [23].

Relative to a free phosphate ion in solution, the phosphate esters DHAP, G3P, and PGA have lower pK_as (5.6 for DHAP vs 6.8-7.2 for $H_2PO_4^-$ [15]). Well-solvated phosphate-esters have

pK_as close to 7, but that is not the case for buried ligands where the pK_a will be lower [23]. Guallar et al also mentioned the expectation of a shifted pK_a for a buried phosphate group [24]. The K_d of arsnate, another competitive inhibitor of TIM, is larger than that of phosphate (12 mM vs 5 mM for yeast TIM) and thus would likely not provide any new insight [25].

Adding labels to the protein will be a valuable means of evaluating interactions of the ligand with the protein. Recently, the CO carbons of Gly 232 and Gly 233, as well as the amide N of Gly 233 have been assigned [26]. These residues are known to bind the phosphate moiety of TIM ligands [27]. Phosphorous correlation experiments (i.e. TEDOR, [28]) can indicate whether the ligand-protein interactions are specific or non-specific. Confirmation that the observed anisotropic interaction is the specific interaction of the ligand with the active site will confirm the validity of dynamics experiments. If ^{15}N resonances for the opened and closed forms of the loop are distinguishable, these correlations may also provide confirmation of a species where the ligand is bound to the loop in the open conformation. Furthermore, significant deviation from P-N,C distances observed in the crystal structures can also be viewed as an indicator of dynamics. The details of this deviation could provide insight into the dynamic process. A challenge of these measurements however could be the long intranuclear distances and weak dipolar couplings.

We also seek to test the hypothesis that the dynamics of PO_4^{3-} as observed via $R_{1\rho}$ measurements are due to the ligand moving in and out of the active site while the loop remains in the open position. Approaches to this may include $R_{1\rho}$ measurements of PGA, which is known to induce the closed loop conformation, with slow timescale dynamics; in addition this ligand does not

hydrolyze as has been reported for DHAP and G3P [15, 29]. With this tightly binding ligand, we expect $R_{1\rho}$ experiments to be spin-lock field strength independent over a broad range of temperatures comparable to those previously utilized (dynamics will be below the timescale that $R_{1\rho}$ measurements are accessible to at all temperatures). In addition, measurements of $R_{1\rho}$ for the PGA ligand may provide a good measure of R_2^0 contributions to the observed relaxation rate. Future $R_{1\rho}$ measurements of both PO_4^{3-} and PGA will utilize uniformly deuterated protein and buffer to eliminate any residue relaxation from dipolar contributions. The merits of using G3P rather than PO_4^{3-} should also be considered. The dynamics of this ligand are known to be on the millisecond timescale [30] and may be detectible with $R_{1\rho}$ measurements. CPMG experiments or other solid state NMR dynamics methods may complement $R_{1\rho}$ studies by accessing different timescales [31]. If spin labels are added to the protein itself as discussed above, $R_{1\rho}$ measurements of the loop dynamics can provide complementary information (for example Gly 171), and may help solidify the hypothesis that the loop is in an open conformation during the observed dynamic process of the ligand.

It has been shown that TIM can be mutated such that the closed state of loop 6 is no longer stabilized (Y208F) [32, 33]. In TIM with this mutation, we may observe the same behavior as reported in Chapter 4, providing further evidence that the ligand is moving in and out of the active site in the absence of loop closure. Other mutations of loop 7 have a similar impact on the dynamics of loop 6 [34]. Mutations of the loop 6 hinge residues (166-PVW-168 to 166-PGG-168 and 174-KTA-176 to 174-GGG-176) lead to an increase in nanosecond timescale fluctuations of the loop [35]. While providing supporting evidence, relaxation rates measured from mutants like these are unlikely to be conclusive regarding the loop dynamics.

In conclusion, this work can set the stage for obtaining greater insight into the catalytic mechanism and the role of loop dynamics of TIM.

7.2.2 Future Studies of TIM Loop Dynamics

Using selective labeling and deuteration for 3-dimnesional spectra can determine the inter- and intra- residue correlations of the observed resonances [36] and precise assignment of the selectively labeled spectra. In particular for the assignment of Glu 165, the extension of the low temperature measurements and N-C correlation measurements with the shifted nitrogen carrier to a third dimension may allow the assignment of the Pro 166 – Glu 165 correlation, as well Glu 165 side chain resonances. Given the downfield nitrogen shift of Pro 166, using a shifted nitrogen carrier will allow further study of this resonance. Low temperature measurements have great potential for future assignments by dramatically slowing the dynamics, as evidenced by the appearance of many new resonances in the spectrum reported in Chapter 5. Combining low temperatures with deuterated protein will help mitigate the anticipated linebroadening.

To successfully measure the dynamics of loop 6 of TIM with $R_{1\rho}$ experiments, several modifications can be made to the work discussed here. As shown from model compound studies, deuteration can make a significant difference in $R_{1\rho}$ measurements by reducing dipolar couplings as well as reducing sample heating and Hartmann-Hahn effects from proton

decoupling. Sample temperature is an important consideration that can be better controlled through the use of an E-free probe.

There are many possibilities for extending the work described in this thesis to gain further insight into the catalytic mechanism and dynamics of TIM.

7.3 References

[1] D.L. Vanderhart, A.N. Garroway, C-13 Nmr Rotating Frame Relaxation in a Solid with Strongly Coupled Protons - Polyethylene, J Chem Phys, 71 (1979) 2773-2787.

[2] J.R. Lewandowski, H.J. Sass, S. Grzesiek, M. Blackledge, L. Emsley, Site-Specific Measurement of Slow Motions in Proteins, J Am Chem Soc, 133 (2011) 16762-16765.

[3] A. Krushelnitsky, T. Zinkevich, D. Reichert, V. Chevelkov, B. Reif, Microsecond Time Scale Mobility in a Solid Protein As Studied by the N-15 R-1 rho Site-Specific NMR Relaxation Rates, J Am Chem Soc, 132 (2010) 11850-11853.

[4] M. Veshtort, R.G. Griffin, SPINEVOLUTION: A powerful tool for the simulation of solid and liquid state NMR experiments, J Magn Reson, 178 (2006) 248-282.

[5] C.H. Chu, Y.J. Lai, H.M. Huang, Y.J. Sun, Kinetic and structural properties of triosephosphate isomerase from Helicobacter pylori, Proteins, 71 (2008) 396-406.

[6] C.L.M.J. Verlinde, M.E.M. Noble, K.H. Kalk, H. Groendijk, R.K. Wierenga, W.G.J. Hol, Anion Binding at the Active-Site of Trypanosomal Triosephosphate Isomerase - Monohydrogen Phosphate Does Not Mimic Sulfate, Eur J Biochem, 198 (1991) 53-57.

[7] P. Hartmann, J. Vogel, B. Schnabel, The Influence of Short-Range Geometry on the P-31 Chemical-Shift Tensor in Protonated Phosphates, J Magn Reson Ser A, 111 (1994) 110-114.

[8] R. Desamero, S. Rozovsky, N. Zhadin, A. McDermott, R. Callender, Active site loop motion in triosephosphate isomerase: T-jump relaxation spectroscopy of thermal activation, Biochemistry-Us, 42 (2003) 2941-2951.

[9] A.B. Siemer, K.Y. Huang, A.E. McDermott, Protein-ice interaction of an antifreeze protein observed with solid-state NMR, P Natl Acad Sci USA, 107 (2010) 17580-17585.

[10] A.B. Siemer, K.Y. Huang, A.E. McDermott, Protein Linewidth and Solvent Dynamics in Frozen Solution NMR, Plos One, 7 (2012).

[11] A.B. Siemer, A.E. McDermott, Solid-State NMR on a Type III Antifreeze Protein in the Presence of Ice, J Am Chem Soc, 130 (2008) 17394-17399.

[12] J.P. Richard, A Paradigm for Enzyme-Catalyzed Proton Transfer at Carbon: Triosephosphate Isomerase, Biochemistry-Us, 51 (2012) 2652-2661.

[13] T.K. Harris, C. Abeygunawardana, A.S. Mildvan, NMR studies of the role of hydrogen bonding in the mechanism of triosephosphate isomerase, Biochemistry-Us, 36 (1997) 14661-14675.

[14] G. Jogl, S. Rozovsky, A.E. McDermott, L. Tong, Optimal alignment for enzymatic proton transfer: Structure of the Michaelis complex of triosephosphate isomerase at 1.2-angstrom resolution, P Natl Acad Sci USA, 100 (2003) 50-55.

[15] I.D. Campbell, R.B. Jones, P.A. Kiener, S.G. Waley, Enzyme-Substrate and Enzyme-Inhibitor Complexes of Triose Phosphate Isomerase Studied by P-31 Nuclear Magnetic-Resonance, Biochem J, 179 (1979) 607-621.

[16] W.J. Albery, J.R. Knowles, Free-Energy Profile for Reaction Catalyzed by Triosephosphate Isomerase, Biochemistry-Us, 15 (1976) 5627-5631.

[17] B. Plaut, J.R. Knowles, Ph-Dependence of Triose Phosphate Isomerase Reaction, Biochem J, 129 (1972) 311-&.

[18] C. Gardiennet-Doucet, X. Assfeld, B. Henry, P. Tekely, Revealing successive steps of deprotonation of L- phosphoserine through C-13 and P-31 chemical shielding tensor fingerprints, J Phys Chem A, 110 (2006) 9137-9144.

[19] R.B. Jones, S.G. Waley, Spectrophotometric Studies on the Interaction between Triose Phosphate Isomerase and Inhibitors, Biochem J, 179 (1979) 623-630.

[20] S. Un, M.P. Klein, Study of P-31 Nmr Chemical-Shift Tensors and Their Correlation to Molecular-Structure, J Am Chem Soc, 111 (1989) 5119-5124.

[21] J. Gajda, S. Olejniczak, I. Bryndal, M.J. Potrzebowski, Elucidation of Structural Restraints for Phosphate Residues with Different Hydrogen Bonding and Ionization States, J Phys Chem B, 112 (2008) 14036-14044.

[22] Y. Tomita, E.J. Oconnor, A. Mcdermott, A Method for Dihedral Angle Measurement in Solids - Rotational Resonance Nmr of a Transition-State Inhibitor of Triose Phosphate Isomerase, J Am Chem Soc, 116 (1994) 8766-8771.

[23] M. Wojciechowski, T. Grycuk, J.M. Antosiewicz, B. Lesyng, Prediction of secondary ionization of the phosphate group in phosphotyrosine peptides, Biophys J, 84 (2003) 750-756.

[24] V. Guallar, M. Jacobson, A. McDermott, R.A. Friesner, Computational modeling of the catalytic reaction in triosephosphate isomerase, J Mol Biol, 337 (2004) 227-239.

[25] A.M. Lambeir, F.R. Opperdoes, R.K. Wierenga, Kinetic-Properties of Triose-Phosphate Isomerase from Trypanosoma-Brucei-Brucei - a Comparison with the Rabbit Muscle and Yeast Enzymes, Eur J Biochem, 168 (1987) 69-74.

[26] W. Li, Investigation of Slow Dynamics in Proteins: NMR Pulse Development and Application in Triosephosphate Isomerase, in: Department of Chemistry, Columbia University, New York, 2012.

[27] J.P. Richard, Acid-Base Catalysis of the Elimination and Isomerization-Reactions of Triose Phosphates, J Am Chem Soc, 106 (1984) 4926-4936.

[28] A.W. Hing, S. Vega, J. Schaefer, Transferred-Echo Double-Resonance Nmr, J Magn Reson, 96 (1992) 205-209.

[29] Y. Xu, Solid State NMR Approach to Conformational Change and Chemical Exchange of Triosephosphate Isomerase, in: Department of Chemistry, Columbia University, New York, 2009.

[30] S. Rozovsky, A.E. McDermott, The time scale of the catalytic loop motion in triosephosphate isomerase, J Mol Biol, 310 (2001) 259-270.

[31] A. Krushelnitsky, D. Reichert, Solid-state NMR and protein dynamics, Prog Nucl Mag Res Sp, 47 (2005) 1-25.

[32] R.B. Berlow, T.I. Igumenova, J.P. Loria, Value of a hydrogen bond in triosephosphate isomerase loop motion, Biochemistry-Us, 46 (2007) 6001-6010.

[33] N.S. Sampson, J.R. Knowles, Segmental Motion in Catalysis - Investigation of a Hydrogen-Bond Critical for Loop Closure in the Reaction of Triosephosphate Isomerase, Biochemistry-Us, 31 (1992) 8488-8494.

[34] Y. Wang, R.B. Berlow, J.P. Loria, Role of Loop-Loop Interactions in Coordinating Motions and Enzymatic Function in Triosephosphate Isomerase, Biochemistry-Us, 48 (2009) 4548-4556.

[35] J.G. Kempf, J.Y. Jung, C. Ragain, N.S. Sampson, J.P. Loria, Dynamic requirements for a functional protein hinge, J Mol Biol, 368 (2007) 131-149.

[36] V.A. Higman, J. Flinders, M. Hiller, S. Jehle, S. Markovic, S. Fiedler, B.J. van Rossum, H. Oschkinat, Assigning large proteins in the solid state: a MAS NMR resonance assignment strategy using selectively and extensively C-13-labelled proteins, J Biomol Nmr, 44 (2009) 245-260.

Chapter 8

Appendix

8.1 Detailed Derivation of Theoretical Expression for $R_{1\rho}$ as Applied in the Solid State

This derivation outlines how $R_{1\rho}$ relaxation is a monitor of conformational dynamics from a theoretical perspective. An analogous derivation exists for reorientation of a dipolar tensor, but only derivation of $R_{1\rho}$ for the CSA tensor is covered here. This derivation is based on references [1-3].

The Hamiltonian (*H*) for the chemical shift anisotropy is rotated into an interaction frame such that no external static or oscillatory fields explicitly appear:

$$\mathcal{H}_{CSA}(t) = U\mathcal{H}_{CSA}^{lab}U^{-1} \tag{8.1}$$

U is the rotation operator in spin space. The Hamiltonian for the CSA tensor is written as

$$\mathcal{H}_{CSA} = \sum_{q=-1}^{1}(-1)^q \delta_{2,-q}(t)T_{2,q}(\mathbf{n},\mathbf{I}) \tag{8.2}$$

This Hamiltonian has both spin $[T_{2,q}(\mathbf{n},\mathbf{I})]$ and spatial $[\delta_{2,-q}(t)]$ components. q indicates the components of the second rank spherical tensor operator. The tensor components for the spatial components are:

$$\delta_{2,q}(t) = \sqrt{\frac{3}{2}}\delta\omega_I \sum_{n=-2}^{2} F_n(\eta,t)D_{n,q}^{(2)}(\Omega_{RL}(t)) \tag{8.3}$$

where δ and η have the familiar forms for the reduced anisotropy

$$\delta = \delta_{zz} - \frac{1}{3}(\delta_{xx} + \delta_{yy} + \delta_{zz}) \tag{8.4}$$

and the asymmetry

$$\eta = \frac{(\delta_{xx} - \delta_{yy})}{\delta} \tag{8.5}$$

$F_n(\eta,t)$ describe the random modulations of the CSA interaction as a function of time:

$$F_n(\eta,t) = D_{0,n}^{(2)}\big(\Omega_{PR}(t)\big) + \frac{\eta}{\sqrt{6}}\left(D_{2,n}^{(2)}\big(\Omega_{PR}(t)\big) + D_{-2,n}^{(2)}\big(\Omega_{PR}(t)\big)\right) \tag{8.6}$$

These random modulations of the tensor can be depicted as

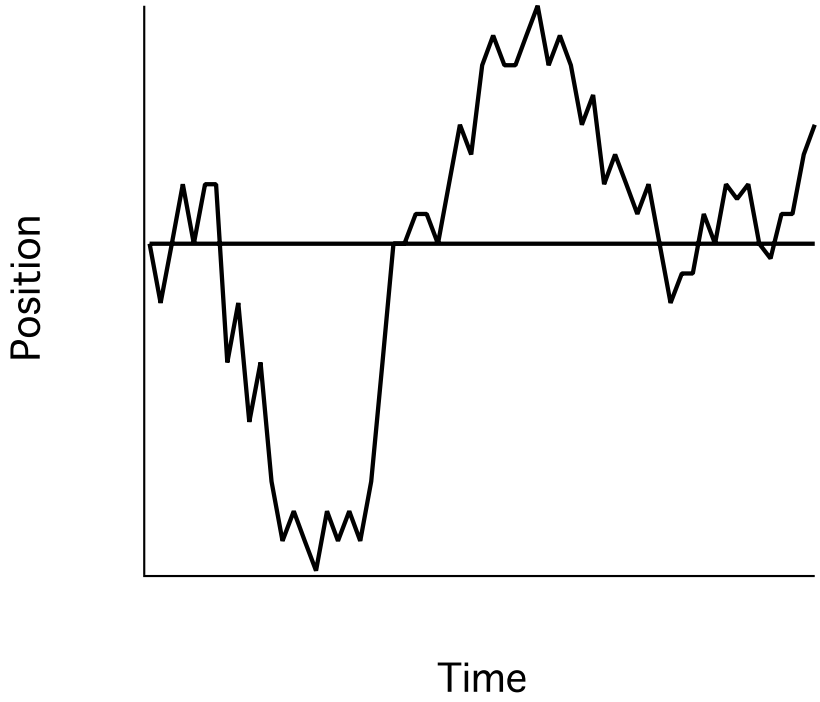

Figure 8.1. Depiction of the random modulations (position) of a spin or tensor as a function of time

$\Omega_{PR}(t)$ are the Euler angles for the PAS to rotor frame transformation:

$$\Omega_{PR}(t) = (0, \theta, \varphi)$$

and $(0, \theta, \varphi)$ are the angles describing random fluctuations of the CSA tensor.

$D^{(2)}_{0\pm2,n}$ are the Wigner rotation matrix elements which are expressed in terms of spherical harmonics (Y).

$$D^{(2)}_{0\pm2,n} \rightarrow Y_{2,-2:2}(\theta, \varphi)$$

The spin and spatial components of the CSA Hamiltonian are separated.

$$\mathcal{H}_{CSA} = \sum_{q=-1}^{1}(-1)^q \delta_{2,-q}(t)\langle 110q|2q\rangle T_{1,q}(\mathbf{I}) \tag{8.7}$$

and the Clebsch-Gordan coefficients are

$$\langle 11pq|2(p+q)\rangle$$

Making substitutions, the spatial component of the Hamiltonian is summarized in single term, $C_\rho(t)$:

$$C_\rho(t) = \sqrt{\frac{3}{2}}\delta\omega_I \sum_{q=-1}^{1}\sum_{n=-2}^{2}(-1)^q e^{-q\omega t}\langle 110q|2q\rangle e^{-p\omega_e t} d_{pq}^{(1)}(\theta_\rho) F_n(\eta,t) D_{n,-q}^{(2)}(\Omega_{RL}(t)) \quad (8.8)$$

Therefore,

$$\mathcal{H}_{CSA}(t) = \sum_{p=-1}^{1} C_p(t)\, T_{1,p}(\mathbf{I}) \quad (8.9)$$

$R_{1\rho}$ is determined from the solution of the master equation for the density matrix. The master equation is

$$\frac{d\rho}{dt} = -\int_0^\infty \overline{[\mathcal{H}(t),[\mathcal{H}(t+\tau),\rho]]}\, d\tau \quad (8.10)$$

The development of the master equation is based on Redfield theory [4, 5]. Redfield theory is only valid in the regime where $k > R_2$ [6]. Multiplying both sides of the master equation by $I_z = T_{1,0}(I)$ and taking the trace gives

$$\frac{d\langle I_z\rangle}{dt} = -\int_0^\infty Tr\{\overline{\left[\mathcal{H}(t),[\mathcal{H}(t+\tau),\rho]\right]}, T_{1,0}(\boldsymbol{I})\} dt \quad (8.11)$$

Making substitutions from A9 into A11,

$$\frac{d\langle I_z\rangle}{dt} = -\frac{1}{2}\sum_{p=-1}^{1}\int_{-\infty}^{+\infty} \overline{C_p(t)C_{-p}(t+\tau)}\, d\tau p^2(\langle I_z\rangle - \langle I_z\rangle_0) \quad (8.12)$$

The relaxation rate $R_{1\rho}$ is

$$R_{1\rho}^{CSA} = -\frac{1}{2}\sum_{p=-1}^{1} p^2 \int_{-\infty}^{+\infty} \overline{C_p(t)C_{-p}(t+\tau)}\, d\tau \quad (8.13)$$

Referring back to A8,

$$R_{1\rho}^{CSA} = \frac{3}{4}(\delta\omega_I)^2 \sum_{p,q=-1}^{1} \sum_{n=-2}^{2} p^2 \langle 110q|2q\rangle^2 \left[d_{pq}^{(1)}(\theta_\rho)\right]^2 \left[d_{n,-q}^{(2)}(\beta_R)\right]^2 J_q(\eta, q\omega + p\omega_e + n\omega_R) \tag{8.14}$$

β_R is the MAS angle and $J(\eta, \omega)$, the spectral density functions, are the Fourier transformations of the autocorrelation functions $G_n(t)$:

$$J_q(\eta, \omega) = \int_{-\infty}^{\infty} G_q(\eta, \omega)\, e^{-i\omega\tau} d\tau \tag{8.15}$$

and

$$G_q(\eta, \tau) = \overline{F_q(\eta, t) F_{-q}(t + \tau)} \tag{8.16}$$

Given that $|q\omega| >> |p\omega_e + n\omega_R|$, $R_{1\rho}^{CSA}$ is

$$R_{1\rho} = \frac{1}{6}(\delta\omega_I)^2 \left(\frac{1}{2}J_0(\eta, \omega_e - 2\omega_R) + J_0(\eta, \omega_e - \omega_R) + J_0(\eta, \omega_e + \omega_R) + \frac{1}{2}J_0(\eta, \omega_e + 2\omega_R)\right) \tag{8.17}$$

To analyze relaxation data, a form for the correlation functions must be established. Two of the most commonly applied motional models are wobbling in a cone and an N-site hop. The correlation functions [G(t)] for an anisotropic motion in the solid state are the sum of averaging and non-averaging components:

$$G_m(t) = \frac{1}{5}[S^2 + (1 - S^2) \cdot \sum_{i=1}^{N} p_i e^{-t/\tau_i}], \sum_{i=1}^{N} p_i = 1 \tag{8.18}$$

S^2 is the order parameter defining the non-averaging part of the correlation function, N is the number of exponential components of the time-dependent part of the correlation function. p_i and τ_i are the amplitude and correlation times of the exponential components. The correlation time and corresponding rate of chemical exchange are the key parameters of interest in our work. For N > 1, the spectral density function is

$$J_m(\omega) = \frac{2}{5}(1 - S^2)\sum_{i=1}^{N} \frac{p_i \tau_i}{1+(\omega\tau_i)^2} \tag{8.19}$$

In the model-free approach presented by Lipari and Szabo [7], they proposed that only one effective correlation time, τ_e, was necessary to approximate the correlation function:

$$J_m(\omega) = \frac{2}{5}(1 - S^2)\frac{\tau_e}{1+(\omega\tau_e)^2} \tag{8.20}$$

Due to fast tumbling in solution, the parameters S^2 and τ_e are the same for $J_0(\omega)$, $J_1(\omega)$, and $J_2(\omega)$. An important insight from Kurbanov et al based on simulations was that the spectral density functions $J_m(\omega)$ are essentially the same for a solid state isotropic (powder averaged) sample as well. This had not been previously believed to be the case. Thus they concluded that solid state relaxation could be analyzed using the model-free approach commonly applied in solution NMR, regardless of correlation time.

Simulations did indicate that for a large angle hop (90° vs 30°), the correlation function is multi-exponential. To handle this, Kurbanov et al introduced a distributed correlation function:

$$J(\omega) \sim \frac{\beta}{\omega}\frac{(\omega\tau)^{\beta}}{1+(\omega\tau)^{2\beta}} \tag{8.21}$$

β is the term that parameterizes the distribution function.

The derivation above describes how correlation times and exchange rates can be determined from $R_{1\rho}$ by applying the master equation to the CSA Hamiltonian and establishing a form for the spectral density functions.

8.2 Peak Reports for ^{31}P One-Dimensional Spectra

The tables below provide further information on the properties of various spectra in Section 4.3. The isotropic chemical shifts and distances between spinning sidebands provide further information on the species observed in slow and fast MAS spectra. Notable properties include the temperature dependence, and the indication that the anisotropic species appears upfield of the isotropic species.

Spectrum	δ_{iso} (ppm)	δ_{iso} (Hz)
-40°C	1.01	244.5
-20°C	0.79	192.4
+20°C	0.74	178.3

Table 8.1 Chemical shifts of the centerband observed at -20°C and -40°C, along with the dominant peak for the spectrum at +20°C, collected at 3 kHz MAS with direct excitation in ^{31}P slow MAS one-dimensional spectra of 50/50 TIM-bound/unbound PO_4^{3-}..

Spectrum	Downfield First Sideband (Hz)	Centerband (Hz)	Upfield First Sideband (Hz)
-40°C, DE	3079.3	244.5	-2966.0
Distance From Centerband	2833.3		3210.7
-20°C, DE	3061.2	192.4	-2937.5
Distance From Centerband	2867.3		3128.9
+20°C, DE		178.3	-2843.1
Distance from Centerband		3029.8	
-30°C, DE	10055.9	68.7	-9935.0
Distance From Centerband	9987.9		10004

Table 8.2 Distance between centerband and first upfield and downfield sidebands (when present) in ^{31}P slow MAS one-dimensional spectra of 50/50 TIM-bound/unbound PO_4^{3-}.

Temperature	δ_{iso} (ppm) Peak 1	δ_{iso} (ppm) Peak 2	δ_{iso} (ppm) Peak 3	δ_{iso} (ppm) Peak 4
-40°C 22 kHz MAS	2.75	1.81	0.78	-2.58
+20°C 22 kHz MAS	2.42	1.84	0.32	-2.59

Table 8.3 Isotropic chemical shifts for the four phosphorous resonances observed in fast MAS spectra of 50/50 TIM-bound/unbound PO_4^{3-} collected at 22 kHz MAS. Peak one indicates the downfield most peak and peak 4 is the upfield most peak.

Spectrum	Linewidth (Hz)
-40°C, 3 kHz MAS	268
-20°C, 3 kHz MAS	205
+20°C, 3 kHz MAS	127
-40°C, 22 kHz MAS	139
+20°C, 22 kHz MAS	205

Table 8.4 Linewidths for ^{31}P slow MAS one-dimensional spectra of 50/50 TIM-bound/unbound PO_4^{3-} collected at 3 and 22 kHz MAS.

8.3 Sample Spinevolution [8] and MINUET Input Files Used for Simulations and Calculations

8.3.1 Spinevolution Dispersion Curve Simulations for Dimethyl Sulfone

```
****** The System ***********************************
spectrometer(MHz)  400
spinning_freq(kHz) 10
channels           C13
nuclei             C13 C13
atomic_coords      *
cs_isotropic       *
csa_parameters     1 -36.77 0.0625 0 -54 0 ppm
csa_parameters     2 -36.77 0.0625 0  54 0 ppm
j_coupling         *
quadrupole         *
dip_switchboard    *
csa_switchboard    *
exchange_nuclei    (1 2)
bond_len_nuclei    *
bond_ang_nuclei    *
tors_ang_nuclei    *
groups_nuclei      *
******* Pulse Sequence ******************************
CHN 1
timing(usec)       (100)4000
power(kHz)          15
phase(deg)          0
freq_offs(kHz)      0
******* Variables ***********************************
variable k_1=0.5
variable power_1_1=A
scan_par A/0 5 10 15 20 25 30 35 40 45 50 55 60 65 70 75 80 85 90 95 100/
variable data_re=hypot(data_re,data_im)
******* Options **************************************
rho0               F1x
observables        F1p
EulerAngles        zcwt538
n_gamma            *
line_broaden(Hz)   *
zerofill           *
FFT_dimensions     *
options            -re
************************************************************
```

8.3.2 Spinevolution Cross Polarization Build-up Curve Simulations

```
****** The System **********************************
spectrometer(MHz)  400
spinning_freq(kHz) 10
channels           C13 H1
nuclei             C13 H1 C13 H1
atomic_coords      *
cs_isotropic       *
csa_parameters     1 -36.77 0.0625 0 54 0 ppm
csa_parameters     3 -36.77 0.0625 0 -54 0 ppm
j_coupling         *
quadrupole         *
dip_switchboard    *
csa_switchboard    *
exchange_nuclei    (1 3)
bond_len_nuclei    *
bond_ang_nuclei    *
tors_ang_nuclei    *
groups_nuclei      *
******* Pulse Sequence ******************************
CHN 1
timing(usec)       [(0)128]30
power(kHz)         [0]30
phase(deg)         [0]30
freq_offs(kHz)     [0]30
CHN 2
timing(usec)       [(0)]30
power(kHz)         [0]30
phase(deg)         [0]30
freq_offs(kHz)     [0]30
******* Variables ***********************************
power_1_[1:30]_1=50+[0:29]*6/29
power_2_[1:30]_1=63
pulse_1_[1:30]_1=1
pulse_2_[1:30]_1=1
data_re=hypot(data_re,data_im)
k_1=1
******* Options *************************************
rho0               F2x
observables        F1p
EulerAngles        zcwt538
n_gamma            *
line_broaden(Hz)   *
zerofill           *
FFT_dimensions     *
options            -zxmatrampcp5.zxmat -re -t07
******* Options *************************************
```

8.3.3 Minuet Files for Protonated DMS Data-Fitting

MINUET Executable

```
*
* $Id: minexam.F,v 1.1.1.1 1996/03/07 14:31:32 mclareni Exp $
*
* $Log: minexam.F,v $
* Revision 1.1.1.1  1996/03/07 14:31:32  mclareni
* Minuit
*
*
      PROGRAM MNEXAM
C             Minuit test case.  Fortran-callable.
C             Fit randomly-generated leptonic K0 decays to the
C       time distribution expected for interfering K1 and K2,
C       with free parameters Re(X), Im(X), DeltaM, and GammaS.
*
* $Id: d506dp.inc,v 1.1.1.1 1996/03/07 14:31:32 mclareni Exp $
*
* $Log: d506dp.inc,v $
* Revision 1.1.1.1  1996/03/07 14:31:32  mclareni
* Minuit
*
*
*
*
* d506dp.inc
*
C ************ DOUBLE PRECISION VERSION *************
      IMPLICIT DOUBLE PRECISION (A-H,O-Z)
*     EXTERNAL FCNK0, FCNK2, FCNK3,FCNK1
      EXTERNAL FCNK3
CC    OPEN (UNIT=6,FILE='DSDQ.OUT',STATUS='NEW',FORM='FORMATTED')
      DIMENSION NPRM(30),VSTRT(30),STP(30),OLOW(30),HIGH(30)
      DIMENSION SCANPAR(4)
      CHARACTER*10 PNAM(30)
      INTEGER NUMVAR

      DATA ZERO,ONE,THREE,FIVE / 0.0, 1.0, 3.0, 5.0 /
        DATA two,four,six,seven,eight,onine,ten /2.0,4.0,6.0,7.0,8.0,9.0,10.0/
      DATA PI, TWOPI,ompi / 180, 360,-180 /
      DATA omTH,pTH,FIFTY,hpi /-200.0, 200.0, 50.0, 90.0 /
      DATA eleven,twelve /11.0, 12.0/
      DATA thirteen,fourteen,fifteen,sixteen /13.0,14.0,15.0,16.0/
      DATA seventeen,eighteen,onineteen,twenty /17.0,18.0,19.0,20.0/
      DATA twentyone,twentytwo,onehundred /21.0, 22.0,100.0/
      DATA ofive,omfive /0.5,-5.0/

      open(unit=12,file='MINUIT.OUT',status='unknown',access='append')
      open(unit=14,file='STATUS.OUT',status='unknown',access='append')

      OPEN (2, FILE='MIN_INIT.TXT',STATUS='OLD')
```

```
            READ(2,*) NUMVAR
          DO I=1, NUMVAR
            READ(2,*) NPRM(I), PNAM(I), VSTRT(I), STP(I),OLOW(i),HIGH(I)
          ENDDO
        CLOSE(2)


        CALL MNINIT(5,12,7)

        DO I=1, NUMVAR
            CALL
MNPARM(NPRM(I),PNAM(I),VSTRT(I),STP(I),OLOW(I),HIGH(I),IERFLG)
        ENDDO


        CALL MNSETI('FIT MY LINESHAPE!')

c       Request FCN to read in (or generate random) data (IFLAG=1)
        OPEN (2, FILE='rmsd.in',STATUS='unknown')
            write(2,*) 999.99
        CLOSE(2)


! FIT ORIENT dipope

        CALL MNEXCM(FCNK3, 'CALL FCN', ONE ,1,IERFLG, 0)
!

        CALL MNEXCM(FCNK3, 'SET STRATEGY', TWO ,2,IERFLG, 0)

          !CALL MNEXCM(FCNK3,'SEEK',ZERO,0,IERFLG,0)

           CALL MNEXCM(FCNK3,'RELEASE',one,1,IERFLG,0)
        CALL MNEXCM(FCNK3,'RELEASE',two,1,IERFLG,0)



        CALL MNEXCM(FCNK3,'SIMPLEX',ZERO,0,IERFLG,0)
        CALL MNEXCM(FCNK3,'MINIMIZE', ZERO ,0,IERFLG,0)
        !CALL MNEXCM(FCNK3,'SCAN',ZERO,0,IERFLG,0)
        CALL MNEXCM(FCNK3,'SEEK',ZERO,0,IERFLG,0)
        CALL MNEXCM(FCNK3,'MINIMIZE', ZERO ,0,IERFLG,0)
        CALL MNEXCM(FCNK3,'IMPROVE', ZERO ,0,IERFLG,0)

        !CALL MNEXCM(FCNK3,'FIX',eight,1,IERFLG,0)

        !CALL MNEXCM(FCNK3,'SCAN',ZERO,0,IERFLG,0)
        CALL MNEXCM(FCNK3,'SIMPLEX',ZERO,0,IERFLG,0)
          CALL MNEXCM(FCNK3,'SEEK',ZERO,0,IERFLG,0)
        CALL MNEXCM(FCNK3,'MINIMIZE', ZERO ,0,IERFLG,0)
        CALL MNEXCM(FCNK3,'IMPROVE', ZERO ,0,IERFLG,0)
        CALL MNEXCM(FCNK3,'SIMPLEX',ZERO,0,IERFLG,0)
        CALL MNEXCM(FCNK3,'MINIMIZE', ZERO ,0,IERFLG,0)
        !CALL MNEXCM(FCNK3,'SCAN',ZERO,0,IERFLG,0)
```

```
      CALL MNEXCM(FCNK3,'SEEK',ZERO,0,IERFLG,0)
      CALL MNEXCM(FCNK3,'MINIMIZE', ZERO ,0,IERFLG,0)
      CALL MNEXCM(FCNK3,'IMPROVE', ZERO ,0,IERFLG,0)

        !CALL MNEXCM(FCNK3,'SCAN',ZERO,0,IERFLG,0)
      CALL MNEXCM(FCNK3,'MINOS',ZERO,0,IERFLG,0)
!
      !OPEN (2, FILE='rmsd.in',STATUS='unknown')
      !     write(2,*) 999.99
      !CLOSE(2)
      !call system('cp par.dat par.ORIENT.dat')


            close(12)
            close(14)
      END
```

Fitting Sub-Routine (FCNK3)

```
      SUBROUTINE FCNK3(NPAR,GIN,rmsd3,X,IFLAG)
      IMPLICIT DOUBLE PRECISION (A-H,O-Z)
      DIMENSION X(*),GIN(*)
      COMPLEX sig1(4096),sim1(4096)
      CHARACTER*32 datafile(32), simfile(32),name,word,simim(32)
      CHARACTER*32 difout(32), simout(32), datout(32), specout(32)
      DOUBLE PRECISION scale, dscale, nscale, rmsd2(32),iscale,bscale
      DOUBLE PRECISION A(32,32), B(32,32), dum, rmsd1(32), rmsd
      DOUBLE PRECISION AI(32,32), BI(32,32),tempreal(32),tempimag(32)
      DOUBLE PRECISION bscale1(32), ascale(32)
      DOUBLE PRECISION rmsd3,X1(128),rmsd4,phase,bphase(32)
      DOUBLE PRECISION btheta_1,br_1,br_2 ,bcs_ani_3,bcs_asy_3
      DOUBLE PRECISION bT2XQ_T, bT2XQ_R,phase1,dphase,pi,drfac
      DOUBLE PRECISION bcs_beta_3,bT2SQ_1,bT2SQ_2,bT2ZQ_2_3,bT2DQ_2_3

      INTEGER i, j, k, l, m, n, IFLAG,NPAR,ismax, nphase, jphase
      integer imax(32), jmax, icheck, inorm(32),ibnorm(32)
      icheck = 0


      OPEN(2,file='fit3.in',status='old')
          read(2,*) ismax
      read(2,*) (datafile(i),i=1,ismax)
      read(2,*) (simfile(i),i=1,ismax)
!           read(2,*) (simim(i),i=1,ismax)
!           read(2,*) (difout(i),i=1,ismax)
      read(2,*) (simout(i),i=1,ismax)
      read(2,*) (datout(i),i=1,ismax)
!           read(2,*) (specout(i),i=1,ismax)
      read(2,*) (imax(i),i=1,ismax)
      read(2,*) iscale, dscale, nscale
      read(2,*) phase1, dphase, nphase
      CLOSE(2)
      pi = 3.14159265358979
```

```
      drfac=pi/180.0
      phase1=phase1*drfac
      dphase=dphase*drfac
      OPEN(2,file='rmsd.in',status='old')
      read(2,*) rmsd
      CLOSE(2)
      !DO i=1, 10
      !     X1(i)=X(i)
      !enddo
!     echo "1 $ndelta $neta $nalpha $nbeta $ngamma" >> par.csa
!     echo "2 $cdelta $ceta $calpha $cbeta $cgamma" >> par.csa

      OPEN(2,file='CSA_t1rho_pw3.par',status='unknown')
 1000        FORMAT('k_1=',F16.4)
      write(2,1000)  X(1)
 200        FORMAT('T2SQpw3=',F16.4)
      write(2,200)  X(2)
      CLOSE(2)

      OPEN(2,file='CSA_t1rho_pw5.par',status='unknown')
 300        FORMAT('k_1=',F16.4)
      write(2,300)  X(1)
 400        FORMAT('T2SQpw5=',F16.4)
      write(2,400)  X(3)
      CLOSE(2)

            OPEN(2,file='CSA_t1rho_pw8.par',status='unknown')
 500        FORMAT('k_1=',F16.4)
      write(2,500)  X(1)
 600        FORMAT('T2SQpw8=',F16.4)
      write(2,600)  X(4)
      CLOSE(2)

      do j=1, ismax
            OPEN(2,file=datafile(j),status='old')
                ascale(j)=0.0
            do i=1, imax(j)
                  tempreal(i)=0.0
                  !tempimag(i)=0.0
                        read(2,*) tempreal(i)
                        !read(2,*) tempimag(i)
                        A(i,j) = tempreal(i)
                        !AI(i,j) = tempimag(i)*((-1.d0)**(i+1))
                        !if(A(i,j).gt.ascale(j))then
                        !     ascale(j)=A(i,j)
                        !endif
                  enddo
            CLOSE(2)
      enddo
c
c     do j=1, ismax
c           do i=1, imax
c                 A(i,j) = A(i,j)/ascale(j)
c           enddo
```

```
c     enddo

      call system('simulate3.txt')

       write(*,*) "calculating..."

      do j=1, ismax
            OPEN(2,file=simfile(j),status='old')
            do i=1, imax(j)
                        read(2,*) dum, B(i,j)
                        !write(*,*) i, j
                  enddo
            CLOSE(2)
      enddo
      !stop
!     do j=1, ismax
!           OPEN(2,file=simim(j),status='old')
!                 do i=1, imax(j)
!                       read(2,*) dum, BI(i,j)
!                 enddo
!           CLOSE(2)
!     enddo

      rmsd3 = 100000

      do j=1,ismax
          rmsd2(j) = 1000.0
          do jphase=1, nphase

            phase=phase1+real(jphase-1)*dphase
            !write(*,*) phase
            do jj=1, imax(j)
                        tempreal(jj) = 0.0
                        !tempimag(jj) = 0.0
                        tempreal(jj)=A(jj,j)
                        !tempimag(jj)=(-
A(jj,j)*sin(phase))+(AI(jj,j)*cos(phase))


                  enddo
                  do k=1,nscale
                        scale = (iscale + (dscale*(k-1)))

                        rmsd1(j) = 0.0

                        inorm(j) = 0
                        do i=1,imax(j)


                              inorm(j) = inorm(j) + 1
                              rmsd1(j) = rmsd1(j) + (tempreal(i)-
(scale*B(i,j)))**2.0
                              !rmsd1(j) = rmsd1(j) + (tempimag(i)-
(scale*BI(i,j)))**2.0
```

```
                        enddo

                        if(rmsd1(j).lt.rmsd2(j))then
                              rmsd2(j)   = rmsd1(j)
                              ibnorm(j)  = inorm(j)
                              bscale1(j) = scale
                              bphase(j) = phase
                        endif

                  enddo
            enddo
            !stop
      enddo
      rmsd4=0.0
      !write(*,*) (ibnorm(i),i=1,ismax)
      !write(*,*) ismax
      do j=1, ismax
            rmsd4 = rmsd4 + rmsd2(j)/(ibnorm(j))
      enddo
      rmsd3 = 1000.d0*sqrt(rmsd4/(ismax))

c                 if(rmsd2.lt.rmsd3)then
c                       rmsd3   = rmsd2
c                       bscale1 = scale
c                 endif



100           Format(30(1X,F16.10,1X))
            OPEN(2,file='rmsd.txt',status='unknown',access='append')
            write(2,100) rmsd3, (X(ii),ii=1,5)
            CLOSE(2)

            if(rmsd3.lt.rmsd)then
                  rmsd = rmsd3
!                 call system('cp ROCSA.R1817.par par.dat')

                  OPEN(2,file='rmsd.in',status='unknown')
                        write(2,*) rmsd
                  CLOSE(2)
                  do, j=1, ismax
                  do jj=1, imax(j)
                        tempreal(jj) = 0.0
                        !tempimag(jj) = 0.0
                        tempreal(jj)=A(jj,j)
                        !tempimag(jj)=(-
A(jj,j)*sin(bphase(j)))+(AI(jj,j)*cos(bphase(j)))
                        A(jj,j) = tempreal(jj)
                        !AI(jj,j) = tempimag(jj)

                  enddo
                  enddo
```

```
!                  do j=1,ismax
!                        open(30,file=difout(j),status='unknown')
!                              do i=1,imax(j)
!                                    write(30,*) i, (A(i,j)-
bscale1(j)*(B(i,j))),
!    &                                (AI(i,j)-bscale1(j)*(BI(i,j)))
!                              enddo
!                        close(30)
!                  enddo

                   do j=1,ismax
                         open(31,file=simout(j),status='unknown')
                               do i=1,imax(j)
                                     write(31,*) i, bscale1(j)*(B(i,j))
                               enddo
                         close(31)
                   enddo

                   do j=1,ismax
                         open(32,file=datout(j),status='unknown')
                               do i=1,imax(j)
                                     write(32,*) i, A(i,j)
                               enddo
                         close(32)
                   enddo

                 do j=1,ismax
                         do i=1,4096
                               sig1(i)=(0.0,0.0)
                               sim1(i)=(0.0,0.0)
                         enddo
                         do i=1,imax(j)
                               sig1(i)=complex(A(i,j),AI(i,j))
                               !write(*,*) sig1(i)
                         enddo
                         do i=1, imax(j)

      sim1(i)=complex(bscale1(j)*B(i,j),bscale1(j)*BI(i,j))
                         enddo
                         !write(*,*) specout
                         sim1(1)=sig1(1)

!                        call fft(sig1,9,1)
!                        call fft(sim1,9,1)
                         !write(*,*) specout
                         !open(39,file=specout(j),status='unknown')
                         !     do k=257,512
                         !           write(39,*)real(k-512)*1.0/(512.0e-
6*90.0),real(sig1(k)),real(sim1(k))
                         !enddo
                               !do k=1,256
                               !     write(39,*)real(k)*1.0/(512.0e-
6*90.0),real(sig1(k)),real(sim1(k))
                         !enddo
```

```
                        !do k=1,512
                              !     write(39,*)real(sig1(k))!,real(sim1(k))
                        !enddo
                        close(39)
                  enddo
            endif
            !stop
      END
```

User-Specified Starting Parameters for Variables to be Fit (MIN_INIT.txt)

```
1    k_1          0.1      2.0    0.0    20.0
2    T2SQpw3        100      5.0          0.0    1000.0
3    T2SQpw5         90       3.0    0.0    1000.0
4    T2SQpw8        50       5.0    0.0    1000.0
```

Excerpt from fit3.in: Files Called by MINUET During Data-Fitting

```
DMS_t1rho_pw3_13_1.traj
DMS_t1rho_pw3_14_2.traj
DMS_t1rho_pw3_15_4.traj
.
.
.
CSA_t1rho_pw3_13.txt_re.dat
CSA_t1rho_pw3_14.txt_re.dat
CSA_t1rho_pw3_15.txt_re.dat
.
.
.
FIT_pw3_13.dat
FIT_pw3_14.dat
FIT_pw3_15.dat
.
.
.
DAT_pw3_13.dat
DAT_pw3_14.dat
DAT_pw3_15.dat
```

Spinevolution Executable Called by MINUET (Excerpt, simulate3.txt)

```
spinev CSA_t1rho_pw3_13.txt > /dev/null 2>&1
spinev CSA_t1rho_pw3_14.txt > /dev/null 2>&1
spinev CSA_t1rho_pw3_15.txt > /dev/null 2>&1
```

Sample Spinevolution File Used to Generate Curves to Minimize Fit Parameters Relative to Experimental Data (CSA_t1rho_pw5_19.txt)

```
****** The System **********************************
spectrometer(MHz)  400
spinning_freq(kHz) 10
channels           C13
nuclei             C13 C13
atomic_coords      *
cs_isotropic       *
csa_parameters     1 -36.77 0.0625 0 -54 0 ppm
csa_parameters     2 -36.77 0.0625 0 54 0 ppm
j_coupling         *
quadrupole         *
dip_switchboard    *
csa_switchboard    *
exchange_nuclei    (1 2)
bond_len_nuclei    *
bond_ang_nuclei    *
tors_ang_nuclei    *
groups_nuclei      *
******* Pulse Sequence ******************************
CHN 1
timing(usec)       (100)1
power(kHz)          33.34
phase(deg)          0
freq_offs(kHz)      0
******* Variables ***********************************
variable CSA_t1rho_pw5.par
variable T2SQ_1_1=T2SQpw5
variable T2SQ_2_1=T2SQpw5
scan_par B/1000 6000 11000 16000 21000 26000 31000 36000 41000/
pulse_1_1_1=B
data_re=hypot(data_re,data_im)
******* Options **************************************
rho0               F1x
observables        F1p
EulerAngles        zcwt538
n_gamma            *
line_broaden(Hz)   *
zerofill           *
FFT_dimensions     *
options            -re -split6
*************************************************************
```

Sample Input Raw Decay Data (DMS_t1rho_pw3_13_1.traj/ DAT_pw3_13.dat)

```
2.2256
2.0995
2.003
1.9118
1.8009
1.7209
1.6454
1.5751
1.5021
```

Sample 'Best Fit' Output Decay Data Generated By Spinevolution During MINUET Fitting

(corresponds to raw decay curve in 7.3.7, FIT_pw3_13.dat)

```
1  2.1783322
2  2.0763248
3  1.9834045
4  1.8975891
5  1.8166753
6  1.7382277
7  1.6620736
8  1.5895528
9  1.520904
```

Sample MINUET Output

```
MINUIT RELEASE 96.03  INITIALIZED.  DIMENSIONS 100/ 50  EPSMAC=  0.89E-15

PARAMETER DEFINITIONS:
NO.    NAME         VALUE      STEP SIZE      LIMITS
1     'k_1        '0.10000       2.0000       0.0000       20.000
 MINUIT WARNING IN PARAMETR
 ============== VARIABLE   1 BROUGHT BACK INSIDE LIMITS.
2 'T2SQpw3    '    100.00       5.0000         0.0000       1000.0
     3 'T2SQpw5    '    90.000       3.0000         0.0000       1000.0
     4 'T2SQpw8    '    50.000       5.0000         0.0000       1000.0
 **********
 **    1 **CALL FCN   1.000
 **********
MINUIT RELEASE 96.03  INITIALIZED.   DIMENSIONS 100/ 50  EPSMAC=  0.89E-15

 PARAMETER DEFINITIONS:
    NO.    NAME         VALUE      STEP SIZE      LIMITS
     1 'k_1        '   0.10000       2.0000         0.0000       20.000
 MINUIT WARNING IN PARAMETR
 ============== VARIABLE   1 BROUGHT BACK INSIDE LIMITS.
     2 'T2SQpw3    '    100.00       5.0000         0.0000       1000.0
     3 'T2SQpw5    '    90.000       3.0000         0.0000       1000.0

 **********
```

```
 **    1 **CALL FCN    1.000
 **********

 FCN=    74.33894      FROM CALl fcn  STATUS=RESET           1 CALLS         1
TOTAL
                       EDM= unknown       STRATEGY= 1      NO ERROR MATRIX

  EXT PARAMETER                CURRENT GUESS       PHYSICAL LIMITS
  NO.    NAME         VALUE           ERROR       NEGATIVE      POSITIVE
   1    k_1          0.10000         2.0000         0.0000         20.000
   2    T2SQpw3       100.00         5.0000         0.0000         1000.0
   3    T2SQpw5       90.000         3.0000         0.0000         1000.0
   4    T2SQpw8       50.000         5.0000         0.0000         1000.0
 **********
 **    2 **SET STRATEGY    2.000        4.000
 **********

 NOW USING STRATEGY  2: MAKE SURE MINIMUM TRUE, ERRORS CORRECT

 **********
 **    3 **RELEASE    1.000
 **********
 PARAMETER   1 ALREADY VARIABLE.  IGNORED.
 **********
 **    4 **RELEASE    2.000
 **********
 PARAMETER   2 ALREADY VARIABLE.  IGNORED.
 **********
 **    5 **SIMPLEX
 **********
 START SIMPLEX MINIMIZATION.     CONVERGENCE WHEN EDM .LT.   0.10E+00

 FCN=    74.33894      FROM SIMPLEX    STATUS=UNCHANGED      12 CALLS        13
TOTAL
                       EDM=   0.66E+02     STRATEGY= 2      NO ERROR MATRIX

  EXT PARAMETER                CURRENT GUESS       PHYSICAL LIMITS
  NO.    NAME         VALUE           ERROR       NEGATIVE      POSITIVE
   1    k_1          0.10000         2.0000         0.0000         20.000
   2    T2SQpw3      100.000         5.0000         0.0000         1000.0
   3    T2SQpw5       90.000         3.0000         0.0000         1000.0
   4    T2SQpw8       50.000         5.0000         0.0000         1000.0
 SIMPLEX MINIMIZATION HAS CONVERGED.

 FCN=    50.18635      FROM SIMPLEX    STATUS=PROGRESS      137 CALLS       138
TOTAL
                       EDM=   0.39E-01     STRATEGY= 2      NO ERROR MATRIX
  EXT PARAMETER                CURRENT GUESS       PHYSICAL LIMITS
  NO.    NAME         VALUE           ERROR       NEGATIVE      POSITIVE
   1    k_1          0.66695E-01     2.0000         0.0000         20.000
   2    T2SQpw3       135.25         5.0000         0.0000         1000.0
   3    T2SQpw5       108.16         3.0000         0.0000         1000.0
   4    T2SQpw8       48.111         5.0000         0.0000         1000.0
 **********
```

```
 **    6 **MINIMIZE
 **********
 START MIGRAD MINIMIZATION.  STRATEGY 2.  CONVERGENCE WHEN EDM .LT. 0.10E-03
 COVARIANCE MATRIX CALCULATED SUCCESSFULLY
.
.
.
.
FCN=   43.17703     FROM HESSE     STATUS=NOT POSDEF    57 CALLS      704
TOTAL
                     EDM=  0.19E+06    STRATEGY= 2      ERR MATRIX NOT POS-DEF

  EXT PARAMETER                APPROXIMATE        STEP         FIRST
  NO.   NAME         VALUE          ERROR          SIZE      DERIVATIVE
   1    k_1          0.10977        0.22093E-01   0.88483E-04   -2.6582
   2    T2SQpw3       124.84        0.24884       0.17232E-02    13.924
   3    T2SQpw5       126.22        0.32379       0.50595E-03   -22.857
   4    T2SQpw8       48.447         590.87       0.23029E-03   -72.229
 MIGRAD FAILS TO FIND IMPROVEMENT
 MINUIT WARNING IN HESSE
 ============== Negative diagonal element  3 in Error Matrix
 MINUIT WARNING IN HESSE
 ============== Negative diagonal element  4 in Error Matrix
 MINUIT WARNING IN HESSE
 ==============     0.63E+06 added to diagonal of error matrix
 COVARIANCE MATRIX CALCULATED SUCCESSFULLY

 FCN=   43.17703     FROM HESSE     STATUS=OK             31 CALLS      746
TOTAL
                     EDM=  0.69E+04    STRATEGY= 2      ERROR MATRIX ACCURATE

  EXT PARAMETER                                     STEP         FIRST
  NO.   NAME         VALUE          ERROR          SIZE      DERIVATIVE
   1    k_1          0.10977        0.41625E-02   0.24422E-02  -0.88769
   2    T2SQpw3       124.84        0.59275       0.17232E-02    13.924
   3    T2SQpw5       126.22        0.67594       0.50595E-03   -22.857
   4    T2SQpw8       48.447         795.00       0.23029E-03   -72.229

 MIGRAD MINIMIZATION HAS CONVERGED.

 MIGRAD WILL VERIFY CONVERGENCE AND ERROR MATRIX.
 MINUIT WARNING IN HESSE
 ============== Second derivative enters zero, param    1
 MINUIT WARNING IN HESSE
 ============== Second derivative enters zero, param    2
 MINUIT WARNING IN HESSE
 ============== Second derivative enters zero, param    3
 MINUIT WARNING IN HESSE
 ============== Second derivative enters zero, param    4
 MINUIT WARNING IN HESSE
 ============== Negative diagonal element  3 in Error Matrix
 MINUIT WARNING IN HESSE
 ==============     0.91E+05 added to diagonal of error matrix
 EIGENVALUES OF SECOND-DERIVATIVE MATRIX:
```

```
       -0.5104E+01   0.9950E+00   0.1000E+01   0.7109E+01
 MINUIT WARNING IN HESSE
 ============== MATRIX FORCED POS-DEF BY ADDING   5.1110     TO DIAGONAL.
 MIGRAD TERMINATED WITHOUT CONVERGENCE.

 FCN=    43.09740      FROM MIGRAD    STATUS=FAILED        720 CALLS       858
TOTAL
                      EDM=   0.37E+05    STRATEGY= 2      ERR MATRIX NOT POS-DEF

  EXT PARAMETER                APPROXIMATE        STEP         FIRST
  NO.    NAME         VALUE          ERROR          SIZE      DERIVATIVE
   1    k_1          0.10976        0.57006E-01   0.23997E-02   -8.5114
   2    T2SQpw3       124.84        0.61590       0.15804E-02    15.210
   3    T2SQpw5       126.22         651.18       0.50595E-03   -22.900
   4    T2SQpw8       48.886        0.35172       0.18575E-02    17.466

 EXTERNAL ERROR MATRIX.    NDIM=  50    NPAR=  4    ERR DEF=  1.00
  0.325E-02-0.490E-02 0.224E+03-0.622E-02
 -0.490E-02 0.379E+00-0.339E+03 0.944E-02
  0.224E+03-0.339E+03 0.155E+08-0.431E+03
 -0.622E-02 0.944E-02-0.431E+03 0.124E+00
 ERR MATRIX NOT POS-DEF

 PARAMETER  CORRELATION COEFFICIENTS
       NO.   GLOBAL     1     2     3     4
        1  0.99884  1.000-0.139 0.999-0.310
        2  0.13986 -0.139 1.000-0.140 0.044
        3  0.99884  0.999-0.140 1.000-0.311
        4  0.31123 -0.310 0.044-0.311 1.000
 ERR MATRIX NOT POS-DEF
 START SIMPLEX MINIMIZATION.     CONVERGENCE WHEN EDM .LT.   0.10E+00

 FCN=    43.04812      FROM SIMPLEX   STATUS=PROGRESS       12 CALLS       870
TOTAL
                      EDM=   0.34E+02    STRATEGY= 2      ERR MATRIX NOT POS-DEF

  EXT PARAMETER                APPROXIMATE        STEP         FIRST
  NO.    NAME         VALUE          ERROR          SIZE      DERIVATIVE
   1    k_1          0.11907        0.57006E-01   0.61729E-02   -8.5114
   2    T2SQpw3       124.84        0.61590       0.18633E-02    15.210
   3    T2SQpw5       126.22         651.18       0.31372       -22.900
   4    T2SQpw8       48.886        0.35172       0.26098E-03    17.466
 SIMPLEX TERMINATES WITHOUT CONVERGENCE.

 FCN=    43.04812      FROM SIMPLEX   STATUS=CALL LIMIT     13 CALLS       871
TOTAL
                      EDM= unknown       STRATEGY= 2      ERR MATRIX NOT POS-DEF

  EXT PARAMETER                APPROXIMATE        STEP         FIRST
  NO.    NAME         VALUE          ERROR          SIZE      DERIVATIVE
   1    k_1          0.11907        0.57006E-01   0.61729E-02   -8.5114
   2    T2SQpw3       124.84        0.61590       0.18633E-02    15.210
   3    T2SQpw5       126.22         651.18       0.31372       -22.900
   4    T2SQpw8       48.886        0.35172       0.26098E-03    17.466
```

```
 **********
 **    7 **SEEK
 **********
 MNSEEK: MONTE CARLO MINIMIZATION USING METROPOLIS ALGORITHM
 TO STOP AFTER   180 SUCCESSIVE FAILURES, OR   1800 STEPS
 MAXIMUM STEP SIZE IS    3.000 ERROR BARS.

 FCN=    43.04812      FROM SEEk       STATUS=UNCHANGED    180 CALLS      1051
TOTAL
                       EDM= unknown       STRATEGY= 2      ERR MATRIX NOT POS-DEF

  EXT PARAMETER                 APPROXIMATE     INTERNAL      INTERNAL
  NO.   NAME         VALUE          ERROR       STEP SIZE       VALUE
   1    k_1          0.11907       0.57006E-01   0.22230       -1.4163
   2    T2SQpw3       124.84         0.61590     0.11180E-01   -0.84854
   3    T2SQpw5       126.22          651.18       6.2832      -0.84437
   4    T2SQpw8       48.886         0.35172     0.97867E-02    -1.1249
 **********
 **    8 **MINIMIZE
 **********
 START MIGRAD MINIMIZATION.  STRATEGY 2.  CONVERGENCE WHEN EDM .LT. 0.10E-03
 EIGENVALUES OF SECOND-DERIVATIVE MATRIX:
        -0.1107E+00  0.9976E+00  0.1000E+01  0.2113E+01
 MINUIT WARNING IN HESSE
 ============== MATRIX FORCED POS-DEF BY ADDING  0.11280      TO DIAGONAL.

 FCN=    43.04812      FROM HESSE      STATUS=NOT POSDEF     35 CALLS      1086
TOTAL
                       EDM=  0.39E+02     STRATEGY= 2      ERR MATRIX NOT POS-DEF

  EXT PARAMETER                 APPROXIMATE        STEP         FIRST
  NO.   NAME         VALUE          ERROR          SIZE      DERIVATIVE
   1    k_1          0.11907       0.54919     0.21916E-02    -4.1510
   2    T2SQpw3       124.84         46.420     0.15804E-02   -0.39924
   3    T2SQpw5       126.22         130.78     0.35978E-02    -28.935
   4    T2SQpw8       48.886         8.3379     0.60407E-03     17.839
```

8.3.4 Spinevolution Exchange Rate Data-Fitting for Deuterated DMS

```
****** The System **********************************
spectrometer(MHz)  400
spinning_freq(kHz) 10
channels           C13
nuclei             C13 C13
atomic_coords      *
cs_isotropic       *
csa_parameters     1 -36.77 0.0625 0 54 0 ppm
csa_parameters     2 -36.77 0.0625 0 -54 0 ppm
j_coupling         *
quadrupole         *
dip_switchboard    *
csa_switchboard    *
exchange_nuclei    (1 2)
bond_len_nuclei    *
bond_ang_nuclei    *
tors_ang_nuclei    *
groups_nuclei      *
******* Pulse Sequence ******************************
CHN 1
timing(usec)      (5000)9
power(kHz)         0
phase(deg)         0
freq_offs(kHz)     0
******* Variables ***********************************
scan_par A/25.6 31.3 35.7 38.5 41.7/
power_1_1_1=A
relax_model_1=2
T2SQ_1_1=556
T2SQ_2_1=556
fit_par k_1 signal_sf
******* Options *************************************
rho0               F1x
observables        F1x
EulerAngles        zcwt538
n_gamma            *
line_broaden(Hz)   *
zerofill           *
FFT_dimensions     *
options            -re -dt1 -lv -split7 -confint -covmat
************************************************************
```

8.3.5 ^{31}P CSA Data-Fitting: Peak Intensities

```
****** The System *******
spectrometer(MHz)  600
spinning_freq(kHz) 3
channels           P31
nuclei             P31
atomic_coords      *
cs_isotropic       *
csa_parameters     1 14 0.7 0 0 0
j_coupling         *
quadrupole         *
dip_switchboard    *
csa_switchboard    *
exchange_nuclei    *
bond_len_nuclei    *
bond_ang_nuclei    *
tors_ang_nuclei    *
groups_nuclei      *
******* Pulse Sequence ******************************
CHN 1
timing(usec)      (0)32
power(kHz)         0
phase(deg)         0
freq_offs(kHz)     0
******* Variables ***********************************
pulse_1_1_1=1000/spinning_freq/32
fit_par cs_ani_1 cs_asy_1 signal_sf
******* Options **************************************
rho0               I1x
observables        I1p
EulerAngles        lebind29o
n_gamma            *
line_broaden(Hz)   *
zerofill           *
FFT_dimensions     1
options            -re -fft1 -sz5 -ws -confint
************************************************************
```

8.3.6 ^{31}P CSA Data-Fitting: Full Lineshape

```
****** The System *******
spectrometer(MHz)  600
spinning_freq(kHz) 3
channels           P31
nuclei             P31 P31
atomic_coords      *
cs_isotropic       0.1 0.57
csa_parameters     1 15 0.5 0 0 0
csa_parameters        2 0 0 0 0 0
j_coupling         *
quadrupole         *
dip_switchboard    *
csa_switchboard    *
exchange_nuclei    (1 2)
bond_len_nuclei    *
bond_ang_nuclei    *
tors_ang_nuclei    *
groups_nuclei      *
******* Pulse Sequence ******************************
CHN 1
timing(usec)       (33.33)616
power(kHz)          0
phase(deg)          0
freq_offs(kHz)      0
******* Variables ***********************************
k_1=0.5
signal_sf=0.03
fit_par cs_ani_1 cs_asy_1 signal_sf
******* Options **************************************
rho0               F1x
observables        F1p
EulerAngles        zcwt538
n_gamma            *
line_broaden(Hz)   10
zerofill           *
FFT_dimensions     1
options            -re -confint -covmat -split7
************************************************************
```

8.3.7 ^{31}P Lineshape Simulation

```
****** The System *******
spectrometer(MHz)  600
spinning_freq(kHz) 3
channels           P31
nuclei             P31 P31
atomic_coords      *
cs_isotropic       0.1 0.57
csa_parameters     1 14 0.74 0 0 0
csa_parameters        2 0 0 0 0 0
j_coupling         *
quadrupole         *
dip_switchboard    *
csa_switchboard    *
exchange_nuclei    (1 2)
bond_len_nuclei    *
bond_ang_nuclei    *
tors_ang_nuclei    *
groups_nuclei      *
******* Pulse Sequence ******************************
CHN 1
timing(usec)       (33.33)616
power(kHz)          0
phase(deg)          0
freq_offs(kHz)      0
******* Variables ***********************************
k_1=0.5
******* Options *************************************
rho0               F1x
observables        F1p
EulerAngles        zcwt538
n_gamma            *
line_broaden(Hz)   *
zerofill           *
FFT_dimensions     1
options            -re
************************************************************
```

8.3.8 $R_{1\rho}$ Dispersion for ^{31}P Ligand Exchange

```
****** The System **********************************
spectrometer(MHz)  600
spinning_freq(kHz) 7
channels           P31
nuclei             P31 P31
atomic_coords      *
cs_isotropic       0 0.15
csa_parameters     1 16 0.6 0 0 0
csa_parameters     2 0 0 0 0 0
j_coupling         *
quadrupole         *
dip_switchboard    *
csa_switchboard    *
exchange_nuclei    (1 2)
bond_len_nuclei    *
bond_ang_nuclei    *
tors_ang_nuclei    *
groups_nuclei      *
******* Pulse Sequence ******************************
CHN 1
timing(usec)       (100)4000
power(kHz)          25
phase(deg)          0
freq_offs(kHz)      0
******* Variables ***********************************
variable power_1_1=A
scan_par A/1 2 3 4 5 6 7 8 9 10 11 12 13 14 15 16 17 18 19 20 21 22 23 24 25
26 27 28 29 30 31 32 33 34 35 40 45 50 55 60 65 70 75 80 85 90 95 100 105 110
115 120 125 130 150 200/
k_1=100
******* Options **************************************
rho0               F1x
observables        F1p
EulerAngles        zcwt538
n_gamma            *
line_broaden(Hz)   *
zerofill           *
FFT_dimensions     *
options            -re -lv -dt1 -split7
*************************************************************
```

8.3.9 $R_{1\rho}$ Dispersion for Loop Dynamics of Valine 167 in Triosephospahte Isomerase

```
****** The System **********************************
spectrometer(MHz)  400
spinning_freq(kHz) 10
channels           N15
nuclei             N15
atomic_coords      *
cs_isotropic       0
csa_parameters     1 0 0 0 0 0
j_coupling         *
quadrupole         *
dip_switchboard    *
csa_switchboard    *
exchange_nuclei    *
bond_len_nuclei    *
bond_ang_nuclei    *
tors_ang_nuclei    *
groups_nuclei      *
******* Pulse Sequence ******************************
CHN 1
timing(usec)       (100)4000
power(kHz)          30
phase(deg)          0
freq_offs(kHz)      0
******* Variables ***********************************
cs_iso_1_$1=5.328
cs_iso_1_$2=5.230
cs_ani_1_$1=3.454
cs_ani_1_$2=3.819
cs_asy_1_$1=0.263
cs_asy_1_$2=0.134
cs_beta_1_$1=0
cs_beta_1_$2=30
k_exch(1,2)=10
k_exch(2,1)=10
p0_exch(1)=0.5
p0_exch(2)=0.5
pe_exch(1)=0.5
pe_exch(2)=0.5
variable power_1_1=A
scan_par A/0 5 10 15 20 25 30 35 40 45 50 55 60 65 70 75 80 85 90 95 100/
******* Options **************************************
rho0               F1x
observables        F1p
EulerAngles        zcwt538
n_gamma            *
line_broaden(Hz)   *
zerofill           *
FFT_dimensions     *
options            -re -xn2 -split7
************************************************************
```

8.4 References

[1] J. Cavanaugh, W.J. Fairbrother, A.G. Palmer, M. Rance, N.J. Skelton, Protein NMR Spectroscopy: Principles and Practices, 2nd ed., Elsevier, Burlington, MA, 2007.

[2] C. Fares, J. Qian, J.H. Davis, Magic angle spinning and static oriented sample NMR studies of the relaxation in the rotating frame of membrane peptides, J Chem Phys, 122 (2005).

[3] R. Kurbanov, T. Zinkevich, A. Krushelnitsky, The nuclear magnetic resonance relaxation data analysis in solids: General R-1/R-1 rho equations and the model-free approach, J Chem Phys, 135 (2011).

[4] R.K. Wangsness, F. Bloch, The Dynamical Theory of Nuclear Induction, Phys Rev, 89 (1953) 728-739.

[5] A.G. Redfield, On the Theory of Relaxation Processes, Ibm J Res Dev, 1 (1957) 19-31.

[6] C.P. Slichter, Principles of magnetic resonance, 3rd enl. and updated ed., Springer-Verlag, Berlin ; New York, 1992.

[7] G. Lipari, A. Szabo, Model-Free Approach to the Interpretation of Nuclear Magnetic-Resonance Relaxation in Macromolecules .1. Theory and Range of Validity, J Am Chem Soc, 104 (1982) 4546-4559.

[8] M. Veshtort, R.G. Griffin, SPINEVOLUTION: A powerful tool for the simulation of solid and liquid state NMR experiments, J Magn Reson, 178 (2006) 248-282.